Ocean Surface Roughness Anomalies in Spaceborne Microwave Remote Sensing: Wind Retrieval Biases, Marine Litter Detection and Algal Bloom Characterization

by

Gopal B. Sundaram

A dissertation submitted in partial fulfillment
of the requirements for the degree of
Climate and Space Sciences and Engineering
in the University of Michigan
2026

Doctoral Committee:

Professor Christopher S. Ruf, Chair
Assistant Professor Jessica V. Fayne
Professor Mark Flanner
Dr. Darren McKague
Associate Professor Yulin Pan

Gopal B. Sundaram

gopalsun@umich.edu

ORCID iD: 0009-0006-3581-2289

Dedication

To my family, alive and passed, for never giving up on helping me pursue my dreams. I couldn't ask for a better support system.

Acknowledgements

I'm not going to make this too extensive, because the number of people I could thank for their support and love is numerous.

I'd first like to thank Chris Ruf, my advisor. I'm incredibly grateful to have an advisor who understands me, both professionally and personally. Having an advisor who pushed me to be the best professional version of myself is all I could really ask for, and you did just that. Obviously, I have more room to grow, but the foundational skills and processes that have been laid with you as my advisor will help me immensely for years to come.

I'd like to thank my committee members, Darren McKague, Jessica Fayne, Yulin Pan and Mark Flanner. Thank you for agreeing to be a part of this journey, and for your support and advice. At some point all of you have been there to help me through a research (or a life) problem, and I appreciate all your presence in my graduate student life.

I'd like to thank the CLaSP staff and IT support, specifically Bryan, Jim and Mike for helping me out when I've needed computer and IT support. I'd especially like to shoutout Jim for dealing with me ducking his security vulnerabilities emails even when I probably shouldn't.

I would like to thank my lab mates, past and present: Dinan Bai, Charlie Powell, Maddy Evans, and the postdocs and undergrads who have rotated through our lab. It's been a lot of fun chatting and learning with you all over the years. CLaSP Room 2520 has been a fun place to work due to all of you.

A quick shoutout to the friends I've made over the years: you have made my life so much more fun. From the department, to GradTONES, to college and from back home, I'm so grateful to call you friends. I'd specifically like to shoutout Maya Fields and Erica Whiting. We've been friends since Day 1 of school, and here we are about to wrap up. Isn't that crazy? I can't wait to see where life takes you two.

To Catherine- thank you for being you. Your presence in my daily life has made my day so much better. I'm so thankful to have you as my partner. You pick me up when I stumble, and you give me pasta salad when I forget to eat dinner. What more could I ask for?

Finally, I'd like to thank my family. Mama, Papa, Uma and Ma, you guys have been there for my entire school journey. I'd like to specifically thank my mom and dad for educating me, supporting me, and believing in my abilities. With you both behind me, it feels as if I could do anything I set my mind to.

Preface

The motivation for this dissertation arose from the premise that there may be a fast and effective way to detect and track microplastics. Microplastics have been the subject of much public attention, due to their still-uncertain effects on ecosystems and human health. Large amounts of microplastics are distributed across the global ocean, from subtropical accumulation zones to coastlines. When it comes to the detection of microplastics in the ocean, the most direct approach to check for their presence is to collect the plastics using net trawls, which requires a boat to go out and collect in-situ samples of plastics across the oceans. This practice is expensive and slow, as it takes weeks to months for these ships to go across the ocean, and costs a lot of energy and manpower to conduct. Because of this, researchers have turned to other methods of trying to track microplastics, most notably using remote sensing methods. However, traditional remote sensing methods have proven challenging, as the plastics are small (<5mm) so optical remote sensing struggles to accurately place the microplastics. As an alternative, there have been microwave remote sensing methods, specifically using GNSS-R, that are suggested as a potential approach to detect and track these microplastics.

This method of detecting and tracking microplastics is an indirect method, as microwave remote sensing methods are not measuring the plastic itself, but rather the surfactant concentration that acts as a tracer of the plastics. This is possible due to all surfactant laden material's ability to damp the waves on the surface of the ocean. The dampening of the waves leads to a change in the fundamental relationship between surface roughness and near surface wind speed. This means that along with microplastics, anything that distorts the relationship between wind driven waves and wind speed can cause errors.

This thesis addresses two related but distinct objectives in the study of wind speed anomalies. The first objective is to characterize anomalies as errors or artifacts that degrade the quality of the original wind speed record. The second objective views anomalies not only as problems to be corrected, but also as signals that may contain useful information about the physical or environmental conditions that produced them. Chapter 1 introduces relevant microwave remote sensing concepts, specifically how to retrieve near-surface wind speed from these instruments. It will also provide insight into where and why the geophysical model functions (GMFs) used to estimate ocean surface wind from remote sensing observations can have shortcomings, and why the residual errors in estimated wind speed can be related to other geophysical signals. Chapter 2 will dive into two of these geophysical signals, air-sea temperature difference and precipitation rate, using the spaceborne ASCAT radar as our instrument of choice. Chapter 3 provides a justification for why the CYGNSS radar, among other microwave instruments, should be able to detect and track algal blooms, which are both a quantity of interest and a false alarm for microplastics. We do so through a wave-tank experiment, with subsequent model development from the wave-tank data and validation with satellite data. Chapter 4 provides a first look into using the KaRIn radar on the NASA SWOT mission for marine litter detection. Chapter 5 will summarize the main findings and outlines opportunities for future work towards more robust detection of pollutants and a better understanding of the causes of biases in ocean surface wind speed estimates made by spaceborne radars.

Together, these chapters frame a progression from understanding and correcting retrieval biases, to developing controlled forward models for surfactant-related roughness anomalies, to exploring higher resolution observations that may improve pollutant monitoring in coastal regions.

Table of Contents

List of Tables

List of Figures

List of Appendices

List of Acronyms

MSS Mean Square Slope

ASTD Air Sea temperature difference

PR Precipitation rate

LHF Latent heat flux

GNSS-R Global Navigation Satellite System Reflectometry

ECMWF European Center for Midrange Weather Forecasting

ERA5 ECMWF Reanalysis Data Product 5

FFT Fast Fourier Transform

ASCAT Advanced Scatterometer

CYGNSS Cyclone Global Navigation Satellite System

SWOT Surface Water and Ocean Topography

KaRIn Ka-band Radar Interferometer

SWH Significant wave height

VIIRS Visual Infrared Imaging Radiometer Suite

GMF Geophysical Model Function

N(B)RCS Normalized (Bistatic) Radar Cross Section

WSB Wind Speed Bias

MWCC MSS-Wind-Chlorophyll Concentration

ITCZ Intertropical Convergence Zone

Abstract

This thesis addresses two related but distinct objectives in the study of wind speed anomalies. The first objective is to characterize anomalies as errors or artifacts that degrade the quality of the original wind speed record. In this context, anomalies are treated as features to be detected, understood, and potentially mitigated. By identifying their spatial, temporal, and statistical signatures, it becomes possible to improve the reliability of the wind speed product, reduce bias, and support more accurate downstream applications such as climate analysis, resource assessment, and model validation.

The second objective views anomalies not only as problems to be corrected, but also as signals that may contain useful information about the physical or environmental conditions that produced them. In this case, the presence, structure, or frequency of anomalies can be used to infer the occurrence of underlying causes, such as surface conditions, atmospheric phenomena, sensor limitations, retrieval failures, or other geophysical processes. Thus, anomaly characterization serves a dual purpose: improving the original wind speed dataset while also enabling anomalies themselves to function as indirect indicators of the processes or objects responsible for their formation.

First, the relationship between ASCAT and ERA5 wind speeds and air-sea temperature difference (ASTD) and precipitation rate (PR) is examined. ASCAT is a real-aperture C-band radar that measures backscatter from the ocean surface, from which near-surface wind speed is estimated. However, backscatter variance is not fully explained by wind speed alone, and other environmental factors can perturb the signal. While ASCAT's retrieval algorithm attempts to correct for these effects and is largely successful, we focus on two geophysical variables, PR and ASTD, which correlate strongly with residual biases in both ASCAT and ERA5 wind speed products. Correction algorithms are developed to remove the dependence of bias on these variables for both products. With corrections applied, ASCAT's mean global wind speed bias is

reduced and regional variations in bias are narrowed. These biases are estimated to cause a 2.1% average global error in latent heat flux transferred from the ocean to the atmosphere.

Next, we explain why the CYGNSS radars, among other microwave instruments, should be able to detect and track algal blooms, which are both a quantity of interest and a false alarm for microplastics. Algal blooms harm marine ecosystems, threaten water quality, and can be toxic. A common detection method is hyperspectral remote sensing, which measures chlorophyll-a concentrations. Recently, evidence has suggested remote sensing measurements using the Global Navigation Satellite System Reflectometry (GNSS-R) method (e.g., CYGNSS) can also detect and track blooms. One CYGNSS data product is the Mean Square Slope (MSS) of the ocean surface, a parameter describing its roughness which is largely caused by local winds; from this we derive MSS anomalies not consistent with the local wind speed. Roughness anomalies have been linked to surfactant concentrations, and algae contain surfactants in their cells. However, GNSS-R can produce false alarms, since MSS Anomaly can also be caused by microplastics, oil, or seaweed, making algal blooms difficult to isolate without supporting data. This motivates the need to understand the connection between MSS and algae concentration. At present, there are no models linking algae concentration to MSS, highlighting the need for controlled experiments to develop forward models for improved bloom detection.

We conducted a wave tank experiment investigating how algae concentration affects surface roughness. Algae concentration and wind speed were varied, and algae runs were compared to clean-water control runs. A precision fan generated wind-waves on the water surface, and six ultrasonic probes measured surface height with high temporal resolution. The height measurements were transformed into a surface roughness spectrum via FFT and then into MSS via integration of the appropriate high order moment of the roughness spectrum. Algae concentration was assessed using Secchi disk readings. The results yield a model relating algae concentration (mg/m^3) to MSS (unitless) and near-surface wind speed (m/s), allowing any two of these parameters to be related to the third.

To evaluate this MSS-algae concentration-wind speed model, we applied it to an algal bloom that expanded from the Mississippi into the Gulf of Mexico in July 2020. The model predicted MSS changes across the inception, peak, and decay of the bloom that were generally consistent with direct observation of MSS by the CYGNSS radar.

Finally, we provide a first look at using the KaRIn radar on NASA's SWOT mission for marine litter detection. Marine litter accumulation in aquatic ecosystems presents a serious problem for subsurface marine life and human ecosystems. The CYGNSS Microplastic Product, now the Marine Litter Product, enables consistent global tracking of marine litter, but its coarse resolution and exclusion of grid cells containing land limit monitoring of coastal pollutants. To mitigate these issues, this project uses SWOT's ~2 km resolution Ka-band radar to assess coastal ocean roughness and process it into its own marine litter product using an MSS anomaly approach like CYGNSS. VIIRS chlorophyll-a data is used as a reference to assess how well the SWOT-based product can detect and track algal blooms. A preliminary SWOT Algal Bloom Product is also developed.

Chapter 1 Introduction

This chapter will review and summarize the background of the dissertation, including the foundational research that preceded it.

1.1 Background

1.1.1 Wind Driven Waves

When wind blows across the surface of the ocean, it initiates a process that roughens the surface. The friction between the air and the water surface places stress on the surface, which transfers energy and momentum from the air to the water. The energy transfer causes the water surface to roughen, initially creating small ripples. As the wind continues to blow, the energy in these small ripples cascades into larger waves, eventually resulting in a fully developed spectrum of surface roughness [1]. The winds driving these waves are a critical quantity to understanding Earth's energy balance.

1.1.2 Observations of Wind Speed

Direct observations of near-surface wind speed are traditionally obtained from anemometers mounted on ocean buoys. However, because buoys are fixed in place and sparsely distributed, these in situ measurements provide limited spatial coverage and can miss important variability across broader regions. To capture wind fields with both rapid temporal sampling and global spatial coverage, wind speed must be measured using remote sensing approaches. Remote sensing enables frequently repeated monitoring of near-surface winds over large domains, providing a practical pathway to observing wind variability at scales that stationary platforms cannot resolve. Some examples of sensors capable of detecting wind include scatterometers and passive microwave radiometers, each of which infer wind speed through its interaction with the ocean surface.

1.1.3 Retrieval Algorithms for Wind Speed Direction

Remote-sensing retrieval algorithms are most often developed empirically, especially in their earliest iterations. The basic goal is to infer a geophysical variable of interest from an observable measured by a sensor. In practice, this inference commonly proceeds by constructing a geophysical model function (GMF), which provides a one-to-one mapping between a measurement space and a geophysical parameter space. For ocean surface wind retrievals, the measurement may be the normalized radar cross section, denoted as σ_0. σ_0 serves as a proxy for sea surface roughness. Given an assumed relationship between roughness and near-surface wind speed, the GMF translates the observed backscatter into a wind speed estimate. Widely used examples of this approach include the CMOD (C-band Geophysical Model Function) family of GMFs for scatterometry and the GMFs used in the CYGNSS mission for GNSS reflectometry. Figure 1.1 from Ruf et al, 2022 [2] shows the CYGNSS GMF.

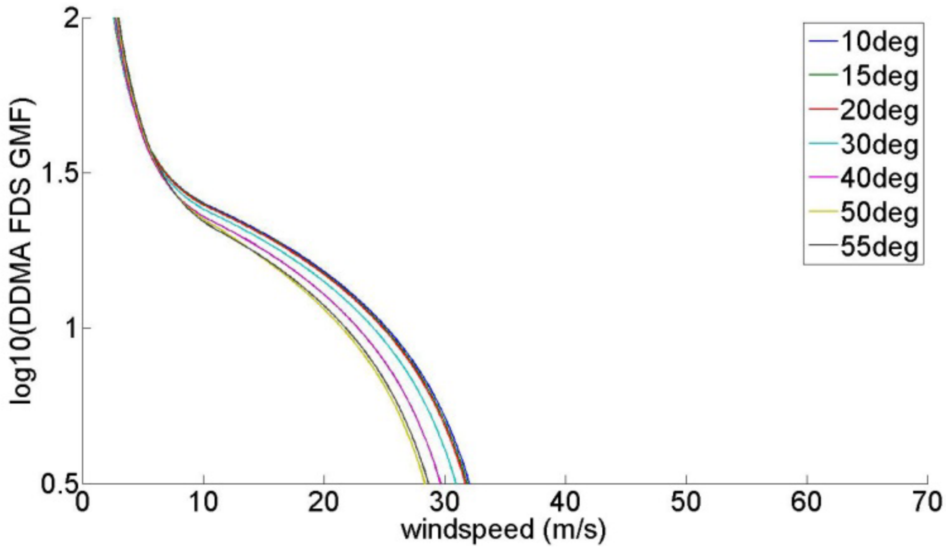

Figure 1.1: Ocean surface wind speed plotted against scattering Cross Section (DDMA, σ_0) at different incidence angles of the measurement geometry. This is the GMF used by CYGNSS to retrieve wind speed from the direct radar observable [2].

Figure 1.1 illustrates the relationship between ocean surface wind speed and the direct measurement of σ_0 and that is assumed by the CYGNSS wind speed retrieval algorithm. It is generated empirically by matching up a large population of CYGNSS measurements with coincident values of wind speed as defined by the ECMWF Reanalysis (ERA5) 10 m height referenced neutral stability wind speed product. The retrieval algorithm relies on the premise that sea surface roughness is uniquely determined by wind speed. Other physical processes that modify the surface roughness and resulting value of σ_0 can introduce a bias or error into the retrieved wind speed. Note that because the GMF is created empirically, the effects of these other physical processes are also present in the large population of data used to train the GMF. The GMF effectively averages over the impact of the other processes when creating a model function that is indexed only by wind speed. For this reason, the errors in retrieved wind speed that are caused by other physical processes result when a process deviates from its average behavior in the training population.

1.2 Anomalous Responsiveness of the Ocean Surface

Anomalous responsiveness of the ocean surface to wind speed arises when processes other than wind forcing modify the surface roughness that microwave sensors are effectively observing. When the ocean surface roughens or smooths for reasons not captured by the baseline GMF assumptions, errors can occur in the wind speed estimates. Understanding the sources of these errors is therefore essential both for improving wind products and for interpreting roughness anomalies as potential indicators of other phenomena.

1.2.1 Geophysical Parameters

An example of a source of uncertainty in the GMF is geophysical parameters that alter air-sea coupling, particularly atmospheric stability, often represented by the air-sea temperature difference. Stability modifies the efficiency with which momentum is transferred from the atmosphere to the ocean surface. Under stable conditions, reduced turbulence can suppress wave growth for a given wind speed, while unstable conditions can enhance it, shifting the effective roughness-wind relationship away from the neutral-stability form assumed by many GMFs.

Precipitation rate is another source that can produce wind-retrieval anomalies through both radiometric and physical pathways. From a measurement perspective, rain can attenuate or contaminate satellite signals, for example by energy scattered by hydrometeors and altering the apparent return received by the sensor. From an oceanographic perspective, raindrop impacts modify surface roughness directly, with the sign and magnitude of the effect depending on the length scales to which a given instrument is sensitive. Rain can increase small-scale roughness through splash and ring-wave generation while simultaneously influencing longer-scale wave fields through changes in air-sea fluxes and near-surface stratification [3].

Even when the influence of stability and precipitation is modest at any given time, small and persistent biases can accumulate into meaningful errors when products are averaged spatially and temporally or used as inputs to other calculations. Wind speed is a foundational geophysical variable, and many derived heat fluxes and parameterizations incorporate wind as an input so a minor systematic wind bias can translate into a large bias in air-sea exchanges. Variables central to Earth's energy budget, such as latent heat flux, are sensitive to near-surface wind speed and stability. Consequently, diagnosing and correcting stability and rain-dependent wind biases has implications that extend beyond improving wind fields themselves, affecting coupled atmosphere-ocean analyses and climate-relevant budgets.

1.2.2 Marine Litter

A second source of uncertainty in the GMFs is marine litter and surface films that damp short waves and therefore perturb microwave-observed roughness. In this context, "marine litter" is used broadly to include oil slicks, algal blooms, microplastics, sargassum, and other floating materials or surfactant-associated features that can modify the sea surface. These materials are problematic because of their impact on marine ecosystems and human health. A critical remote sensing issue is that they can mimic each other in microwave observations: multiple phenomena can produce similar smoothing signatures, creating ambiguity if roughness anomalies are interpreted without supporting information. The following sections will focus on two sources of marine litter that are central to this thesis.

1.2.2.1 Microplastics

Microplastics are plastics that have broken down to be smaller than 5 mm. Prior to 2015, it was common to see microplastics appear in cosmetic items such as toothpastes and cleansers. The United States banned the use of microbeads (a common form of microplastics) from personal care products, but companies and factories around the world still use them [4]. Microplastics can also come from larger plastics, such as plastic water bottles, old baby bottles, and Tupperware decomposing in the ocean. The sun's radiation and the waves break apart the plastic into smaller pieces, however those smaller pieces only decompose so far before a species mistakes it for food [5]. Sometimes these plastics are recycled, but for the most part factories dump the remains into landfills and rivers, much of which eventually flows into the ocean.

Marine wildlife have a difficult time distinguishing microplastics from small ocean creatures. Ingesting plastic has negative consequences for the health of wildlife such as turtles and fish. Plastic straws get stuck in turtles' throats causing respiratory issues, while buildups of toxic plastics in fish lead to health problems in their guts and can be fatal for the fish [6]. Unhealthy marine wildlife damages both the marine ecosystem and the human ecosystem, as fish suffering from microplastic poisoning damage fisheries by depleting supply, or by allowing humans to ingest microplastics from the fish [7]. A decrease in supply will affect economies in coastal towns, as entire regions' agriculture is based on seafood tourism. In summary, growing microplastic concentrations pose a big problem for the health of the Earth.

1.2.2.2 Algal Blooms

Algae are accumulations of phytoplankton that proliferate when sufficient sunlight coincides with elevated nutrient availability. These nutrients are most often supplied by runoff delivered through watersheds. When this accumulation occurs in an uncontrolled manner and reaches a high biomass over a broad area, it is commonly characterized as an algal bloom [8]. Such blooms occur across a wide range of marine environments including rivers, lakes and the open ocean. Algal blooms frequently concentrate along coastlines adjacent to major river outflows, where nutrient inputs and physical transport processes can promote sustained growth and aggregation [9].

Algal blooms can degrade marine ecosystem health [10]. Dense blooms may contribute to oxygen depletion in the water column, killing fish and other organisms through hypoxic conditions [11]. In addition, bloom events can impair drinking water supplies and may produce toxins that pose risks to human health through exposure or consumption of contaminated water or seafood [11]. Therefore, reliable detection and monitoring of algal blooms are essential.

1.3 Examples of Spaceborne Microwave Radars for Ocean Applications

1.3.1 Advanced SCATteromter (ASCAT)

ASCAT is a real aperture radar designed by the European Space Agency [12]. There have been three ASCAT instruments launched on three separate satellites. MetOP-A launched in 2006, MetOP-B in 2012, and MetOP-C in 2018. ASCAT uses C-band (5.7 cm wavelength) microwave scatterometry to determine the wind vectors over the ocean surface. ASCAT operations are crucial for weather forecasting, climate research, and marine weather forecasting.

ASCAT operates on a sun-synchronous polar orbit, which allows it to cover the entire globe in a 3-day period [12].

The MetOp satellites operate in a sun-synchronous polar orbit at an altitude of approximately 817 km, with an orbital inclination of about 98.7° and an orbital period of roughly 101 minutes [13]. This corresponds to about 14 orbits per day. The orbit is designed to provide consistent local solar-time sampling, with an equator crossing time of approximately 09:30 local time for the descending node. ASCAT ocean wind products are commonly distributed on wind vector cell grids with nominal spatial resolutions of 25 km and, for some products, 12.5 km [13]. Due to ASCAT's polar orbit, temporal sampling can vary depending on latitude, often providing observations roughly every 12 hours or better in many regions.

ASCAT does not measure wind speed directly. Instead, it measures the normalized radar cross section, σ^0, of the ocean surface. The relationship between σ^0 and the near-surface wind vector is described using a geophysical model function, GMF. For ASCAT, this is typically a member of the CMOD family of C-band model functions, such as CMOD5, CMOD5.N, or CMOD7 [14]. Similarly to the CYGNSS GMF, CMOD takes radar cross section, incidence angle (θ) and azimuthal angle (φ) and remaps it to 10 meter wind speed. The ability to use azimuthal angle in the GMF allows ASCAT to be able to map wind speed and direction [14].

The physical basis for ASCAT's sensitivity to ocean surface winds is Bragg resonance. For microwave radar backscatter from a rough ocean surface, the dominant contribution often comes from surface waves whose wavelengths satisfy the Bragg scattering condition [15]. In the backscatter geometry, constructive interference occurs when the ocean surface wavelength is approximately one-half of the radar wavelength projected onto the line of propagation between the radar and the sea surface. The resonant surface wavenumber is

$$k_B = 2ksin(\theta) \tag{1.1}$$

where k is the radar wavenumber and θ is the incidence angle. Using ASCAT's radar wavenumber, this gives Bragg-resonant ocean waves of roughly 3-7 cm. These short gravity-capillary waves respond quickly to local wind stress [16]. This means ASCAT is particularly sensitive to a specific portion of the ocean wave roughness spectrum, denoted S(k).

1.3.2 Surface Water and Ocean Topography (SWOT) Mission

We consider use of the NASA Surface Water & Ocean Topography (SWOT) Mission's radar as well [13]. SWOT carries a Ka-Band (0.86 cm wavelength) altimetric radar and its primary mission objective is water surface height topography. It makes ocean surface roughness measurements (specifically, σ_0) as a secondary correction for sea surface height. SWOT's Low-Rate Sea Surface Height Data Product has a resolution of 2km in both the cross-track and along-track directions [17]. SWOT flies in a non-sun-synchronous orbit with an altitude of approximately 891 km, an inclination of about 77.6°, and an orbital period of roughly 112 minutes. The science orbit has a 21-day exact repeat cycle, during which the ground tracks repeat after 292 orbits [17]. This orbit was selected to provide broad coverage of the global ocean and inland water surfaces while avoiding the aliasing characteristics that would result from a sun-synchronous sampling pattern. SWOT is a near-nadir altimeter, with incidence angles between 0.8˚ and 4˚ [17].

A geophysical model function can be used to relate SWOT σ_0 to environmental and observational parameters. For near-nadir Ka-band observations, the relevant GMF differs substantially from the ASCAT GMF. The ASCAT GMF is physically dominated by Bragg resonance, which is central to interpreting moderate incidence angle scatterometer measurements [15]. However, Bragg resonance does not provide the primary physical explanation for SWOT σ_0. SWOT observes at very small near-nadir incidence angles, where the backscatter is dominated instead by quasi-specular reflection. Quasi-specular reflection from SWOT is dependent on three factors: wind speed, incidence angle, and significant wave height [18, 19].

Wind speed affects the waves in the way described in Section 1.1. Incidence angle dependance is especially strong for near-nadir instruments because as incidence angle increases across the SWOT KaRIn swath away from nadir, the signal reflected back to the SWOT satellite decreases. This concept will be explored in Section 4.2.5. Significant wave height (SWH) affects σ_0 through alterations of the ocean surface due to swell. Including SWH in the GMF accounts for the fact that SWOT backscatter is not only a function of locally generated capillary waves and short gravity waves, but also of the broader sea-state conditions that control surface slopes [19].

Because of its σ_0 measurements, it has the potential for marine litter detection. This concept will be explored in Chapter 4.

[Need to expand on this SWOT section. Include the following: orbit parameters of the satellite; temporal sampling (revisit time); description of the GMF, including its dependence on wind speed, incidence angle, and significant wave height; explanation of why Bragg resonance does not apply to SWOT measurements of σ_o and how its measurements are related to the roughness spectrum, S(k)]

1.3.3 CYclone Global Navigation Satellite System (CYGNSS)

The Cyclone Global Navigation Satellite System (CYGNSS) is a constellation of eight small satellites that were sent into Low Earth Orbit (LEO) in December 2016. CYGNSS uses bistatic radar, meaning the transmitter and receiver are separate objects. The eight small satellites are receivers, using L-Band signals transmitted from military GPS, operating at a wavelength of 19 cm. Their main purpose is to detect and track the progress and strength of hurricanes using a novel method, known as Global Navigation Satellite System Reflectometry (GNSS-R). This wavelength allows the signal to penetrate through the clouds of a hurricane, and to not be scattered or attenuated by the heavy rain that takes place in the eyewall of a hurricane. The signal is then reflected off the ocean surface and sent back to a receiver that measures the bistatic radar cross section (BRCS), which is the principal output variable of the CYGNSS mission [20].

At launch, the constellation had an altitude of approximately 500-520 km, an inclination of about 35°, and an orbital period of roughly 95 minutes. The CYGNSS Level 2 wind observations are irregularly distributed along the specular-point tracks and are commonly treated as having an effective spatial resolution on the order of 25 km, while gridded Level-3 products are typically provided on regular latitude-longitude grids, for example 0.2°×0.2°, with temporal averaging intervals such as daily or sub-daily composites [21]. In Section 1.1.3 the CYGNSS GMF was discussed and similarly to SWOT, it does not use Bragg scattering as its main physical mechanism. Because CYGNSS uses a forward scattering specular geometry for its measurements, Bragg resonance is not a relevant scattering mechanism and the scattering cross section depends more generally on the roughness spectrum, S(k).

Most of the work that went into the introduction of this thesis was done using CYGNSS as the primary imager. The discussion of the state of the art before this thesis will involve using CYGNSS, more than ASCAT or SWOT.

1.4 The state of the art before this dissertation

At the start of the work for this dissertation, the CYGNSS Microplastic Product v3.2 had been released [22]. The microplastic product is known to be more of a marine litter product due to how it is developed, but until the changes from the body of this dissertation are made, it remains as such.

For this dissertation, the process of developing the CYGNSS Microplastic Product is introduced and the method used for MSS Anomaly calculation is highlighted, as the MSS Anomalies represent spatial and temporal deviations from an expected MSS-wind relationship, and therefore quantify, in an observational sense, the residual errors or unmodeled variability in the baseline GMF.

1.4.1 MSS Anomaly Development

CYGNSS MSS Anomaly is a derived product that describes how different the ocean roughness is from a modeled "normal" version of ocean roughness forced by near surface ocean wind. Global maps of MSS Anomaly illustrate areas where ocean roughness suppression occurs, which is hypothesized to be directly caused by surfactant concentrations and indirectly correlated with microplastic and algal bloom concentrations.

The MSS Anomaly is defined by

$$MSS_{ANOM} = \frac{MSS_{obs} - MSS_{mod}}{MSS_{mod}} \tag{1.2}$$

where MSS_{obs} is the observed MSS from satellite data and MSS_{mod} is a theoretical MSS value calculated using an empirical MSS model forced by ECMWF Reanalysis (ERA5) wind speed data [23]. The model was constructed from MSS observations and wind data taken from a clean ocean region free from contaminants and anomalous conditions.

The MSS observations themselves are calculated using

$$MSS_{obs} = \frac{|R(\epsilon, \theta)|^2}{\sigma_0} \tag{1.3}$$

where $R(\varepsilon, \theta)$ is the Fresnel Reflection coefficient and σ_0 is the normalized radar cross section (NRCS) [24]. NRCS is measured by the SWOT radar and is notably sensitive to near surface wind speed.

1.4.2 MSS Model (MSS$_{MOD}$), **Control Region Generation**

To understand how ocean pollutants affect the ocean surface, a region of the Earth with minimal contamination should serve as the control, to show a clear relationship between MSS and windspeed. The microplastic model shown in Figure 1.2 identifies locations with low plastic concentration that can serve as our control region for this project.

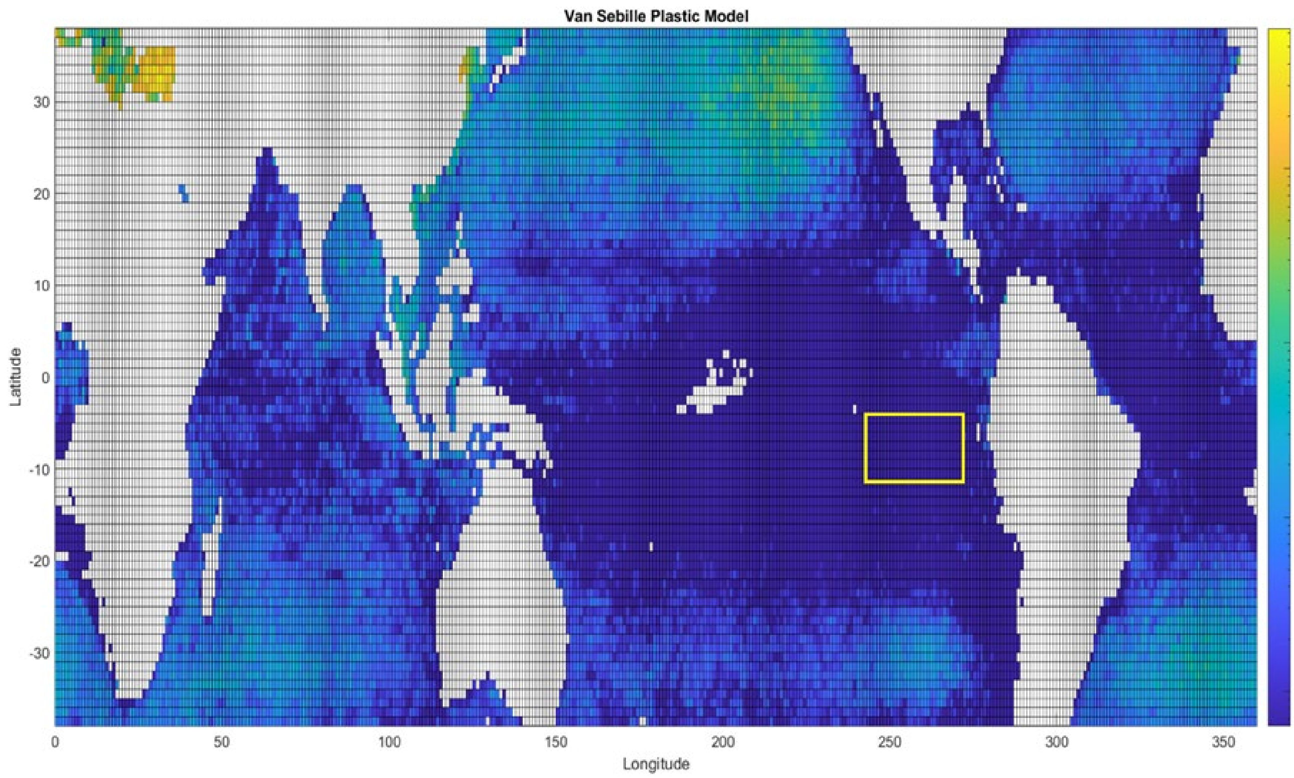

Figure 1.2: Global Microplastic Distribution from the Van-Sebille model with Control Region overlaid on top.

With this control region, a density scatter plot is made of the MSS vs. ERA5 Wind Speed data, and a least square polynomial expression is fit to it as the MSS Model.

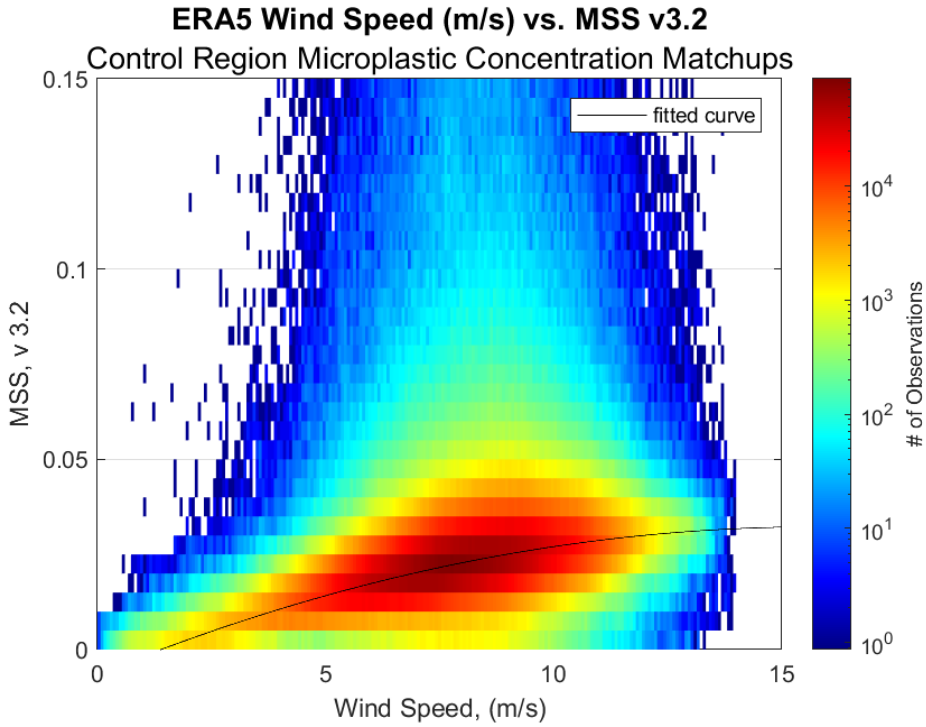

Figure 1.3: Density scatter plot of CYGNSS observed MSS vs. ERA5 Wind Speed. Polynomial fit equation on right [15].

The least squares fit gives us an empirical relationship between MSS and Wind Speed that serves as the model MSS in Equation 1.2. Using this model, for a given wind speed a modeled MSS is calculated and compared to the CYGNSS observation. From this, an MSS Anomaly is created for each data point taken by CYGNSS.

1.4.3 MSS Anomaly: Quantified Errors in the Wind Speed Retrieval Algorithm

Using the methodology developed in the previous section, plots of the global MSS Anomaly can be produced for the 2021 calendar year. The results are shown in Fig. 1.4.

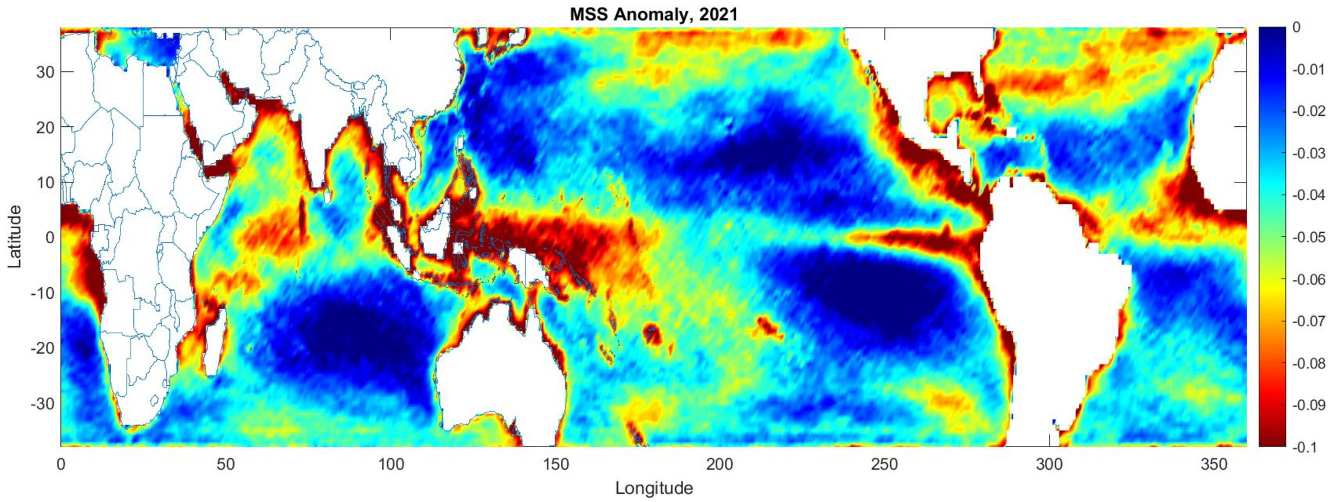

Figure 1.4: CYGNSS MSS Anomaly, 2021 average. The more negative the anomaly, the more the ocean roughness is suppressed.

Figure 1.4 demonstrates where the notable hotspots of MSS Anomaly are across the year. Interpreting MSS Anomaly in a physically meaningful way requires separating contributions from atmospheric conditions and from surface-film or floating-material effects. Treating anomalies as structured residuals rather than noise supports both targeted GMF corrections for improved wind retrieval and the development of detection strategies for marine litter and other non-wind signals.

1.5 Novel Contributions of this Dissertation

This thesis addresses two related but distinct objectives in the study of wind speed anomalies. The first objective is to characterize anomalies as errors or artifacts that degrade the quality of the original wind speed record. In this context, anomalies are treated as features to be detected, understood, and potentially mitigated. By identifying their spatial, temporal, and statistical signatures, it becomes possible to improve the reliability of the wind speed product, reduce bias, and support more accurate downstream applications such as climate analysis, resource assessment, and model validation.

The second objective views anomalies not only as problems to be corrected, but also as signals that may contain useful information about the physical or environmental conditions that produced them. In this case, the presence, structure, or frequency of anomalies can be used to infer the occurrence of underlying causes, such as surface conditions, atmospheric phenomena, sensor limitations, retrieval failures, or other geophysical processes. Thus, anomaly characterization serves a dual purpose: improving the original wind speed dataset while also enabling anomalies themselves to function as indirect indicators of the processes or objects responsible for their formation.

In summary, the work presented in this thesis makes the following novel contributions.

1.5.1 Characterization of Residual Biases in the ASCAT and ERA5 Wind Speed Product

This study evaluates the relationships between ASCAT- and ERA5-derived wind speeds and two environmental variables: the air–sea temperature difference (ASTD) and precipitation rate (PR). ASCAT is a real-aperture C-band scatterometer that measures microwave backscatter from the ocean surface, from which near-surface wind speed is retrieved. However, variability in the backscatter signal is not solely attributable to wind forcing; additional geophysical and atmospheric processes can perturb the measurement. Although the ASCAT retrieval algorithm includes corrections for several such effects and performs well overall, we isolate PR and ASTD because they exhibit strong associations with residual wind-speed biases in both ASCAT and ERA5. We develop bias-correction schemes that remove the dependence of wind-speed bias on PR and ASTD for each product. After applying these corrections, the global-mean ASCAT wind-speed bias is reduced, and the magnitude of regional bias variability is decreased. The uncorrected biases are estimated to contribute an average global error of 2.1% in ocean-to-atmosphere latent heat flux.

1.5.2 MSS-Algal Bloom-Wind Speed Forward Model

We next describe why the CYGNSS mission, and GNSS reflectometry (GNSS-R) more broadly, has the potential to detect and monitor algal blooms.

Here, we compute MSS anomalies and interpret them as indicators of roughness perturbations. A central challenge, however, is non-uniqueness: MSS anomalies can also arise from other slick-forming materials such as microplastics, oil, or floating vegetation. Consequently, GNSS-R-based detection can produce false positives unless supplemented with independent information. This motivates quantifying the functional relationship between MSS and algal concentration.

To address this gap, we performed controlled wave-tank experiments to quantify the dependence of surface roughness on algal concentration under varying wind forcing. We systematically varied algal concentration and wind speed and compared algae treatments against clean-water control runs. Wind waves were generated using a fan, and wave elevations were recorded using six ultrasonic probes. Time-series measurements were converted to a wave-roughness spectrum using a fast Fourier transform (FFT) and subsequently integrated to estimate MSS. Algal concentration was quantified using Secchi disk measurements. These experiments yield an empirical model relating algal concentration to MSS and near-surface wind speed, enabling any one of the three variables to be inferred from the other two.

We evaluated the resulting MSS-algae concentration-wind speed model using a case study of an algal bloom that expanded from the Mississippi River outflow into the Gulf of Mexico in July 2020. The model predicted MSS variations associated with the bloom's initiation, peak intensity, and subsequent decay which were generally consistent with direct observations of MSS by the CYGNSS constellation of radars.

1.5.3 SWOT Algal Bloom Product

Finally, we present an initial assessment of the KaRIn instrument on NASA's SWOT satellite for detecting marine litter. Marine litter accumulation in aquatic ecosystems poses significant risks to subsurface marine organisms and to human communities that depend on these environments. The CYGNSS Microplastic Product supports consistent global monitoring of marine litter, but its relatively coarse spatial resolution and exclusion of grid cells containing land constrain its utility for tracking coastal pollution.

To address these limitations, we leverage SWOT's Ka-band radar observations at ~2 km resolution to characterize coastal ocean surface roughness and to generate a SWOT-based marine litter product using an MSS-anomaly methodology analogous to that used for CYGNSS. Product performance is evaluated using VIIRS chlorophyll-a observations to test the capability of the SWOT-based approach to detect and track algal blooms. Upon successful development, we also provide an initial demonstration of a SWOT Algal Bloom Product.

These novel contributions have resulted in journal publications and conference proceedings. The following list of papers, proceedings and presentations contributed to the development of this thesis.

1.6 Summary of Written and Presented Work

1.6.1 Journal Articles, Published or In Review

Sundaram, G. B. & Ruf, C. S. Identifying and Correcting for Residual Biases in the ASCAT and ERA5 Wind Speed Products. *IEEE Journal of Selected Topics in Applied Earth Observations and Remote Sensing* **19**, 1438–1451 (2026).

Sundaram, G. B. et al., Characterizing the Effects of Algal Blooms on Ocean Surface Roughness via a Wavetank Experiment and Spaceborne Radar Demonstration (*Nature: Scientific Reports, in review, 2026*).

Sundaram, G. B. & Ruf, C. S., Monitoring Coastal Ocean Pollutant Dynamics with NASA SWOT Remote Sensing Observations (*Remote Sensing, in review, 2026*).

1.6.2 Peer Reviewed Conference Proceedings

G. B. Sundaram and C. S. Ruf, "A Zero Current Equivalent Wind Correction for Remotely Sensed Winds," *IGARSS 2024 - 2024 IEEE International Geoscience and Remote Sensing Symposium*, Athens, Greece, 2024, pp. 5973-5975, doi: 10.1109/IGARSS53475.2024.10640526

G. B. Sundaram and C. S. Ruf, "The Detection and Tracking of Ocean Surface Roughness Suppression by Ocean Pollutants Via Surfactants," *IGARSS 2024 - 2024 IEEE International Geoscience and Remote Sensing Symposium*, Athens, Greece, 2024, pp. 6045-6048, doi: 10.1109/IGARSS53475.2024.10642822

1.6.3 Conference Presentations

"Identifying and Correcting for Residual Biases in the ASCAT Wind Speed Product" Gopal Sundaram, American Meteorological Society, Houston, TX, 1/29/2026. (Oral Session)

"Quantifying the Effects of Algal Blooms on Ocean Surface Roughness via a Wave tank experiment and Hyperspectral Imager Data" Gopal Sundaram, American Geophysical Union, New Orleans, LA., 12/16/2025 (Poster Session)

"The Effect of Algal Blooms on Ocean Surface Roughness, and their Detection via GNSS-R Satellites" Gopal Sundaram, American Geophysical Union, Washington, D.C., 12/13/2024. (Poster Session)

"The Detection and Tracking of Ocean Pollutants using Surfactants as a tracer with a GNSS-R Spaceborne Radar", Gopal Sundaram, American Geophysical Union, San Francisco, CA, 12/15/2023. (Oral Session)
"A Potential Zero Current Equivalent Wind Correction for GNSS-R and Other Remotely Sensed Wind Products", Gopal Sundaram, American Geophysical Union, San Francisco, CA, 12/14/2023 (Poster Session)
"The Detection of Algal Blooms by Their Suppression of Ocean Surface Roughness", Gopal Sundaram, IEEE Geosciences and Remote Sensing Symposium, Pasadena, CA, 7/20/2023 (Talk)
"The Detection of Algal Blooms and Microplastics via Suppression of Ocean Surface Roughness using a GNSS+R Spaceborne Radar", Gopal Sundaram, GNSS+R Workshop, Boulder, CO, 5/25/2023 (Oral Session)
"The Suppression of Ocean Surface Roughness by Algal Blooms and Surfactants Acting as Microplastic Tracers", Gopal Sundaram, American Geophysical Union, Chicago, IL, 12/16/2022 (Oral Session)

1.7 References for Chapter 1

1. Pizzo, N., Deike, L. & Ayet, A. How does the wind generate waves? *Physics Today* **74**, 38–43 (2021).

2. Ruf. C. S. et al. CYGNSS Handbook (2nd ed.), Michigan Publishing Services, Ann Arbor, MI, ISBN 978-1-60785-549-1, https://doi.org/10.3998/mpub.12741920, 227 pp, 2022.

3. Laxague, N. J. M. & Zappa, C. J. The Impact of Rain on Ocean Surface Waves and Currents. *Geophysical Research Letters* **47**, e2020GL087287 (2020).

4. Rochman, C. M. *et al.* Scientific Evidence Supports a Ban on Microbeads. *Environ. Sci. Technol.* **49**, 10759–10761 (2015).

5. Amaral-Zettler, L. A., Zettler, E. R. & Mincer, T. J. Ecology of the plastisphere. *Nat Rev Microbiol* **18**, 139–151 (2020).

6. Li, Y., *et al.,* "Research on the Influence of Microplastics on Marine Life," *IOP Conf. Ser.: Earth Environ. Sci.,* vol 631, 2021

7. Campanale, C., Massarelli, C., Savino, I., Locaputo, V. & Uricchio, V. F. A Detailed Review Study on Potential Effects of Microplastics and Additives of Concern on Human Health. *International Journal of Environmental Research and Public Health* **17**, 1212 (2020).

8. Application of Novel Nanomaterials for Chemo- and Biosensing of Algal Toxins in Shellfish and Water. in *Novel Nanomaterials for Biomedical, Environmental and Energy Applications* 353–414 (Elsevier, 2019). doi:10.1016/B978-0-12-814497-8.00012-6.

9. Hudnell, H. K. The state of U.S. freshwater harmful algal blooms assessments, policy and legislation. *Toxicon* **55**, 1024–1034 (2010).

10. Lopez, C. B. Scientific assessment of freshwater harmful algal blooms. (2008).

11. Misiou, O. & Koutsoumanis, K. Climate change and its implications for food safety and spoilage. *Trends in Food Science & Technology* **126**, 142–152 (2022).

12. Klaes, K. D. The EUMETSAT Polar System. in 192–219 (Elsevier, 2018). doi:10.1016/B978-0-12-409548-9.10318-5.

13. Advanced Scatterometer (ASCAT) Wind Product User Manual, Version 1.17. Ocean and Sea Ice SAF Project Team, 2021

14. Hersbach, H., Stoffelen, A. & de Haan, S. An improved C-band scatterometer ocean geophysical model function: CMOD5. *Journal of Geophysical Research: Oceans* **112**, (2007).

15. Wright, J. W. & Keller, W. C. Doppler Spectra in Microwave Scattering from Wind Waves. *Phys. Fluids* **14**, 466–474 (1971).

16. Liu, Y. & Yan, X.-H. The Wind-Induced Wave Growth Rate and the Spectrum of the Gravity-Capillary Waves. *Journal of Physical Oceanography* **25**, 3196–3218 (1995).

17. Surface Water Ocean Topography (SWOT). 2025. SWOT Level 2 KaRIn Low Rate Sea Surface Height Data Product, Version D. Ver. D. PO.DAAC, CA, USA. Dataset accessed [2026-01-14] at https://doi.org/10.5067/SWOT-SSH-D

18. McQuillan, K. A., Allen, G. H., Fayne, J., Gao, H. & Wang, J. Estimating Wind Direction and Wind Speed Over Lakes With Surface Water Ocean Topography and Sentinel-1 Satellite Observations. *Earth and Space Science* **12**, e2024EA003971 (2025).

19. Stiles, B. W. *et al.* Ocean Surface Wind Speed Retrieval for SWOT Ka-band Radar Interferometer. in *IGARSS 2024 - 2024 IEEE International Geoscience and Remote Sensing Symposium* 1422–1425 (2024). doi:10.1109/IGARSS53475.2024.10640472.

20. Ruf, C.S. et al. *CYGNSS Handbook.* Ann Arbor, MI: Michigan Publishing Services, 2022. https://doi.org/10.3998/mpub.12741920. PDF.

21. Clarizia, M. P., Ruf, C. S., Gleason, S., Balasubramaniam, R. & McKague, D. Generation of cygnss level 2 wind speed data products. in *2017 IEEE International Geoscience and Remote Sensing Symposium (IGARSS)* 2647–2649 (2017). doi:10.1109/IGARSS.2017.8127539.

22. Evans, M. C, Ruf, C. S. & Sundaram, G. B. CYGNSS Microplastic Product Version 3.2 Algorithm Theoretical Basis Document, (2024)

23. Hersbach, H. et al., "ERA5 hourly data on single levels from 1940 to present," Copernicus Climate Change Service (C3S) Climate Data Store (CDS), 2023. [Online] Available: doi:10.24381/cds.adbb2d47. Accessed: Dec. 3, 2025.

24. Ruf, C.S. *et al.* "Level 2 Mean Square Slope Retrieval" in *CYGNSS Handbook,* 2nd ed. Ann Arbor, MI, U.S.A: UofM Press, 2022, ch. 6 sec. 3, pp. 71-72

Chapter 2 Identifying and Correcting for Residual Biases in the ASCAT and ERA5 Wind Speed Products

2.1 Introduction

Ocean winds play a critical role in Earth's climate system by driving oceanic heat transport. Heat is transported across the globe through ocean currents, which are influenced by the near surface winds. The currents transporting heat regulate temperature and influences weather patterns across the planet. Therefore, the ability to monitor and track ocean winds is critical to monitoring changes in global weather patterns. Directly measuring the wind requires devices such as an anemometer, and while these machines have been around for centuries, having an in-situ network of anemometers and monitors is impractical. Thus, we turn to satellite-borne techniques and sensors [1]. Satellite coverage allows for near real time global observations of ocean winds. These remote sensing methods are the standard observational method for the best spatial and temporal coverage.

This leads to three questions: What exactly are the satellites measuring? What kind of sensors measure wind speed? How accurate are these satellite-borne measurements? We consider answers to these questions in the following sections.

2.1.1 Wind Driven Waves

When wind blows across the surface of the water, it initiates a process that roughens the surface. The friction between the air and the water surface places stress on the surface, which transfers energy and momentum from the air to the water. The energy transfer causes the water surface to roughen, initially creating small ripples. As the wind continues to blow, the energy in these small ripples cascades into larger waves, eventually resulting in a fully developed spectrum of surface roughness [2].

The friction between the wind and the water can be intensified by unstable atmospheric conditions. Unstable atmospheric conditions occur when the sea surface temperature is warmer than the near surface air temperature, leading to warm air rising from the surface of the ocean. The sinking of higher cold air parcels and the rising of lower warm air parcels increases the vertical mixing. Vertical mixing of winds leads to an increase in turbulent flow, which leads to greater interaction between surfaces [3]. A higher rate of interaction between the atmosphere and ocean surface increases the friction between them. A common way to quantify the stability of the atmosphere is by the difference between the sea surface temperature and the near surface air temperature, henceforth referred to as the air-sea temperature difference [4].

2.1.2 Satellite Based Wind Speed Products

2.1.2.1 Scatterometers

For satellite wind products, the most common active sensor used is a scatterometer, which is a type of microwave radar [5]. Scatterometers are designed to measure the backscatter of radar signals from the Earth's surface. When a radar signal is incident on the surface of the ocean, reflection and scattering occur. The extent of the signal power that scatters in various directions is primarily determined by the roughness of the ocean surface [6]. The backscattered power received by the radar is proportional to the normalized radar cross-section, σ_0, of the surface, from which it is possible to derive the near ocean surface wind velocity [7]. Notable examples of scatterometers include SeaWinds [8], SCATSAT-1 [9], and ASCAT [10]. This paper focuses on the wind speeds retrieved by the ASCAT satellite system.

The Advanced Scatterometer (ASCAT) is a real aperture radar designed by the European Space Agency [11]. There have been three ASCAT instruments launched on three separate satellites. MetOP-A launched in 2006, MetOP-B in 2012, and MetOP-C in 2018. ASCAT uses C-band microwave scatterometry to determine the wind vectors over the ocean surface. ASCAT operations are crucial for weather forecasting, climate research and marine weather forecasting. ASCAT operates on a sun-synchronous polar orbit which allows it to cover the entire globe in a 3-day period [11].

2.1.2.2 Relationship between Satellite Data and Wind Speed

As mentioned above, it is possible to derive the near ocean surface wind velocity from the normalized radar cross-section (σ_0) of ASCAT. The bridge between these two variables is described by the radar range equation and geophysical modeling functions (GMFs). The radar range equation is the relationship between σ_0, and the power received by the radar, as given by

$$P_r = \frac{P_t G^2 \lambda^2 A L}{(4\pi)^3 R^4} \sigma_0 \tag{2.1}$$

where P_r and P_t represent the received and transmitted power, G is the antenna gain, λ is the wavelength, R is the distance from the radar to the target, A is the area of the radar target, L is a generalized loss factor that accounts for atmospheric attenuation and system loss, and σ_0 is the normalized radar cross section [12]. Everything on the right side of the equation aside from σ_0 is known from the engineering of the sensor, antenna, and spacecraft. Received power is our incoming data, so (2.1) can be rearranged to solve for σ_0.

The relationship between σ_0 and wind speed is determined using a geophysical modeling function (GMF). A geophysical modeling function is an empirical fit which uses a training data set to establish an empirical monotonic relationship between NRCS and wind speed. For the ASCAT operational wind product, a GMF named CMOD5 is used [13]. Since the GMF uses a global distribution of training data, it may not fully account for regional differences where conditions are significantly different from the global norm.

2.1.3 Environmental Parameters

Near ocean-surface wind velocity is not the only environmental variable that affects scatterometer retrievals. Overall, σ_0 is determined by ocean surface roughness and surface dielectric properties. Wind-driven waves affect the surface roughness through processes described below (see the Wind Driven Waves section). However, there are other environmental parameters that affect the surface dielectric properties like sea surface salinity and temperature. There are also variables that affect the received power (P_r), such as humidity and precipitation [14]. These external variables can change the received power, which can change the estimate of σ_0 and cause errors if the environmental factors are not properly corrected.

Precipitation Rate (PR) is defined as the rate at which water falls onto the surface, for a given period. Precipitation has been shown to affect remote sensing measurements of the ocean surface. It can cause attenuation of the radar signal affecting the received power in (1), increase the roughness of the ocean surface with ring-waves [15], and cause reflections off the raindrops themselves. There are a multitude of missions designed to track precipitation, one of which is the Global Precipitation Measurement (GPM) Mission. GPM has been tracking precipitation data for over ten years and is a global standard for precipitation data.

Air Sea Temperature Difference (ASTD) refers to the difference in temperature between the air just above the surface of the ocean (T_a) and the surface water itself (T_s) and is defined as

$$ASTD = T_s - T_a. \tag{2.2}$$

ASTD directly affects the atmospheric stability of the air-ocean boundary layer. If it is positive, the conditions are unstable. As mentioned in the Wind Driven Waves section, unstable conditions at the ocean surface lead to an increase in turbulence and vertical mixing, which enhances the surface stress on the ocean. Increasing the vertical mixing at the ocean boundary layer raises surface waves [16], which affects the relationship between ocean surface roughness and near surface wind velocity.

2.1.4 ERA5 Data & Buoy Data

The ECMWF ERA5 wind speed data product is often utilized for validation purposes due to its gap-free data and consistent spatial and temporal resolution. The ERA5 wind speed data product is produced by reprocessing current climate observations through modern data assimilation systems, integrating records from surface weather stations, satellite data, and airborne sources to create a spatially gridded dataset updated every hour [17]. This makes ERA5 useful for ASCAT data comparisons. The ERA5 from 0900 and 1000 is used to temporally interpolate an 0930 measurement. The same process is used between 2100 and 2200. This project uses this temporally interpolated ERA5 data collocated to the ASCAT orbit, at 0930 and 2130. This is true for any standard or derived ERA5 product used.

It is important to note that ERA5 is not ground truth, it is a reanalysis model [18]. Its accuracy can be affected in areas with sparse or inaccurate observations. Therefore, while ERA5 provides one means for assessing ASCAT accuracy, it is prudent to supplement it where possible with other estimates of environmental parameters. One such data source is in-situ measurements collected by ocean buoys.

Buoy measurements generally include wind speed, wind direction, sea surface temperature and 2-meter air temperature. Buoy data are accessed via the NOAA National Data Buoy Center (NDBC) [19].

2.1.5 Project Objectives

This paper seeks to identify and correct residual biases in the ASCAT and ERA5 wind speed products, recognizing the potential issues in both. Refining both products, even with corrections on the order of 0.5 m/s, can have a large impact on other variables and products that use wind speed as an input. We correlate residual biases in the ERA5 and ASCAT wind speed product with two environmental variables, precipitation rate (PR) and air-sea temperature difference (ASTD). Precipitation rate (PR) and air-sea temperature difference data are taken from ERA5 reanalysis data products. After correlating the biases, a correction algorithm is developed to correct for these residual biases.

2.2 Methodology

2.2.1 Data Source Description

Table 1 details the specific datasets used, and includes details such as spatial and temporal gridding, version number/access data, and the URL where the datasets are available.

Table 2.1: Data Description and Source Location

Product↓/ Descriptor →	Data type	Version Number/Access Date	Spatial/Temporal Gridding	Data Duration	URL for dataset
ERA5 2-meter air temperature (T_a)	Reanalysis Data	V5, Accessed 09/09/2024 from Copernicus Climate Data Store	0.2˚x0.2˚, 1 hour	01/01/2021-12/31/2021	https://cds.climate.copernicus.eu/datasets/reanalysis-era5-single-levels?tab=download
ERA5 Sea Surface Temperature (T_s)	Reanalysis Data	V5, Accessed 09/09/2024 from Copernicus Climate Data Store	0.2˚x0.2˚, 1 hour	01/01/2021-12/31/2021	https://cds.climate.copernicus.eu/datasets/reanalysis-era5-single-levels?tab=download
ERA5 10m Wind (U_{10})	Reanalysis Data	V5, Accessed 02/01/2024 from Copernicus Climate Data Store	0.2˚x0.2˚, 1 hour	01/01/2021-12/31/2021	https://cds.climate.copernicus.eu/datasets/reanalysis-era5-single-levels?tab=download
ERA5 10m Zero Current Equivalent Wind (U_{zc})	Modified Reanalysis Data	V1, Created 08/19/2023	0.5˚x0.5˚, 1 hour	01/01/2021-12/31/2021	Local Host
ASCAT Wind Speed (U_{ASCAT})	Satellite Data (ASCAT-C sensor, aboard MetOP-C)	V02.1, Accessed 02/01/2024 from Remote Sensing Systems	0.25˚x0.25˚, 1 day	01/01/2021-12/31/2021	ftp://ftp.remss.com/ascat
NDBC Buoy Winds (U_{BUOY})	In-situ wind speed data collected from various buoys	Accessed 03/14/2025 from NDBC	0.001˚x0.001˚, 1 hour	08/01/2018-05/31/2020	https://www.ndbc.noaa.gov/obs.shtml

2.2.2 Exploring the Data Sources and Examining the Variables

2.2.2.1 Standard ASCAT Wind Speed Bias Maps

ASCAT wind speed bias is defined here as the difference between the ASCAT wind speed (U_{ASCAT}) and the ERA5 Zero Current equivalent wind speed (U_{zc}), given by

$$WSB_{ASCAT} = U_{ASCAT} - U_{ZC}. \qquad (2.3)$$

WSB_{ASCAT} is gridded on a 0.5˚x0.5˚ grid, as U_{zc} was developed on that grid size. WSB_{ASCAT} is a daily product, which can then be averaged over seasons or the year. U_{zc} is a reference wind that takes the standard ERA5 10m winds and adjusts them for ocean surface currents. The Zero Current Equivalent Wind is used to account for the difference in reference frames between satellite-based wind products and the ERA5 reanalysis winds. See Appendix A for a full explanation of U_{zc} and its use.

To evaluate (2.3), the spatial and temporal grids of both righthand variables must be the same size. The temporal grid and duration are the same size, but there is a difference in the spatial grid (see Table 1). Thus, spatial regridding must be done to match the products. A nearest neighbor averaging scheme is used to change the ASCAT wind speeds from a 0.25˚x0.25˚ grid to a 0.5˚x0.5˚ grid. Fig. 1 is a global map of the wind speed bias averaged over CY 2021. Averaging over a full year shows the areas of persistent bias throughout the year, although it may wash out seasonal biases that change sign throughout the year.

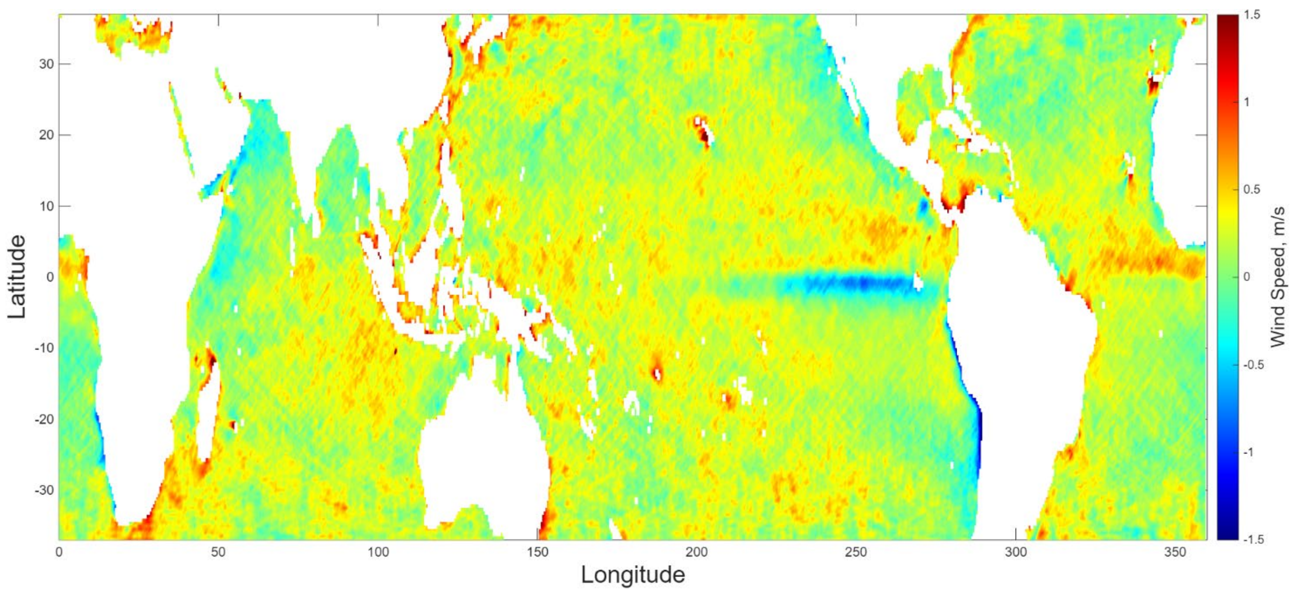

Figure 2.1: ASCAT wind speed bias plot averaged over 2021. The ERA5 Zero Current Equivalent Wind is the reference wind used as ground truth. Notable areas of wind speed bias include the ITCZ, around the Kuroshio and Gulf Currents and around Indonesia.

As shown by Fig. 1, there are regions where persistent wind speed biases are present. The ITCZ in both the Pacific and Atlantic Oceans has a consistent positive bias, meaning ASCAT is overestimating wind speeds when compared to the model. The Gulf Stream [280˚-290˚ E, 15˚-35˚ N], the Kuroshio Current [120˚-145˚E, 15˚-35˚ N] and the Agulhas Current [25˚-35˚ E, 30˚-37˚ S] all have persistent positive wind speed biases as well. There are very few areas of negative wind speed bias, but the notable areas are around the Equatorial Counter Current directly west of the Galapagos Islands and the Western Indian Ocean. As was noted in the Introduction, environmental parameters can affect ASCAT's ability to retrieve wind speeds. In the next section, we consider possible environmental sources of the biases.

2.2.2.2 Examining the Environmental Variables

Because T_s and T_a in (2.2) are on the same spatial and temporal grid, they can be used directly to create a product for air-sea temperature difference. Both precipitation rate and air-sea temperature are on a finer grid resolution than the ASCAT wind speed bias, therefore a nearest neighbor algorithm is used to interpolate the environmental products. To make sense of the precipitation rate and air-sea temperature difference products, we generate histograms and cumulative distribution functions (CDFs) for each of the variables. The air-sea temperature difference histogram is binned every 0.0625˚ C, and the precipitation rate histogram is binned every 0.007 mm/hr. The histograms and CDFs are calculated after refitting the environmental data to the same resolution as the ASCAT wind speed bias data.

(a)

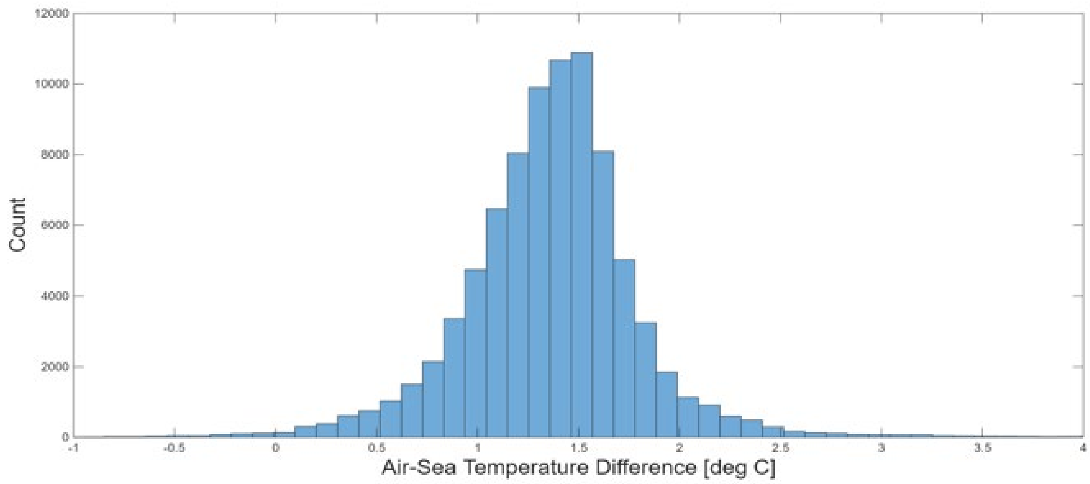

12000
10000
8000
6000
4000
2000
0
Count
-1
-0.5
0
0.5
1
1.5
2
2.5
3
3.5
4
Air-Sea Temperature Difference [deg C]

(b)

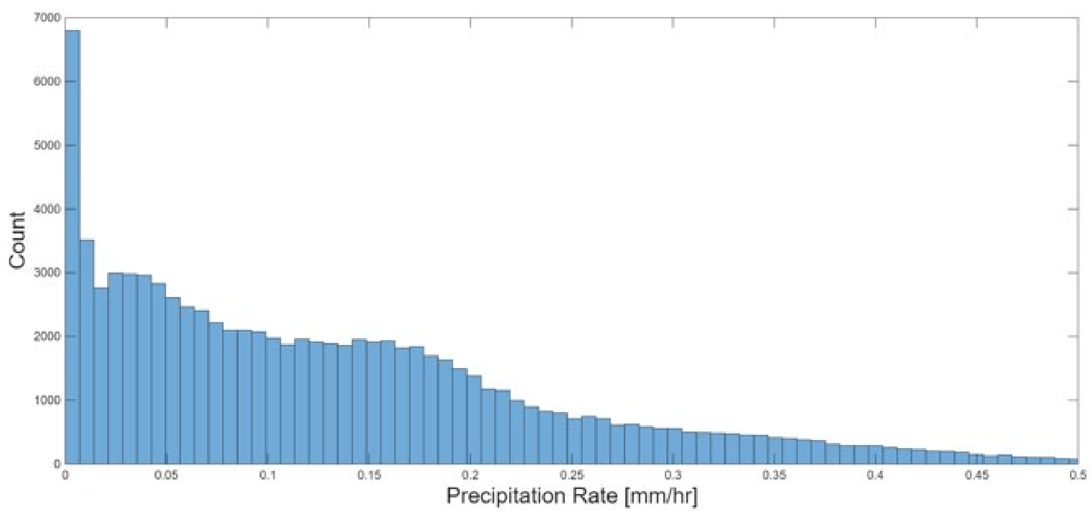

7000
6000
5000
4000
3000
2000
1000
0
Count
0
0.05
0.1
0.15
0.2
0.25
0.3
0.35
0.4
0.45
0.5
Precipitation Rate [mm/hr]

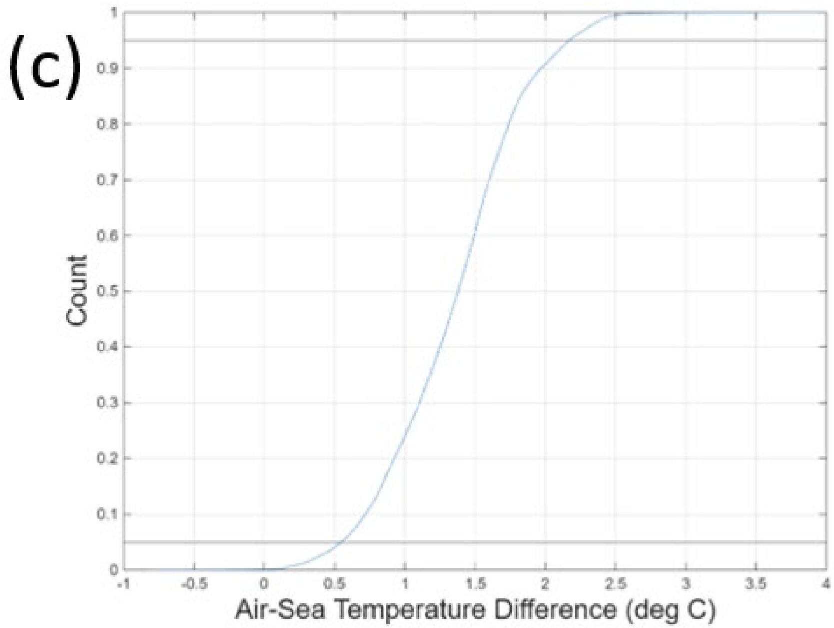

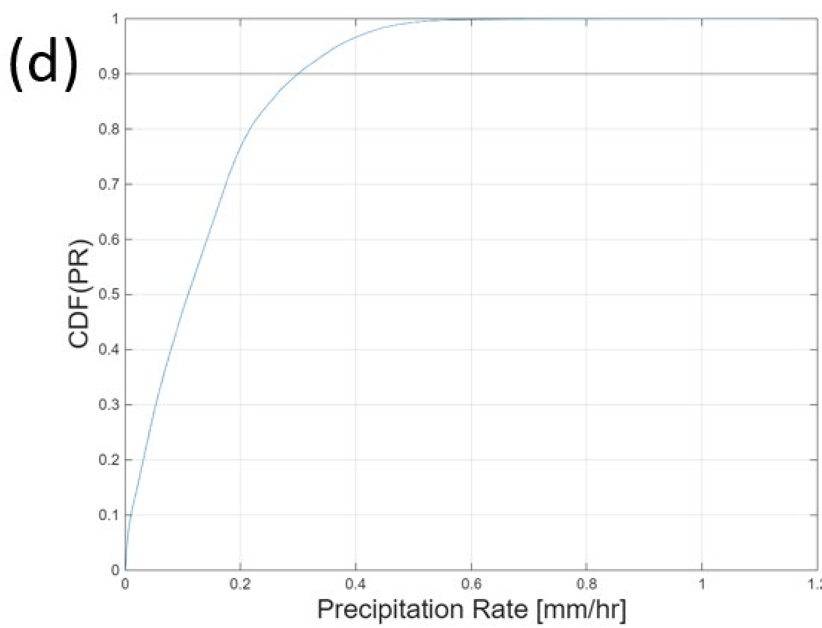

Figure 2.2: (a) A histogram of air-sea temperature difference (ASTD). ASTD is gridded in 0.5x0.5˚ bins and averaged over 2021. (b) A histogram of Precipitation Rate (PR) in mm/hr. Precipitation Rate is taken from IMERG data, gridded in 0.5x0.5˚ bins and averaged over 2021. (c) A cumulative distribution function for the air-sea temperature difference. (d) A cumulative distribution function for the precipitation rate.

Fig. 2.2(a) and 2.2(b) are histograms describing the distributions of the air-sea temperature difference and precipitation rate for CY 2021. The values used in the histograms collocate directly to ASCAT values at the same time. ASTD has a mean value of 1.36˚ C, and a standard deviation of 0.47˚ C. PR is a one-sided distribution, with the mode between 0-0.01 mm/hr. Fig. 2.2(c) and 2.2(d) are the cumulative distribution functions (CDFs) of the air-sea temperature difference and precipitation rate yearly gridded data. The rise on the left of Fig. 2.2(d) is due to the large amount of area that has minimal precipitation throughout the year.

Fig 2.2(c) and 2.2(d) also give us a definition for what "anomalous" means for both precipitation and air-sea temperature difference. We take the values below the 5th percentile and above the 95th percentile to define anomalously low and high air-sea temperature difference. These boundaries are 0.6˚C and 2.02˚ C. Anomalously high precipitation is defined as a rate above the 90th percentile, which is above 0.3 mm/hr. This definition makes it easier to pinpoint anomalous regions when making maps of the environmental data products. Fig. 2.3(a) is a map of the air-sea temperature difference, gridded on a 0.5x 0.5˚grid and averaged over CY 2021. Fig. 2.3(b) is a map of the precipitation rate, gridded on a 0.5x0.5˚grid and averaged over CY 2021.

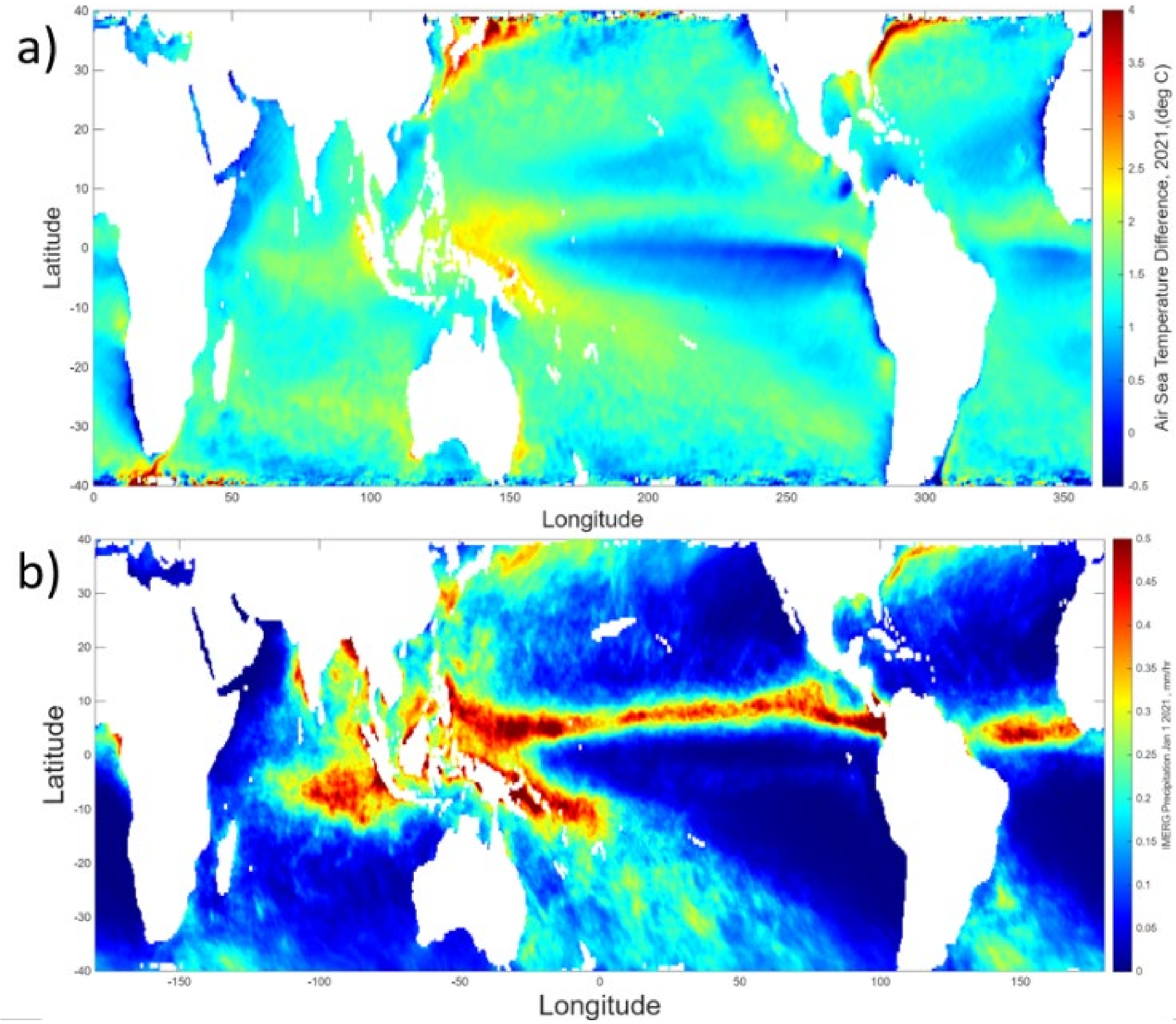

Figure 2.3: (a) Map of Air Sea Temperature Difference averaged over 2021 using ERA5's 2-meter temperature and sea surface temperature. (b) Map of Precipitation Rate averaged over 2021. Precipitation Rate is taken from IMERG data.

Maps of precipitation rate and air-sea temperature difference display similar characteristics to the ASCAT wind speed bias maps. Fig. 3a pinpoints many regions of anomalously high and low air-sea temperature difference. As defined earlier, anomalous regions of air-sea temperature difference are regions outside of the 0.6-2.02˚C range. The Gulf Stream, the Kuroshio Current and the Agulhas Current have anomalously high air-sea temperature differences. The water around Indonesia also has a high air-sea temperature difference. There are fewer areas of anomalously low air-sea temperature difference, but the notable areas are around the Equatorial Counter Current directly west of the Galapagos Islands and the Western Indian Ocean.

One major feature of Fig. 3b is the large band of precipitation that extends across the ITCZ. At its peak, the rain band averages 0.6 mm/hr of rain throughout the year, which equates to 5.26 m of rain per year. The high precipitation rate band also extends over the mainland of Indonesia. The Gulf Stream and the Kuroshio Current have moderately high rates of precipitation. This is due to a phenomenon associated with sea surface temperatures. The currents transport warm, tropical water from the Equator towards the poles. The tropical water is transported north and evaporates, rising into the atmosphere. The rising warm, moist air from the tropics increases the moisture content in the air, which leads to precipitation [20].

2.2.2.3 Adjusting the standard ERA5 winds to account for discrepancies with buoy winds

The Eastern Pacific portion of the Intertropical Convergence Zone (ITCZ) [90-140 W, 10N-10S] is of interest as the only area exhibiting a pronounced ASCAT negative wind speed bias. We examine the source of this bias, specifically whether it arises from ASCAT or ERA5. In this section, a comparison of ERA5 with in-situ buoy data is used. We use the TAO Buoy Array [19], with buoys stationed approximately every 2 degrees in latitude and 5 degrees in longitude. Figure 4 shows the buoy locations in the Eastern Pacific ITCZ Region.

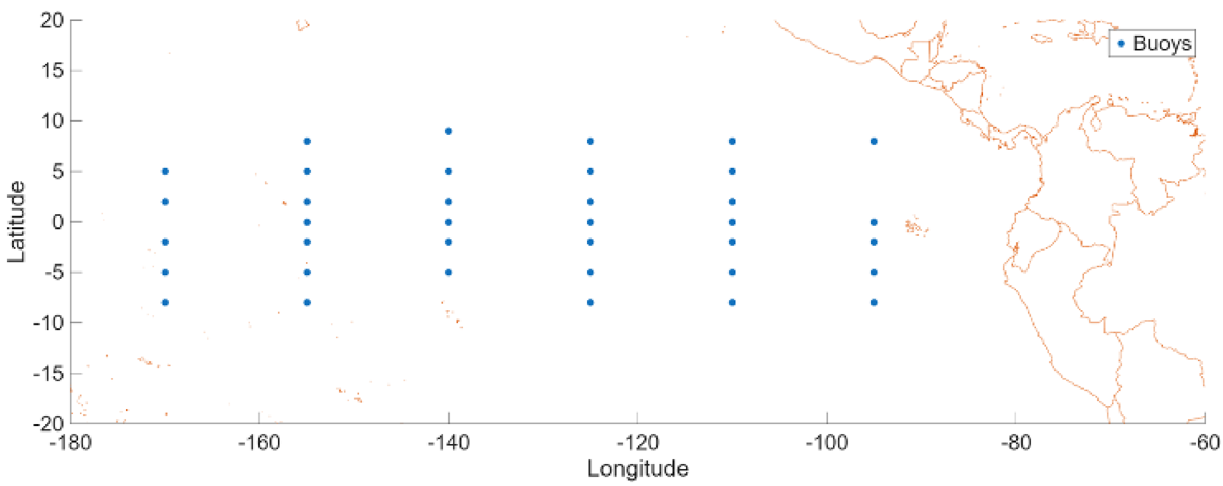

Figure 2.4: (a) Buoy locations across the Eastern Pacific. All buoys are used for the precorrection assessment. Data sampled on odd numbered days of the year are used for training the correction models, and data sampled on even days are used to evaluate the corrected ERA5 wind speed product.

The TAO buoy array measures wind speeds every 30 minutes. The buoy locations are listed in Table 2:

Table 2.2: TAO Buoy Network Locations

Latitude	Longitudes
8 S	95 W, 110 W, 125 W, 155 W, 170 W
5 S	95 W, 125 W, 140 W, 155 W, 170 W
2 S	95 W, 110 W, 125 W, 140 W, 155 W, 170 W
0 N	95 W, 110 W, 125 W, 140 W, 155 W
2 N	110 W, 125 W, 140 W, 155 W, 170 W
5 N	110 W, 125 W, 140 W, 155 W, 170 W
8 N	95 W, 110 W, 125 W, 155 W, 170 W
9 N	140 W

To assess ERA5 accuracy we examine its mean difference from collocated buoy data. The ERA5 wind speed bias is given by

$$WSB_{ERA5,BUOY} = < U_{ERA5} - U_{BUOY} > \tag{2.4}$$

where the expectation operator <> refers to the mean of coincident samples over the period 08/01/2018 to 05/31/2020. If the ERA5 data performs like the buoy data, $WSB_{ERA5,\,BUOY}$ will be near zero. To effectively use the buoy data, half the buoy data (all odd numbered days) are used to train the correction, and the other half are used to test the correction. To understand the data before applying any corrections, a visualization of the data is useful. Fig. 2.5 is a series of benchmark density scatter plots. Fig. 2.5a plots buoy measured wind speed versus ERA5 wind speed. Data used in the figure is from all buoy locations, on the time interval of 08/01/2018-05/30/2020. This is the baseline for the relationship between buoy winds and ERA5. The goal here is to see how effective our corrections are in removing environmentally dependent biases between ERA5 and buoy winds. Fig. 2.5b plots ERA5 wind speed versus ASCAT wind speed. This serves as a baseline for the correction developed for ASCAT winds.

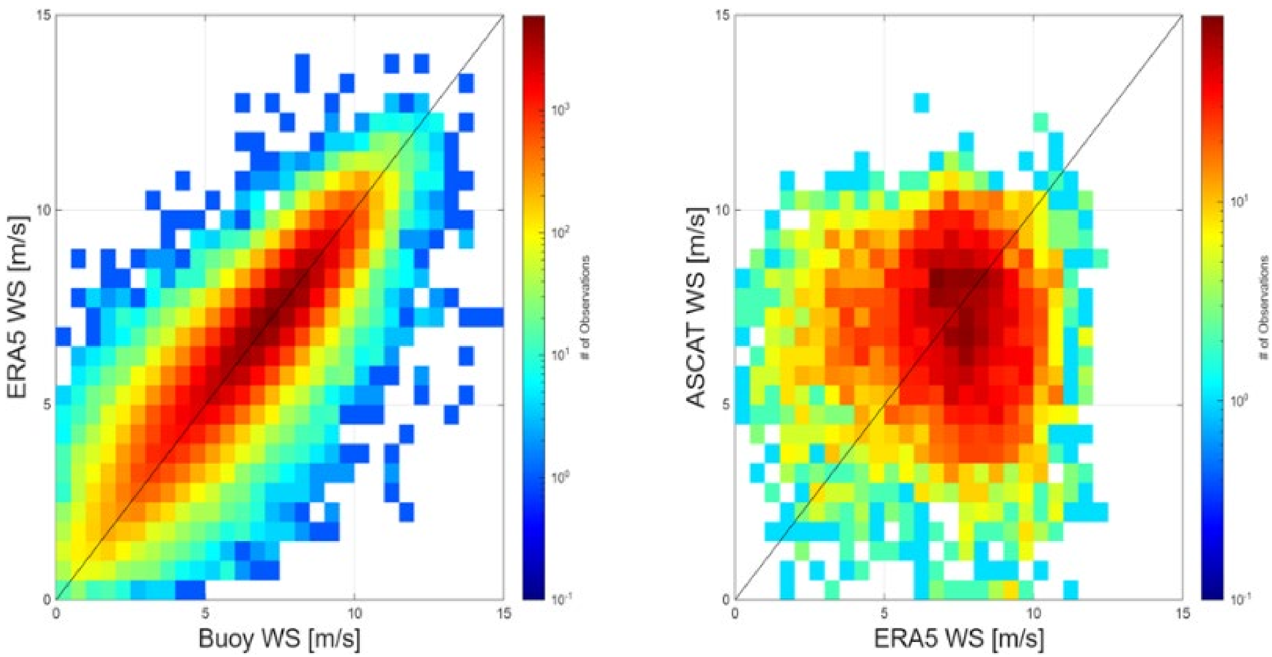

Figure 2.5: (a) Buoy locations across the Eastern Pacific. All buoys are used for the precorrection assessment. Data sampled on odd numbered days of the year are used for training the correction models, and data sampled on even days are used to evaluate the corrected ERA5 wind speed product.

As shown in Fig. 2.5(a), buoy winds and ERA5 winds have a high correlation, with the highest density of samples closely following the 1-to-1 line of perfect agreement. Fig. 2.5(b) has markedly low correlation. This behavior is particular to the Eastern Pacific ITCZ, and this degraded behavior in ASCAT wind retrievals is a primary focus of our corrections. Both these plots will be redone with corrected data at the end of this analysis to evaluate the effectiveness of our method.

We examine the dependence of the wind speed bias on other environmental variables. If the bias depends on an environmental variable, this is an indication of a possible error in ERA5, e.g. due to improper accounting for the effects of that variable on the wind speed. Two such dependencies are considered here, those with respect to the air-sea temperature difference

(ASTD) and the presence of precipitation. Figure 2.6(a) plots $WSB_{ERA5,\ BUOY}$ against buoy-measured air-sea temperature difference. Figure 2.6(b) plots $WSB_{ERA5,\ BUOY}$ against the IMERG-determined precipitation rate.

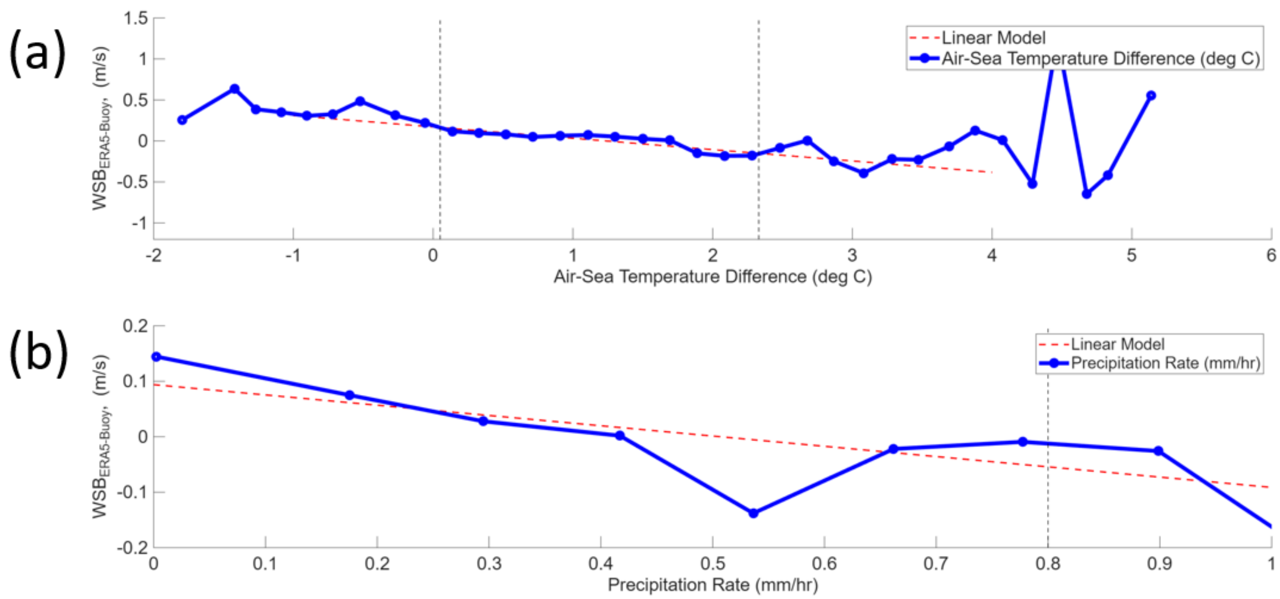

Figure 2.6: (a) Buoy air-sea temperature difference plotted against $WSB_{ERA5,\ BUOY}$ (U_{ERA5}-U_{BUOY}) with a linear model fit to the data. Vertical dashed lines at 0.03˚C and 2.33˚C denote the lower and upper bounds of the 95% confidence interval. (b) IMERG precipitation rate plotted against $WSB_{ERA5,\ BUOY}$ with a linear model fit to the data. The vertical dashed line at 0.8 mm/hr represents the 97.5 percentile threshold.

Fig. 2.6 demonstrates a dependance of the ERA5 wind speed bias on both environmental variables. Corrections are derived to the ERA5 wind speed to remove the dependence of its bias on these two environmental variables. This correction is performed in two steps. First, we fit a least-squares polynomial curve to the dependencies shown in Fig. 2.6. Then an ERA5 wind speed bias correction is applied based on the polynomial curve.

In Fig. 2.6a, 95% of the data falls between an ASTD of 0.05˚ and 2.33˚ C. The dependence of wind speed bias on ASTD over this range is nearly linear; therefore, we use a linear fit to model the wind speed bias dependence. In Fig. 2.6b the data above 0.8 mm/hr accounts for only 2.5% of the data, so adjustments for the data are weighted to favor the data from 0 to 0.8 mm/hr. The dependence of wind speed bias on precipitation rate is nearly linear; therefore we use another linear fit to model the wind speed bias dependence.

The linear fit in Fig. 2.6a is given by

$$WSB_{ERA5,BUOY}(ASTD) = -0.138 * (ASTD) + 0.171 \tag{2.5}$$

where ASTD represents the air-sea temperature difference data and $WSB_{ERA5,\ BUOY}$ represents the wind speed bias between ERA5 and buoy winds. The fit in Fig 2.6b is given by

$$WSB_{ERA5,BUOY}(PR) = -0.185 * (PR) + 0.93876 \tag{6}$$

where PR represents the precipitation rate.

These adjustments are applied to the ERA5 dataset

$$U_{EC} = U_{ERA5} - WSB_{ERA5,BUOY}(ASTD) - WSB_{ERA5,BUOY}(PR). \tag{7}$$

Implementing both adjustments results in a new version of the ERA5 wind data, defined as the environmentally corrected ERA5 wind, or U_{EC}. U_{EC} will serve as the reference wind dataset for the subsequent comparison with ASCAT wind speeds. U_{EC} averaged from 01/01/2021 to 12/31/2021 is displayed in Fig. 7.

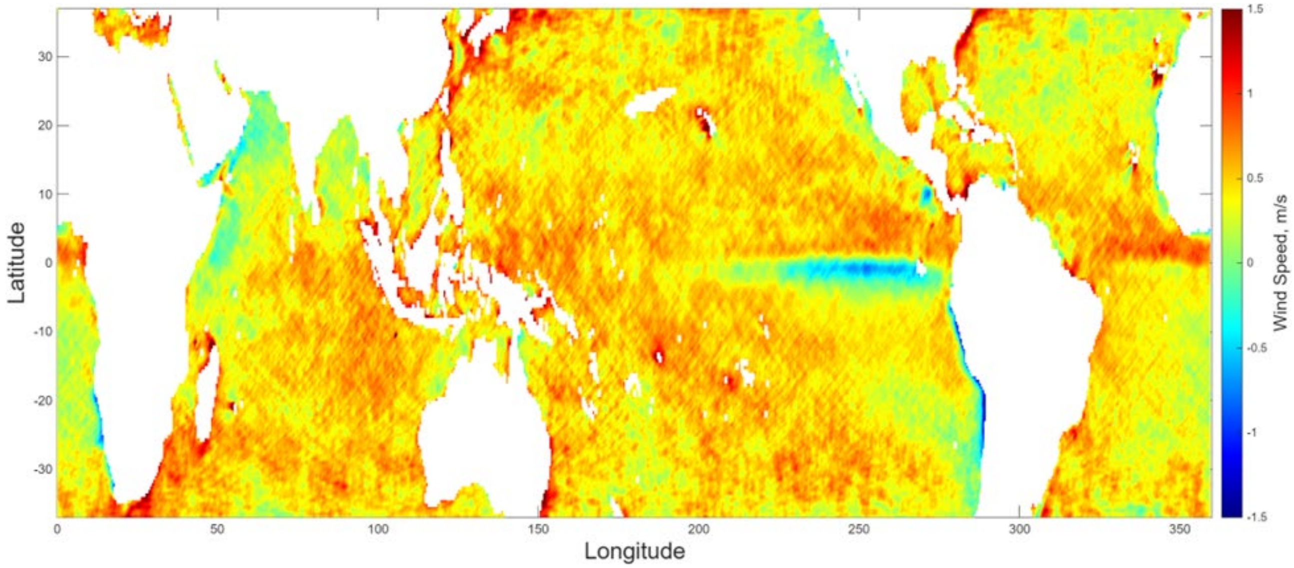

Figure 2.7: ASCAT wind speed bias relative to ERA5 Environmentally Corrected wind speeds (U_{EC}). Data used in figure averaged from 01/01/2021 to 12/31/2021.

Comparing Fig. 2.7 to Fig. 2.1, there is a general increase in wind speed bias across the globe. However, wind speed bias in the Eastern Pacific ITCZ and Atlantic ITCZ have stayed largely the same. The increase in wind speed bias is not an indication of the correction failing, but rather an indication that ERA5 and ASCAT may be in more disagreement than previously perceived.

2.2.2.4 Seasonal Bias Issues

Using a yearly average instead of a seasonal average can obscure changes in the environment that happen on a seasonal scale. For section 2.2.2 of the methodology a yearly average has been used to assess the air-sea temperature difference and the precipitation rate. While this makes it possible to see persistent regional issues across the globe, it can negate changes that occur on a seasonal basis. Fig. 2.8 takes the ASCAT wind speed bias data averaged in three-month seasonal periods and zooms in on the North Pacific Gyre to show a large seasonal change and the Eastern Pacific ITCZ demonstrates a small seasonal change. The easiest time to see seasonal variations is by comparing DJF and JJA maps, so those averages are used.

(a)

(b)

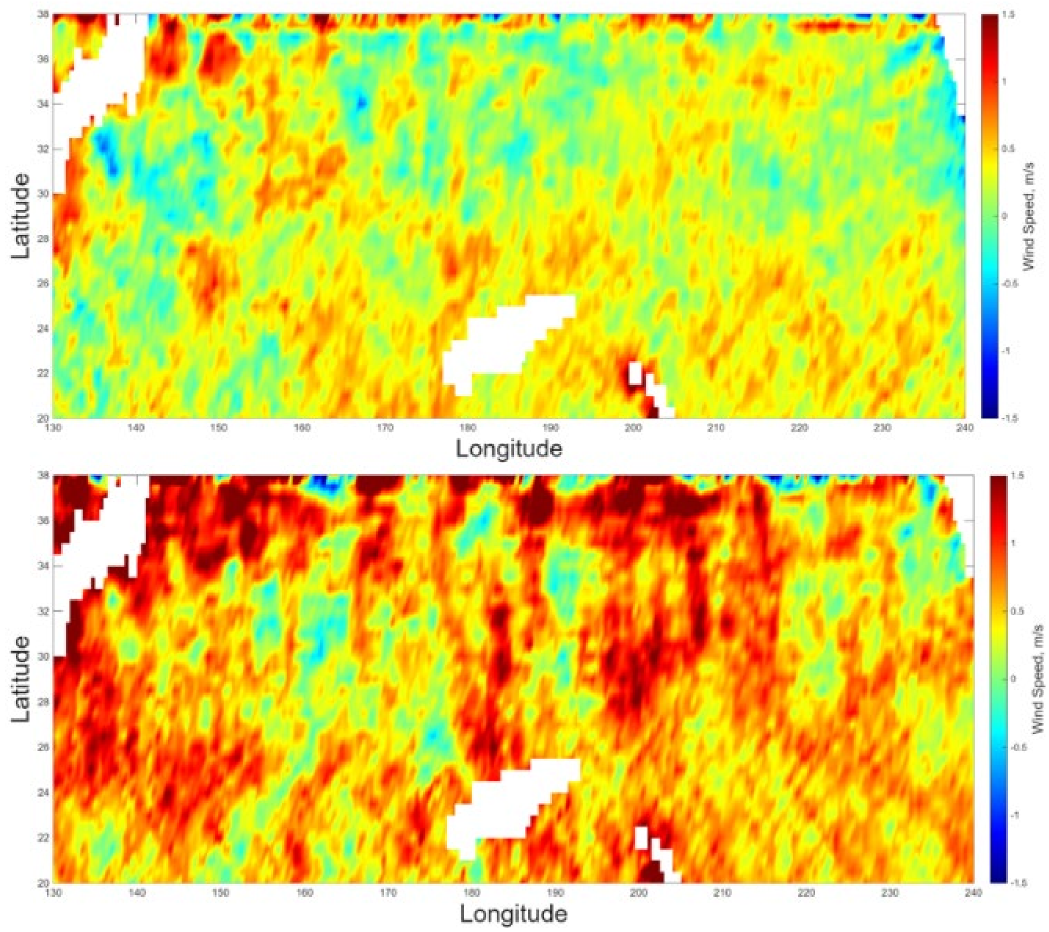
Latitude
Longitude
Wind Speed, m/s
Latitude
Longitude
Wind Speed, m/s

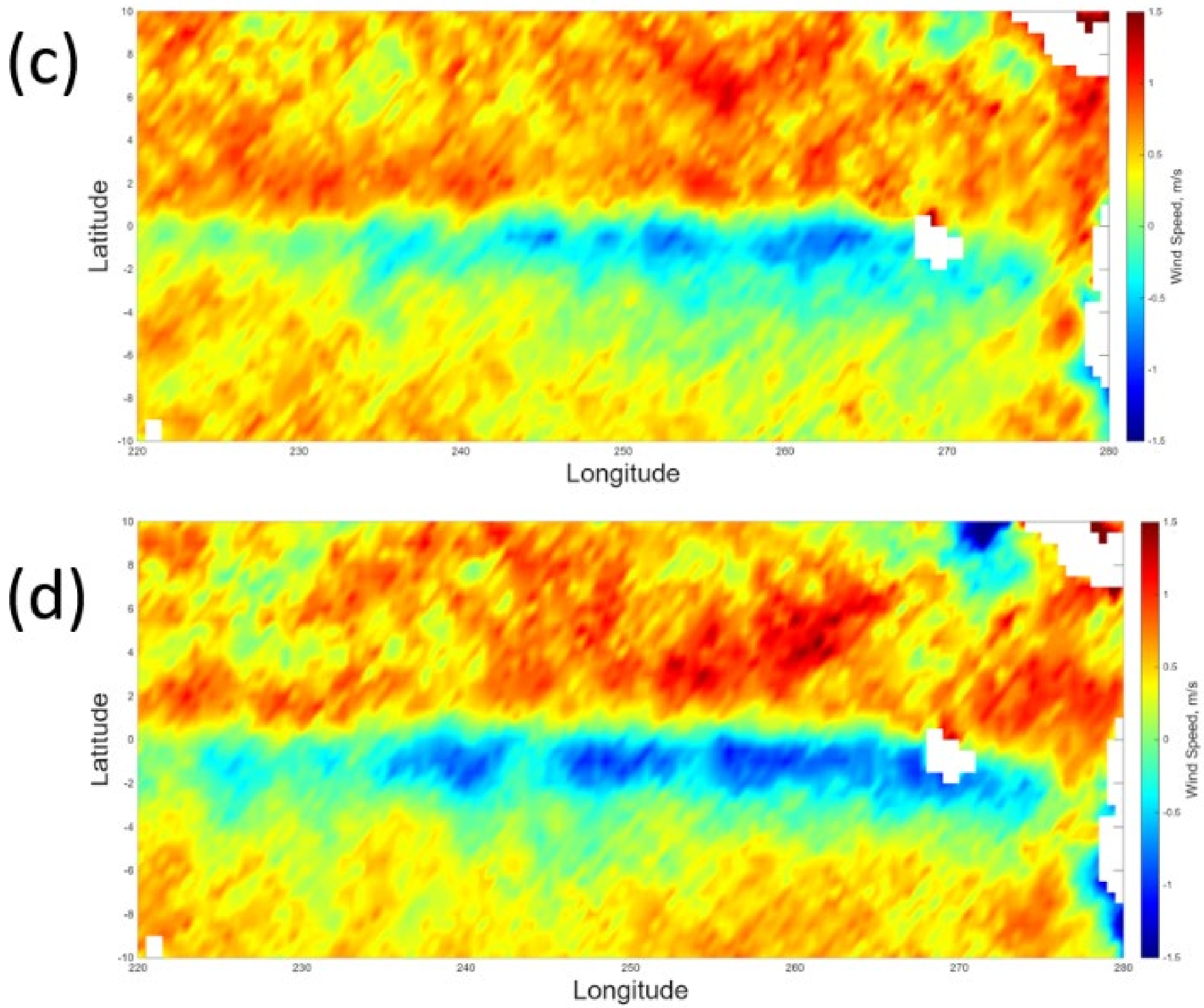

Figure 2.8: Regional matchups between the Northern Hemisphere Summer (JJA) and Winter (DJF). (a) and (b) are a comparison of the North Pacific, which is overestimated in the winter months, but slightly underestimated during the summer months. (c) and (d) look at the Eastern Pacific near the Galapagos Islands, and there is a consistent underestimation of wind speed all throughout the year.

Fig. 2.8 shows snapshots of two regions. One where the seasonal and yearly averages are similar and one where the seasonal variation is obscured. Areas further from the Equator, where seasonal variations are higher, will be most impacted by this change.

2.2.2.5 Correlation between the ASCAT Wind Speed Bias and the Environmental Variables

There are clear visual parallels between Fig. 2.3 and 2.7, particularly in the ITCZ, where there is the anomalously low region of air-sea temperature difference in the Eastern Pacific Ocean. This makes the ITCZ a good test region to check if there is a correlation between the ASCAT wind speed bias map and the environmental variables, which is done in Fig. 2.9.

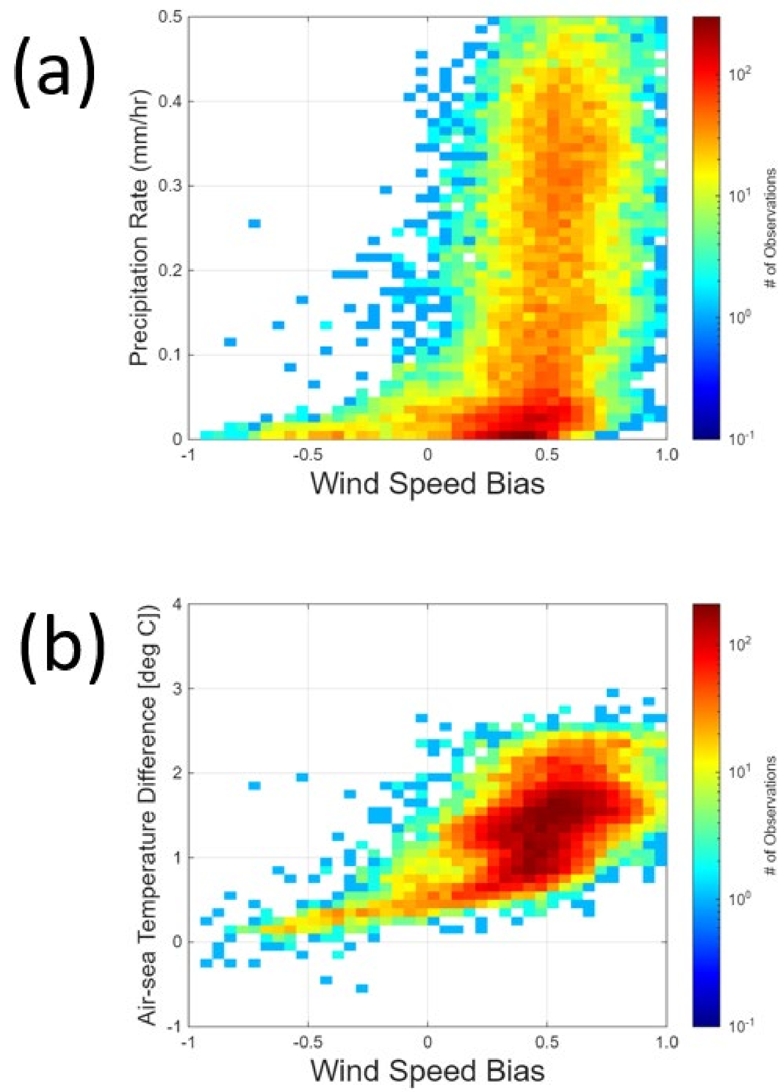

Figure 2.9: (a) Density Scatter Plot of ASCAT wind speed bias and Precipitation Rate for CY2021, specifically in the ITCZ. There is a positive monotonic and linear relationship between WSB and PR. (b) Density Scatter Plot of ASCAT

wind speed bias and air-sea temperature difference. There is a weak positive monotonic correlation between wind speed bias and air-sea temperature difference.

In Fig. 2.9a, there is a general positive monotonic relationship between ASCAT wind speed bias and precipitation rate. The densest region of data is around 0.5 m/s on the x axis and 0 mm/hr on the y axis, but for the points above 0.05 mm/hr, the positive monotonic relationship is clear. This means that areas of anomalously high precipitation coincide with high ASCAT wind speed bias. A similar analysis is done for ASTD in Fig. 2.9b, but there is a larger spread when compared with 2.9a. Fig. 2.9b also has a left-skewed tail, implying that there is a matchup between areas of anomalously low air-sea temperature difference and negative wind speed bias. Fig. 2.10 is a comparison of air-sea temperature difference to ASCAT wind speed bias. Both products are averaged over a year and zoom into the Eastern Pacific [220˚-280˚ E, 10˚N-10˚S] and Gulf Stream [270˚-300˚E, 15˚-37˚N] regions. These two regions are picked to display the visual alignment between the satellite product and the environmental variable.

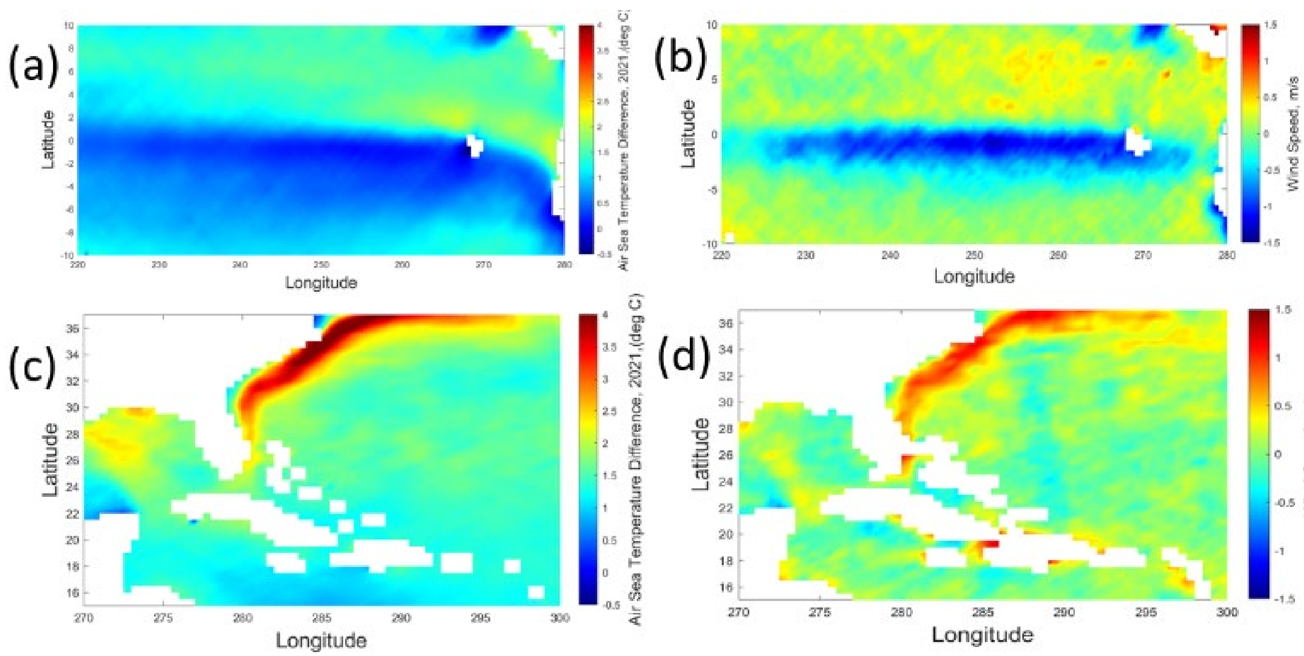

Figure 2.10: Regional matchups of ASCAT wind speed bias and air-sea temperature difference. Displayed to show visual similarities between biases and environmental parameters. (a) and (b) are a comparison of the underestimated wind speed bias region of the Eastern Pacific and the anomalously low air-sea temperature

difference region. (c) and (d) are a comparison of the Gulf Stream region, where anomalously high air-sea temperature difference correlates with high wind speed bias.

Fig. 2.10 displays regions where the anomalies align. The correlations seen in the data are consistent with the physical processes that drive them, bolstering our ability to relate them as cause and effect. Precipitation Rate has a positive monotonic increase starting around 0.01 mm/hr, implying that in rainy conditions ASCAT overestimates the wind speed. Rainfall attenuates the transmitted signal, which lowers the received power [18]. Taken at face value, this suggests that wind speed should be underestimated by ASCAT. However, especially in conditions of low wind speed, rainfall can also cause an increase in backscatter due to the signal scattering from raindrops back toward the sensor. In addition to this, the raindrops hitting the surface can grow centimeter-scale ring waves, roughening the surface further than normal [19].

Air-sea temperature difference in Fig. 2.9b has a large negative tail, which equates to ASCAT underestimating the wind speed in areas of higher atmospheric stability. Regions that are highly stable are unusual, as most of the oceans fall within ASTD = 1-2˚ C, which is mildly unstable. Having a region be this stable means there is little vertical mixing, and less vertical wind stress being placed on the ocean surface [22]. The lack of upward-directed stress leads to smaller wave generation, which is consistent with an underestimation of the wind speed [4]. The opposite is true in areas of high air-sea temperature difference, for example in the Western Boundary Currents. The increase in vertical stress at the surface generates larger waves for a given wind speed, leading to an overestimation in the wind.

2.2.3 Potential Adjustments to the Wind Speed Bias

This section attempts a first order correction to reduce or remove the biases identified in the previous sections. It is intended to illustrate the potential for such a correction. In practice, operational corrections to the retrieval algorithm would be better performed by the ASCAT Project data product developers.

The correction method is a bias subtraction, as described by the following three steps.

1) Fit a polynomial between ASCAT WSB and one of the variables. In this case, Precipitation Rate (PR) is used first. This best fit polynomial represents what the wind speed bias would be if only based on precipitation rate, denoted as WSB(PR).

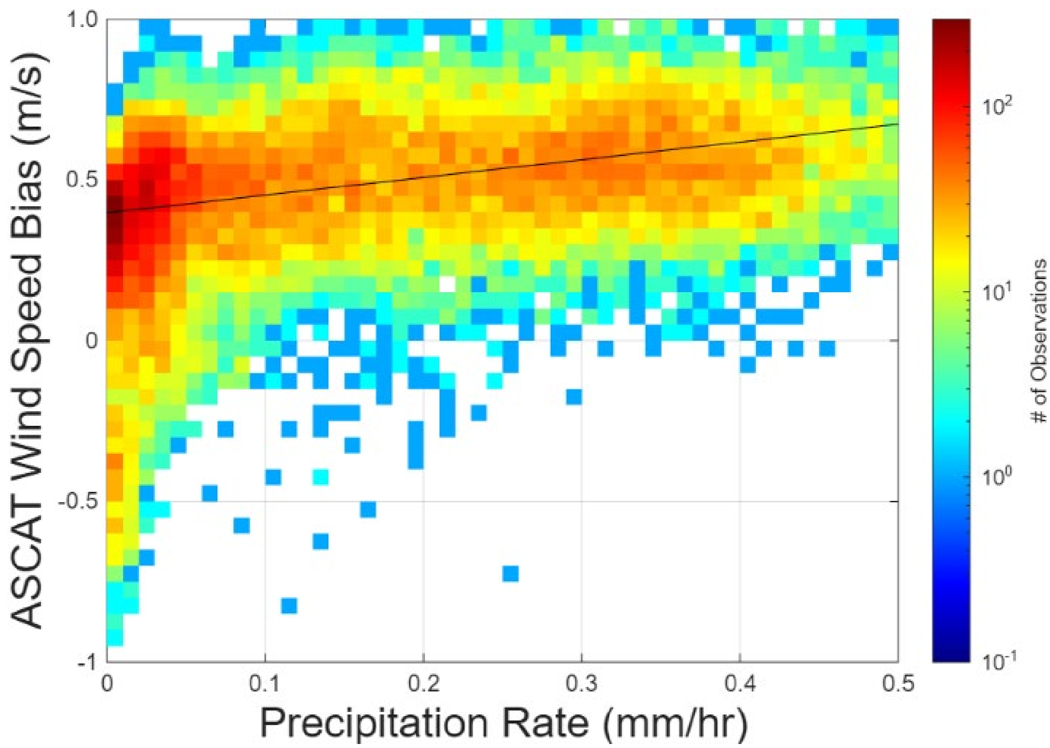

Figure 2.11: Density Scatter Plot of ASCAT wind speed bias and precipitation rate, with the best fit line. Equation (8) is the wind speed bias based solely on precipitation. The axes have been flipped from Fig. 2.9a to keep (2.8) in a y = mx+b format.

Fig. 2.11 adds a best fit line to Fig. 2.9a and rotates the axes to be in slope-intercept form. The best fit line is given by

$$WSB(PR) = 0.5504PR + 0.3978. \tag{2.8}$$

2) Adjust the ASCAT Wind Speeds (U_{ASCAT}) by WSB(PR) to create the Precipitation Rate Corrected ASCAT Wind Speeds ($U_{ASCAT, PR}$). Mathematically, this is described by

$$U_{ASCAT,PR} = U_{ASCAT} - WSB(PR). \tag{2.9}$$

3) Derive the new PR Corrected ASCAT wind speed bias ($WSB_{ASCAT,\ PR}$) by differencing $U_{ASCAT,\ PR}$ and the ERA5 Zero Current Equivalent Winds (U_{zc}), as given by

$$WSB_{ASCAT,PR} = U_{ASCAT,PR} - U_{zc}. \tag{2.10}$$

If the precipitation rate correction is done correctly, there should be no correlation between precipitation rate and the new wind speed bias. Fig. 2.12 is a revision of Fig. 2.9a using the new precipitation rate-corrected version of the ASCAT winds.

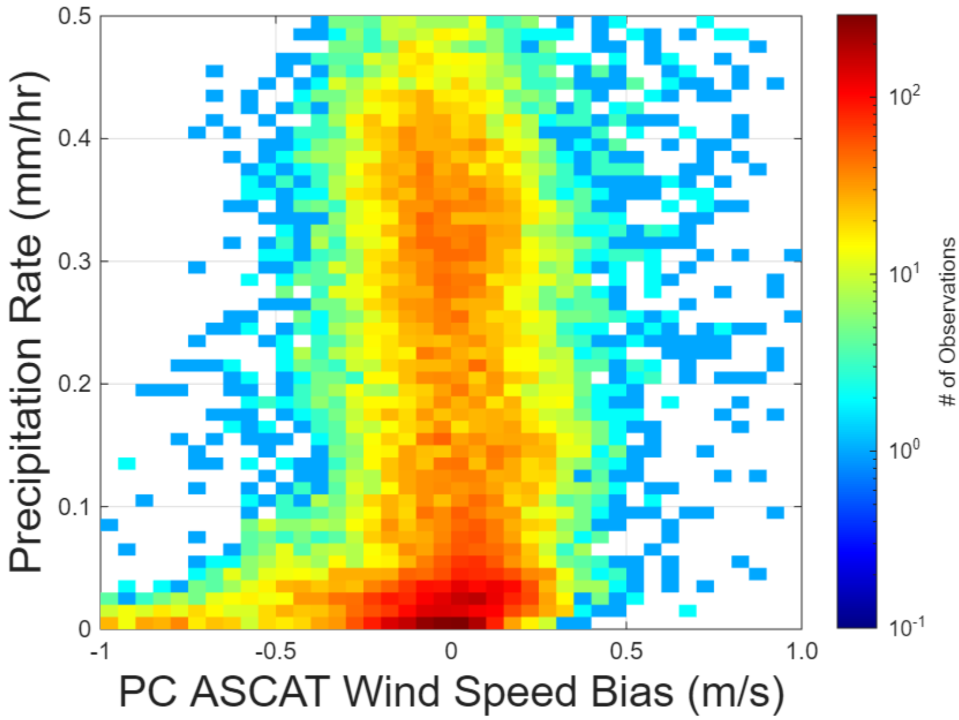

Figure 2.12: Density Scatter Plot of ASCAT wind speed bias and precipitation rate, with the best fit line. Equation (8) is the wind speed bias based solely on precipitation. The axes have been flipped from Fig. 2.9a to keep (2.8) in a y = mx+b format.

Now a similar correction can be performed for the air-sea temperature difference. The first step is to take the density scatter plot of precipitation rate corrected wind speed bias and air-sea temperature difference.

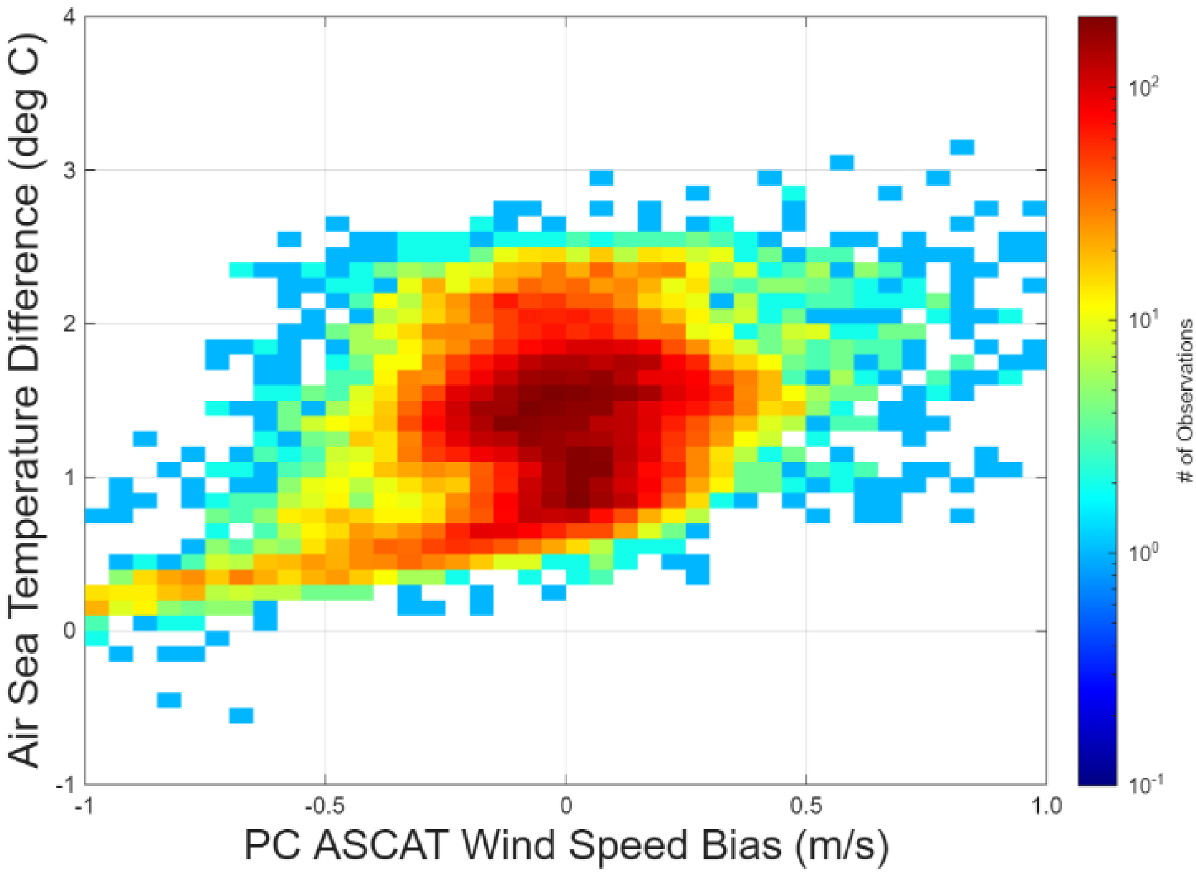

Figure 2.13: Density scatter plot of Precipitation Rate Corrected ASCAT wind speed bias and air-sea temperature difference. Due to the correlation between anomalously high areas of precipitation rate and air sea temperature difference, the new matchup is slightly shifted when compared to Fig. 2.9b.

Fig. 2.13 differs from Fig. 2.9b because areas in the ITCZ have shifted in wind speed bias. This is particularly noticeable above 2˚ C. This trend is no longer linear, so a cubic polynomial is fit to the density scatter plot. Also, due to the lack of data above 2.8˚ C in the ITCZ, the training region has been updated to include the North Pacific and North Atlantic.

The data centers around 0 m/s for the wind speed bias, so this change will only affect regions of anomalous air-sea temperature difference. Above 2˚ C and below 0.6˚ C a change will be made, which works well given our definitions of anomalous air-sea temperature difference. A polynomial fit could not accurately capture both the high and low sides of the distribution, so a piecewise function was used to accurately capture the main bulk of the data and the anomalously low region. The piecewise function is given by

$$\begin{Bmatrix} WSB(ASTD) = \\ -13.961(ASTD - 0.05)^3 + 16.3224(ASTD - 0.05)^2 \\ -3.9159(ASTD - 0.05) - 0.5655 \qquad if\ 0.20 < \ ASTD < 0.68 \end{Bmatrix} \tag{11a}$$

$$\{WSB(ASTD) = 0.2508(ASTD) - 0.689\ if\ ASTD > 0.68\} \tag{11b}$$

$$\{WSB(ASTD) = -0.838\ if\ ASTD < 0.20\ \} \tag{11c}$$

where WSB(ASTD) is the wind speed bias due to air-sea temperature difference.

The piecewise fit can be explained physically by the connection between stability conditions and wind speed.

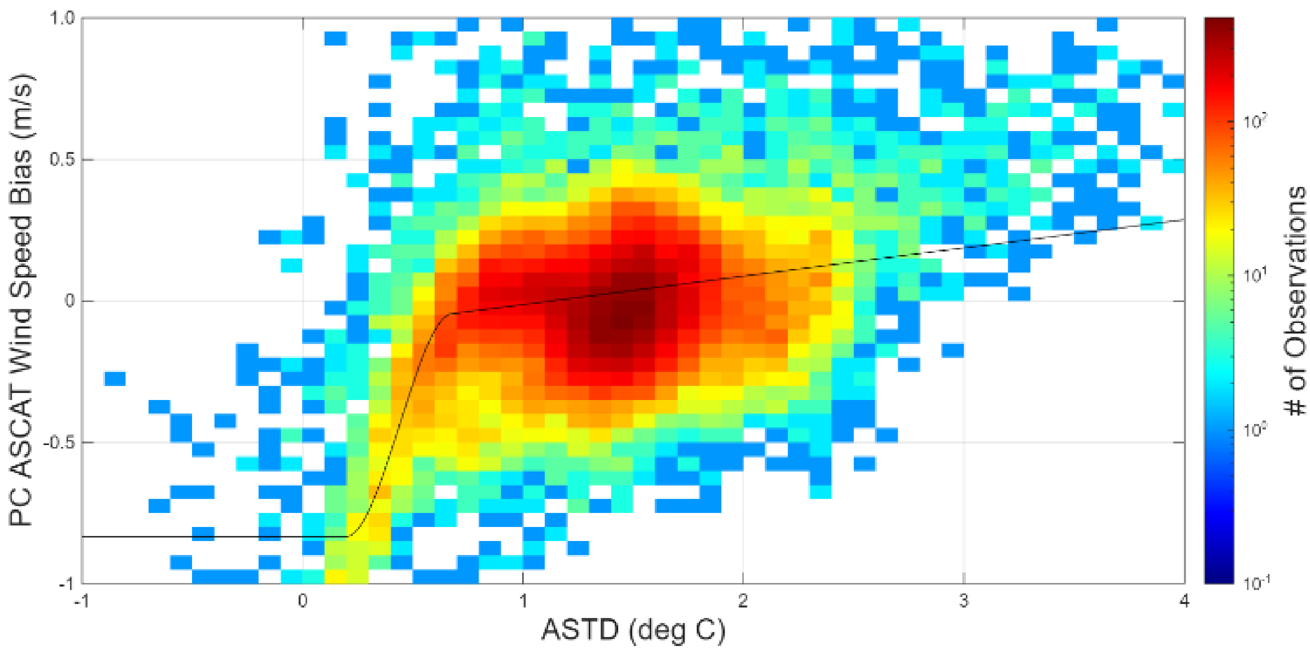

Figure 2.14: Density scatter plot of Precipitation Rate Corrected ASCAT wind speed bias vs. air-sea temperature difference. The piecewise fit to the data described in (2.11) is shown as the black line.

Generally, stability conditions affect ocean wind speeds in low wind conditions, as the vertical air motions are a larger part of the overall wind stress [6]. The tail region of Fig. 14

encompasses the East Pacific ITCZ, which meets both the low wind and low stability condition. The bulk region, which exhibits average ASTD conditions, stay near zero, and the high ASTD region does not have a tail effect due to it not being in a low wind regime. The monotonic section of the fit past the tail exists to stop the fit from overfitting to outliers.

Fig. 2.15a and Fig. 2.15b are the post correction assessments, formulated in the same series of benchmark plots as Fig. 2.5. The buoys not used for training are used to evaluate the corrections made for both the ASCAT and ERA5 winds.

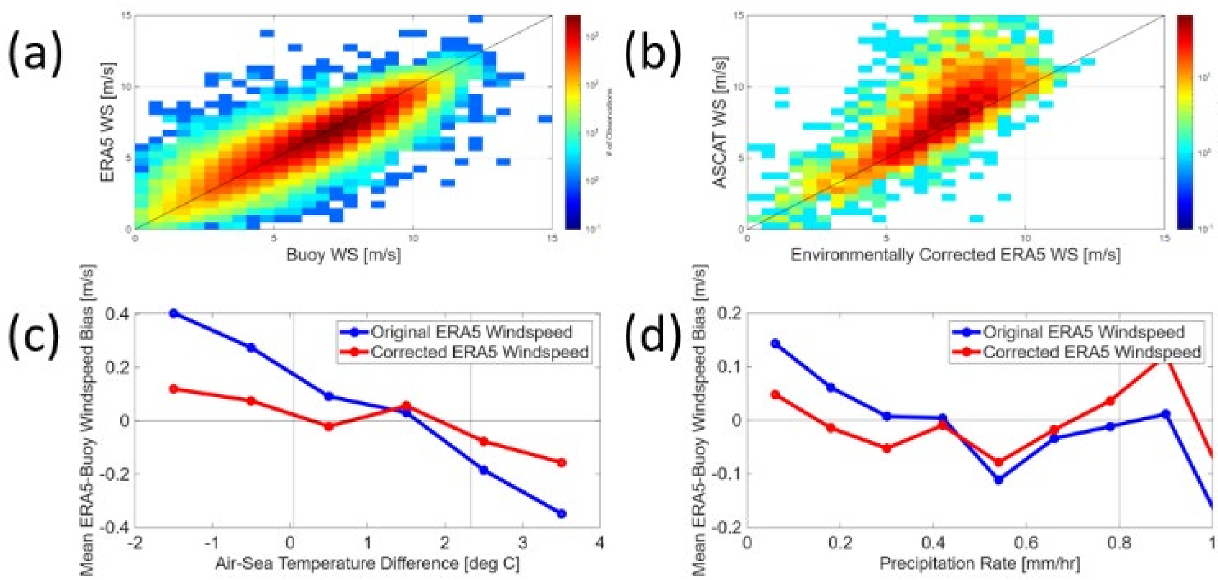

Figure 2.15: Density scatter plot of Precipitation Rate Corrected ASCAT wind speed bias vs. air-sea temperature difference. The piecewise fit to the data described in (2.11) is shown as the black line.

There is marginal improvement in the R^2 and RMSD values for the ERA5 and buoy wind comparison, and a large improvement in the R^2 and RMSD for the ASCAT and ERA5 wind comparison. Fig. 2.15(c) and Fig. 2.15(d) use the pre- and post-corrected ERA5 winds to compare $WSB_{ERA5,BUOY}$ to ASTD and PR, respectively. In both cases, the curves display a reduced negative slope, suggesting the environmental variables have less influence on the ERA5 winds after correction.

The environmental correction procedure produces a new ASCAT wind speed that is bias adjusted for both PR and ASTD. It is referred to as the environmentally corrected ACSAT wind speed.

2.3 Results of Bias Correction

2.3.1 Precipitation Rate Corrected ASCAT Wind Speed Bias

Using the correction method presented in Section C of the Methodology, a plot is created of wind speed bias using the ASCAT wind speeds with a precipitation rate correction. This plot is shown in Fig. 2.16.

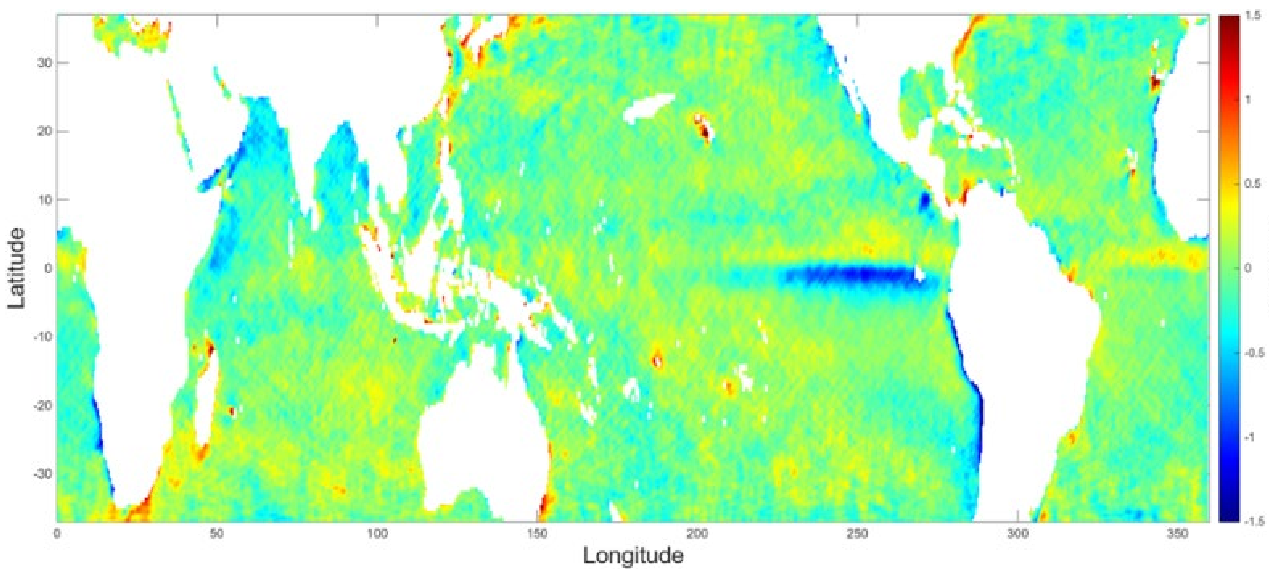

Figure 2.16: ASCAT wind speed bias with a correction for Precipitation Rate. Areas of improvement include the Eastern Pacific ITCZ, Southern Pacific and around Indonesia. There are also minor improvements in the Gulf Stream and Kuroshio.

The precipitation rate corrected ASCAT winds significantly reduce the wind speed bias in both the Pacific and Atlantic ITCZ. The Southern Pacific, which sees a moderate amount of rain according to Fig. 2.3(b), has also improved. The Gulf Stream and Kuroshio Current have had their biases reduced, but the improvement is minor, with the features still being visible in the plot. There is minimal change in the North Pacific, Southern Indian Ocean, and the area of large negative bias in the Eastern Pacific. This makes sense due to there being minimal precipitation there throughout the year.

2.3.2 Precipitation Rate Corrected ASCAT Wind Speed Bias

A similar correction can be done using air-sea temperature difference and compounded with the correction made from the precipitation rate to create the environmentally corrected ASCAT wind speed bias. The map of this is displayed in Fig. 2.17

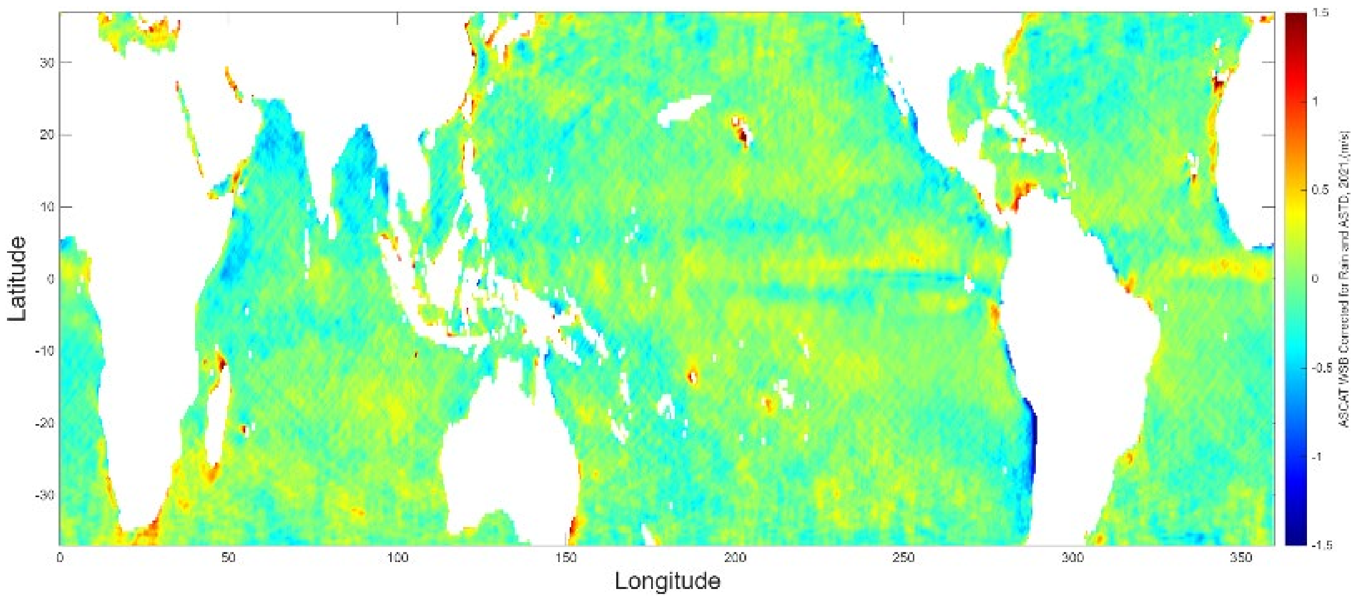

Figure 2.17: The environmentally corrected wind speed bias plot, encompassing corrections for both precipitation rate and air sea temperature difference. A notable area of improvement is the Eastern Pacific ITCZ, specifically the area with a large negative air-sea temperature difference seen in Fig. 2.10b. This area also encompasses most of the tail region from Fig. 2.9b.

The air-sea temperature difference correction targets the anomalously low and high air-sea temperature difference areas shown in Fig. 2.3b. This environmentally corrected ASCAT wind speed bias is not a complete correction, as many other factors that were mentioned in Section 2.1.3 of the Introduction could impact the ASCAT wind speed retrieval and therefore also affect the ASCAT wind speed bias.

2.3.3 Global and Regional Analysis of the Corrections

Given these three distinct versions of ASCAT wind speed bias charts shown in Fig. 2.7, Fig. 2.16 and Fig. 2.17, a statistical analysis of the changes has been made. A global comparison of the mean bias and spread is shown in Fig. 2.18 and Table 2.3.

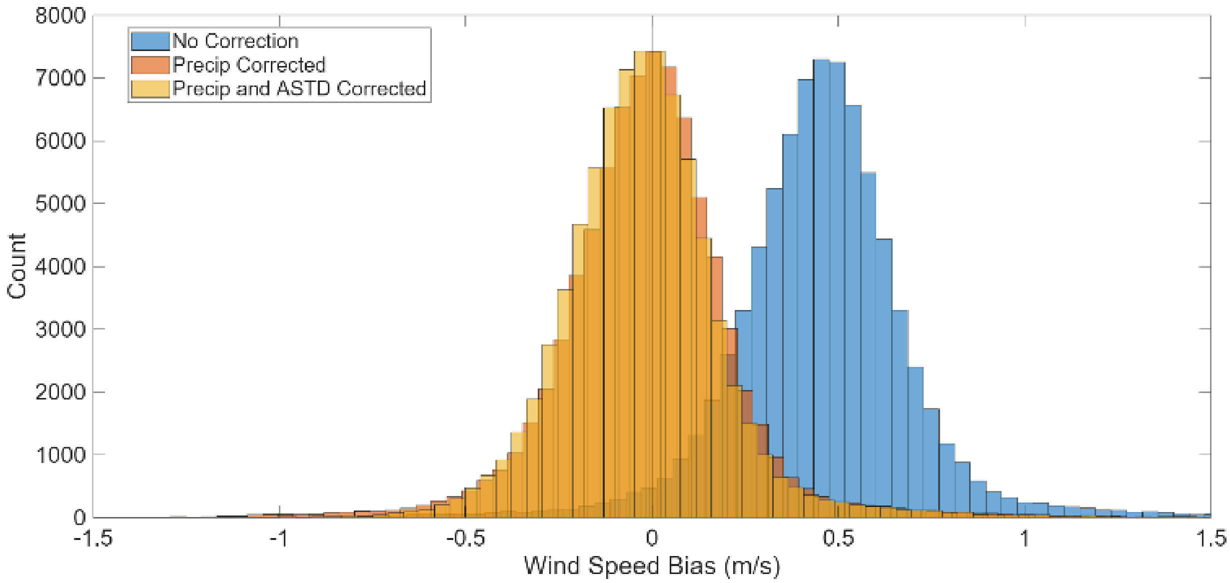

Figure 2.18: A histogram of the ASCAT wind speed biases. The blue distribution is the wind speed bias using the standard ASCAT winds, the red distribution uses a precipitation rate correction, and the yellow distribution uses both precipitation rate and air-sea temperature difference corrections.

Table 2.3: Global Distribution Statistics

Wind speed bias Type↓/Stat→	Mean (μ)	Standard Deviation (σ)
ASCAT WSB w/no corrections	0.21 m/s	0.26 m/s
ASCAT WSB w/Precipitation Correction	-0.02 m/s	0.25 m/s
ASCAT WSB w/Precipitation and Air Sea Temperature Difference Correction	0.03 m/s	0.23 m/s

Correcting for both the air-sea temperature difference and precipitation rate reduces the mean bias from 0.21 to 0.03 m/s. The standard deviation is lowered from 0.26 to 0.23 m/s. In general, the precipitation rate correction shifts the entire distribution of errors left, and the air-sea temperature difference correction targets the tails of the distribution and narrows the spread.

Although the overall global change by the correction is positive, it is nonetheless small. Areas of anomalous environmental conditions are found to have a more significant positive correction. First, the Pacific ITCZ training region is assessed. Figure 2.19 is a histogram of the Pacific ITCZ bias, and Table 2.4 replicates Table 2.3.

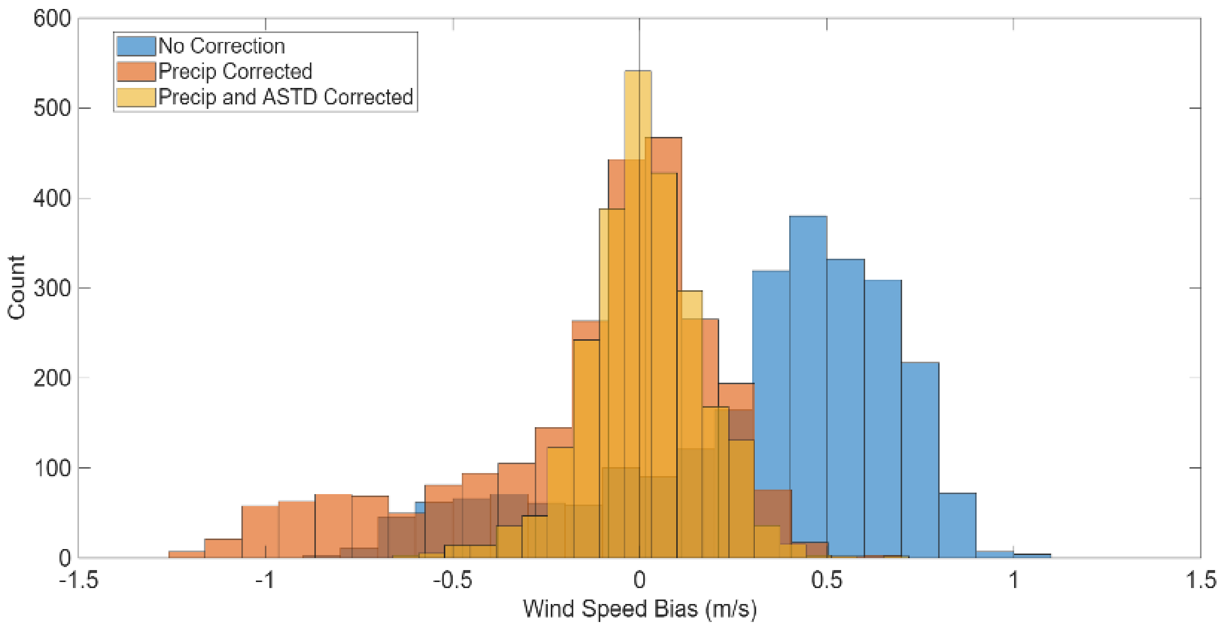

Figure 2.19: A histogram of the ASCAT wind speed biases, specific to the Pacific ITCZ. The blue curve represents the standard ASCAT winds, the red curve has a precipitation rate correction, and the yellow curve is the environmentally corrected ASCAT winds.

Table 2.4: Pacific ITCZ Region Histogram Statistics

Wind speed bias Type↓/Stat→	Mean (μ)	Standard Deviation (σ)
ASCAT WSB w/no corrections	0.32 m/s	0.38 m/s

ASCAT WSB w/Precipitation Correction	-0.13 m/s	0.35 m/s
ASCAT WSB w/Precipitation and Air Sea Temperature Difference Correction	0.09 m/s	0.16 m/s

The Pacific ITCZ is a region of high precipitation, along with an area of anomalously low air-sea temperature difference. Adding the precipitation correction shifts the distribution left, just like the global distribution. The spread is not reduced significantly, but the air-sea temperature difference correction targets specific areas like the Eastern Pacific, so it slightly shifts the distribution while narrowing the spread.

Another region to assess is the Gulf Stream and the North Atlantic. Figure 2.20 and Table 2.5 look at the bias spread in the North Atlantic.

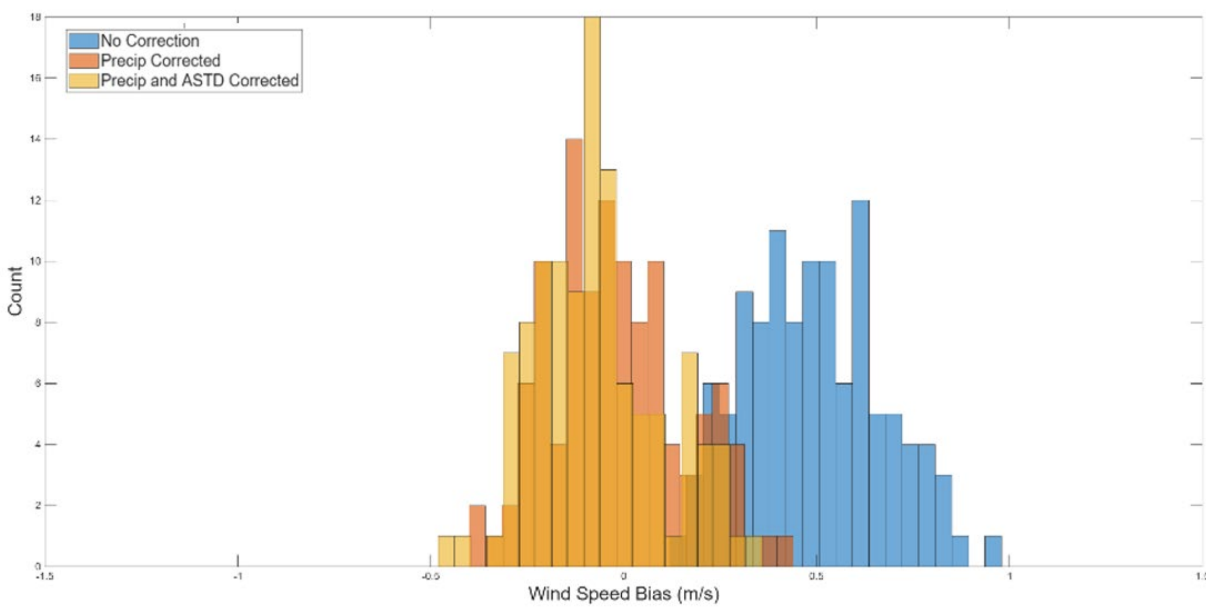

Figure 2.20: A histogram of the ASCAT wind speed biases, specific to the Pacific ITCZ. The blue curve represents the standard ASCAT winds, the red curve has a precipitation rate correction, and the yellow curve is the environmentally corrected ASCAT winds.

Table 2.5: Gulf Stream Region Histogram Statistics

Wind speed bias Type↓/Stat→	Mean (μ)	Standard Deviation (σ)
ASCAT WSB w/no corrections	0.49 m/s	0.18 m/s
ASCAT WSB w/Precipitation Correction	-0.02 m/s	0.17 m/s
ASCAT WSB w/Precipitation and Air Sea Temperature Difference Correction	-0.07 m/s	0.16 m/s

In the Northern Atlantic region, the addition of the air-sea temperature difference correction improved the spread, even if it shifted the mean further from zero. This is still a positive result, due to spread calculations being less susceptible to tuning issues.

2.4 Discussion & Conclusion

2.4.1 Implication for Other Products

Adjusting the ASCAT wind speeds has a significant impact on any geophysical parameter that uses wind speed as an input variable. Even relatively minor changes in wind speed can have significant implications on other geophysical parameters that are derived using wind speed, such as Latent Heat Flux (LHF).

LHF is defined as the flux of heat from the Earth's surface to the atmosphere that is specifically associated with evaporation or condensation of water vapor at Earth's surface. It can be expressed as

$$LHF = \rho_a L_v C_E U(q_{sea} - q_{air}) \tag{2.12}$$

where ρ_a is the air density over the sea, L_v is the heat of vaporization, C_E is the turbulent exchange coefficient for latent heat flux, q_{sea}-q_{air} is air-sea humidity difference and U is the near surface wind speed [23, 24]. The turbulent exchange coefficient is normally parameterized using Monin-Obukhov Similarity Theory (MOST), a method that takes in roughness lengths and stability corrections for momentum and humidity and estimates the turbulent exchange coefficient [25].

LHF is a vital component of Earth's energy balance budget, and significant changes in LHF can have a noticeable effect on applications such as numerical weather prediction. Even with a change in wind speed as small as 0.1 m s^{-1} over a 1-degree grid cell, the LHF can change by up to 0.35 W m^{-2}., or by 3.5×10^9 Watts when averaged over the full grid cell.

To better appreciate the magnitude of the change, a LHF calculation using (2.12) has been made using the standard winds and comparing them to the environmentally corrected winds, globally and regionally. Aside from U, the variables needed for the RHS of (2.12) are taken from ECMWF's Copernicus Climate Data Store. The reanalysis data is regridded from its native 0.2˚x0.2˚ grid to 0.5˚x0.5˚ grid to match the standard and environmentally corrected winds. Regionally, the Gulf Stream [280˚-290˚E, 22˚-33˚N], and Pacific ITCZ [125˚-260˚E, 10˚N-10˚S] are used as test regions. The Coupled Ocean-Atmosphere Response Experiment (COARE) algorithm was used to calculate the results [23, 24]. The COARE algorithm is a mathematical framework used to calculate the exchange of heat, moisture, and momentum via wind stress between the ocean and the atmosphere. It is a model method of turning weather parameters into surface energy exchanges [24]. Calculating LHF using the COARE algorithm gives a result per grid cell in W/m^2, so each 0.5˚x0.5˚ grid cell is multiplied by its area in square meters and summed over its respective region. The results are tabulated in Table 2.6.

Table 2.6: Gulf Stream Region Histogram Statistics

Coverage Area↓/LHF Product→	LHF using ERA5 Uzc Winds	LHF using Standard ASCAT Winds	LHF using Environmentally Corrected ASCAT Winds	LHF Difference

Global	13.6 x10^{15} Watts	14 x10^{15} Watts	13.7 x10^{15} Watts	3.0 x 10^{14} Watts
Gulf Stream	1.4 x10^{15} Watts	1.6 x10^{15} Watts	1.5 x10^{15} W	1.0 x10^{14} Watts
Pacific ITCZ	4 x10^{15} Watts	3.8 x10^{15} Watts	3.85 x10^{15} Watts	5.0 x10^{13} Watts

The global LHF changes from the standard to the environmentally corrected winds amount to 3.0 x 10^{14} Watts, which is a 2.1% change.

This chapter identifies and suggests corrections for residual biases in the ASCAT wind speed product, and it offers evidence that some of the residual biases are due to environmental factors such as atmospheric stability and precipitation. While these biases are small, it is important to correct for them as even a minor change in the wind speed can have a large effect on other variables, as seen by the 2.1% change in global LHF. The correction algorithm used earlier is one method of correcting for these biases, but it is important to reiterate that operational corrections to the retrieval algorithm would be better performed by the ASCAT Project data product developers.

2.5 References for Chapter 2

1. F. M. Naderi, M. H. Freilich, and D. G. Long, "Spaceborne radar measurement of wind velocity over the ocean-an overview of the NSCAT scatterometer system," *Proc. IEEE*, vol. 79, no. 6, pp. 850–866, Jun. 1991, doi: 10.1109/5.90163.
2. N. Pizzo, L. Deike, and A. Ayet, "How does the wind generate waves?," *Physics Today,* vol. 74, no. 11, pp. 38–43, Nov. 2021, doi: 10.1063/PT.3.4880.
3. A. A. Grachev and C. W. Fairall, "Upward Momentum Transfer in the Marine Boundary Layer," *Journal of Physical Oceanography,* vol. 31, no. 7, pp. 1698-1711, Jul. 2001, doi: 10.1175/1520-0485(2001)031<1698:UMTITM>2.0.CO;2
4. R. G. Fleagle, "Note on the effect of air-sea temperature difference on wave generation," *Eos, Transactions American Geophysical Union,* vol. 37, no. 3, pp. 275-277, 1956, doi:10.1029/TR037i003p00275.
5. F. J. Wentz, "Measurement of oceanic wind vector using satellite microwave radiometers," *IEEE Transactions on Geoscience and Remote Sensing*, vol. 30, no. 5, pp. 960–972, Sep. 1992, doi: 10.1109/36.175331.
6. F. T. Ulaby and D. G. Long, "Radar Remote Sensing of the Ocean" in *Microwave Radar and Radiometric Remote Sensing,* 1st ed. Ann Arbor, MI, U.S.A: UofM Press, 2014, ch. 16, sec. 3, pp. 788
7. R. K. Moore and W. J. Pierson, "Measuring sea state and estimating surface winds from a polar orbiting satellite", in *International Symposium on Electromagnetic Sensing of the Earth from Satellites*, Miami Beach, Fla., U.S.A, 1965;

8. T. Lungu, "QuikSCAT science data product user's manual: Overview and geophysical data products," JPL D-18053, Version 2.2, Jet Propulsion Laboratory, Pasadena, CA, 2001, pp. 95
9. R. Kumar et al., "Post-launch calibration-validation and data quality evaluation of SCATSAT-1," *Curr. Sci.,* vol. 117, pp. 973-982, 2019
10. K. D. Klaes et al., "An introduction to the EUMETSAT polar system," *Bull. Amer. Meteor. Soc.,* vol. 88, pp. 1085-1096, 2007.
11. K. D. Klaes, "The EUMETSAT Polar System," in *Comprehensive Remote Sensing,* vol 1, Oxford: Elsevier, 2018, pp. 192-219. Doi: 10.1016/B978-0-12-409548-9.10318-5.
12. F. T. Ulaby and D. G. Long, "Radar Scattering" in *Microwave Radar and Radiometric Remote Sensing,* 1^{st} ed. Ann Arbor, MI, U.S.A: UofM Press, 2014, ch. 5, sec. 5, pp. 170
13. H. Hersbach, A. Stoffelen, and S. de Haan, "An improved C-band scatterometer ocean geophysical model function: CMOD5," *Journal of Geophysical Research: Oceans*, vol. 112, no. C3, 2007, doi: 10.1029/2006JC003743.
14. N. C. Yi Lim *et al.*, "Review of Temperature and Humidity Impacts on RF Signals," in *2020 13th International UNIMAS Engineering Conference (EnCon)*, Oct. 2020, pp. 1–8. doi: 10.1109/EnCon51501.2020.9299327.
15. L. F. Bliven, H. Branger, P. Sobieski, and J. P. Giovanangeli, "An analysis of scatterometer returns from a water surface agitated by artificial rain: evidence that ring-waves are the main feature," *International Journal of Remote Sensing*, vol. 14, no. 12, pp. 2315–2329, Aug. 1993, doi: 10.1080/01431169308954039.
16. A. A. Grachev, C. W. Fairall, J. E. Hare, J. B. Edson, and S. D. Miller, "Wind Stress Vector over Ocean Waves," Nov. 2003, Accessed: Feb. 28, 2025. [Online]. Available: https://journals.ametsoc.org/view/journals/phoc/33/11/1520-0485_2003_033_2408_wsvoow_2.0.co_2.xml
17. H. Hersbach et al., "ERA5 hourly data on single levels from 1940 to present," Copernicus Climate Change Service (C3S) Climate Data Store (CDS), 2023. [Online] Available: doi:10.24381/cds.adbb2d47. Accessed: Sep. 5, 2023.
18. Belmonte Rivas, M. and Stoffelen, A.: Characterizing ERA-Interim and ERA5 surface wind biases using ASCAT, Ocean Sci., 15, 831–852, https://doi.org/10.5194/os-15-831-2019, 2019
19. R. Crout and D. Petraitis, "Physical and meteorological data from the Tropical Atmosphere Ocean (TAO) array in the tropical Pacific Ocean. [9N-8S, 95-140W] NOAA National Data Buoy Center (NDBC), NOAA National Centers for Environmental Information, Accessed on [03/12/2025]}, Dataset. {Link: https://ncei.noaa.gov/access/metadata/landing-page/bin/iso?id=gov.noaa.nodc:NDBC-TAOBuoy}
20. R. Seager and I. R. Simpson, "Western boundary currents and climate change," *Journal of Geophysical Research: Oceans*, vol. 121, no. 9, pp. 7212–7214, 2016, doi: 10.1002/2016JC012156.
21. G. Delrieu, H. Andrieu, and J. D. Creutin, "Quantification of Path-Integrated Attenuation for X- and C-Band Weather Radar Systems Operating in Mediterranean Heavy Rainfall," *J. Appl. Meteor.*, vol. 39, no. 6, pp. 840–850, Jun. 2000, doi: 10.1175/1520-0450(2000)039<0840:QOPIAF>2.0.CO;2.
22. N. J. M. Laxague and C. J. Zappa, "The Impact of Rain on Ocean Surface Waves and Currents," *Geophysical Research Letters*, vol. 47, no. 7, p. e2020GL087287, 2020, doi: 10.1029/2020GL087287.
23. G. R. Foltz, R. Hummels, M. Dengler, R. C. Perez, and M. Araujo, "Vertical Turbulent Cooling of the Mixed Layer in the Atlantic ITCZ and Trade Wind Regions," *Journal of Geophysical Research: Oceans*, vol. 125, no. 2, p. e2019JC015529, 2020, doi: 10.1029/2019JC015529.
24. E. L. Andreas *et al.*, "Parametrizing turbulent exchange over summer sea ice and the marginal ice zone," *Quarterly Journal of the Royal Meteorological Society*, vol. 136, no. 649, pp. 927–943, 2010, doi: 10.1002/qj.618.
25. C. W. Fairall, E. F. Bradley, J. E. Hare, A. A. Grachev, and J. B. Edson, "Bulk Parameterization of Air–Sea Fluxes: Updates and Verification for the COARE Algorithm," *Journal of Climate*, vol. 16, no. 4, pp. 571–591, Feb. 2003, doi: 10.1175/1520-0442(2003)016%3C0571:BPOASF%3E2.0.CO;2.

26. R. Foody, S. Dong, M. Goes, R. Campos, P. Pena, and Z. Barton, “Assessing Air–Sea Surface Turbulent Heat Fluxes from Reanalyses Using Concurrent Shipboard Measurements,” Dec. 2024, doi: 10.1175/JTECH-D-24-0028.1.
27. J. B. Edson *et al.*, “On the Exchange of Momentum over the Open Ocean,” Aug. 2013, doi: 10.1175/JPO-D-12-0173.1.
28. R. Marsh and E. van Sebille, “Chapter 4 - Western boundary currents and drifting organisms,” in *Ocean Currents*, R. Marsh and E. van Sebille, Eds., Elsevier, 2021, pp. 103–143. doi: 10.1016/B978-0-12-816059-6.00014-0.
29. K. Dohan, "Ocean Surface Current Analyses Real-time (OSCAR) Surface Currents - Interim 0.25 Degree (Version 2.0)," Ver. 2.0, PO.DAAC, CA, USA, 2022. [Online]. Available: https://doi.org/10.5067/OSCAR-25I20. Accessed: Sep. 5, 2023.

Chapter 3 Characterizing the Effects of Algal Blooms on Ocean Surface Roughness via a Wavetank Experiment and Spaceborne Radar Demonstration

3.1 Introduction

3.1.1 GNSS-R

Microwave remote sensing instruments take measurements at frequencies between 0.3 GHz and 300 GHz. Below 0.3 GHz lie HF and VHF radio waves and above 300 GHz is the sub-mm and far infrared portion of the electromagnetic spectrum. An example of a spaceborne microwave instrument is the Cyclone Global Navigation Satellite System (CYGNSS). CYGNSS uses GNSS Reflectometry (GNSS-R), a passive bistatic radar technique [1]. Instead of transmitting its own pulses, CYGNSS receivers measure GPS signals after they reflect off the ocean surface. GPS operates at L-Band (19 cm wavelength). CYGNSS infers properties of the sea surface, most notably surface roughness, which is closely related to near-surface wind speed [2]. A principal equation describing measurements of the surface via received power is the Radar Range Equation, defined as

$$P_r = \frac{P_t G_r G_t \lambda^2 L A}{(4\pi)^3 R_t^2 R_r^2} \sigma_0 \tag{3.1}$$

where P_r and P_t represent the received and transmitted power, G_r is the CYGNSS receiver antenna gain, G_t is the GPS transmitting antenna gain, λ is the wavelength, R_t is the distance from the transmitter to the target, R_r is the distance from the target to the receiver, L is a generalized loss factor that accounts for atmospheric attenuation and system loss, A is the scattering area on the ocean surface and σ_0 is the normalized bistatic radar cross section [3].

In practice for CYGNSS, σ_0 is determined from measurement of the received power by inverting equation (3.1) and solving for σ_0 as a function of P_r. From measurements of σ_0, it is possible to determine ocean roughness and therefore near surface wind speeds [4]. σ_0 is a measure of how strongly a surface scatters the incoming electromagnetic wave per unit area toward the receiver [3], which depends strongly on the roughness of the ocean surface. Surface roughness can be characterized by its Mean Square Slope (MSS), which is the expected value of the square of surface slope, averaged over the spectrum of ocean surface height at the appropriate horizontal scales [5]. MSS is defined as

$$MSS = \int_0^{k_c} k^2 S(k) dk \tag{3.2}$$

where k is the wavenumber, S(k) is the omnidirectional wave spectrum and k_c is the cutoff wavenumber, which is a function of radar wavelength and measurement geometry.

MSS as measured by CYGNSS can be derived from its direct measurement of σ_0 using the relationship [5]

$$MSS = \frac{|R(\epsilon,\theta)|^2}{\sigma_0} \tag{3.3}$$

where R(ε,θ) is the Fresnel Reflection Coefficient.

CYGNSS MSS measurements can be compared with meteorological reanalysis datasets like the European Center for Midrange Weather Forecasting Reanalysis 5 (ERA5) dataset [6] to assess variations in the MSS measurements due to wind speed. Variations in the MSS that are not due to wind speed are parameterized as MSS Anomaly (MSS_{ANOM}). Any variable that can affect the sea surface without being directly related to wind speed will be visible in the MSS_{ANOM} data. Figure 1 is an example of MSS_{ANOM} averaged from 01-Jan-2021 to 31-Dec-2021.

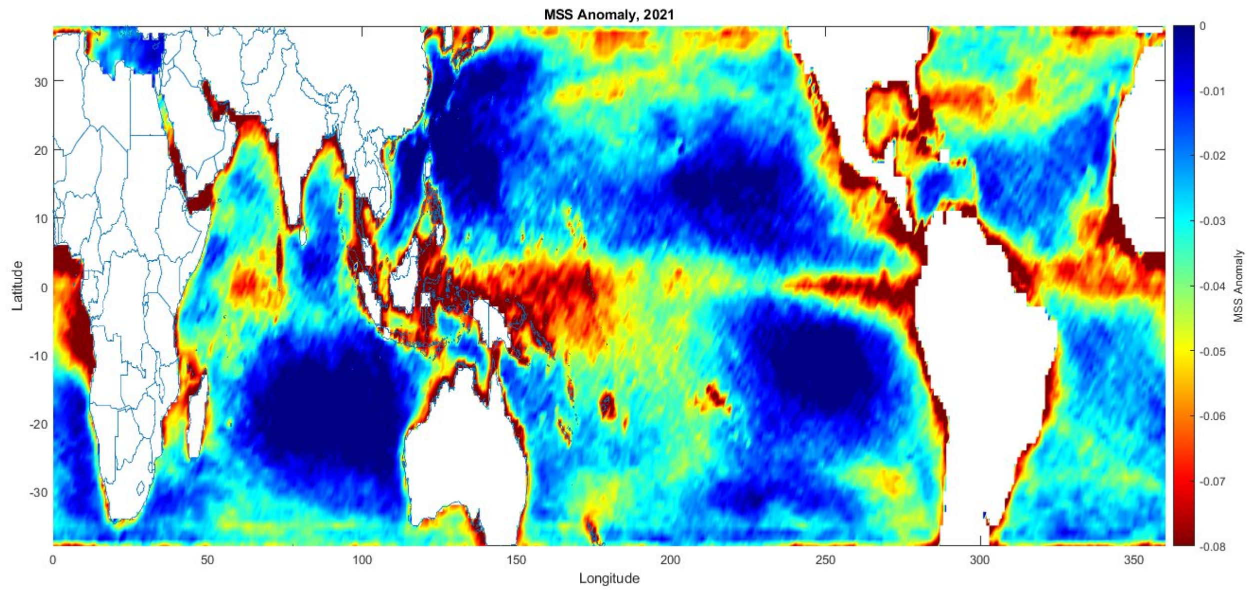

Figure 3.1: MSS_{ANOM} averaged over CY. 2021.

MSS_{ANOM} has peaks around coasts, in the ITCZ, and in the North Pacific Gyre. In Evans & Ruf [7], a correlation between areas with high microplastic concentration and areas of high negative MSS_{ANOM} was established. Sun et al. [8] showed that the cause of these high negative anomalies was surfactants, rather than the microplastics themselves. Surfactants leading to large negative MSS_{ANOM} can come from diverse sources, including algal blooms, microplastics, seaweed, and oil spills, underscoring the challenge of attributing anomalies to specific causes.

3.1.2 Algal Blooms and their effect on the Ecosystem

Algal blooms are a significant concern in marine environments due to their capacity to cause multiple types of damage. These blooms deplete oxygen beneath the surface, threatening the health and survival of marine organisms in those layers [9]. Additionally, they can pollute drinking water sources, posing a direct risk to human health, particularly when the blooms produce toxins [10]. The combination of ecological and public health effects makes the reliable detection and monitoring of algal blooms an important scientific and practical challenge. For coastal and inland waters, in-situ monitors are helpful but can be costly to maintain. Remote sensing methods of detecting algal blooms alleviate some of these concerns.

3.1.3 Project Objectives

Currently, the ability of CYGNSS to uniquely detect algae based solely on MSS anomaly measurements is limited. These measurements cannot differentiate between sources of surface-active substances, meaning that secondary data, such as that from other satellites, are necessary to interpret MSS Anomaly correctly. Moreover, no direct model presently exists to correlate algae concentration with MSS, highlighting a persistent gap in the field. Developing such a model, through controlled experiments with simulated ocean waves and known algae concentrations in a wave tank environment, is an important step for current and future research and could significantly advance the accuracy of remote algae detection.

This chapter will take a twofold approach. First, an experiment simulating ocean waves in a wind-wave tank is conducted. The water surface in the wave tank is contaminated with varying concentrations of algae, to see the effects of the algae on the water surface roughness given a controlled level of wind. A forward model involving chlorophyll concentration (a proxy for algae concentration), wind and MSS is developed from the wave tank results. Then a model with a similar functional form to the model derived in the wave tank is used with CYGNSS MSS data, using satellite and reanalysis inputs for the chlorophyll concentration and wind speed respectively.

3.2 Wavetank Experiment Background and Procedure

The University of Michigan's Marine Hydrodynamics Laboratory wind-wave tank was utilized to simulate ocean waves. The wave tank is 35 meters long and 0.7 meters wide with a maximum water depth of 0.68 meters; however, this water height fluctuated due to it being refilled every week and a slow leak in the tank that persisted at the start of testing. At one end of the tank, there is a vent to facilitate wind wave creation. The other end of the tank contains the fan creating a restrictive wind tunnel for wind waves and a 5° slope beach to dampen wave reflections in the signal. The fan is controlled via a panel that sets the fan's power. Figure 3.2 are photos and schematics of the wavetank.

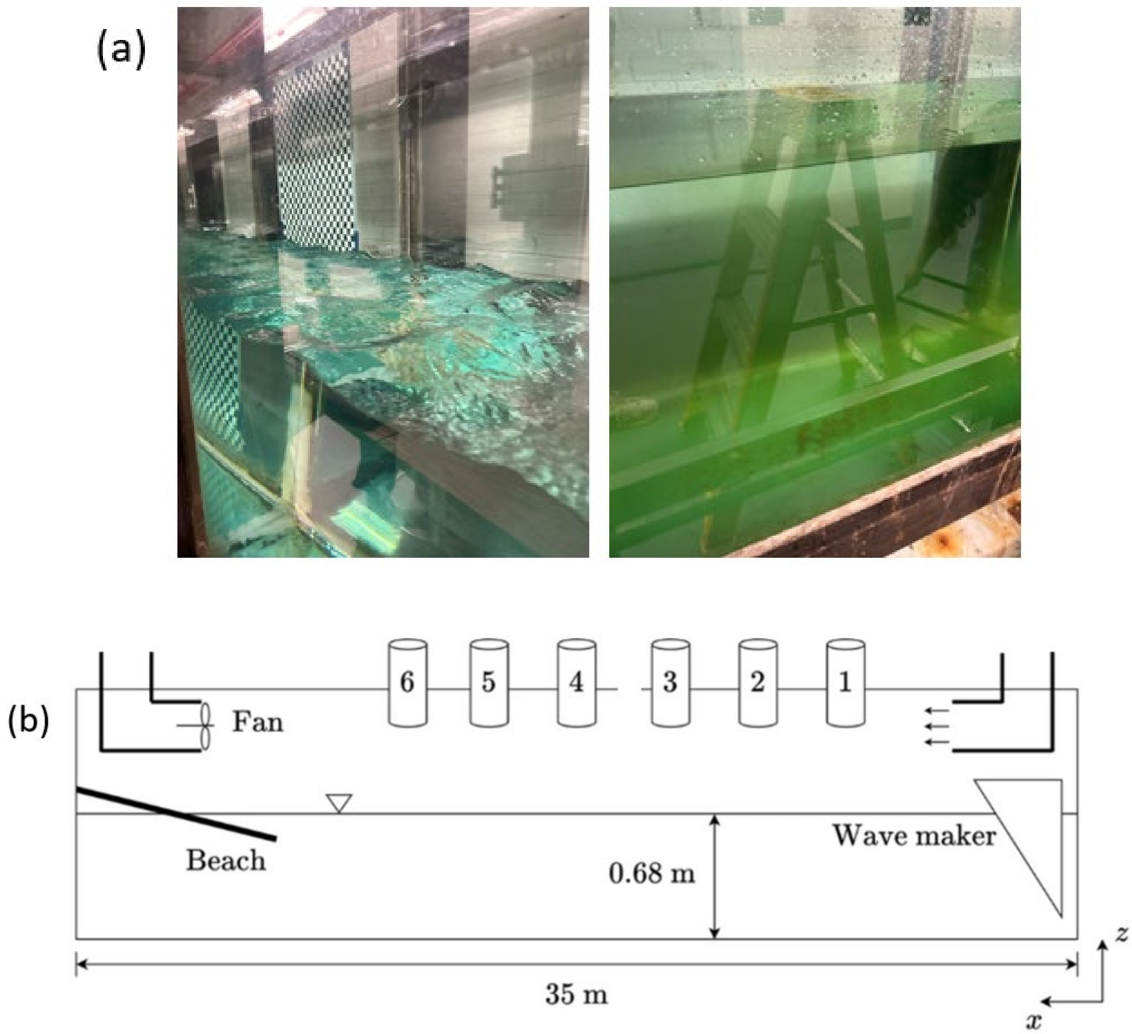

Figure 3.2: (a) Photos of the wavetank, without and with algae. (b) Schematics of the wavetank from Sun et al. [8], with the ultrasonic probes, and the beach at the far end of the tank. The wave maker was not used during this experiment.

Along the top of the tank, six Senix ultrasonic sensors are placed at distances of 2.03 m, 4.06 m, 6.91 m, 11.34 m, 15.44 m, and 21.13 m from the vent entrance to measure a time series of the height of the water surface. Parameter values were set, and sensor data was visualized and saved by a computer at the tank through a LabView controller. The gain of the first three sensors from the vent entrance was set to 5.04 and the final three were set to 10.8. Due to the computer's memory capabilities, the acquisition time of each run was 160 seconds with a CSV sample rate of 100 Hz. In addition to the 160 seconds required to collect data, around 160 seconds are needed to write it to a CSV file; therefore, the time between each consecutive data sample was about 2.5 to 3 minutes.

A HoldPeak Digital Anemometer is in the tank near ultrasonic sensor 3 to determine the fan power percentages and wind speeds. The anemometer provides wind speed accuracy of +/- 3 percent of the reading. Table 1 below matches well with the wind speeds reported in Sun et al., 2023.

Table 3.1: Wind Speeds and Error at Fan Power Percentages

Fan Percentage (%)	**25**	**30**	**35**	**40**	**45**
Wind Speed (m/s)	5.257	6.641	7.831	9.095	10.34
Error +/- (m/s)	0.17771	0.21923	0.25493	0.29285	0.3302

Fan powers of 25%, 35%, and 45% were chosen for the experiment because their speeds are evenly spread out within the range of 5-11 m/s. In this 5-11 m/s range, the CYGNSS MSS Anomaly map presented potential correlations with microplastics [11]. To determine if algae could better characterize some of these anomalies, it was important that wind speeds tested were within this range.

This experiment introduces various concentrations of algae into the wave tank, and the resulting MSS is measured by the ultrasonic probes. For this experiment, six different chlorophyll concentrations were used: 0 mg/m^3, 0.66 mg/m^3, 2 mg/m^3, 4 mg/m^3, 6 mg/m^3 & 8 mg/m^3. This range of values was chosen due to typical values of open ocean algal blooms. The reason for using chlorophyll concentration as a proxy for algae stems from the sensitivity of hyperspectral imagers. Hyperspectral imagers detect ocean color, and the green in the algae is directly due to its chlorophyll concentration.

The goal of the wave tank experiment is to create a forward model that can estimate MSS given chlorophyll concentration and wind speed. The MSS is determined from the surface height measurements made by the ultrasonic sensors, as explained below.

3.2.1 Determination of MSS from Surface Height Time Series

The ultrasonic sensors in the wavetank generates a time series of surface height, denoted by $\eta(t)$. MSS is derived from the time series using equation (3.2). To do so requires a transformation of the time series into an omnidirectional wave spectrum, $S(k)$. This section describes the process of deriving MSS from $\eta(t)$.

1. Take raw data from Senix Ultrasonic Probes

Raw data is collected by 6 Senix Ultrasonic Probes. An ultrasonic pulse is emitted from the sensor, and an echo returns from the target to the sensor. Before taking data, the ultrasonic probes are calibrated using the water surface with no wind as the control surface. Therefore, the data returned from the probes is height data, $\eta(t)$, measured in mm above or below the reference control height.

2. Divide the data into 20 second windows, with 10 seconds of overlap between each subset

A total of 160 seconds of height data is acquired. The data are subdivided into 16 sets of 20 second series. Each 20 second record has a 10 second delay from the start of the previous record. This approach was first formulated in Adak, 1997 [12].

3. Tukey Window filter to smooth out the edges of each record

Using a Tukey Window filter to tapers the edges of the signal with a linear drop-off while keeping the center minimally changed. Tapering the signal to zero at both edges avoids sharp discontinuities that can occur when using a Fast Fourier Transform (FFT). Figure 3.3 is an example of a Tukey Window used to taper the edges of a wave amplitude data record.

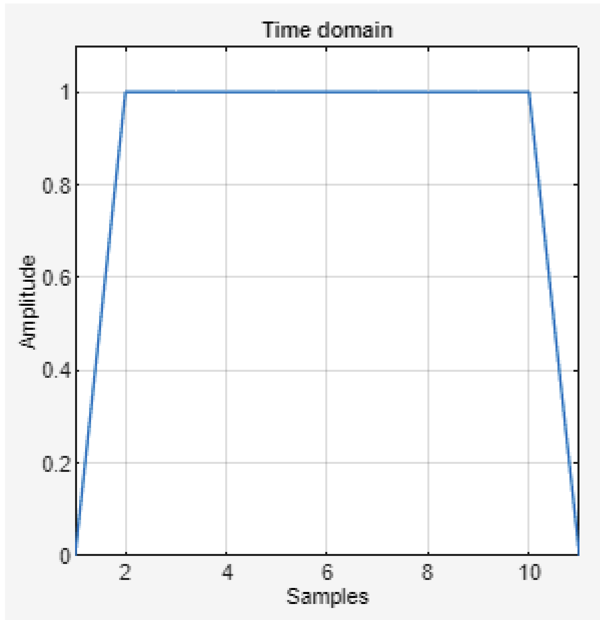

Figure 3.3: Tukey Window Filter Function.

The larger the number of samples is, the smoother the rolloff is at the ends of the function.

1. Fast Fourier Transform of each 20 second snippet of data

This step transforms the time series into frequency space, as given by

$$X(f) = FFT\big(\eta(t)\big) \tag{3.4}$$

2. Transform from X(f) to S(f) by taking the magnitude squared of the FFT and scaling it by 1/(Fs*N)

To manipulate a Fourier Transform into a Power Spectral Density, denoted by S(f), take the magnitude squared of the FFT and scale it by 1/(Fs*N), as described by

$$S(f) = \frac{1}{F_s N}|X(f)|^2 \tag{3.5}$$

where F_s is the sampling frequency and N is the number of samples in the FFT. In our case, F_s = 100 and N = 200 After processing each 20 second window of height data, we can average them together to create an average spectrum across the data run.

3. Map frequency to wavenumber using the deep-water linear dispersion relationship

The dispersion relationship provides a physics-based mapping. The relationship assuming deep-water conditions is given by

$$\omega^2 = gk \tag{3.6a}$$

$$\omega = 2\pi f \tag{3.6b}$$

where ω is the angular frequency of the waves, g is gravity, and k is the wavenumber. Combining (3.6a) and (3.6b) and solving for k gives the transformation relationship

$$k = \frac{4\pi^2 f^2}{g}. \tag{3.7}$$

The transformation of S(f) to S(k) requires rescaling by the Jacobian. This is necessary because spectral densities must satisfy conservation of variance. The resulting rescaling is given by

$$S(f)df = S(k)dk \tag{3.8}$$

$$S(k) = S(f)\left|\frac{df}{dk}\right| \tag{3.9}$$

$$\frac{d(k)}{df} = \frac{8\pi^2 f}{g}, \frac{df}{dk} = \frac{g}{8\pi^2 f} \tag{3.10}$$

Therefore

$$S(k) = S(f)\frac{g}{8\pi^2 f} \tag{3.11}$$

S(k) in (3.11) is the omnidirectional wavenumber spectrum as seen in Equation 3.3, and k has been defined in Equation 3.7. This gives us the two quantities in the integrand of the MSS equation, now the limits must be defined.

4. Choosing the appropriate cut-off wavenumber, k_c

The cut-off wavenumber, k_c is chosen to match the CYGNSS radar wavelength and measurement geometry. CYGNSS has an average cutoff wavenumber of 7.5 rad/m [13].

5. Integrate over 0 to k_c.

The final step to calculate MSS is integration over the appropriate range of wavenumbers, as described by equation (3.2). Numerical integration is performed using a trapezoidal method. Using these steps, MSS is derived from the wave tank surface height time series data.

3.2.2 Omnidirectional wave spectrum smoothing

Figure 3.4 provides examples of the omnidirectional wave spectra (S(k)) calculated using the above procedure from data recorded by the ultrasonic probe at Location #4. Each run is a 160 second data record, with 5 runs being taken. The figure shows a black solid line indicating the cutoff wavenumber, which is located at 7.5 m^{-1}. This is the average cutoff wavenumber from the CYGNSS mission. In addition to the expected general, monotonic roll-off of spectral density with increasing wavenumber, the spectra contain a consistent spectral artifact which must be corrected.

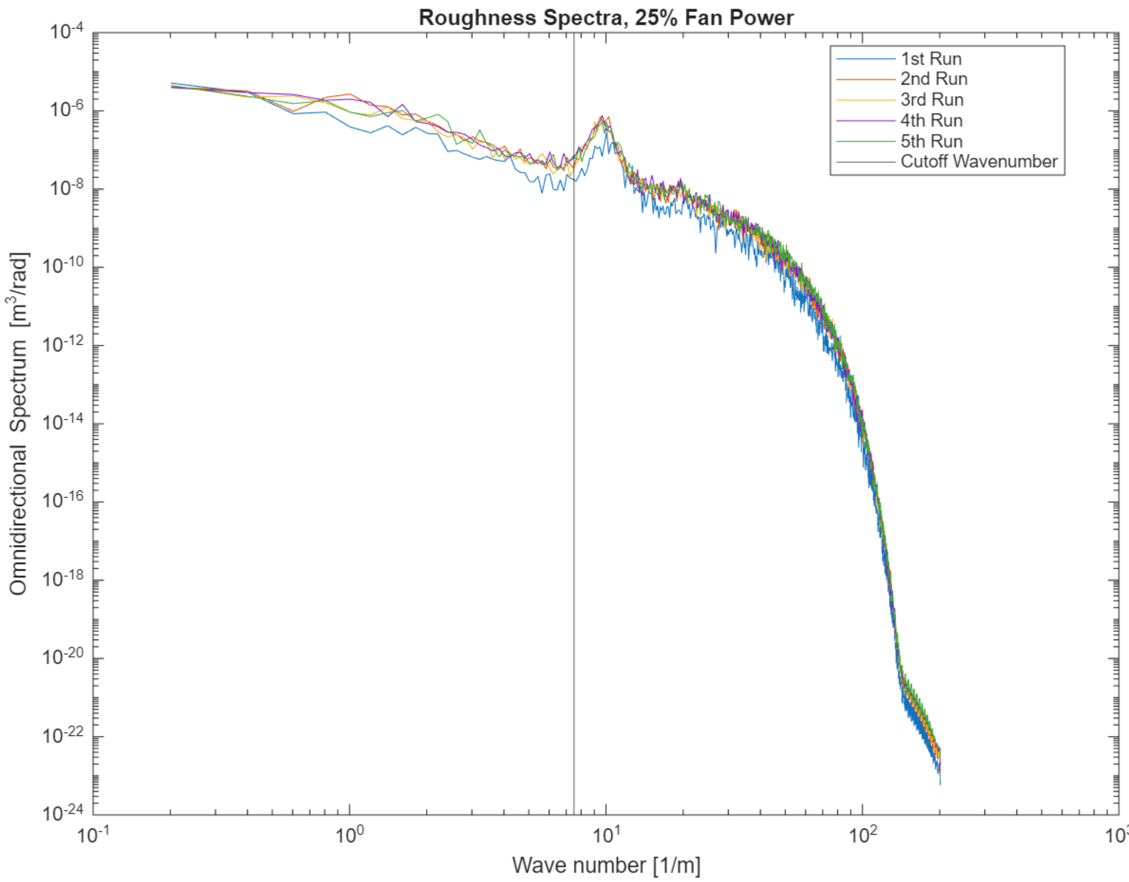

Roughness Spectra, 25% Fan Power
1st Run
2nd Run
3rd Run
4th Run
5th Run
Cutoff Wavenumber
Omnidirectional Spectrum [m^3/rad]
Wave number [1/m]
10^{-4}
10^{-6}
10^{-8}
10^{-10}
10^{-12}
10^{-14}
10^{-16}
10^{-18}
10^{-20}
10^{-22}
10^{-24}
10^{-1}
10^{0}
10^{1}
10^{2}
10^{3}

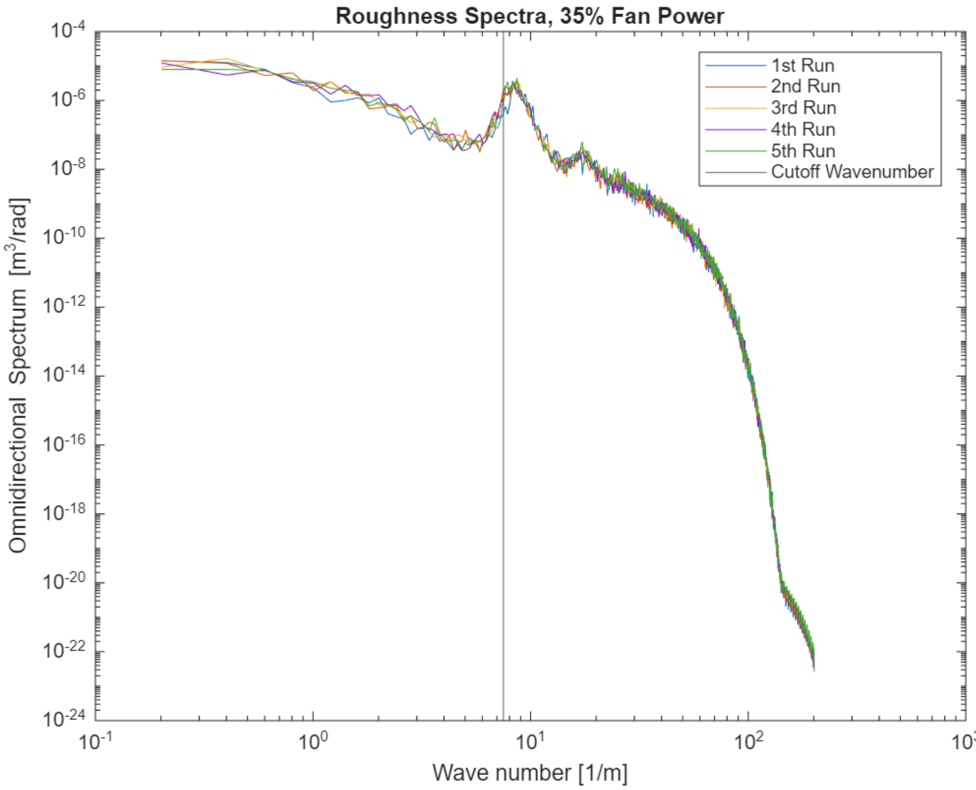

Roughness Spectra, 35% Fan Power
Omnidirectional Spectrum [m^3/rad]
Wave number [1/m]
1st Run
2nd Run
3rd Run
4th Run
5th Run
Cutoff Wavenumber
10^{-4}
10^{-6}
10^{-8}
10^{-10}
10^{-12}
10^{-14}
10^{-16}
10^{-18}
10^{-20}
10^{-22}
10^{-24}
10^{-1}
10^{0}
10^{1}
10^{2}
10^{3}

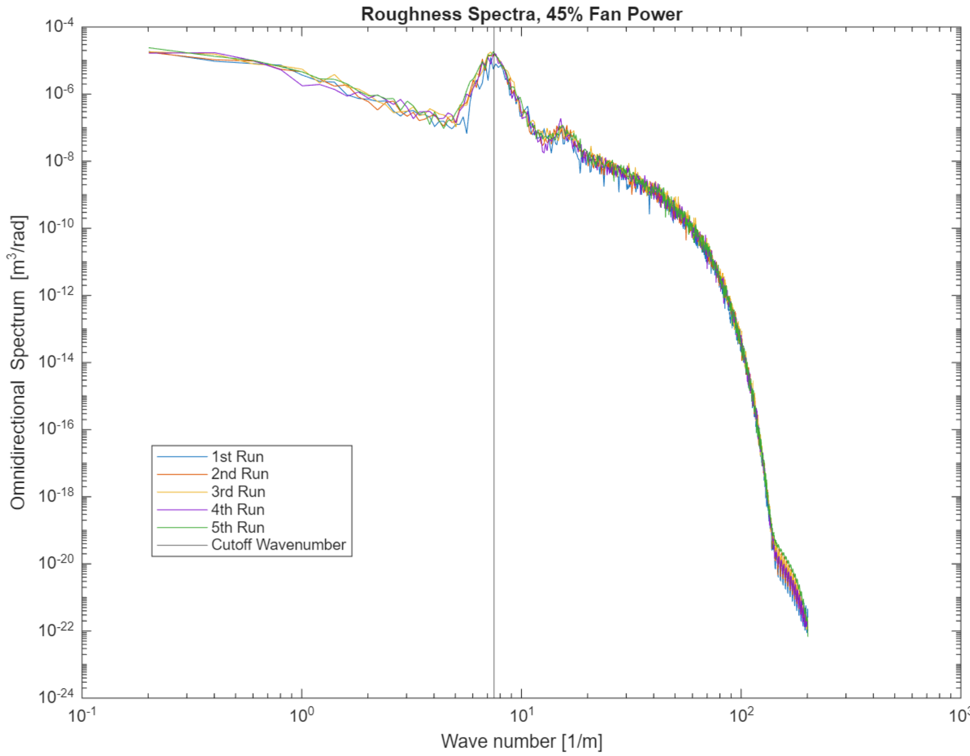

Figure 3.4: Omnidirectional wave spectra of the roughened water surface due to wind speeds of (a) 5.26 m/s. (b) 7.83 m/s. (c) 10.31 m/s.

The “bump” in the spectra in the vicinity of k = ~10 m^{-1} is apparent in all runs. It is due to a partial reflection from the beach at the far end of the wave tank, not due to wind-wave physics [14]. Although it does not affect our calculations at 5 m/s winds, as the winds grow, so does the range of the bump. In open ocean conditions, this bump does not exist. Figure 3.5 below from Elfouhaily et al. [15] shows the expected behavior of the roughness spectrum modeled in the open ocean.

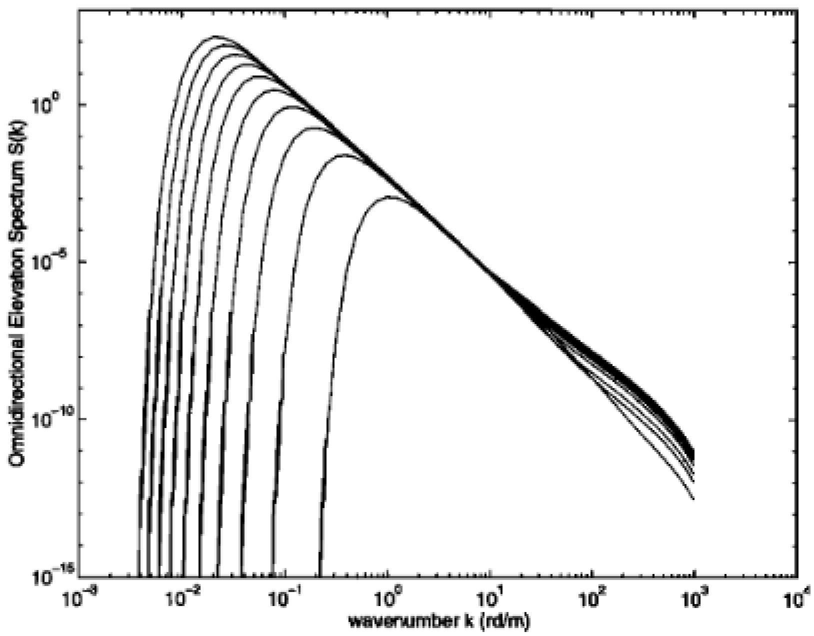

Figure 3.5: S(k) according to the Elfouhaily et al. [14] model. Each curve represents different wind speeds, with each curve changing in wind speed by 2 m/s from left to right.

To emulate spectra that would occur in the open ocean, a corrective spline interpolation is applied to mitigate the effects of the bump, as shown in Figure 3.6 below. The interpolated curve was made by measuring the derivative between each point, noting where the derivative began to curve upwards and removing all the points with slopes that did not follow the Elfouhaily curvature. Figure 3.6 shows the resulting spectra after the spline interpolator has been applied to the spectra shown in Figure 3.4.

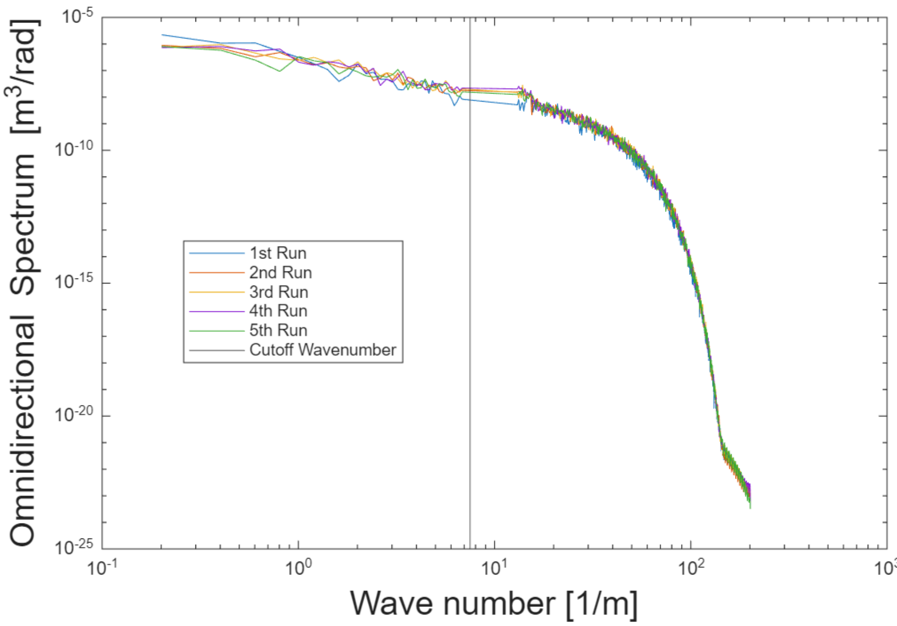
Omnidirectional Spectrum [m^3/rad]
Wave number [1/m]
1st Run
2nd Run
3rd Run
4th Run
5th Run
Cutoff Wavenumber

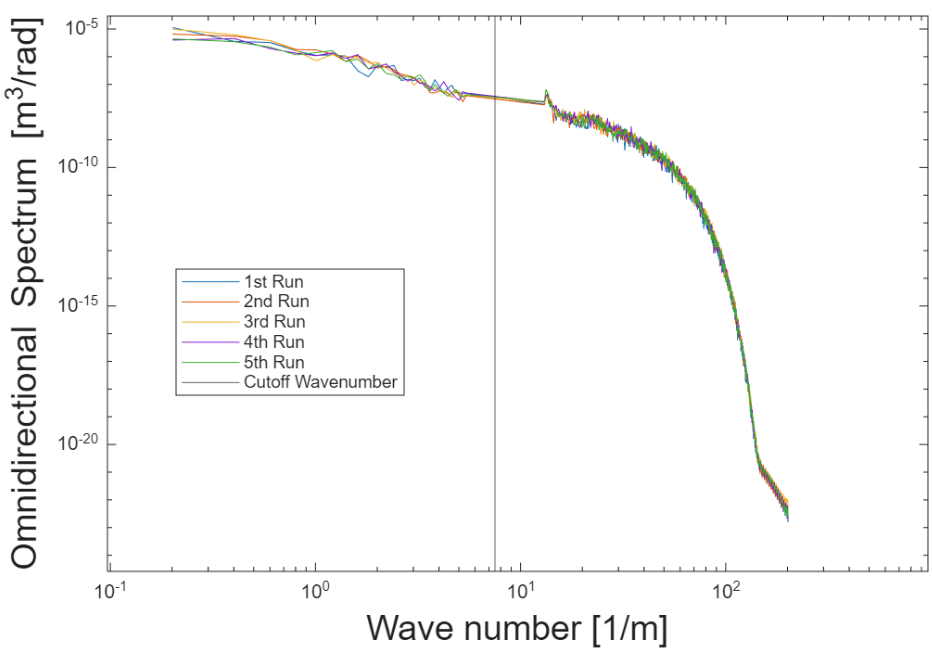
Omnidirectional Spectrum [m^3/rad]
Wave number [1/m]
1st Run
2nd Run
3rd Run
4th Run
5th Run
Cutoff Wavenumber

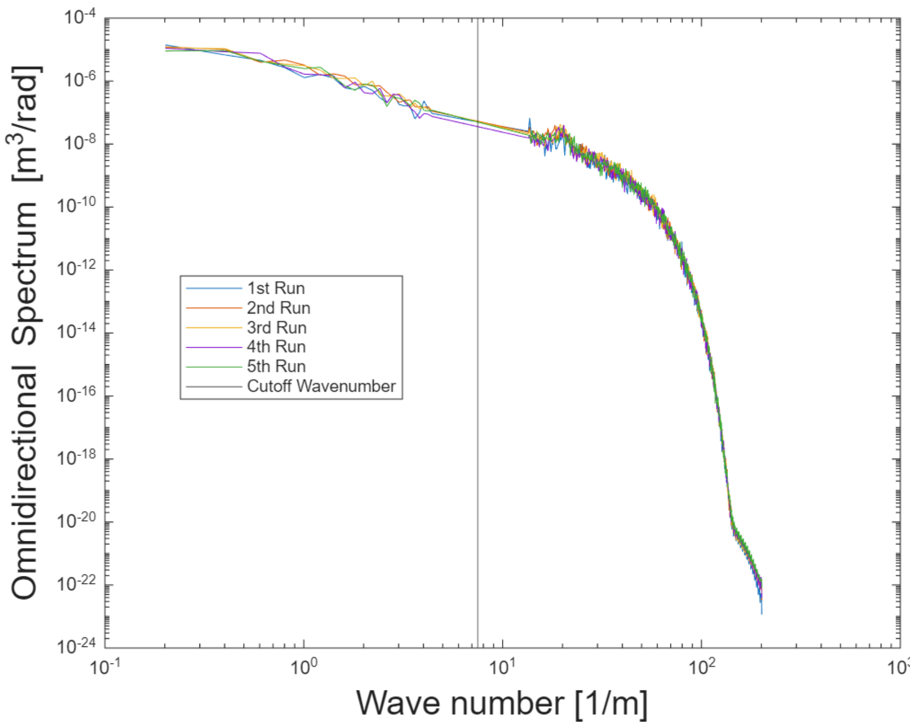

Figure 3.6: Roughness spectra (S(k)) with the wave tank artifact removed by a spline interpolator.

This interpolation correction is used during the MSS processing to improve the accurate simulation of ocean spectral conditions experienced by CYGNSS in the open ocean.

3.2.3 Spin-up time due to Wave Energy Stabilization

Because these experiments are conducted in a wave tank, it is also necessary to account for wave-spectrum energy buildup and the associated spin-up period.

Wave energy from a roughness spectrum is defined as [12]

$$E = \int_0^{k_c} S(k)dk \tag{3.12}$$

where E is the wave energy in m^2, S(k) is the omnidirectional wave spectrum and k_c is the cutoff wavenumber.

Energy spectra were examined throughout each run, and data were only used for which the spectra demonstrated a stable integrated energy. Figure 3.7 shows an example of the integrated energy derived from the wave tank data. In the figure, the fetch length corresponds to distance from the fan. After processing the time series for each probe, each probe has a unique omnidirectional wave spectrum. The omnidirectional wave spectrum is then integrated over wavenumbers to calculate the wave energy at that probe location. The goal is to figure out when the wave energy stays stable from run to run, because we would like the waves to be in their fully developed form.

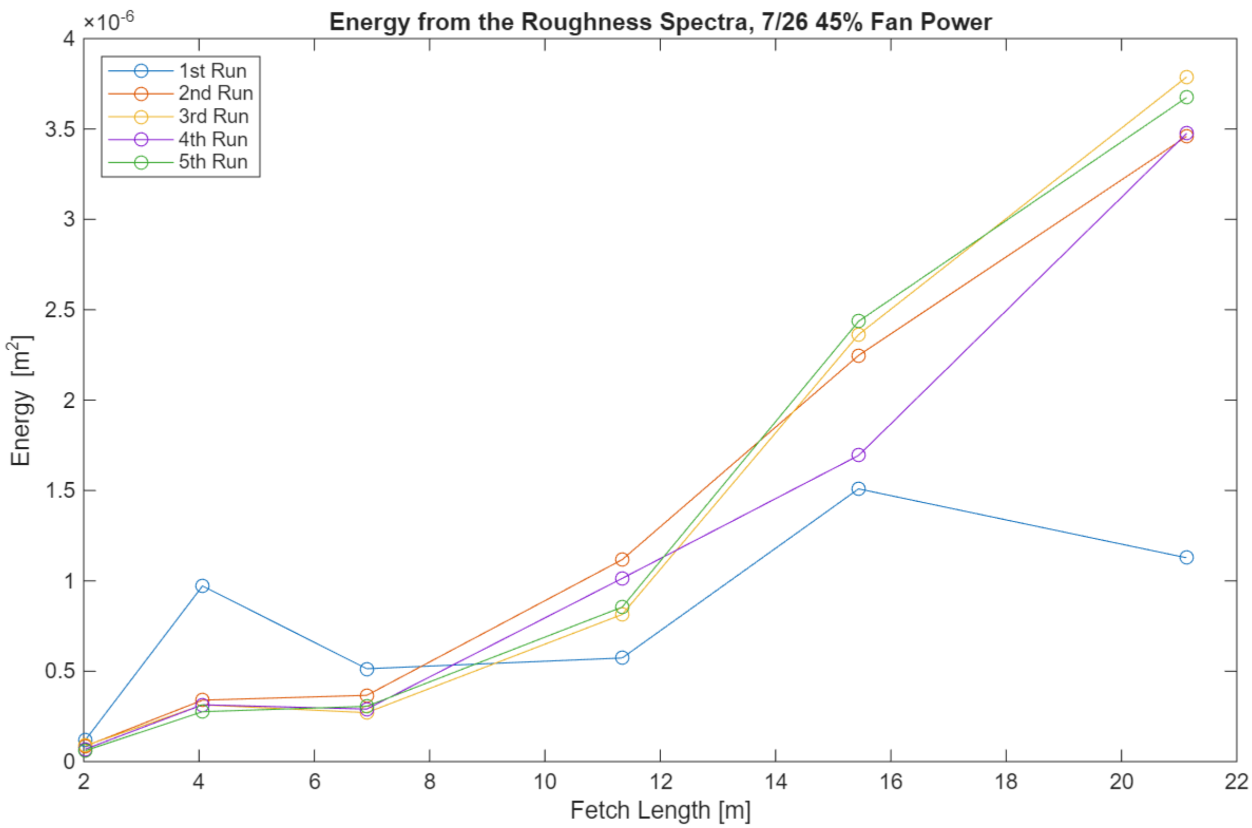

Figure 3.7: Energy spectra taken from a clean-water run of the wave tank. Data was taken on 26-Jul-2024, with a fresh tank of water (no algae in the water), with 5.26 m/s winds.

The “run” in Figure 3.7 refers to a time series data record, taken from the wavetank. Each run records 160 seconds of data, then it takes around 160 more seconds for the data to be written into a CSV file. The 1st run started 15 seconds after the wind-wave generating fan was turned on. The second run occurred 360 seconds after the first one, and the third one occurred 360 seconds after the second run.

Based on Figure 3.7, runs 2 through 5 were used in subsequent analysis. This equates to using runs that start at least five minutes after the fan start time. In addition, MSS results were taken from the fourth probe location: upstream probes did not exhibit sufficient wave energy for damping effects to be observable, while probes farther down-tank were strongly influenced by partially reflecting waves.

3.2.4 What kind of algae was used?

Algal concentration in the wave tank was quantified as dry-weight biomass concentration (mg /m^3). The microalga Nannochloropsis oculata (N. oculata) was selected because it is a robust strain that tolerates a wide range of environmental conditions, reducing the likelihood of culture loss under sub-ideal wave-tank conditions [16]. The algae was purchased from Algae Research and Supply, a wholesale seller in California. Although commonly associated with marine systems, N. oculata can persist across variable salinities and sea surface temperatures, supporting its use in controlled laboratory experiments where the water conditions fluctuate. Target dry-weight concentrations were prepared and verified to enable repeatable dosing and intercomparison among experimental runs.

To assess algal biomass in situ, dry-weight concentration was estimated using a Secchi Disk stick approach in an auxiliary tank and then related to the wave-tank concentrations. A Secchi Disk stick is a measuring stick with a perpendicular attachment located at the bottom of the stick. Figure 3.8 is a side-profile view of a Secchi Disk stick.

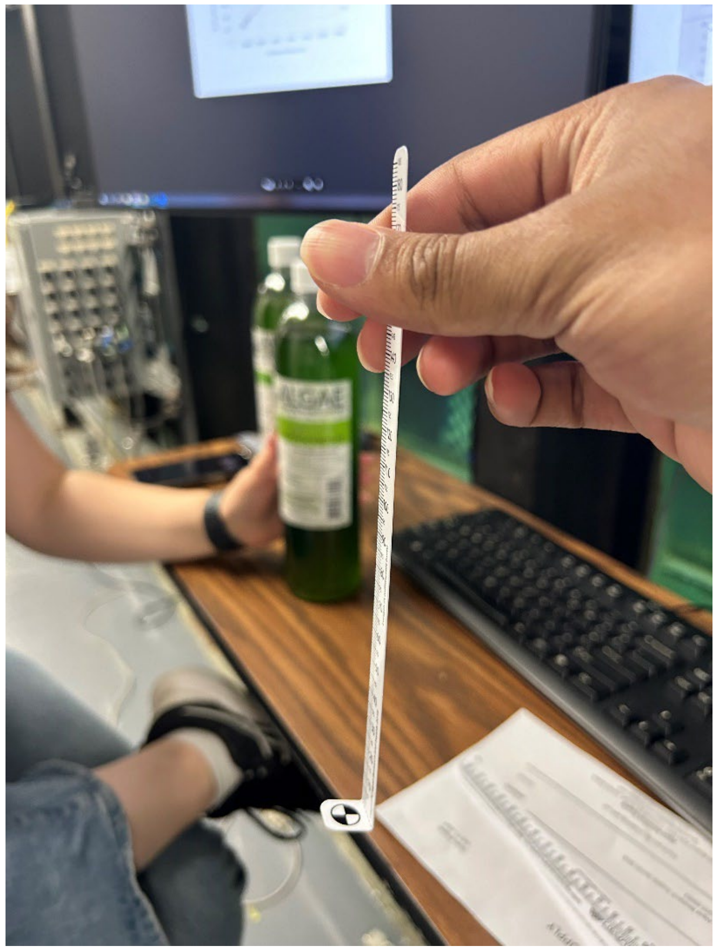

Figure 3.8: Side-profile of a Secchi Disk stick, with the Secchi Disk visible at the bottom of the measuring stick.

Secchi Disks are useful when measuring the opacity of a liquid, and a demonstration of how to use one is demonstrated in Figure 9.

Figure 3.9: Side-profile of a Secchi Disk stick, with the Secchi Disk visible at the bottom of the measuring stick.

Using the readings from the measuring stick, an observer can tell when the disk located at the bottom of the measuring stick becomes obscured by the algae in the container. The depth at which the Secchi Disk disappears corresponds to a specific density of algae cells. In the demonstration from Figure 3.9 I'm using Chlorella Vulgaris algae, but the process applies to Nannochloropsis Oculata as well.

Secchi disk disappearance depth was recorded and converted to algal dry-weight concentration via a disk-depth to algae-concentration calibration chart. This conversion chart from dry-weight concentration to disk depth is plotted in Figure 3.10.

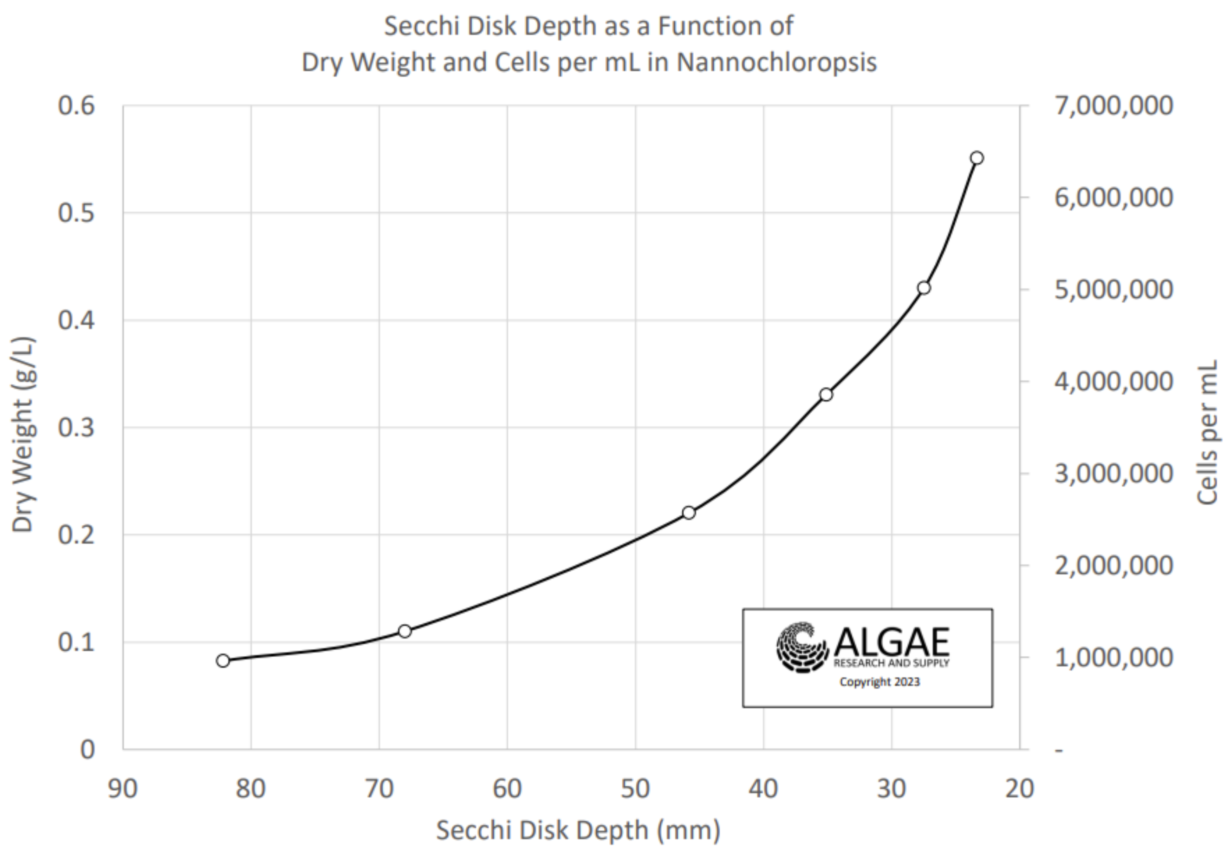

Figure 3.10: Dry weight algae in [g/L] vs. Secchi Disk Depth in mm. Secchi disks helped analytically convert the aqueous algae into a usable concentration metric. Figure courtesy of Algae Research and Supply.

This conversion provides an operationally simple method for adjusting biomass to specified target levels prior to wave measurements. From dry weight algae, Nannochloropsis Oculata tends to have between 0.3-2% of its dry weight be chlorophyll-a [17], so to standardize it, N. Oculata was assumed to be 1% dry weight of chlorophyll, meaning the algae biomass was divided by 100 to get appropriate amounts.

3.2.5 Error Analysis

A key part of the MSS error analysis is identifying uncertainty in the instrument response and in experimental repeatability. The probe's amplitude measurements can introduce both accuracy (systematic bias from calibration, sensor drift, temperature effects, alignment/positioning in the tank, electrical noise) and precision limits (short-term fluctuations, digitization/processing variability). Repeatability also depends on how consistently the flow field is generated: if the fan's output varies run-to-run (or with warm-up time, battery/voltage changes, or slight differences in placement), the turbulence/suspension conditions can change even at the same nominal power setting. Practically, this can be evaluated by repeating identical trials and reporting the run-to-run spread of MSS outputs (e.g., mean ± standard deviation, coefficient of variation), and by testing sensitivity to fan power.

A second major source of uncertainty is how accurately and repeatably the chlorophyll-a (or proxy) concentration is prepared and measured. Errors can enter through tank dimension measurements (affecting volume), measuring cups/cylinders (meniscus reading, calibration class), mass/volume of chlorophyll-a added (scale accuracy, losses during transfer, incomplete mixing), and Secchi disk measurements (observer variability, lighting, viewing angle). These should be quantified by assigning uncertainty to each input (from instrument specs or repeated measurements), then propagating them into the final concentration uncertainty using standard error propagation (combine independent terms in quadrature; include covariance if applicable). A useful check is a clean-water run repeatability to establish the MSS "baseline noise/floor" and any systematic offset. This check also serves as a first look at if the MSS processing has been done correctly, as clean water runs can be compared to past experiments. Figure 3.11, top is from a set of wave tank runs with no algae involved from our experiment, and this follows the MSS results from previous wave-tank experiments, under similar conditions. From the Sun et al. [8] experiment, wave tank MSS given a cutoff wavenumber of 7.5 rad/m was on the order of 10^{-5}, as shown in Figure 3.11 (bottom).

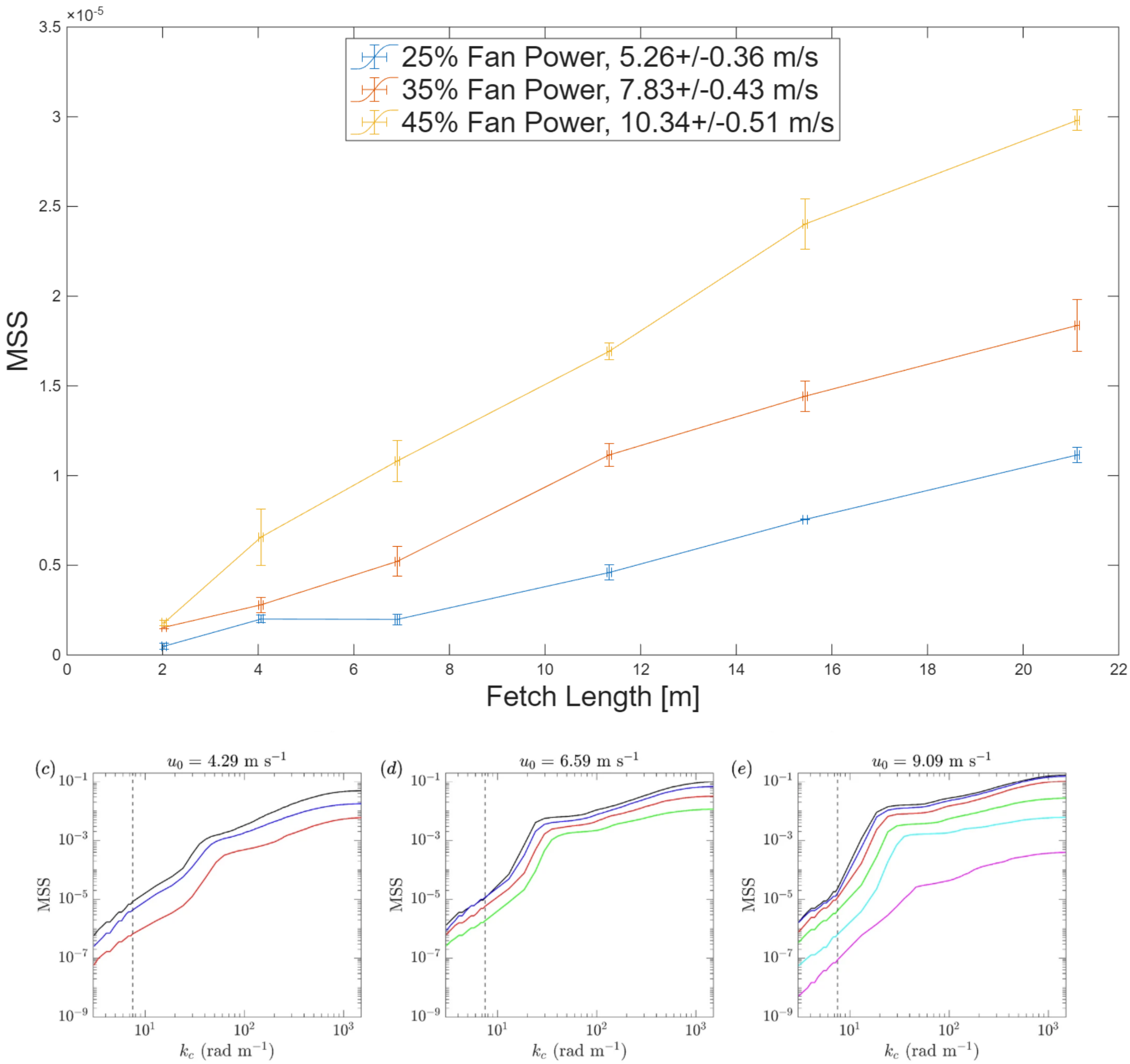

Figure 3.11: (top) Clean water repeatability test runs from our experiment (bottom) MSS plots from Sun et al. [8] showing that at our cutoff wavenumber, the MSS should be on the order of 10^{-5}.

3.2.6 Wavetank Data Processing

Following the MSS calculation procedure described above, MSS values were computed for three different wind speeds across six chlorophyll concentration levels. The primary objective was to compare MSS in the presence of chlorophyll to clean water MSS to determine whether chlorophyll measurably influences surface wave slope statistics. If chlorophyll contributes to enhanced damping, the expected signature would be a reduction in MSS as chlorophyll concentration increases.

After analyzing the wave tank data, each MSS data point was taken per wind speed and chlorophyll concentration. The results are tabulated in Figure 3.12.

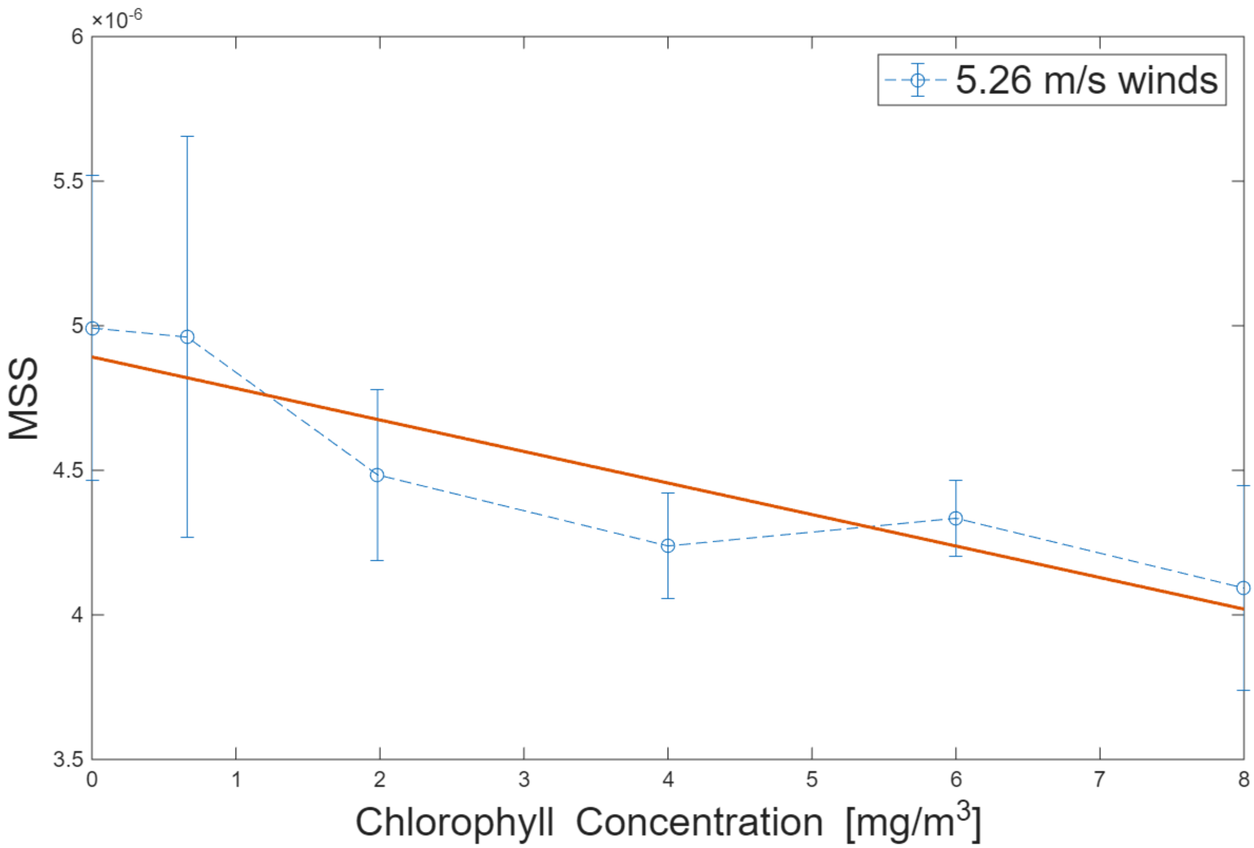

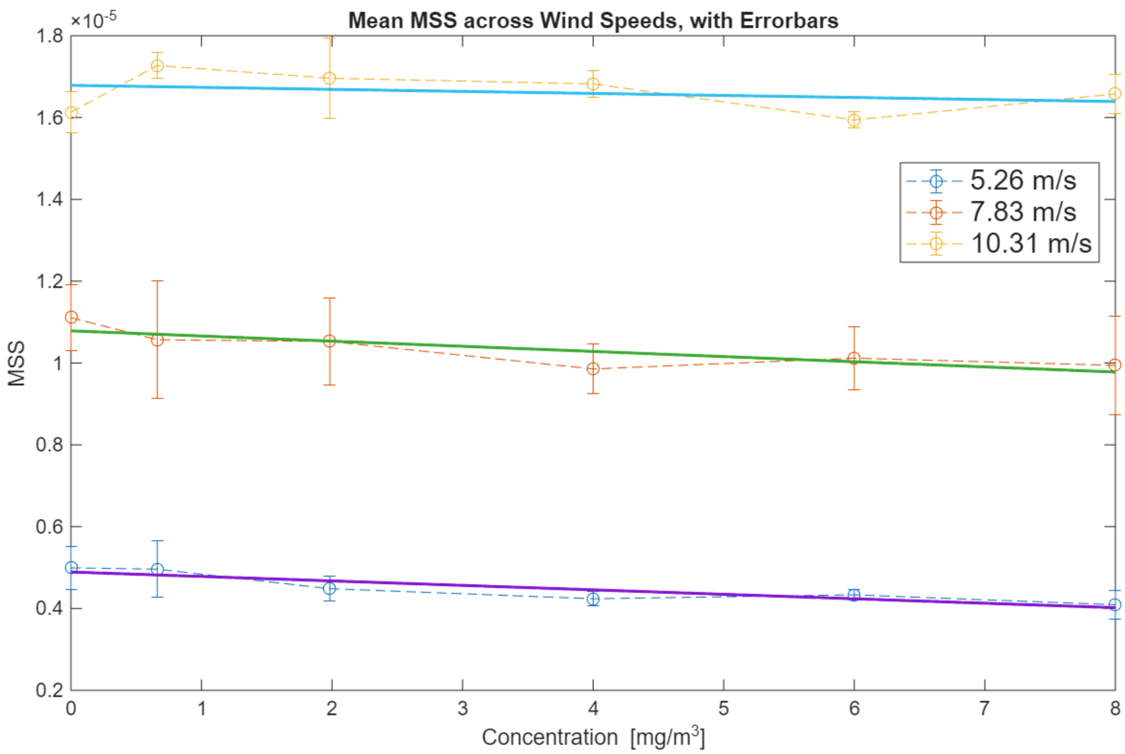

Figure 3.12: (top) MSS and chlorophyll concentration plotted for 5.26 m/s winds. (bottom) MSS plotted over chlorophyll concentration. Each set of points represents a different wind speed.

Figure 3.12 used the mean MSS averaged over data runs 2-5. Figure 3.12 (top) demonstrates that as chlorophyll-a concentration increases, the MSS decreases. This relationship is plotted out for all three wind speeds used, and a best fit line was plotted for each wind speed's data set. The slope and y-intercept of these fits serve as the basis for our MSS-Wind-Chlorophyll Concentration (MWCC) Model. The slope of these curves gives information about the strength of the damping effect of chlorophyll. The y-intercept has information about the scale, as each wind speed changes the scale of the MSS.

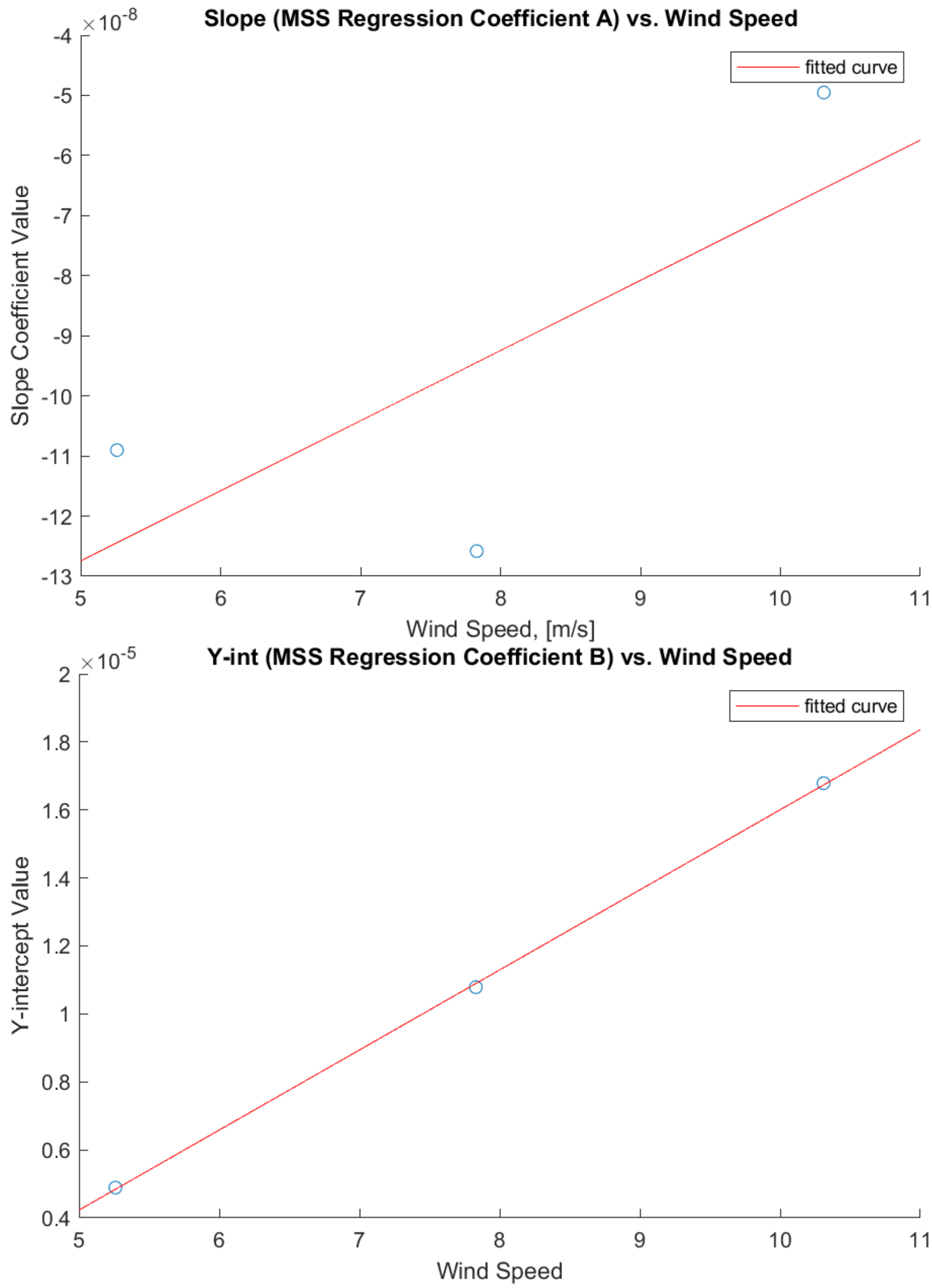

Figure 3.13: Slopes and y-intercepts of the best fit curves between MSS and chlorophyll concentration.

The slopes and y-intercepts of these curves are used to fit a new MSS-Wind Speed-Chlorophyll Concentration model. Because only three fixed wind speeds are used, the model is assumed to depend linearly on wind speed.

3.3 Wavetank Experiment Results

The new MWCC wave tank model is a three-parameter model described by

$$MSS_{WT} = a(WS)CC + b(WS) \tag{3.13a}$$

$$a(WS) = (1.17 * 10^{-8})WS - 1.8 * 10^{-7} \tag{3.13b}$$

$$b(WS) = (2.36 * 10^{-6})WS - 7.5 * 10^{-6} \tag{3.13c}$$

where WS is wind speed in m/s, CC is chlorophyll concertation in mg/m^3, and a(WS) and b(WS) are functions of wind speed. a(WS) and b(WS) are derived from the results shown in Figure 3.13.

To help illustrate model behavior, Figure 3.14 is a color plot showing how MSS varies jointly as a function of wind speed and chlorophyll concentration.

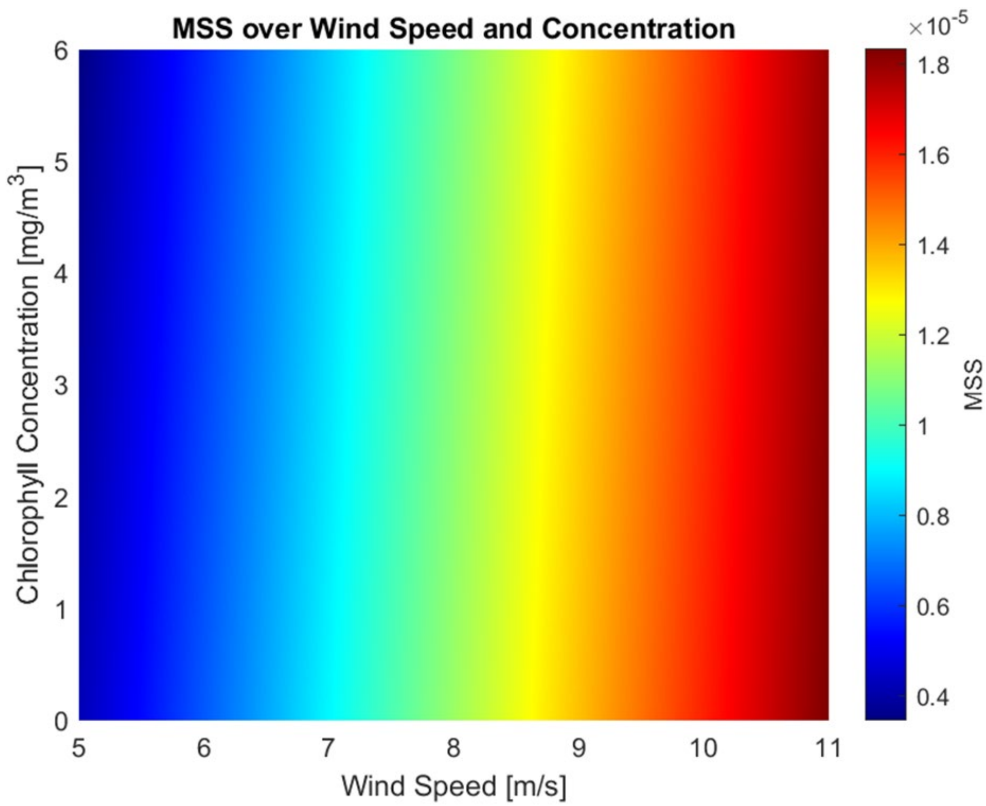

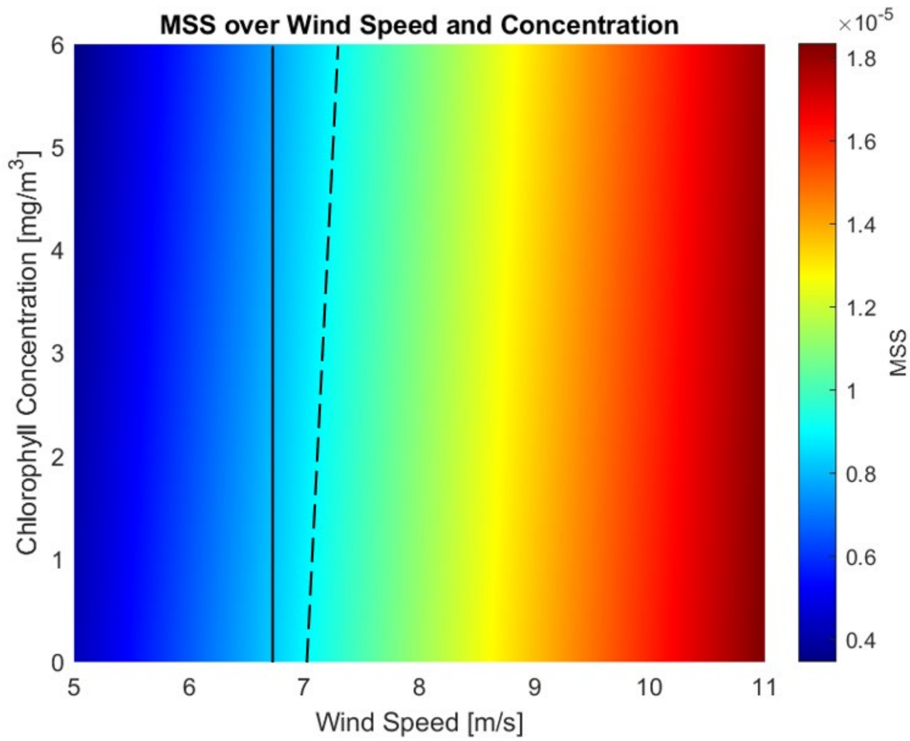

Figure 3.14: (top) MSS-Wind Speed-Chlorophyll-a Concentration (MWCC) model shown via gradients in a colormap. (bottom) The MWCC model with a vertical solid line (i.e. line of constant wind speed) and a dashed MSS isoline.

The wave-tank model demonstrates a strong dependence on wind speed while also exhibiting a measurable, though comparatively weak, sensitivity to chlorophyll-a concentration. If chlorophyll exerted no influence, the MSS isolines would appear vertical; instead, the observed tilt in the MSS contours indicates that chlorophyll modifies the MSS-wind relationship rather than leaving it invariant.

This chlorophyll signal is plausibly muted by tank-specific physical constraints: photographic evidence of Nannochloropsis suggests that the live algae does not form a thick, continuous surface film, limiting its capacity to alter surface roughness in the way an idealized surfactant layer might [18]. Moreover, practical limitations on both the type and quantity of algae that could be introduced into the tank required the use of suboptimal algae conditions, further attenuating the observable effect. Nonetheless, the emergence of any consistent chlorophyll dependence under these constraints is substantively important, because it supports the underlying premise that biological presence can imprint on MSS even in non-ideal experimental settings. Finally, the experiment provides not only empirical evidence but also methodological justification for the model's functional form: decomposing the parameterization into a term that serves as an indicator of algae presence (the first term of Equation 3.13a) and a separate term that scales the response (the second term of Equation 3.13a) establishes an interpretable structure that will be carried forward as the analytic framework for the CYGNSS data.

3.4 Applications of the New MWCC Model Framework

A satellite-based MWCC model in the open ocean is constructed in a similar manner as above using CYGNSS observations of MSS during Jan-Dec 2021 that were coincident and collocated with wind speeds provided by ERA5 and chlorophyll-a concentrations provided by NOAA VIIRS. The MSS measurements were binned and average over increments of wind speed and chlorophyll concentration. The joint dependencies between the 3 variables are generally like those observed in the wave tank. The finer gradations of variability in wind speed and chlorophyll-a concentration afforded by the satellite-based data allows for more degrees of freedom to be adjusted in the current model. This permits the use of a higher order regression model.

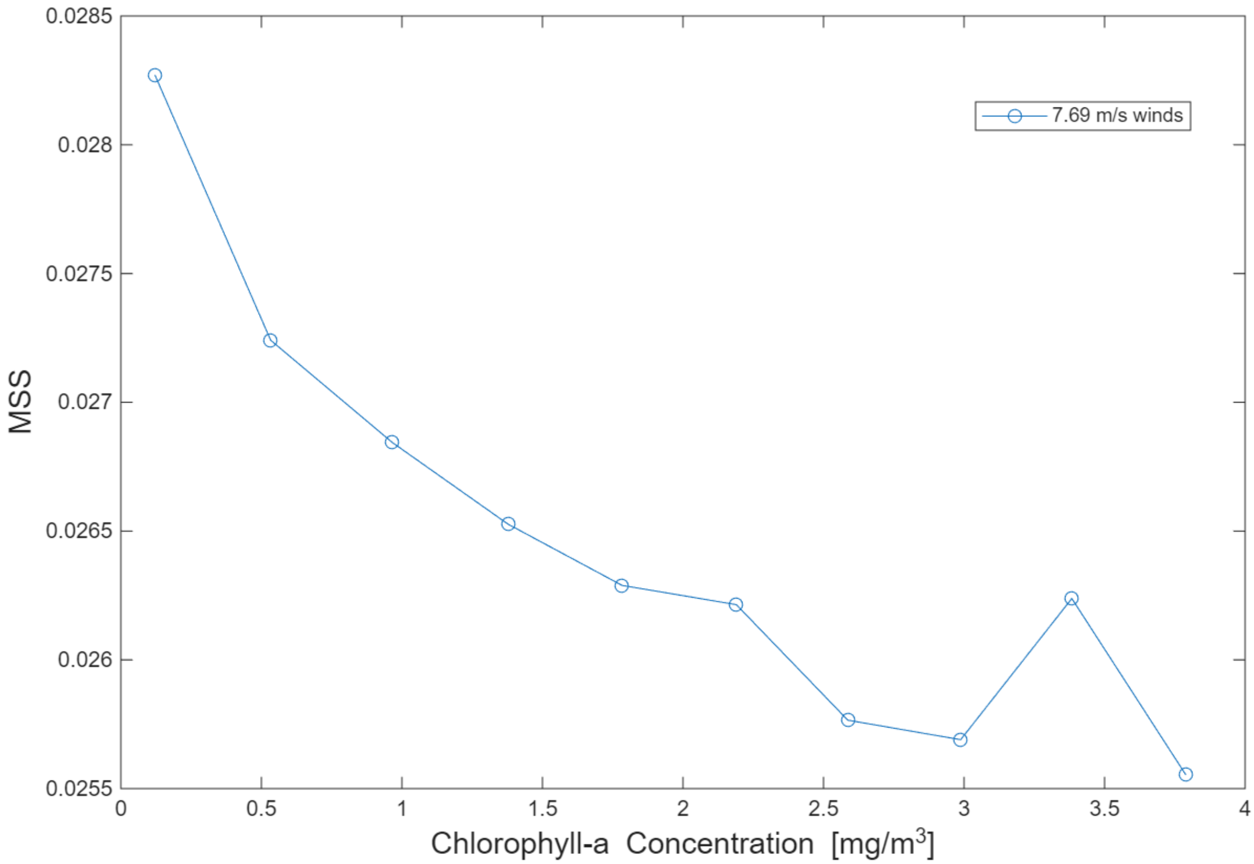

Figure 3.15: MSS vs. Chlorophyll-a Concentration for a wind bin centered at 7.69 m/s.

Figure 3.15 shows an example of the satellite MSS observations vs. CC observations at one wind speed. A similar relationship is found at other wind speeds, with the slope and y-intercept of the best fit line varying as a function of wind speed similarly as in the wave tank case. In the satellite case, the functional form of the dependence of slope and y-intercept on wind speed is found to be well represented by a quadratic in wind speed. This is illustrated in Figure 3.16.

The MWCC model for satellite and reanalysis data is a three-parameter model like the wave tank model, as given by

$$MSS_{CYG} = a(WS)CC + b(WS) \tag{3.14a}$$

$$a(WS) = (1.7 * 10^{-5})WS^2 - (3.0 * 10^{-4})WS + 8.2 * 10^{-4} \tag{3.14b}$$

$$b(WS) = (-1.6 * 10^{-4})WS^2 + (4.6 * 10^{-3})WS + 1.2 * 10^{-3} \tag{3.14c}$$

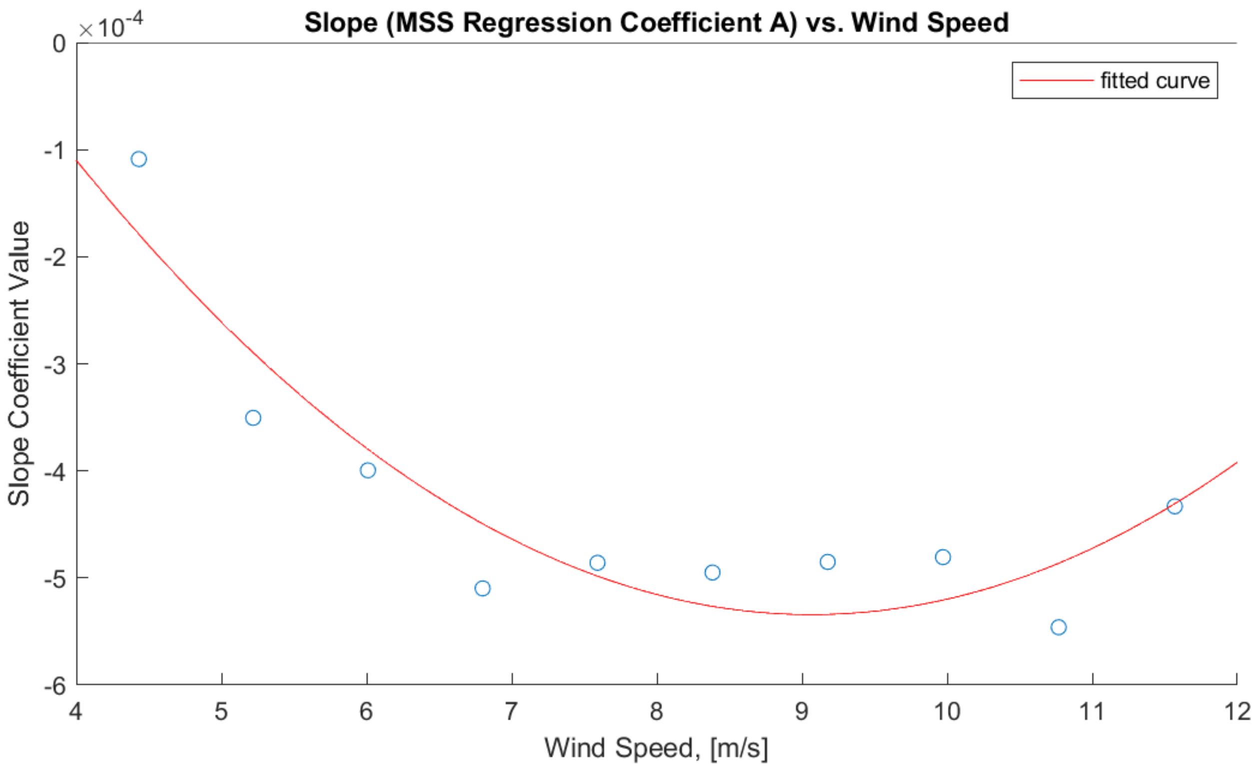
Slope (MSS Regression Coefficient A) vs. Wind Speed
$\times 10^{-4}$
0
-1
-2
-3
-4
-5
-6
Slope Coefficient Value
fitted curve
4
5
6
7
8
9
10
11
12
Wind Speed, [m/s]

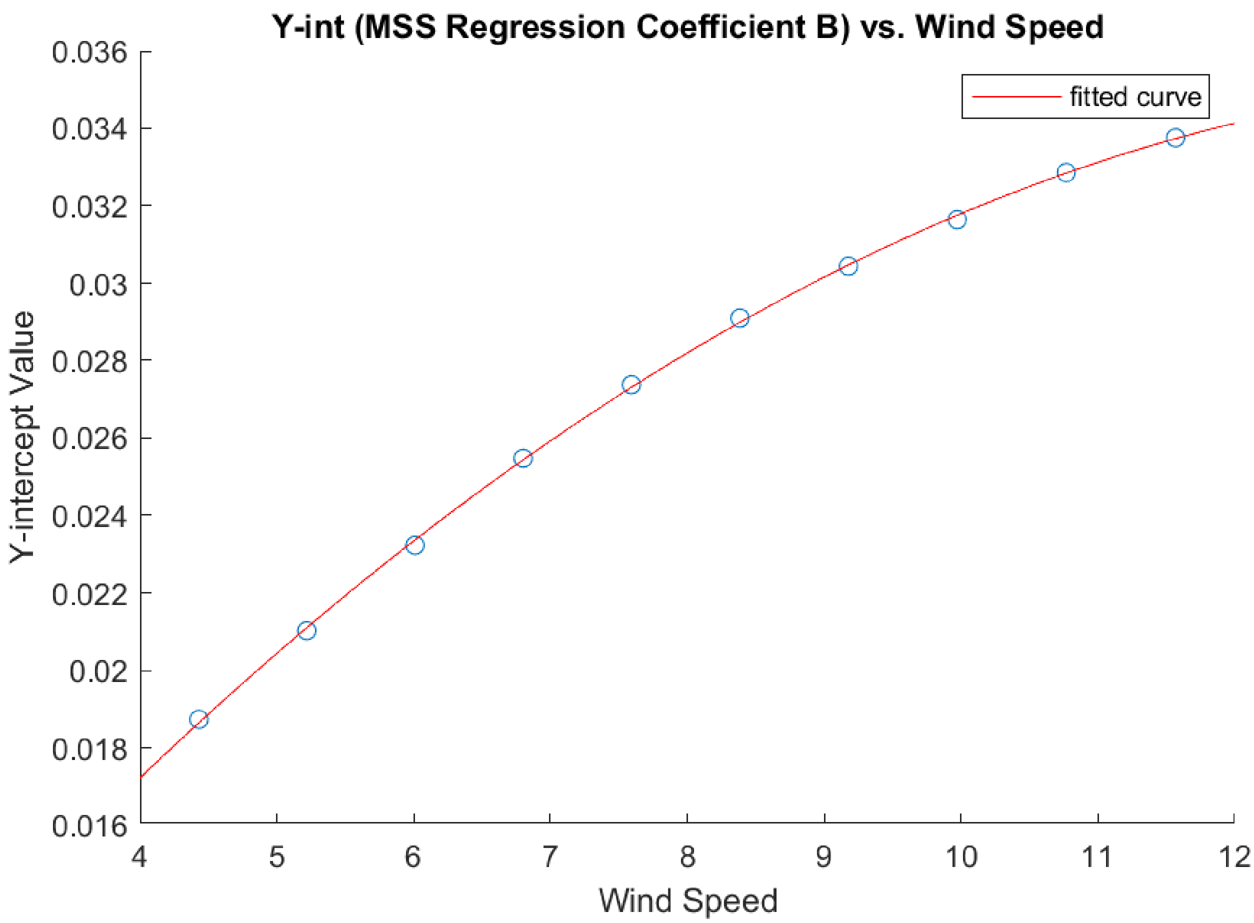

Figure 3.16: Slopes and Y-intercepts of the best fit curves between MSS and chlorophyll concentration, plotted against wind speed.

The behavior of this MSS model jointly as a function of wind speed and chlorophyll concentration is illustrated in Figure 3.17. In the figure, the MSS isoline can be seen to deviate significantly more from the vertical (iso-wind) line than was the case in the wave tank. This indicates that, relative to the wavetank-based model, the satellite model has a noticeably steeper dependence on CC, suggesting that algae suppressed ocean surface roughness more strongly in the open ocean than in the laboratory. The model is constrained to chlorophyll-a concentrations up to 4 mg m^{-3} as above this threshold the results begin to deviate, and the fit becomes less reliable.

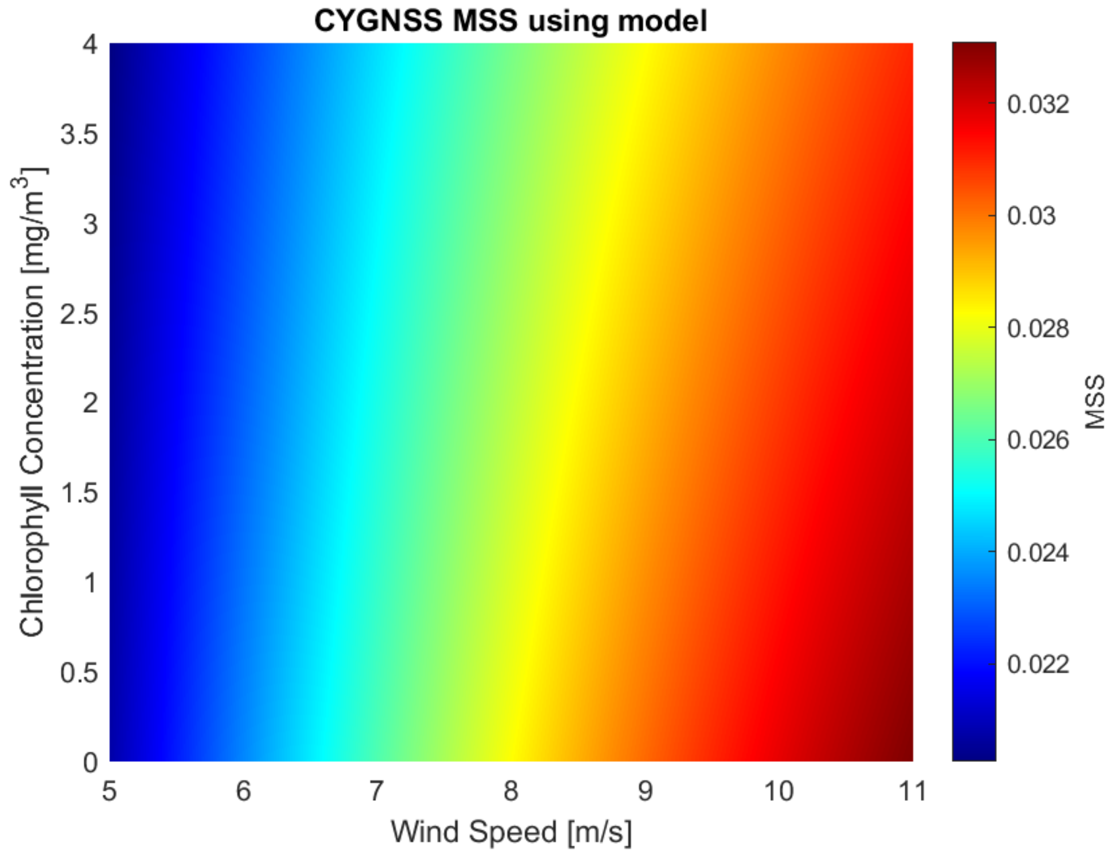

CYGNSS MSS using model
Chlorophyll Concentration [mg/m3]
0
0.5
1
1.5
2
2.5
3
3.5
4
5
6
7
8
9
10
11
Wind Speed [m/s]
MSS
0.022
0.024
0.026
0.028
0.03
0.032

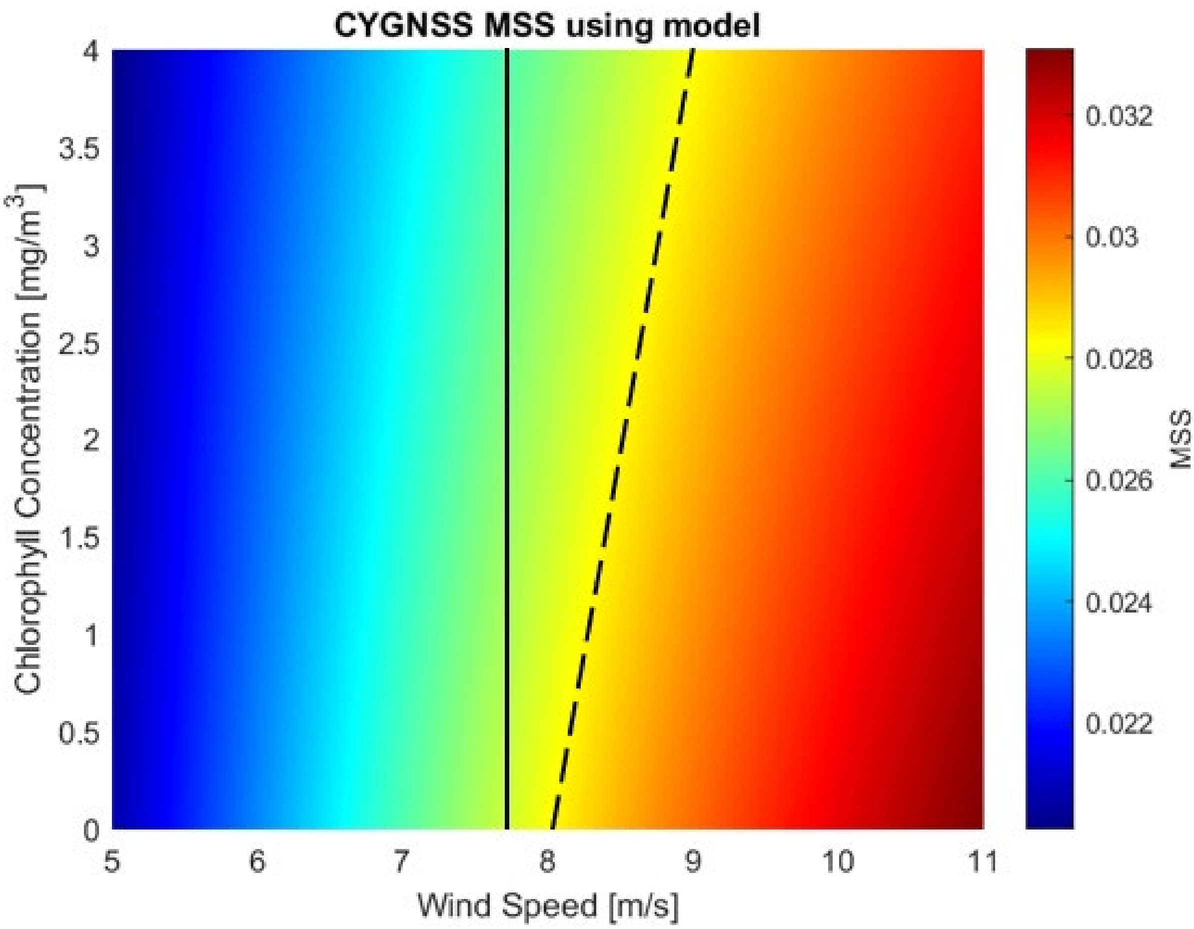

Figure 3.17: (top) The MWCC Model using CYGNSS, ERA5 and VIIRS. (bottom) The MWCC model with a vertical line and an MSS isoline.

3.5 Test Case: July 2020 Gulf of Mexico Bloom

To test how well the MWCC satellite model represents a real-world algae distribution, a test case algal bloom is considered. Previous studies provide an optimal test case with an algal bloom that formed in the Gulf of Mexico during the Summer of 2020. The chlorophyll-a concentration observed by the VIIRS hyperspectral imager on one day during this period is shown in Figure 3.18.

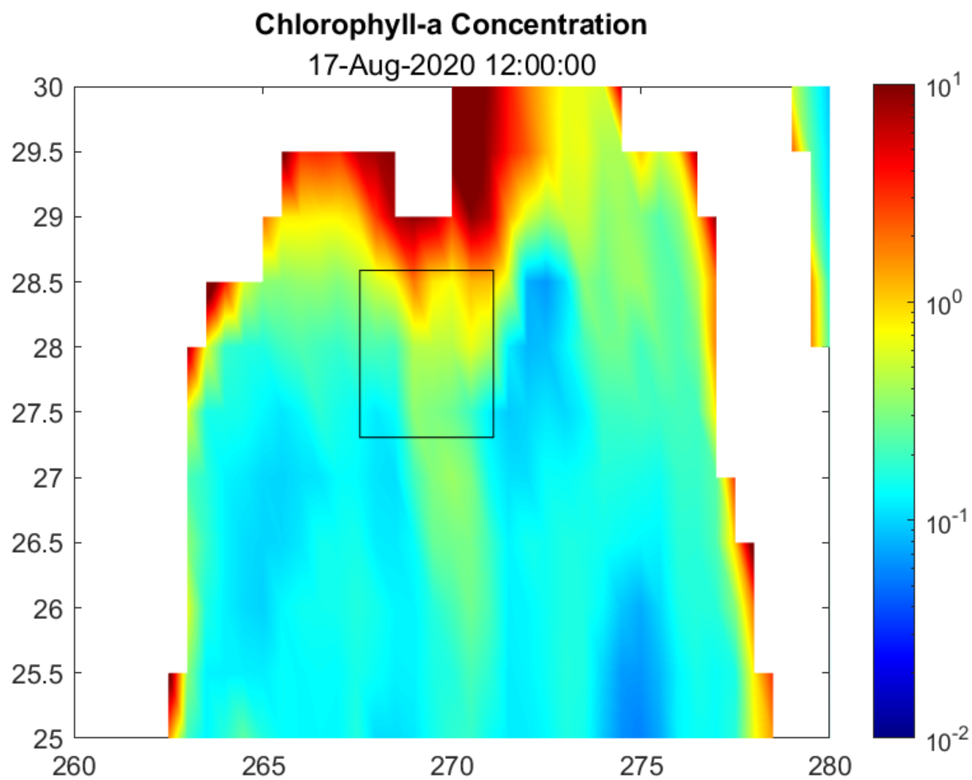

Figure 3.18: Chlorophyll-a concentration (CC) imaged by VIIRS on 17 Aug 2020 in the Gulf of Mexico. The CYGNSS observed MSS and the MSS predicted from the VIIRS CC by the MWCC model will be compared in the boxed region [27-28.5˚ N, 89-92˚ W].

The time period considered spans the algal bloom evolution, including approximately one month prior to bloom onset, the bloom interval, and roughly two weeks following the bloom. The results are presented in two steps. First, CYGNSS MSS is examined for evidence of bloom-related surfactant effects using MSS Anomaly. MSS Anomaly is a measure of ocean surface roughness suppression that looks at changes in MSS from a modeled normal ocean surface. Second, CYGNSS MSS during the test period will be compared to MWCC-modeled MSS. MWCC modeled MSS takes chlorophyll concentration and wind speed as inputs and outputs a predicted MSS.

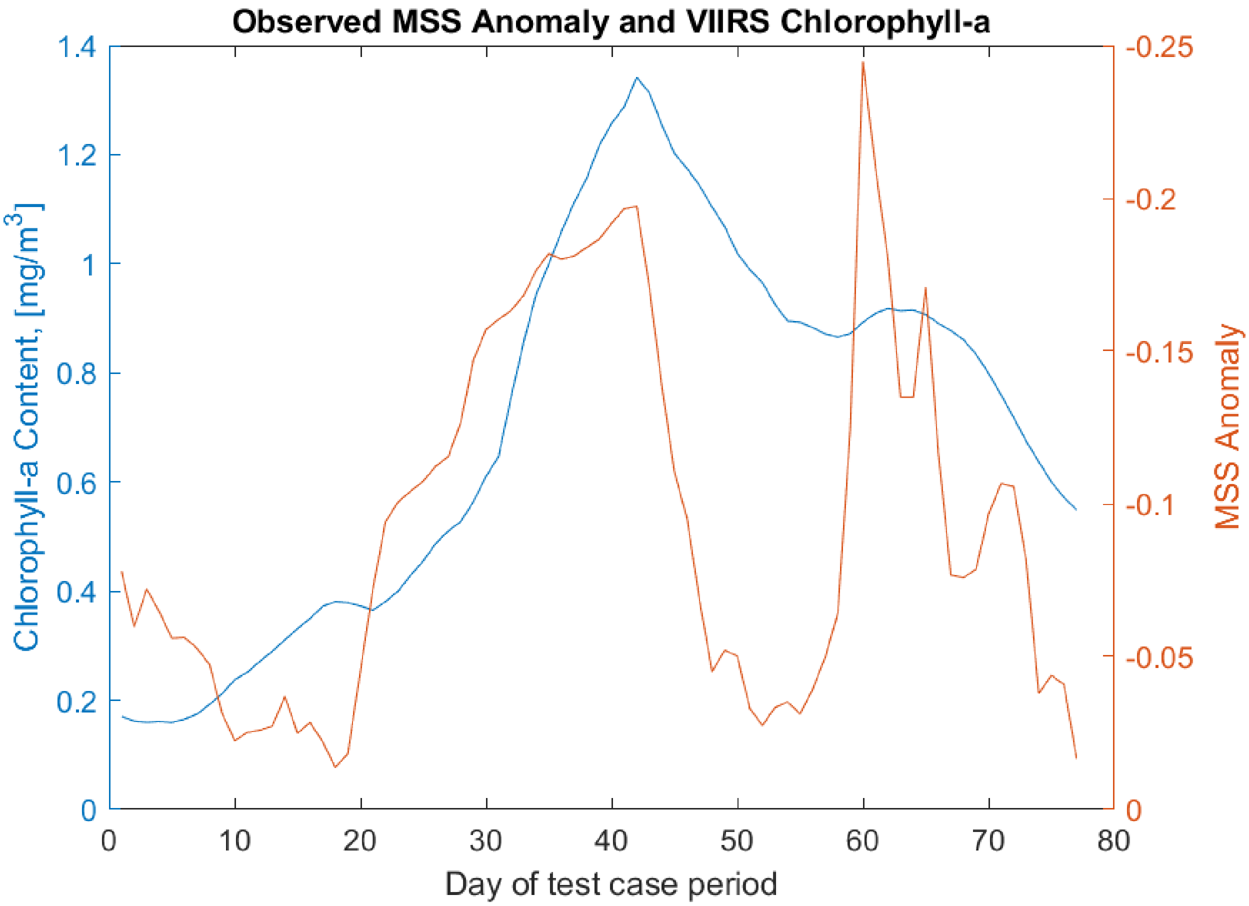

Figure 3.19: (blue) VIIRS chlorophyll-a measurements. Day 0 is 1-Jun-2024. The bloom occurred from 1-Jul-2024 to 31-Jul-2024 (Days 30-60), with a peak in the first week of July. (orange) CYGNSS MSS Anomaly measurements from the same period. Note that the MSS Anomaly axis is inverted to illustrate that higher chlorophyll concentrations are associated with larger roughness suppression (i.e. larger negative MSS Anomaly).

Figure 3.19 plots the average values of chlorophyll-a concentration and MSS Anomaly versus time, with the average performed over the rectangular study region highlighted in Figure 3.18, [27-28.5˚ N, 89-92˚ W]. The figure shows that when the chlorophyll peaks, the negative MSS Anomaly does as well. There is not a perfect 1:1 relationship, and this is to be expected. If there is a match between high chlorophyll content and high MSS Anomaly (specifically in that direction), it's a probable signal. It is possible that the spike in MSS Anomaly during the 60-70-day period may be related to the presence of anomalously large concentrations of seaweed.

We next compare the observed CYGNSS MSS during the bloom to the prediction by the MWCC model. Inputting collocated ERA5 and VIIRS data into the MWCC model produces a predicted MSS.

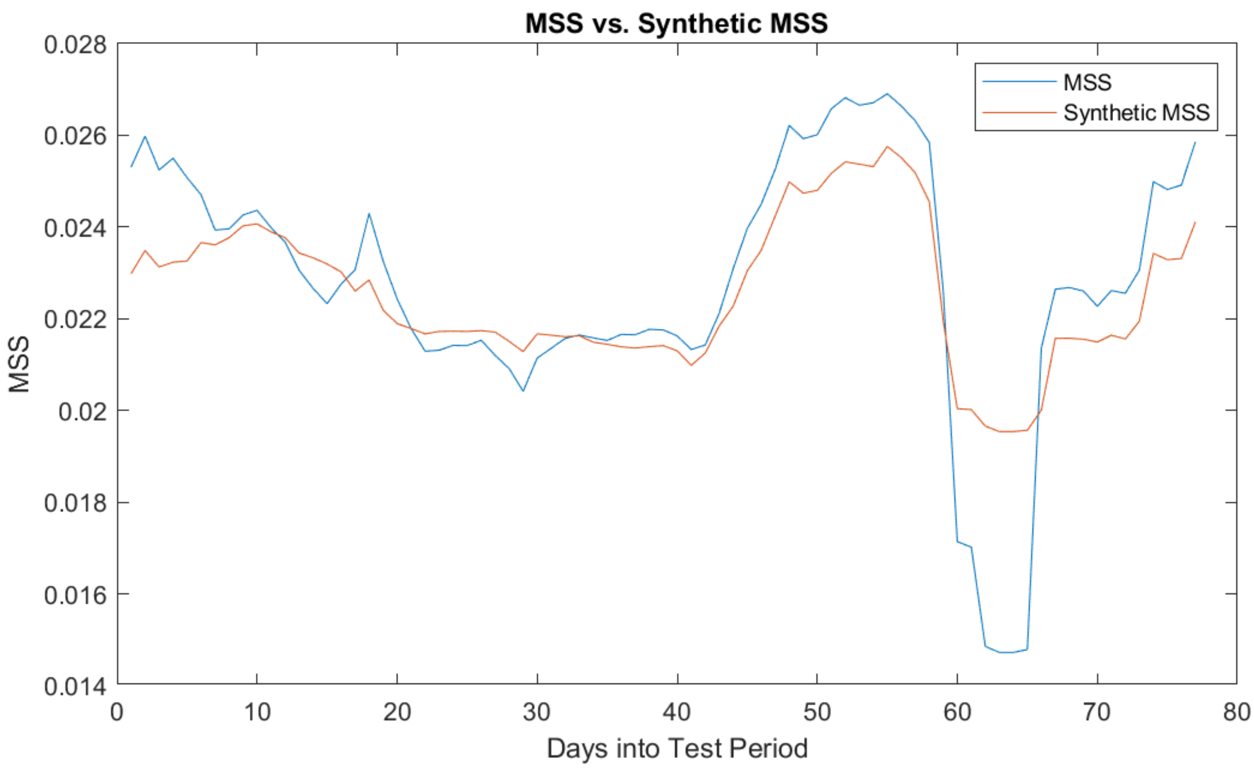

Figure 3.20: (blue) VIIRS chlorophyll-a measurements. Day 0 is 1-Jun-2024. The bloom occurred from 1-Jul-2024 to 31-Jul-2024 (Days 30-60), with a peak in the first week of July. (orange) CYGNSS MSS Anomaly measurements from the same period. Note that the MSS Anomaly axis is inverted to illustrate that higher chlorophyll concentrations are associated with larger roughness suppression (i.e. larger negative MSS Anomaly).

The MWCC modeled MSS is seen to agree well with the CYGNSS observed MSS. The modeled MSS does not seem to pick up the large change in MSS that occurs during days 60-70 of the test period. Given the spike in MSS Anomaly during this time, something may be affecting the ocean roughness that is not wind speed or algae.

3.6 Discussion & Conclusion

This study examines the algae-driven changes in ocean surface properties that can be detected by the spaceborne CYGNSS radars. A wave tank experiment was conducted to demonstrate that the presence of algae produces a measurable suppression of wind-driven roughness on the water surface, supporting the feasibility of identifying algal bloom impacts using CYGNSS-style measurements.

A key outcome of the wave tank work was the development of an empirical model that represents the impact of algae on surface roughness suppression. Having an explicit functional relationship is important because it moves the analysis beyond qualitative descriptions and toward a parameterized predictor of how algae modifies roughness. This functional form provides a practical mechanism for separating and accounting for algae effects within roughness-related observables.

To evaluate how these controlled findings translate to satellite observations, the wave tank derived functional form was applied to CYGNSS observations of MSS in the open ocean. This enabled construction of an empirically derived forward model linking MSS to wind speed and chlorophyll concentration. The resulting MSS-wind speed-chlorophyll concentration model indicates that incorporating chlorophyll information can improve representation of MSS variability when algal blooms are present relative to approaches that treat MSS as primarily wind-driven.

Overall, the forward model offers a pathway to accurately assess the impact of algal blooms on ocean roughness suppression in CYGNSS MSS data. Practically, this suggests CYGNSS-based analyses and products that rely on roughness, especially those interpreting MSS primarily through wind forcing, may benefit from including bloom-related modifiers to reduce bias and better characterize surface conditions during bloom events.

3.7 References for Chapter 3

1. Ruf, C. S. *et al.* New Ocean Winds Satellite Mission to Probe Hurricanes and Tropical Convection. *Bulletin of the American Meteorological Society* **97**, 385–395 (2016).
2. Hersbach, H. Sea Surface Roughness and Drag Coefficient as Functions of Neutral Wind Speed. *Journal of Physical Oceanography* **41**, 247–251 (2011).
3. Ulaby, F. T. and Long, D. G, “Radar Scattering” in *Microwave Radar and Radiometric Remote Sensing,* 1st ed. Ann Arbor, MI, U.S.A: UofM Press, 2014, ch. 5, sec. 5, pp. 170
4. Ruf, C.S. *et al.* “Level 2 Wind Speed Retrieval Algorithm” in *CYGNSS Handbook,* 2nd ed. Ann Arbor, MI, U.S.A: UofM Press, 2022, ch. 7 sec. 4, pp. 89

5. Zavorotny, V. & Voronovich, A. Scattering of GPS signals from the ocean with wind remote sensing applications. IEEE Transactions on Geoscience and Remote Sensing 38 (2), 951–964. (2000).
6. Hersbach, H. et al., "ERA5 hourly data on single levels from 1940 to present," Copernicus Climate Change Service (C3S) Climate Data Store (CDS), 2023. [Online] Available: doi:10.24381/cds.adbb2d47. Accessed: Jun. 10, 2024.
7. Evans, M. C. & Ruf, C. S. Toward the Detection and Imaging of Ocean Microplastics With a Spaceborne Radar. *IEEE Transactions on Geoscience and Remote Sensing* **60**, 1–9 (2022).
8. Sun, Y., Bakker, T., Ruf, C. & Pan, Y. Effects of microplastics and surfactants on surface roughness of water waves. *Sci Rep* **13**, 1978 (2023).
9. Misiou, O. & Koutsoumanis, K. Climate change and its implications for food safety and spoilage. *Trends in Food Science & Technology* **126**, 142–152 (2022).
10. Lopez, C. B. Scientific assessment of freshwater harmful algal blooms. (2008).
11. Evans, M. C, Ruf, C. S. & Sundaram, G. B. CYGNSS Microplastic Product Version 3.2 Algorithm Theoretical Basis Document, (2024)
12. Adak, S. Time-Dependent Spectral Analysis of Nonstationary Time Series. *Journal of the American Statistical Association*, *93*(444), 1488–1501. (1998)
13. Wang, T. *et al.* Improvement of CYGNSS Level 1 Calibration Using Modeling and Measurements of Ocean Surface Mean Square Slope. in *IGARSS 2020 - 2020 IEEE International Geoscience and Remote Sensing Symposium* 5909–5912 (2020). doi:10.1109/IGARSS39084.2020.9323262.
14. Hughes, S. A. *[Physical Models And Laboratory Techniques In Coastal Engineering*. (World Scientific Publishing Co Pte Ltd).
15. Elfouhaily, T. A. *et* al. A unified directional spectrum for long and short wind-driven waves. https://agupubs.onlinelibrary.wiley.com/doi/epdf/10.1029/97JC00467 doi:10.1029/97JC00467.
16. Okoro, V., Azimov, U., Munoz, J., Hernandez, H. H. & Phan, A. N. Microalgae cultivation and harvesting: Growth performance and use of flocculants - A review. *Renewable and Sustainable Energy Reviews* **115**, 109364 (2019).
17. Gkioni, M. D. *et al.* Ultrasound-Assisted Extraction of Nannochloropsis oculata with Ethanol and Betaine: 1,2-Propanediol Eutectic Solvent for Antioxidant Pigment-Rich Extracts Retaining Nutritious the Residual Biomass. *Antioxidants (Basel)* **11**, 1103 (2022).
18. Schneider, N. & Gerber, M. Correlation between viscosity, temperature and total solid content of algal biomass. *Bioresource Technology* **170**, 293–302 (2014).

Chapter 4 Utilizing the NASA SWOT Mission to Detect and Track Coastal Ocean Pollutants

4.1 Introduction

4.1.1 Introduction to Algal Blooms

Algae are accumulations of phytoplankton that proliferate when sufficient sunlight coincides with elevated nutrient availability. These nutrients are most often supplied by runoff delivered through watersheds. When this accumulation occurs in an uncontrolled manner and reaches a high biomass over a broad area, it is commonly characterized as an algal bloom [1]. Such blooms occur across a wide range of marine environments including rivers, lakes and the open ocean. Algal blooms frequently concentrate along coastlines adjacent to major river outflows, where nutrient inputs and physical transport processes can promote sustained growth and aggregation [2].

Algal blooms can degrade marine ecosystem health [3]. Dense blooms may contribute to oxygen depletion in the water column, killing fish and other organisms through hypoxic conditions [4]. In addition, bloom events can impair drinking water supplies and may produce toxins that pose risks to human health through exposure or consumption of contaminated water or seafood [4]. Therefore, reliable detection and monitoring of algal blooms are essential.

Traditional remote-sensing approaches often rely on optical or hyperspectral imaging, using the distinct spectral signatures associated with chlorophyll and related pigments. Many detection algorithms emphasize the green portion of the spectrum (around 532 nm), where reflectance and absorption features can help parse algal blooms from surrounding waters [5]. NOAA’s Visible Infrared Imaging Radiometer Suite (VIIRS) chlorophyll-a product is an example of a hyperspectral imager data product [6]. Fig. 4.1 is a set of example images from VIIRS over the Amazon River in 2024.

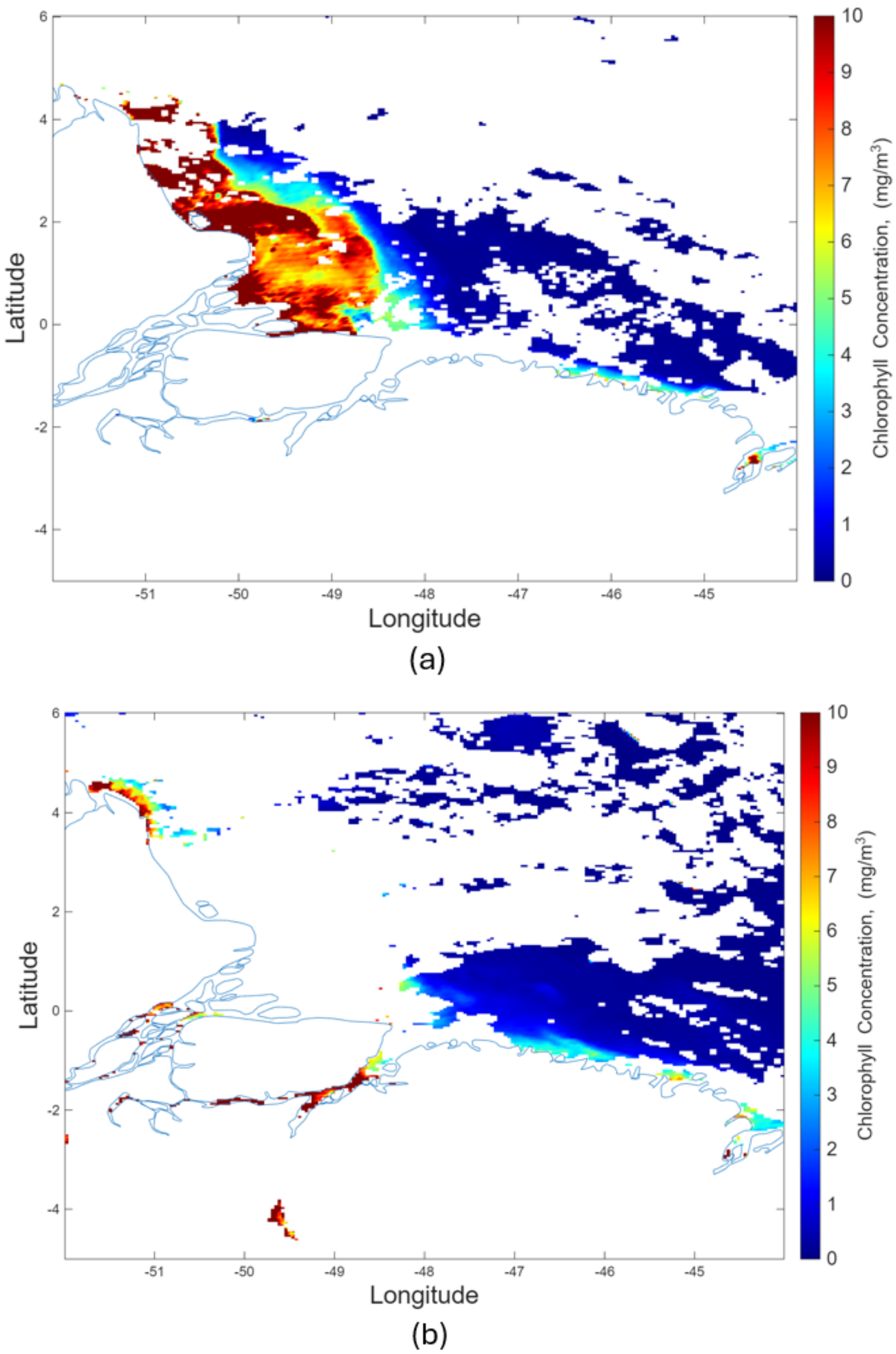

Figure 4.1: A set of images of the chlorophyll-a data product from the VIIRS instrument on NOAA-20, at a 4-kilometer resolution. The images are from (a) 24-Nov-2024 and (b) 11-Jun-2024.

Fig. 4.1 demonstrates both the strengths and weaknesses of the VIIRS product. As shown in Fig. 4.1a, the 2km resolution of the product can describe algal bloom structure in detail. However, Fig. 4.1b shows that cloud cover frequently obscures visible wavelengths from observing the ocean surface, preventing the acquisition of spatially and temporally continuous (gap-free) observations. To mitigate this limitation, we consider algal bloom detection in the microwave regime, where longer wavelengths can penetrate clouds and enable more consistent observing conditions, providing a pathway to more reliable bloom monitoring when optical data are unavailable.

4.1.2 Microwave Imagers

Microwave imagers are instruments that take measurements at frequencies between 0.3 GHz and 300 GHz. Below 300 MHz lie HF and VHF radio waves and above 300 GHz is the sub-mm and far infrared portion of the electromagnetic spectrum. An example of microwave imagers is the Cyclone Global Navigation Satellite System (CYGNSS). CYGNSS uses GNSS Reflectometry (GNSS-R), a passive bistatic radar technique [7]. Instead of transmitting its own pulses, CYGNSS receivers measure GPS signals after they reflect off the ocean surface. GPS operates at L-Band (19 cm wavelength). CYGNSS infers properties of the sea surface, most notably surface roughness, which is closely related to near-surface wind speed [8]. A principal equation describing measurements of the surface via received power is the Radar Range Equation, defined as

$$P_r = \frac{P_t G_r G_t \lambda^2 L A}{(4\pi)^3 R_t^2 R_r^2} \sigma_0 \tag{4.1}$$

where P_r and P_t represent the received and transmitted power, G_r is the CYGNSS receiver antenna gain, G_t is the GPS transmitting antenna gain, λ is the wavelength, R_t is the distance from the transmitter to the target, R_r is the distance from the target to the receiver, L is a generalized loss factor that accounts for atmospheric attenuation and system loss, A is the scattering area on the ocean surface and σ_0 is the normalized bistatic radar cross section [9]. σ_0 is a measure of how strongly a surface scatters the incoming electromagnetic wave back toward the receiver per unit area [9], which depends strongly on the roughness of the ocean surface. Surface roughness can be characterized by its Mean Square Slope (MSS), which is the expected value of the square of surface slope, averaged over the spectrum of ocean surface height at different horizontal scales [10].

In practice for CYGNSS, σ_0 is retrieved from the received reflected power after correcting for known geometry and system factors as described in equation (1). From measurements of σ_0, it is possible to determine ocean roughness and therefore near surface wind speeds [11].

The correlation between deviations in ocean roughness from nominal values, as measured by CYGNSS, and the concentration of microplastics on the ocean surface has been demonstrated [12]. From this correlation, the CYGNSS Ocean Microplastic Product was developed and released to the public [13].

CYGNSS provides coverage from 38 N to 38 S across the globe with an average revisit time of nine hours [14], which allows for consistent tracking of microplastic concentrations and large-scale ocean surface dynamics. In recent years, the CYGNSS Microplastic Product has changed its purview, as ocean pollutants that contain surfactants [15] can also be observed in the product. This includes, but is not limited to, algal blooms, seaweed, and oil spills. To denote this change, the Microplastic Product will be referred to here as the Marine Litter Product (MLP).

A fundamental challenge when working with the CYGNSS MLP is its spatial resolution. CYGNSS has an effective antenna footprint of 25x25km, and the MLP has an effective resolution of 1˚x 1˚. The MLP's resolution is due to the need to integrate data from multiple footprints for one grid cell. 1˚ grid cells are coarse when compared to the scale size of ocean pollutant variability, especially in coastal waters. Along with the coarse resolution, CYGNSS ocean surface measurements must avoid land to prevent interference from land surfaces in the observations. Therefore, all grid cells containing land are removed from the MLP. This is a notable limitation, as microplastics, algae and other ocean pollutants tend to accumulate on and near coastlines. Furthermore, ocean pollutant sources are generally river mouths, so losing access to coastlines detracts from our ability to observe these major sources of ocean pollutants. In a previous study done by Evans and Ruf, major ejections of pollutants from the Yangtze River could be observed

[12], but the low spatial resolution made the details of the pollutant dynamics unclear. This study underscores the need for higher resolution observing capabilities.

4.1.3 The NASA Surface Water & Ocean Topography (SWOT) Mission

To address the limitations in coastal marine litter detections while maintaining the insensitivity to cloud cover, a satellite microwave instrument with a finer spatial resolution than CYGNSS but roughly equivalent ocean roughness sensitivity is needed. We consider use of the NASA Surface Water & Ocean Topography (SWOT) Mission's radar to assess ocean roughness near coastlines [16]. SWOT carries a Ka-Band altimetric radar and its primary mission objective is water surface height topography. It makes ocean surface roughness measurements (specifically, σ_0) as a secondary correction for sea surface height. SWOT's Low-Rate Sea Surface Height Data Product has a resolution of 2km in both the cross-track and along-track directions [16]. This improved spatial resolution enables observations much closer to the coastline.

SWOT's temporal revisit time is a notable limitation. The SWOT orbit has a repeat cycle of 21 days [17], and SWOT's average image revisit time of 11 days will restrict the ability to monitor rapid changes in coastal ocean litter distributions.

SWOT and CYGNSS differ in other ways as well, including the range of incidence angles of observations, Ka-band vs. L-band operation (i.e. 8.6 mm vs. 19 cm wavelength), and an atmospheric correction for the attenuation of the Ka-band signal due to precipitation and other weather events. In this project, we assess the feasibility of a SWOT Marine Litter Product (SMLP) using a similar signal processing approach as was done for CYGNSS, with our main objective being the development of a more detailed and accurate capability for marine litter detection. This project will focus on using algal blooms as our main source of ocean roughness suppression.

4.2 Methodology

The CYGNSS MLP algorithm is based on the principle that microplastics and other ocean pollutants either secrete or have similar transport behavior as surfactants, which causes sufficient ocean surface roughness suppression to be measurable by the satellite. To parameterize ocean roughness suppression, the variable Mean Square Slope Anomaly (MSS Anomaly) is considered. This approach will be used to develop the SWOT MLP.

4.2.1 Deriving the Forward Model: A Mathematical Approach to MSS Anomaly

MSS Anomaly is a derived product that describes how different the ocean roughness is from a modeled "normal" version of ocean roughness forced by near surface ocean wind. Global maps of MSS Anomaly illustrate areas where ocean roughness suppression occurs, which is hypothesized to be directly caused by surfactant concentrations and indirectly correlated with microplastic and algal bloom concentrations.

The MSS Anomaly is defined by

$$MSS_{ANOM} = \frac{MSS_{obs} - MSS_{mod}}{MSS_{mod}} \tag{4.2}$$

where MSS_{obs} is the observed MSS from satellite data and MSS_{mod} is a theoretical MSS value calculated using an empirical MSS model forced by ECMWF Reanalysis (ERA5) wind speed data [18]. The model was constructed from MSS observations and wind data taken from a clean ocean region free from contaminants and anomalous conditions.

The MSS observations themselves are calculated using

$$MSS_{obs} = \frac{|R(\epsilon, \theta)|^2}{\sigma_0} \tag{4.3}$$

where $R(\varepsilon, \theta)$ is the Fresnel Reflection coefficient and σ_0 is the normalized radar cross section (NRCS) [19]. NRCS is measured by the SWOT radar and is notably sensitive to near surface wind speed.

The Fresnel Reflection Coefficient is a function of the relative dielectric permittivity of seawater (ε) and the incidence angle of the satellite observation (θ), as given by [20]

$$R(\epsilon,\theta) = \frac{1}{2}\ [\frac{\epsilon(f,T,S)\cos(\theta) - \sqrt{\epsilon - \sin^2(\theta)}}{\epsilon\cos(\theta) + \sqrt{\epsilon - \sin^2(\theta)}} - \frac{\cos(\theta) - \sqrt{\epsilon - \sin^2(\theta)}}{\cos(\theta) + \sqrt{\epsilon - \sin^2(\theta)}}] \qquad (4.4)$$

The permittivity is also a function of sensor transmitter frequency, sea surface temperature (SST) and sea surface salinity (SSS) conditions of the ocean. For our calculations, we use the double-Debye model as described in [21].

In summary, the MSS Anomaly relies on MSS observations, as shown in equation (2). To obtain MSS observations, spatially and temporally paired measurements of Fresnel Reflection Coefficient are needed. Calculation of the Fresnel Reflection Coefficient requires knowledge of ε, which in turn requires knowledge of SST and SSS. Therefore, to develop a SWOT MSS and MSS Anomaly estimator, the process requires matching σ_0 data to collocated SST and SSS data.

4.2.2 Using the SWOT Product to Calculate MSS

An example of one SWOT orbital pass of NRCS data collocated with SST and SSS provided by ERA5 [22] and SMAP [23] is shown in Fig. 4.2.

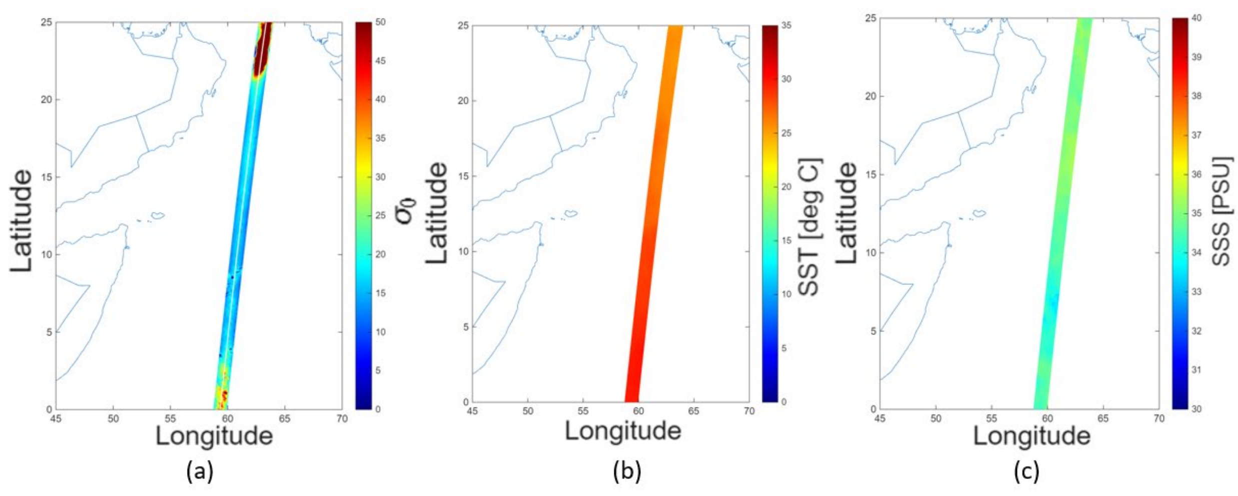

Figure 4.2: A set of images of the chlorophyll-a data product from the VIIRS instrument on NOAA-20, at a 4-kilometer resolution. The images are from (a) 24-Nov-2024 and (b) 11-Jun-2024.

Combining the SST and SSS inputs (see Fig. 4.2b and 4.2c) allows us to obtain the Fresnel Reflection Coefficient described in equation (4.4). Combining the Fresnel Reflection

Coefficient with the σ_0 paths in Fig. 4.2a results in the MSS described in equation (4.3). See Appendix B for an in-depth description of how the ERA5 and SMAP data are used to create the Fresnel Reflection Coefficient.

4.2.3 Developing SWOT MSS Anomaly

Using the Lookup Table Fresnel Reflection Coefficients described in Appendix B, the SWOT MSS estimator was implemented for the testing period of 01-Jan-2024 to 31-December-2024. Fig. 3 below is a density scatter plot of ERA5 Wind Speed matched up with SWOT MSS from 01-Jan-2024 to 31-Jan-2024.

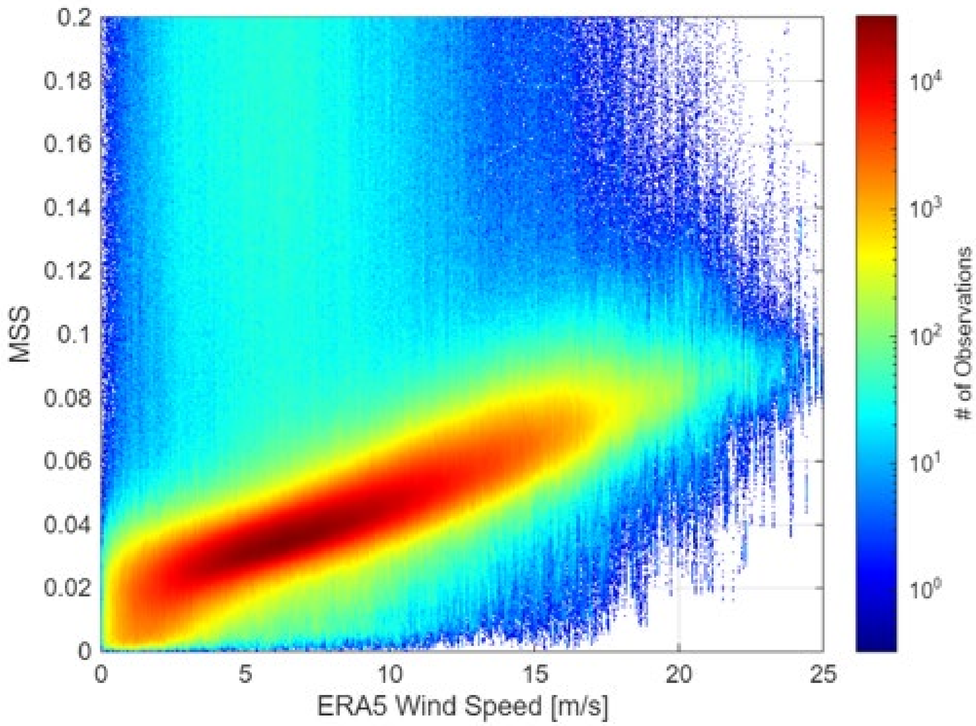

Figure 4.3: Density Scatter Plot of ERA5 Wind Speed and SWOT derived MSS. This plot uses global data from the period 01/01/24-01/31/24.

Fig. 3's results are a positive indication that the matchups are working, as with an increase in wind speed there is an increase in MSS.

4.2.4 Developing the MSS Model (MSS_{MOD}) for MSS Anomaly (MSS_{ANOM})

A control region is selected using microplastic models to find an area of open ocean that is clean of marine litter (microplastics, algae, sargassum). In this case the 3D model from Tseng et al. [24] was used to help find a viable control region. Fig. 4 is a global map of high-density PVC concentration. The control region [28˚-38˚ S, 200˚-260˚ E] used is boxed in red.

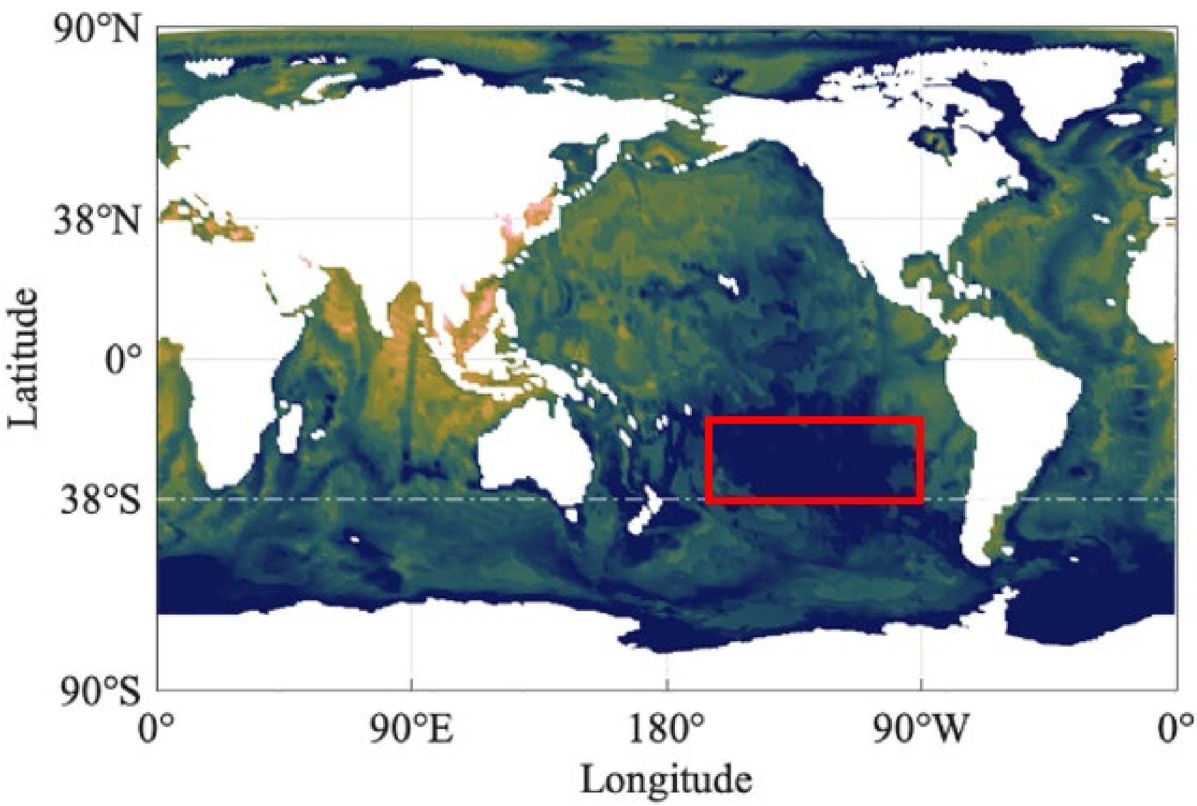

Figure 4.4: A global map of high-density PVC concentration [20], with the projected $MSS_{MOD,\ GLOBAL}$ control region [28-38 S, 200-260 E] highlighted in red.

Although the region is not perfectly free from plastic pollution, it is one of the cleaner areas when looking across the globe. This region is devoid of algae and seaweed though, as it is too far out in the middle of the Pacific Ocean to sustain growth for either. From here, our MSS_{MOD} can be built.

4.2.5 Cross-track Off Specular Point Geometry

One of the main reasons why equation (4.3) is simplified is because it assumes that the geometry of the transmitter and receiver are looking at the specular point [19]. For SWOT, the specular point is located at nadir. The drop-off from the specular point in terms of power is quite drastic, even over a couple of kilometers [19]. Therefore, the signal strength of σ_0 decreases with cross-track distance from nadir. Fig. 4.5 is a density scatter plot from the previously defined Control Region [200-260 E, 28-38S] of cross-track distance from nadir and σ_0.

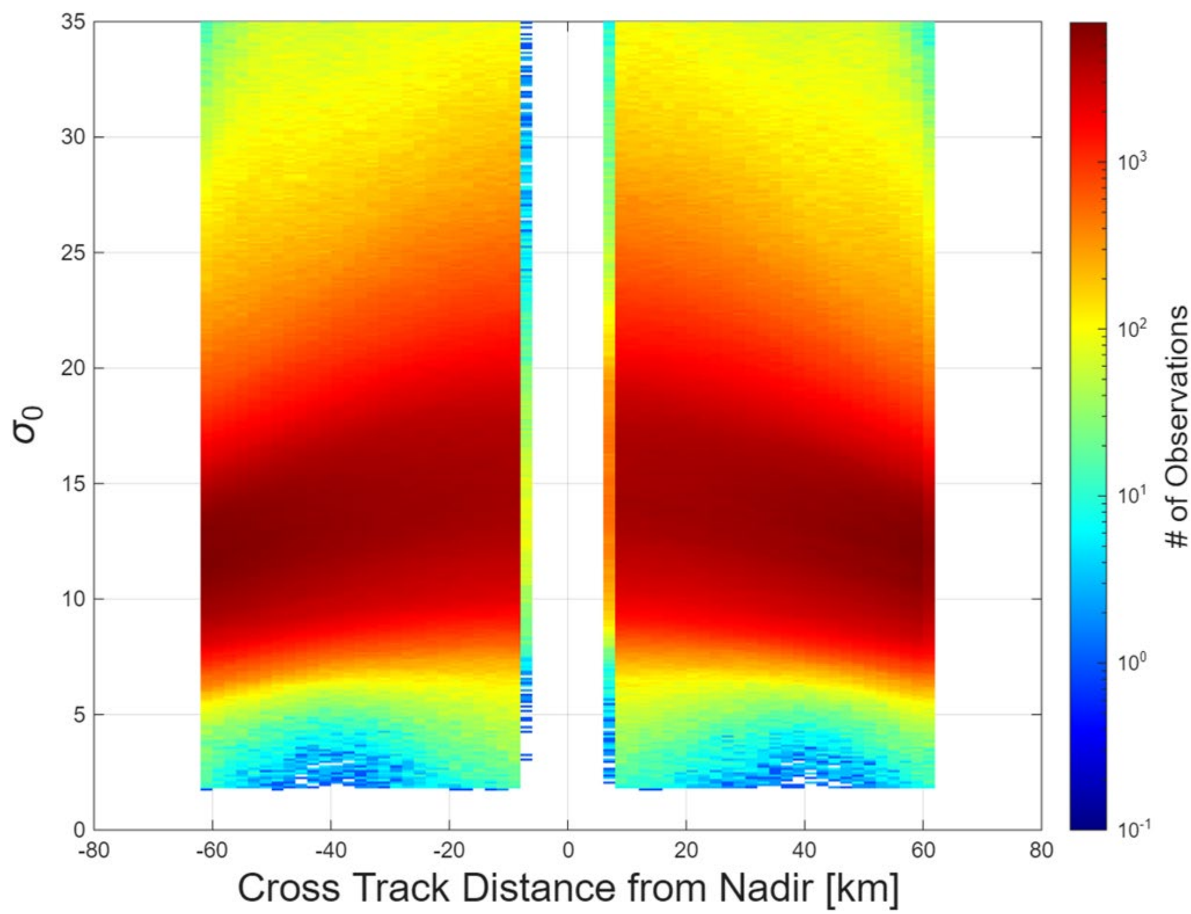

Figure 4.5: A density scatter plot of the cross-track distance from nadir vs. σ_0.

Because of the correlation between cross-track distance and σ_0 the method of creating MSS_{MOD} must be customized as a function of cross-track location. All data are binned every 2 kilometers of cross-track distance, and an individual model is created for each bin. Two examples of MSS vs. Wind Speed are given below; Fig. 4.6a is data from the bin closest to nadir, and Fig. 4.6b uses data from the bin furthest from nadir.

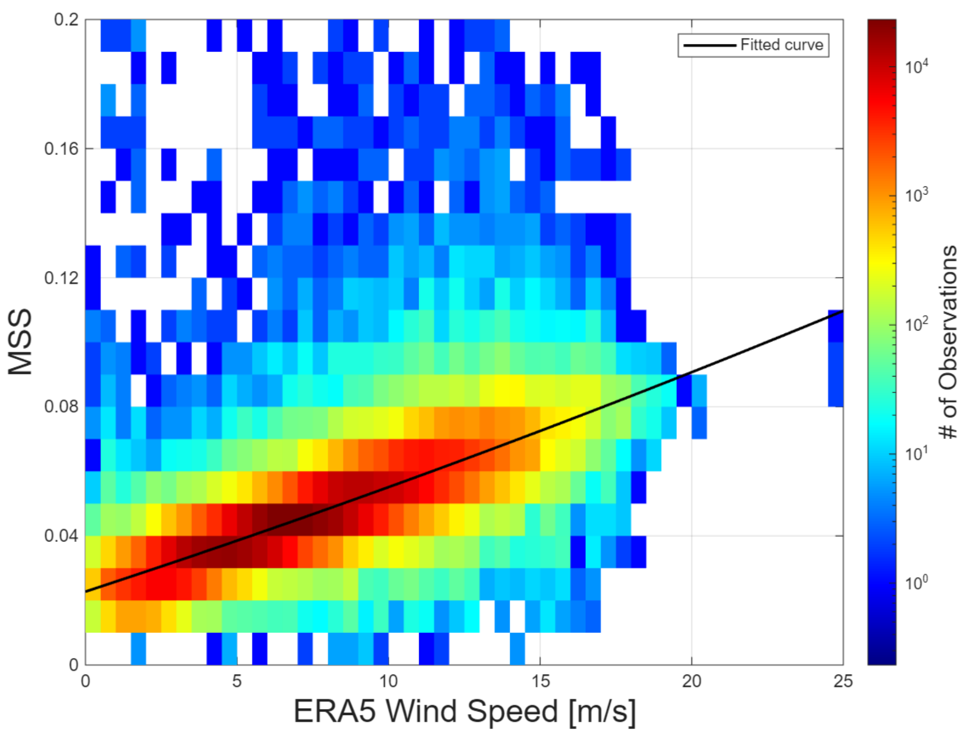

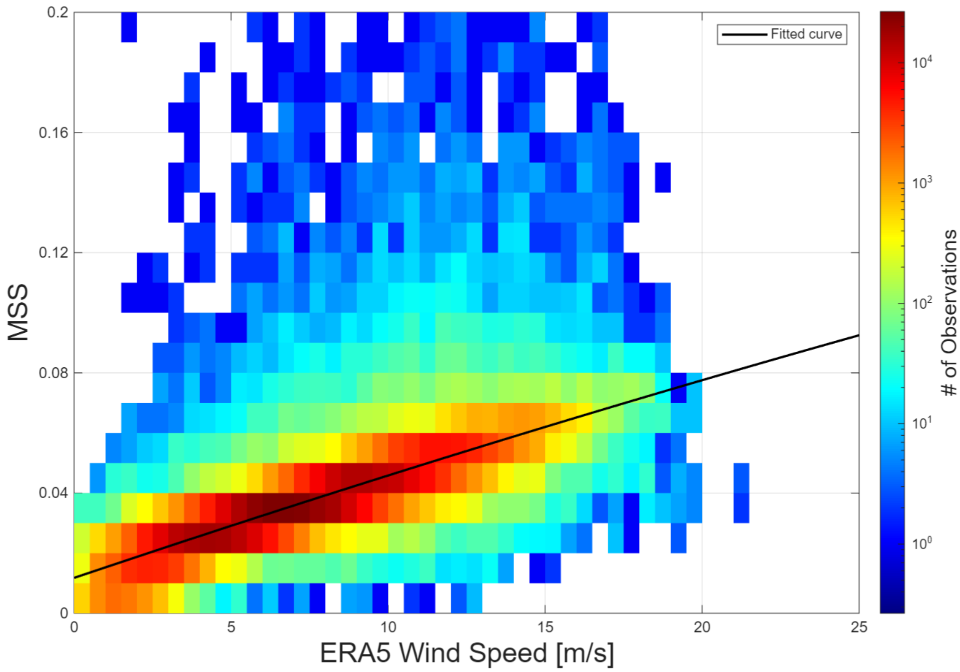

Figure 4.6: (top) Density scatter plot of MSS and wind speed data farthest from nadir of the SWOT swath. The data is overlaid with a best-fit curve to the data. (bottom) Density scatter plot of MSS and wind speed data in the cross-track bin closest to nadir. The data is overlaid with a best-fit curve to the data.

The best-fit curves shown in Fig. 4.6 represent the MSS model used to map wind speed to MSS. The equations for the model take the form of

$$MSS_{MOD}(CT) = a(CT)U^2 + b(CT)U + c(CT) \tag{4.5}$$

where MSS_{MOD} is the modeled MSS for a given wind speed, U is wind speed, and a(CT), b(CT) and c(CT) are constants that depend on the cross-track bin.

From this, equation (4.2) is modified so each observation of MSS is converted into MSS_{ANOM} using the appropriate MSS_{MOD}, described as

$$MSS_{ANOM} = \frac{MSS_{obs}(CT) - MSS_{MOD}(CT)}{MSS_{MOD}(CT)} \tag{4.6}$$

Modifying equation (4.2) to equation (4.6) allows MSS_{ANOM} to be cross-track independent, which is seen in Fig. 4.7. Fig. 4.7 is a density scatter plot of MSS_{ANOM} in the control region compared to cross track distance from nadir.

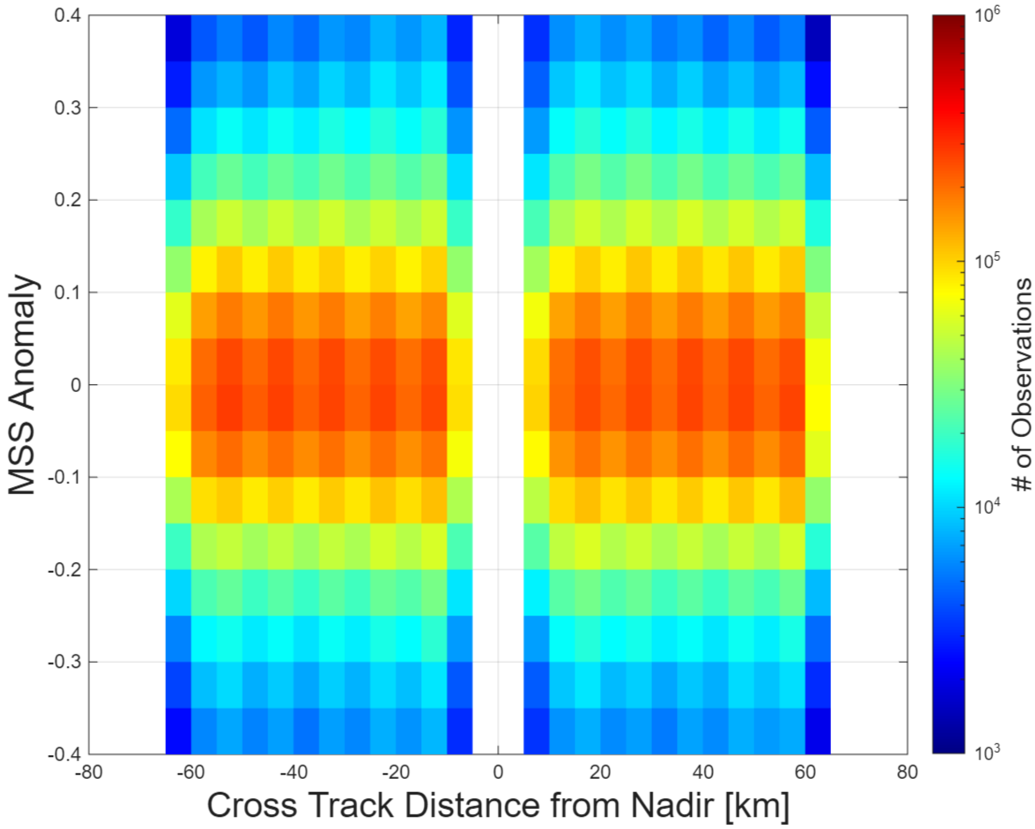

Figure 4.7: Cross-track distance from nadir plotted against MSS Anomaly.

As can be seen in Fig. 4.7, the distribution of MSS_{ANOM} is no longer cross track dependent. Therefore, MSS_{ANOM} measurements can now be used in conjunction with VIIRS gap-filled chlorophyll-a data to train a SWOT MSS_{ANOM}-Algae Model.

4.3 Amazon River Model Training Case

4.3.1 Choosing a region and initial filtering of the data

Using 2024 NOAA VIIRS 2-km gap-filled chlorophyll-a data [25], regions of high chlorophyll-a concentration can be identified throughout the year. Coastal areas generally have consistent background levels of chlorophyll-a, making them less likely to display dramatic short-term changes compared to offshore algal bloom events. However, there are some areas with larger dynamic ranges of chlorophyll-a near coastlines that are good candidates for SWOT MSS-algae model training. The first region of interest is at the mouth of the Amazon River. A snapshot of the Amazon River mouth with the region used for training highlighted by the box is shown in Fig 4.8.

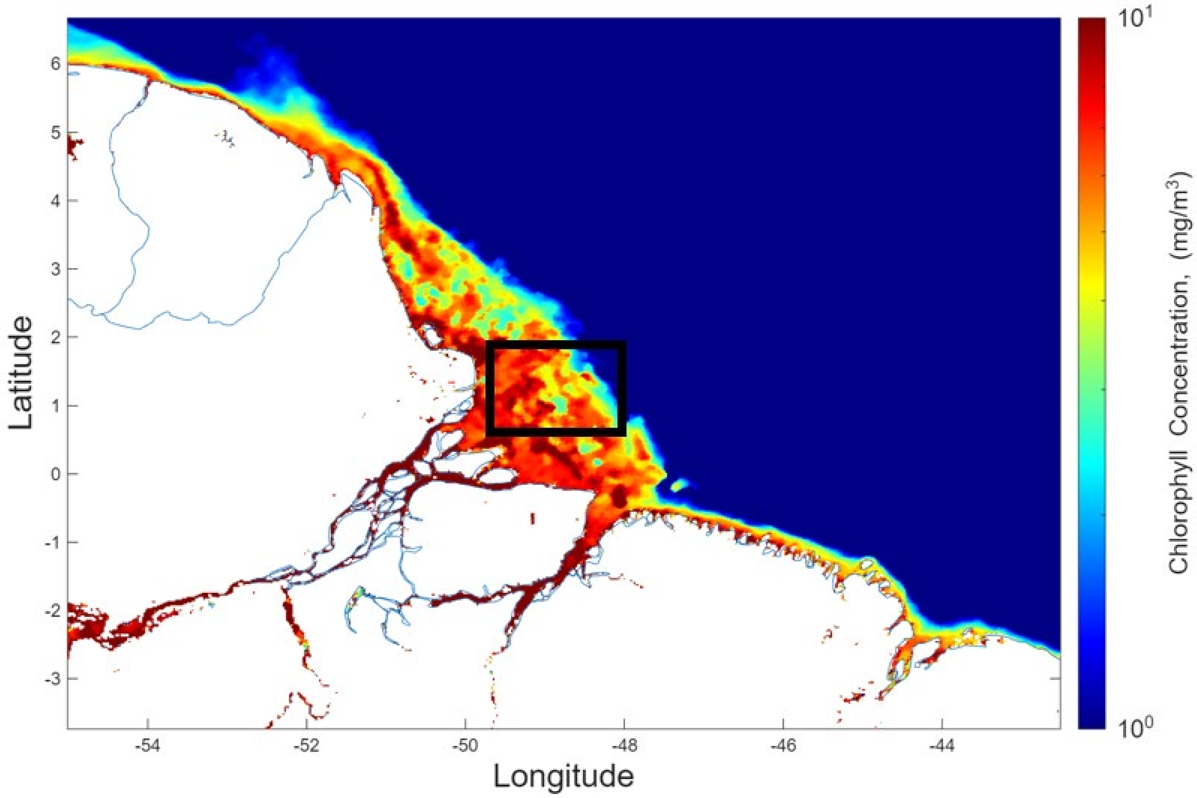

Figure 4.8: A VIIRS chlorophyll-a concentration at the mouth of the Amazon River on 6-Jan-2024. The box outlines the area that will be used to train the SWOT estimator of concentration.

The boxed region [0.6354˚N - 2.22˚N, 48.01-49.76 W] in Fig 8 represents the area in which chlorophyll-a and SWOT will be examined to see if there is a relationship between MSS_{ANOM} and chlorophyll-a data.

A total of 100 SWOT overpasses occurred in the testing region during CY 2024. An example of one of the SWOT overpasses matched-up with VIIRS chlorophyll-a data is illustrated in Fig. 4.9. Fig. 4.9 is a scatter plot between chlorophyll-a concentration on the x-axis and MSS_{ANOM} on the y-axis. Each data point represents one 2km SWOT pixel matched with its nearest 2km grid cell in the VIIRS data.

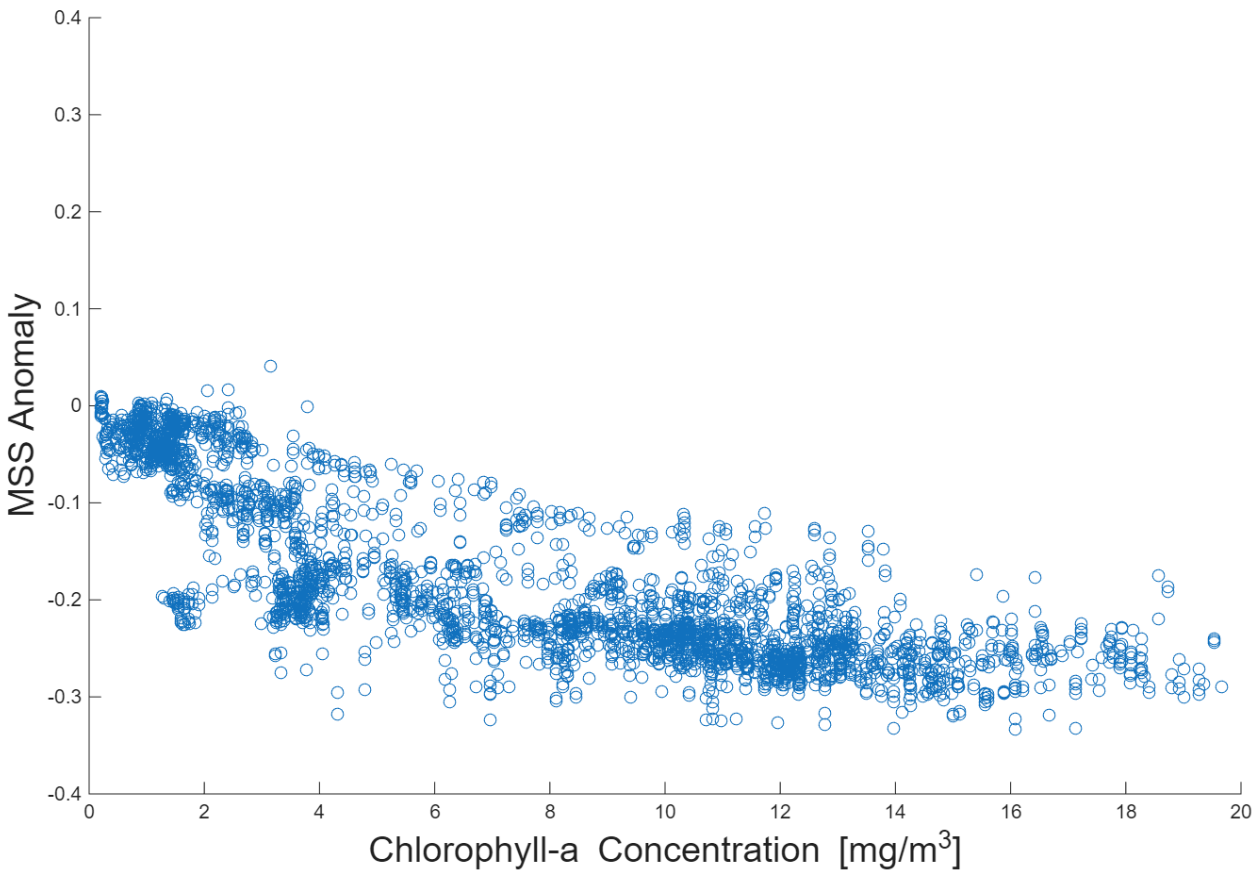

Figure 4.9: A scatterplot of SWOT MSS_{ANOM} and VIIRS chlorophyll-a concentrations. The SWOT data was taken from an overpass on 15-Oct-2024.

Fig. 4.9 is a good representation of some of the qualities needed to establish a model between MSS_{ANOM} and chlorophyll-a data.

The minimum requirements for inclusion in the training dataset are as follows

1) The overpass should capture a sufficiently wide range of chlorophyll-a values, which is quantified by a standard deviation equal to or greater than 2.5 mg/m^3.
2) The overpass must consist of at least 500 points of data.

These filtering criteria reduced the dataset from 100 overpasses to 35. 54 of the overpasses fail to meet the dynamic range threshold, and 56 of the overpasses fail the sample number threshold. Further evaluation of the remaining overpasses revealed that, while linear fits provided reasonable model performance, a quadratic regression gave superior results for most cases. The assumption of a quadratic relationship between concentration and MSS Anomaly is consistent with previous wave tank experiments we conducted in which controlled algae concentration were introduced and the resulting suppression of water surface roughening from wind was observed [26]. Specifically, the application of a quadratic fit improved the R^2 value for all but one overpass, suggesting a more appropriate modeling approach for the relationship between MSS_{ANOM} and chlorophyll-a. Examples of the SWOT overpasses with quadratic fits overlaid on them are shown in Fig. 4.10.

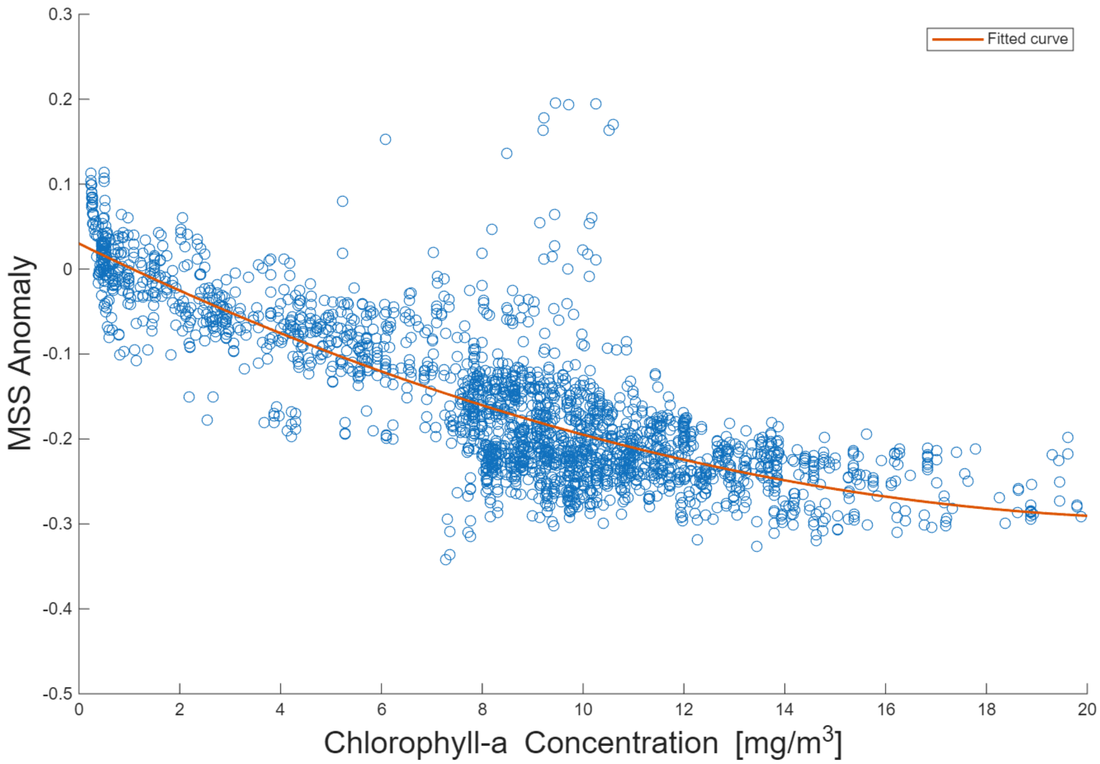

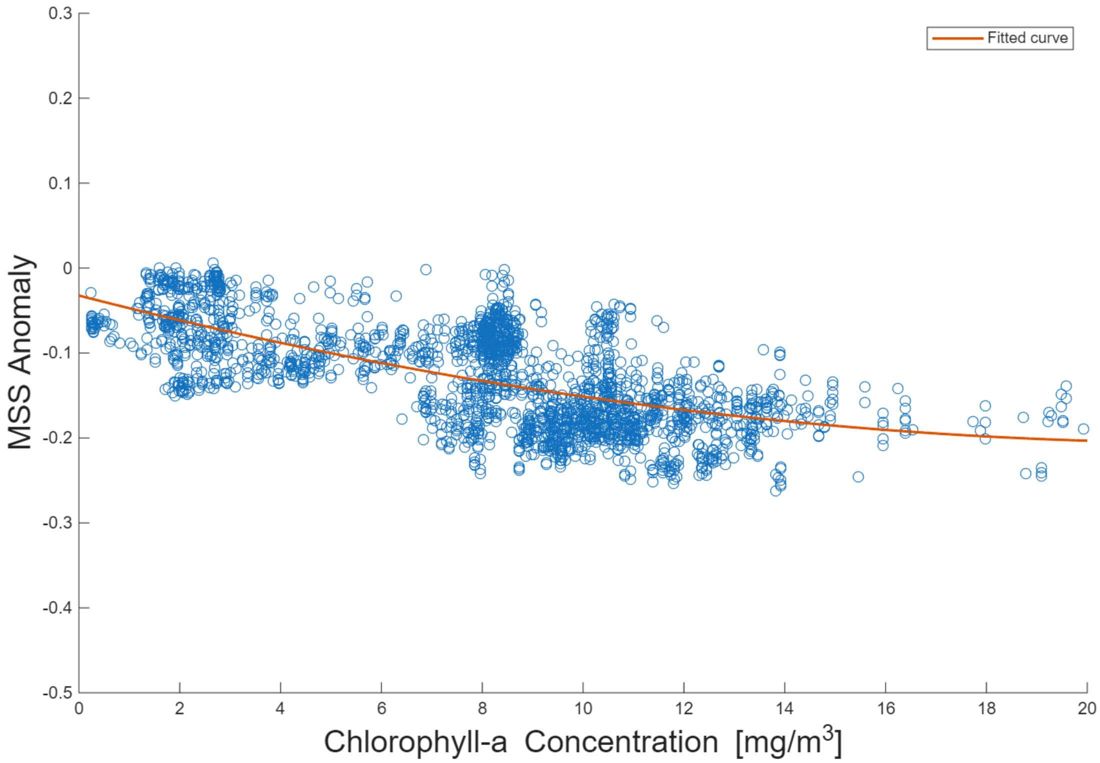

Figure 4.10: Examples of SWOT MSS_{ANOM} matched with VIIRS chlorophyll-a data that has been fit with a quadratic fit. (top) Matchups from 18-Jun-2024 with their individual overpass fit. (bottom) Matchups from 25-Sep-2024 with its individual overpass fit.

The quadratic fits in Fig. 4.10 assumes a relationship of the form

$$MSS_{ANOM} = aCC^2 + bCC + c \tag{4.7}$$

where CC is chlorophyll-a concentration and a, b and c are constants that are unique to each overpass.

4.3.2 Filtering the overpasses further to make the SWOT MSS_{ANOM}-Algae model

From the 35 SWOT overpasses with log fits between MSS_{ANOM} and chlorophyll-a, the RMSD was calculated for each overpass. Fig. 11 displays a histogram of RMSD values.

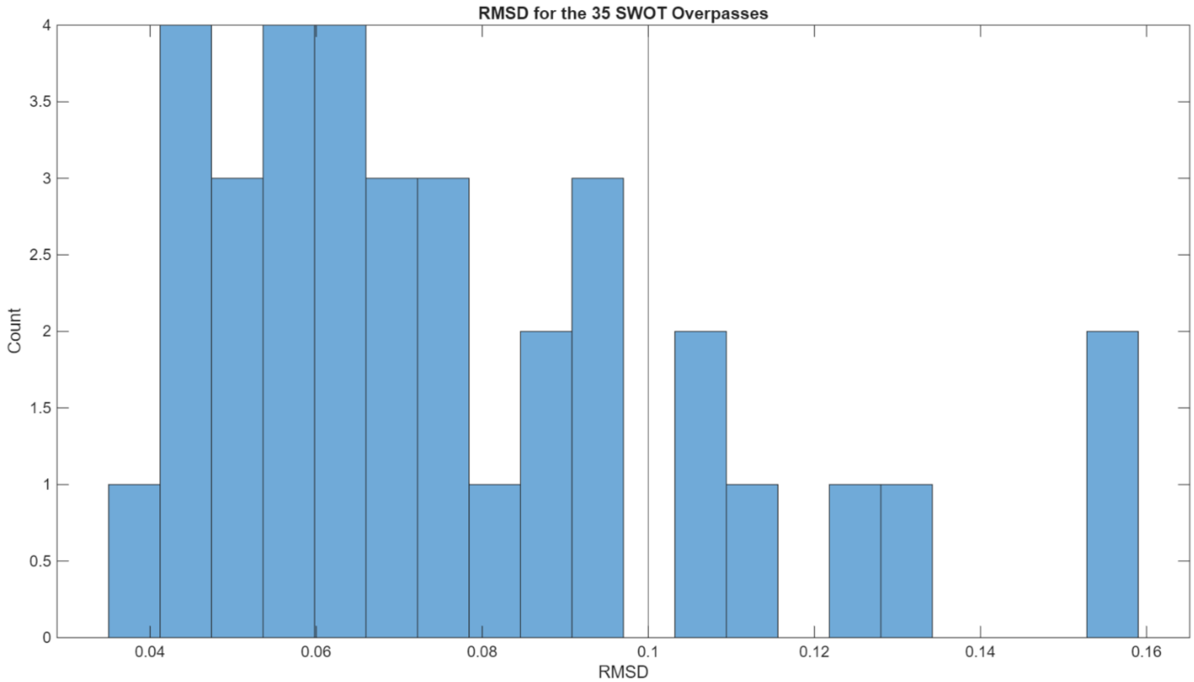

Figure 4.11: A histogram of the RMSD between the logarithmic best fit curves and the SWOT-VIIRS matched up data.

A filtering threshold of RMSD $\leq$ 0.1 was used to capture the mean and mode of the data, while excluding some of the poorer outlier cases.

With this filter, 28 overpasses are now included in the model training dataset. The complete set of 28 overpasses is combined to produce a single aggregate model. Fig. 12 is a scatterplot of all the MSS_{ANOM} and chlorophyll-a matchup data from the 28 overpasses, with a best fit quadratic fit overlaid on top.

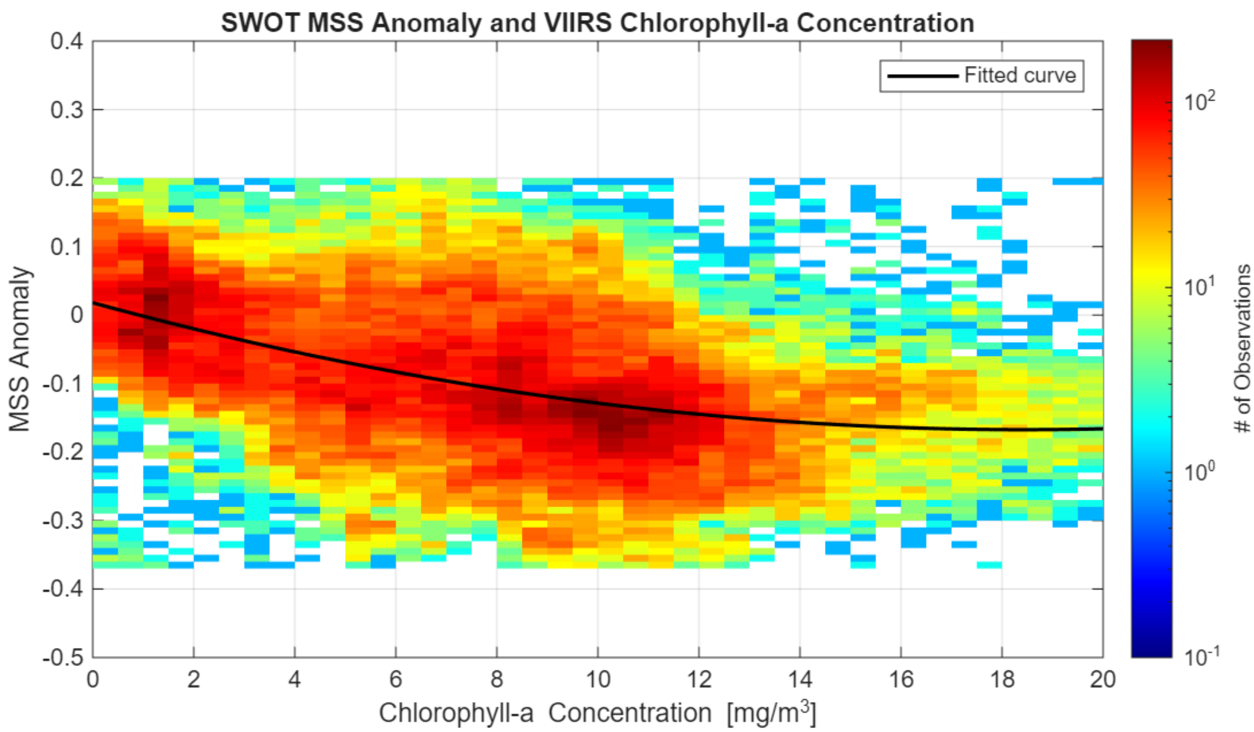

Figure 4.12: A scatterplot of all the SWOT and VIIRS data overlaid with a quadratic best fit line.

The equation for the quadratic fit in Fig. 4.12 is

$$MSS_{ANOM} = (5.4 * 10^{-4})CC^2 - 0.0201CC + 0.0179 \tag{4.8}$$

where MSS_{ANOM} is the MSS Anomaly predicted from CC, the chlorophyll-a concentration.

Fig. 4.12 has an RMSD of 0.0941. This is higher than the majority of the single overpass curves, but this can be parsed by looking at the roll-off terms and scale factor terms of each of the single overpass curves.

From the aggregate fit, we can compare the single overpass fits to the aggregate fit and check the RMSD between the fits. Fig. 4.13a is a histogram of the RMSD between the single overpass fits and the aggregate fits. Fig. 4.13b is a plot of all the single overpass fits overlaid on top of the aggregate fit.

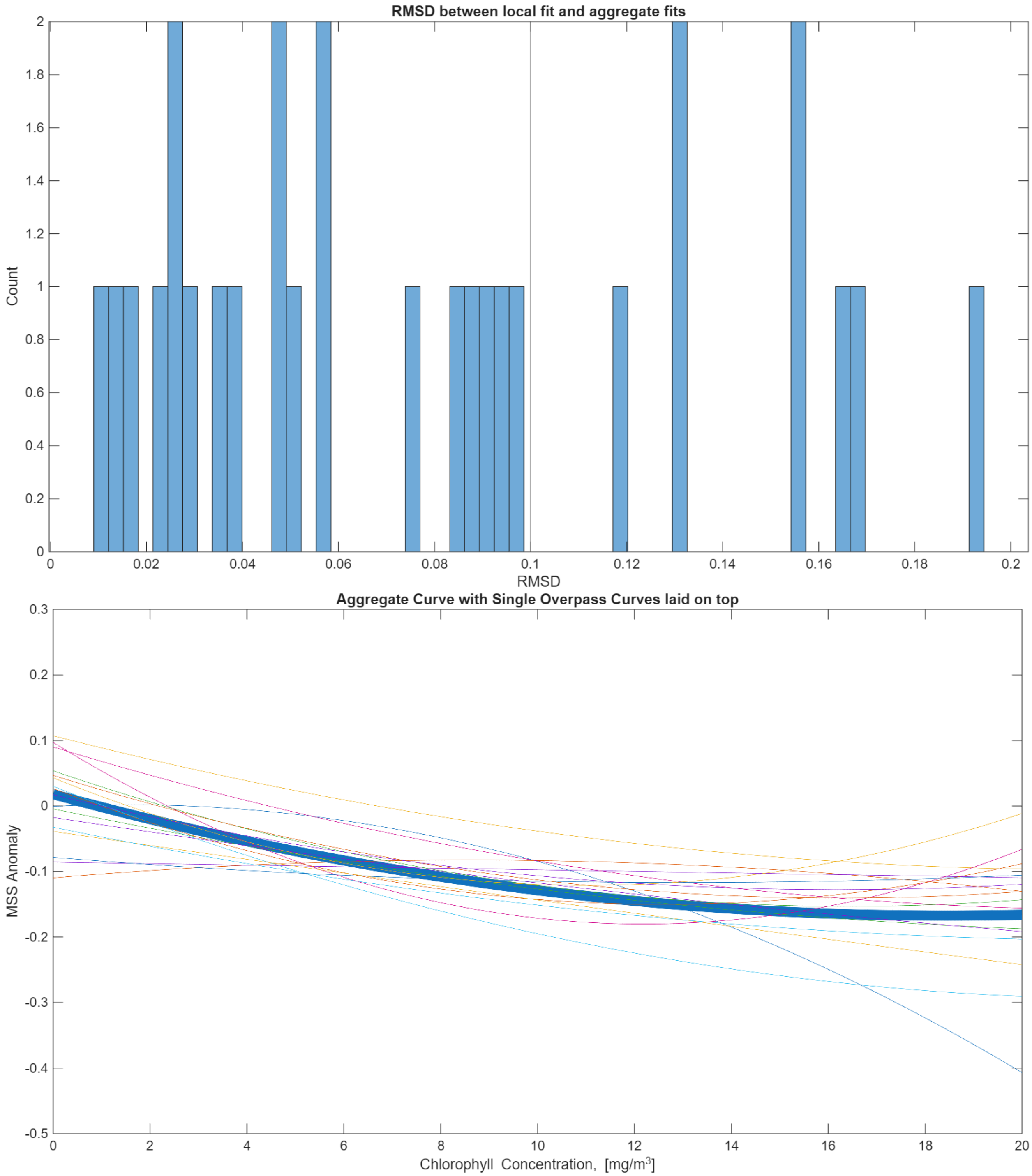

Figure 4.13: (a) A histogram of the RMSD between the single overpass fits and the aggregate fit. (b) The single overpass curves are overlaid on the aggregate curve.

Using the histogram in Fig. 4.13a, another RMSD threshold can be established, again at 0.1. This filters out 13 of the 28 curves, leaving us with 15 overpasses.

Fig. 4.14 shows the newly filtered curves overlaid on the aggregate curve, done in the same style as Fig. 4.13b.

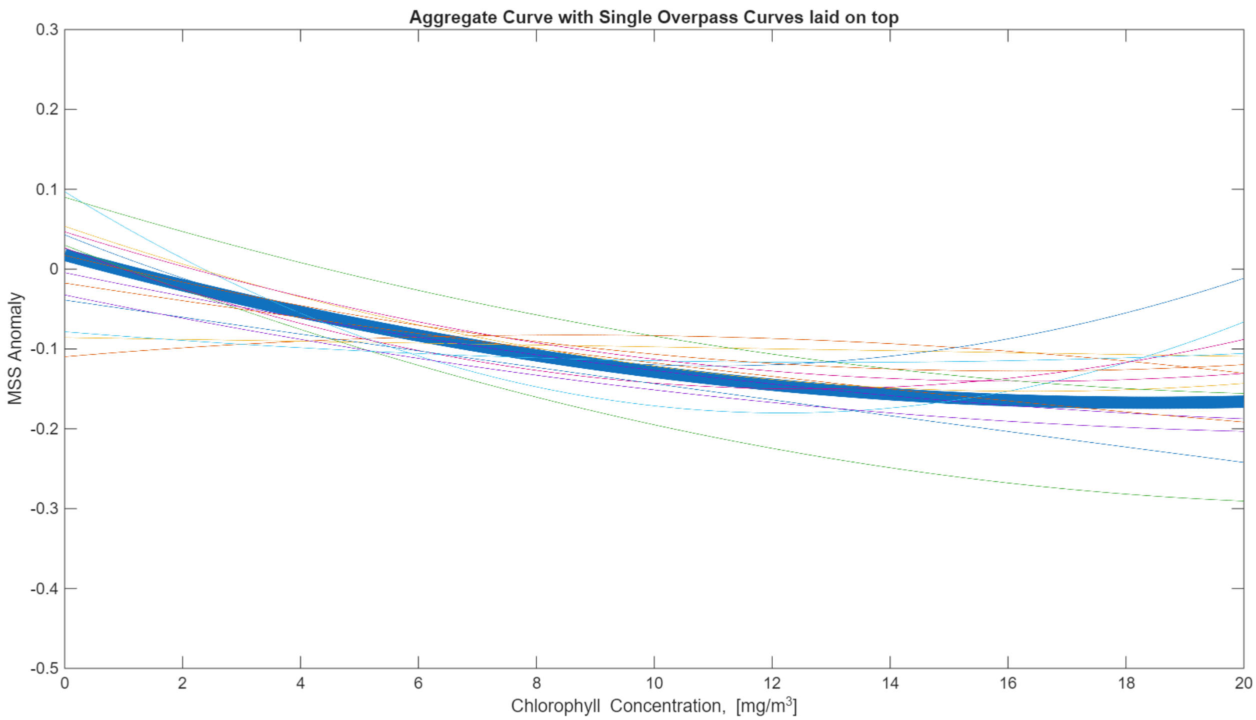

Figure 4.14: The 15 best single overpass curves overlaid on the aggregate curve.

From Fig. 4.14 the process leading to Fig. 4.12 can be repeated, as the new aggregate is plotted with a best fit logarithmic curve, this time deciding what the SWOT MSS_{ANOM}-chlorophyll-a concentration model will look like. Fig. 4.15 is a plot in the same style as Fig. 4.12 but using the twice-filtered data.

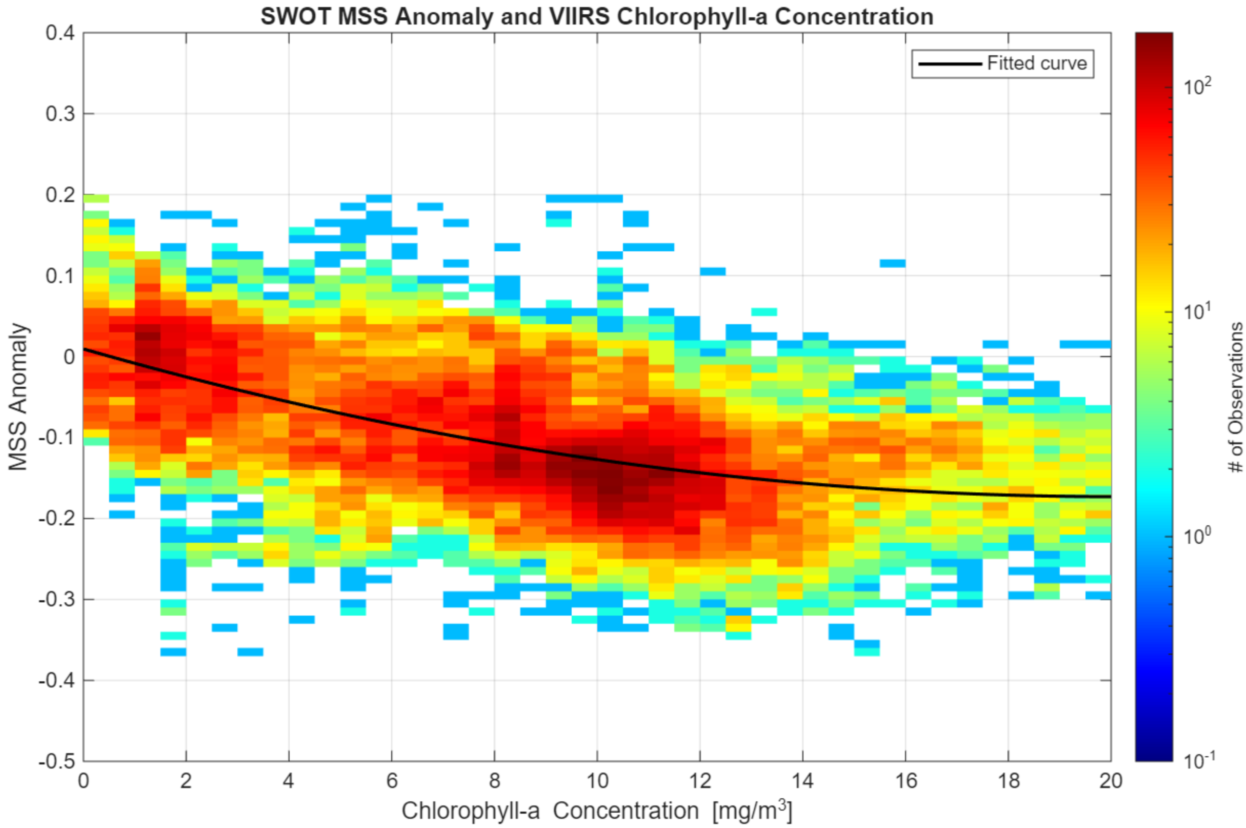

Figure 4.15: Chlorophyll-a concentration and SWOT MSS_{ANOM} from 15 overpasses using the twice-filtered data, overlaid with a best fit quadratic curve, representing the model between the two variables.

The equation for the SWOT MSS_{ANOM}-Algae Model is

$$MSS_{ANOM} = (4.5 * 10^{-4})CC^2 - 0.0181CC + 0.0093 \tag{4.9}$$

The RMSD of the aggregate fit drops from 0.0941 to 0.0660. Finally, it is important to compare the model to some of the data that was not used to train the model. Fig. 16 is a comparison of the MSS_{ANOM}-Algae model to the 20 overpasses that met the original criteria but were not used in the training set.

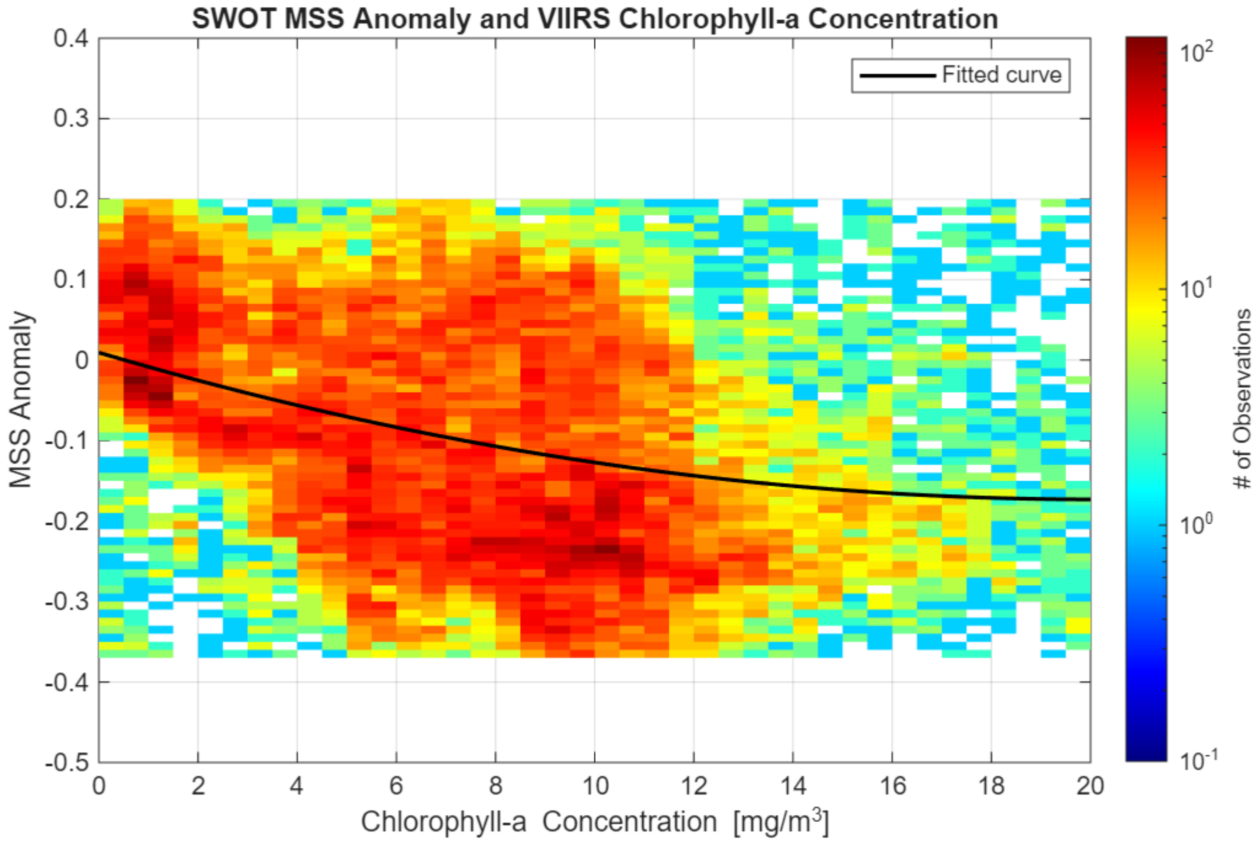

Figure 4.16: The MSS_{ANOM}-Algae Model against the Amazon River Overpasses not used for training.

The RMSD for the test data against the fit is 0.13. As Fig. 16 shows, much of the data is more spread out around the model. The model captures an area of high density in the low chlorophyll regime, but as the chlorophyll goes above 4 mg/m^3, the model has a harder time capturing the dynamics of the chlorophyll.

4.3.3 Histograms of the Chlorophyll-a Concentration

To investigate the relationship between the MSS Anomaly and varying chlorophyll concentrations in the ocean, chlorophyll data were divided into three distinct ranges: low, medium, and high concentrations. Fig. 17a is a histogram used to visualize the distribution of chlorophyll values across these categories. Fig. 17b is a line plot that shows the mean values of both chlorophyll and MSS Anomaly calculated within each concentration range.

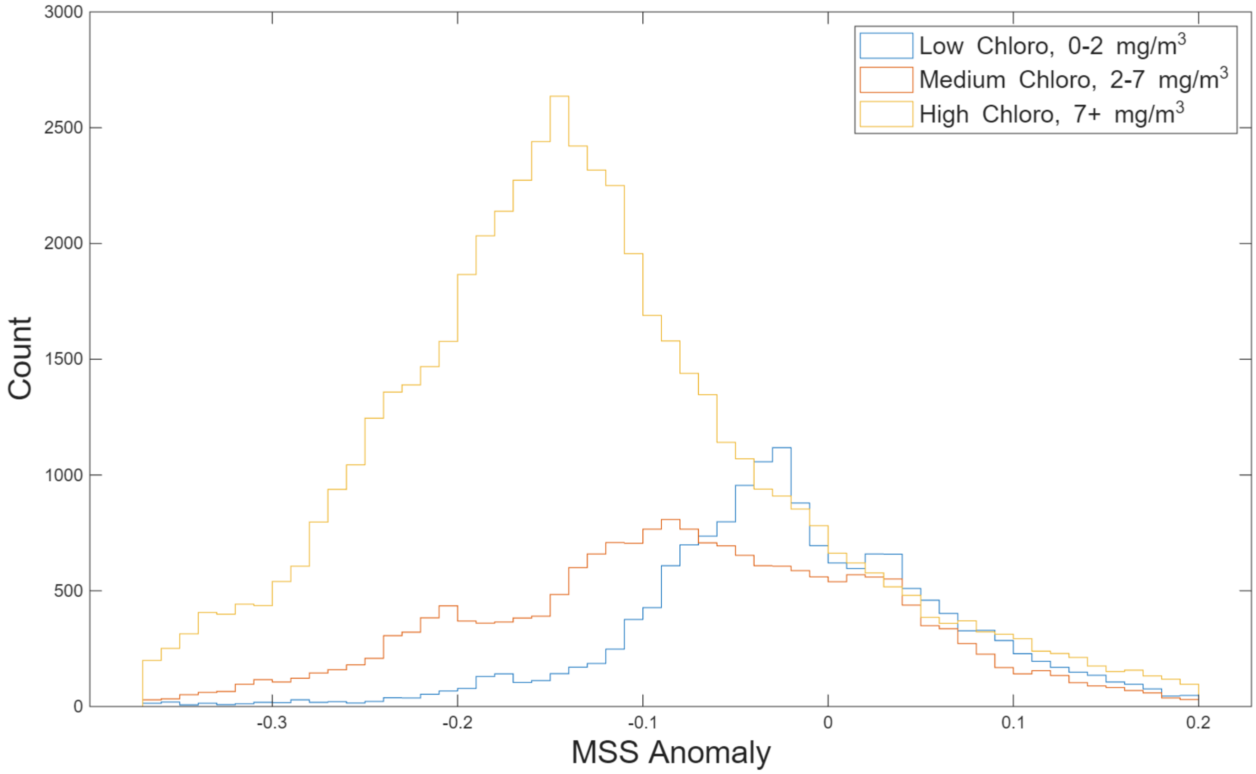

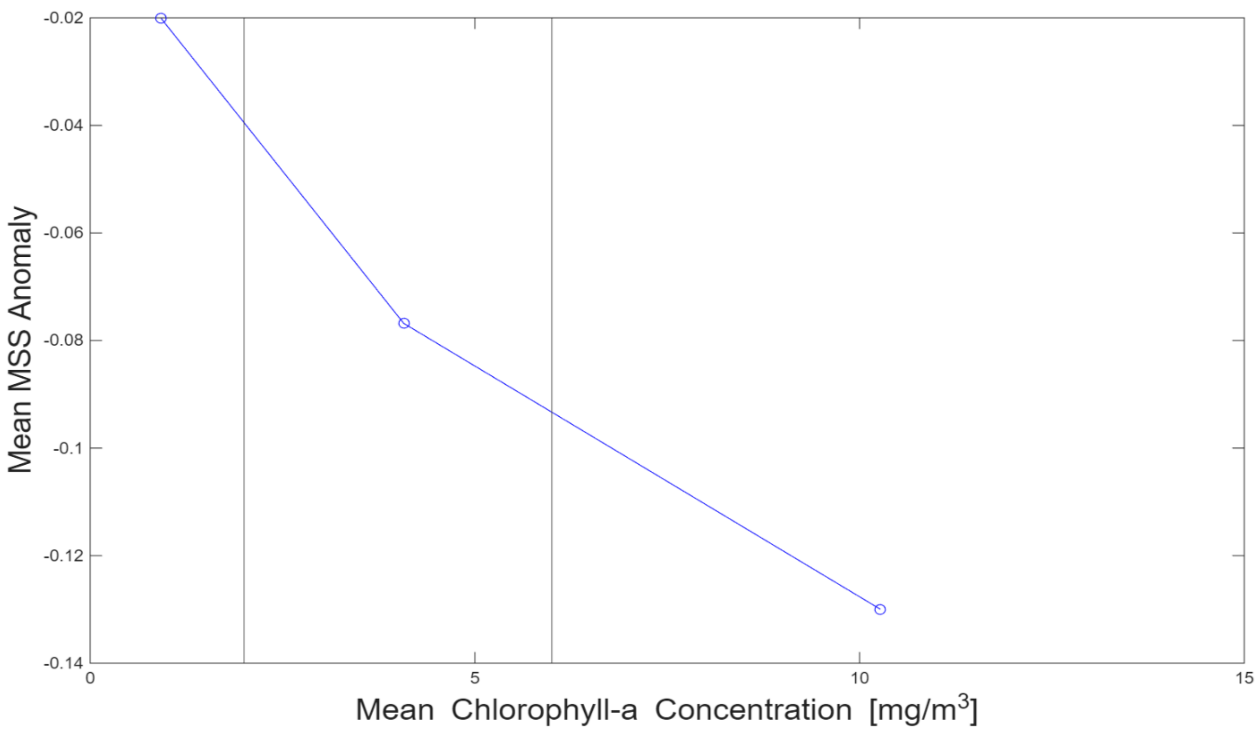

Figure 4.17: (a) Histograms of MSS Anomaly at low (blue), medium (orange) and high (yellow) levels of chlorophyll-a concentration. (b) Mean value of MSS Anomaly for range of concentration.

As demonstrated in Fig. 4.17, an increase in chlorophyll-a concentration pairs with a decrease in the mean MSS Anomaly, which falls from 0.04 to -0.12 across the data range. Notably, the trend persists when chlorophyll-a is binned into smaller, overlapping ranges (e.g., 0–2, 1–3 mg/m^3), confirming the robustness of the relationship between chlorophyll-a concentration and MSS Anomaly across approaches. This case is displayed in Fig. 4.18.

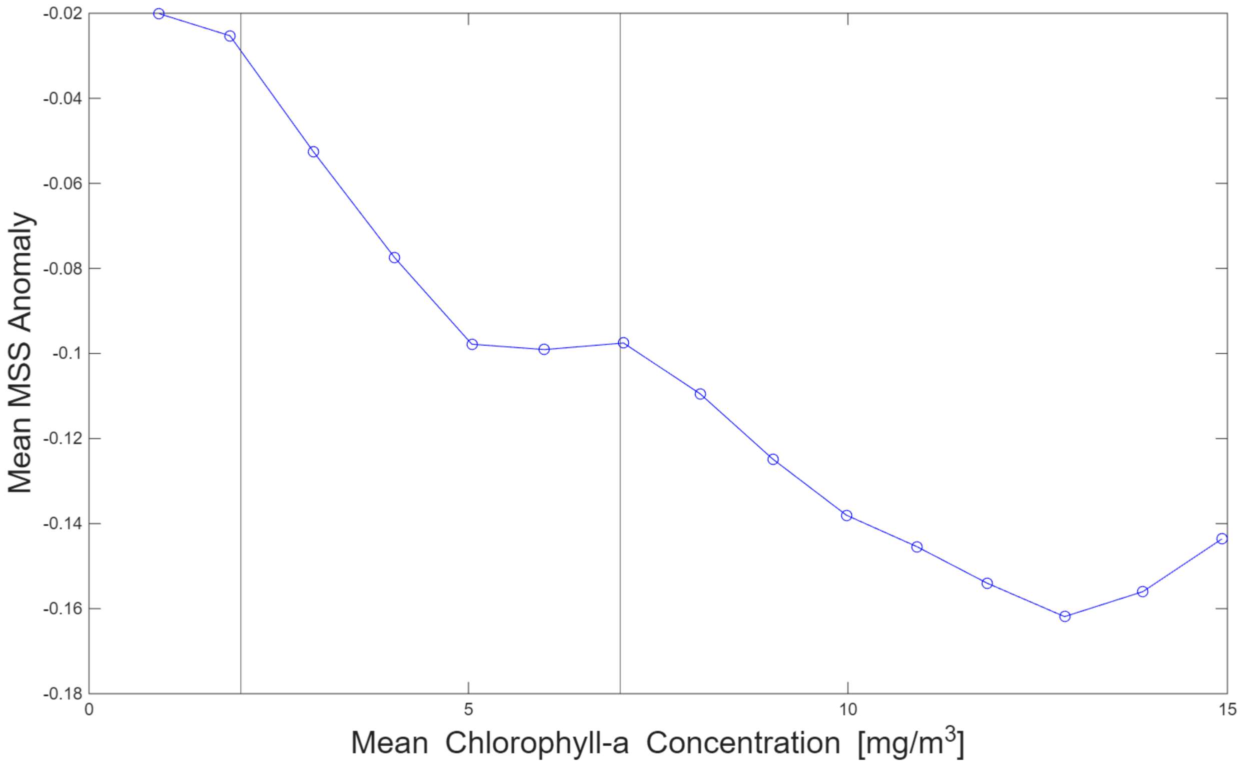

Figure 4.18: Mean chlorophyll-a and MSS Anomaly across small overlapping bins of 2 mg/m^3 each.

The drop-off in Fig. 14 slows as the concentration increases, further bolstering the quadratic relationship used in our model. The tail turning up at the end of the curve is due to both lower amounts of data in the bin, and due to overall variance.

4.4 Results

4.4.1 Validation of Retrieval Algorithm

The SWOT Algal Bloom Product is first validated by comparison to the VIIRS Gap-filled Product during the overpasses used for training the retrieval algorithm. The SWOT retrieval algorithm trained using 15 overpasses from 2024, and Fig. 4.19 is an example of the SWOT chlorophyll-a product and the VIIRS chlorophyll-a product side-by-side.

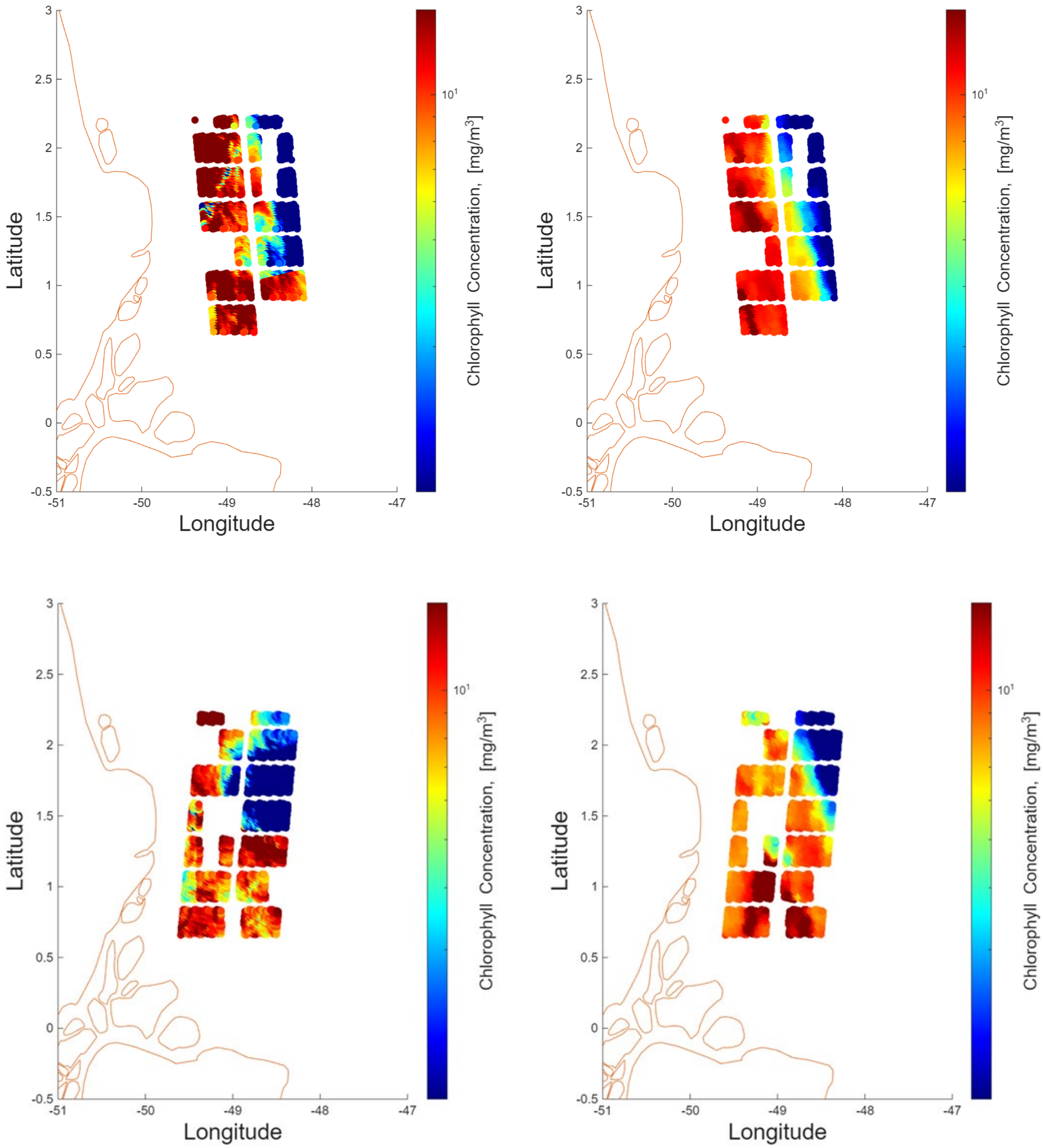

Figure 4.19: (a) SWOT (left) and VIIRS gap-filled (right) chlorophyll-a products for overpasses on 24-Jul-2024 (top) and 23-Dec-2024 (bottom).

Both overpasses show that the SWOT chlorophyll-a product follows the general trend of the VIIRS product. To get an overarching view of the product, Fig. 4.20 is a density scatter plot comparing each SWOT and VIIRS pixel 1-to-1.

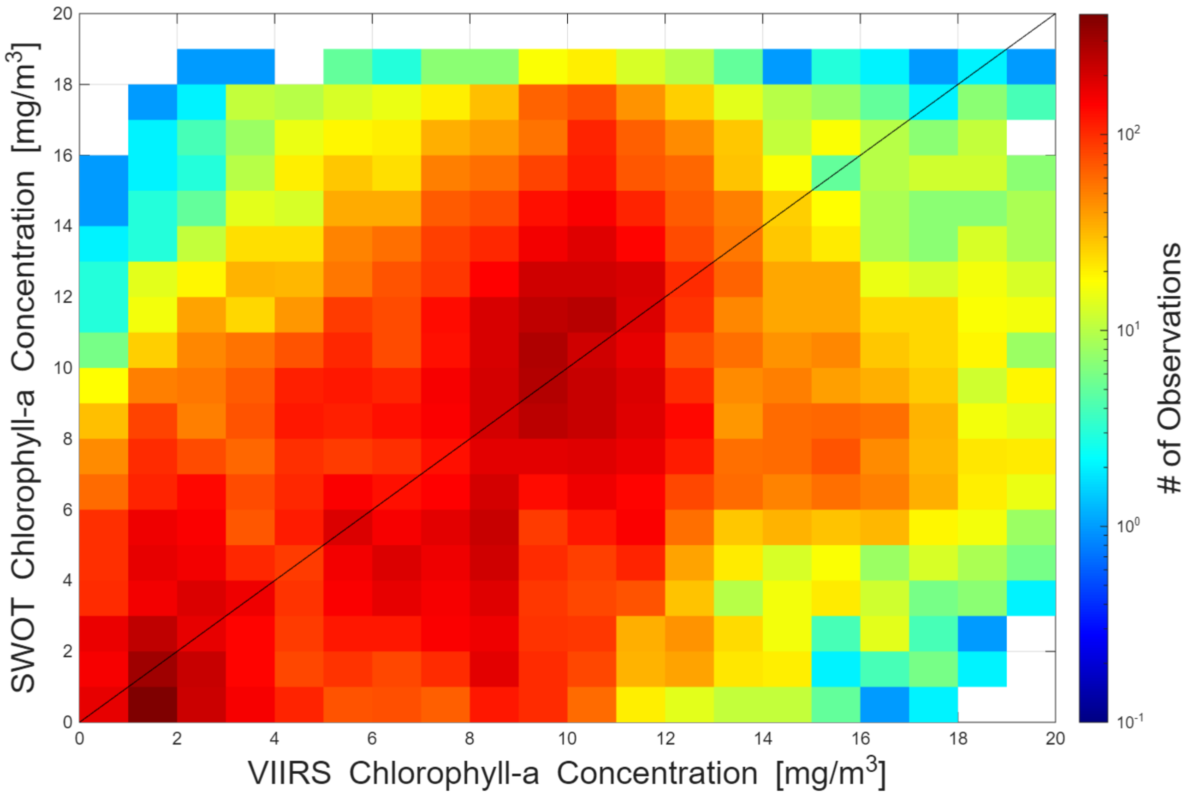

Figure 4.20: A density scatter plot comparing the SWOT chlorophyll-a data to the VIIRS chlorophyll-a data.

The highest density portion of the data in Fig. 4.20 generally follows the 1-to-1 line, but with some scatter at lower densities. Fig. 4.20 shows the results using data in the training region only. Fig. 4.21 considers data from a full overpass on one of the training days, including samples in the Atlantic Ocean far from the training region.

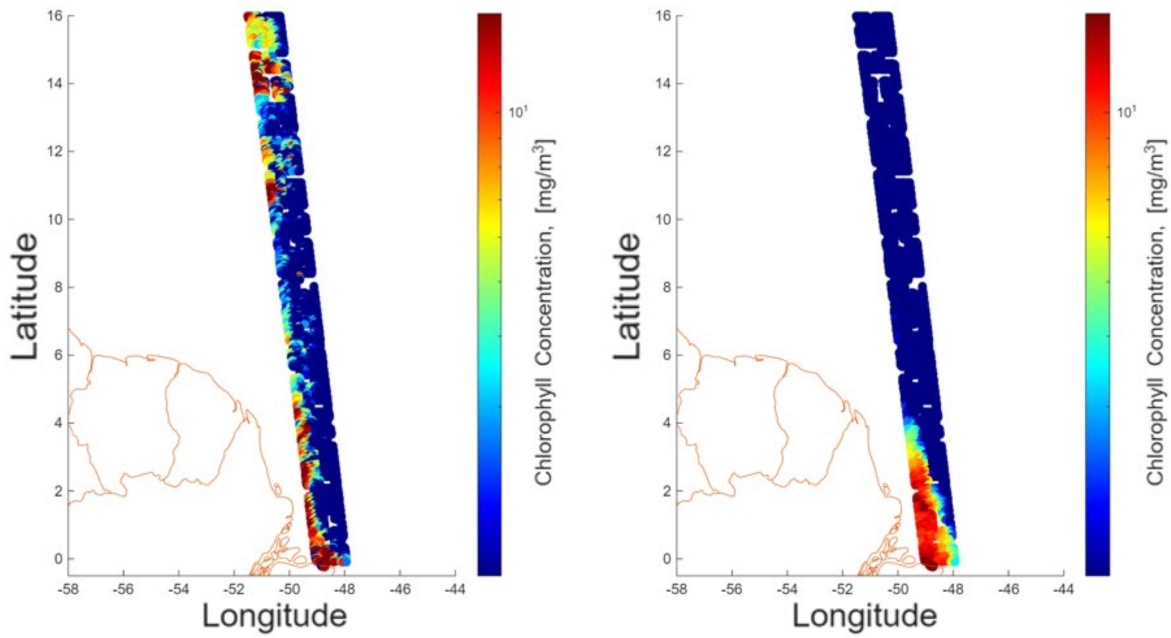

Figure 4.21: SWOT (left) and VIIRS (right) chlorophyll concentration in the Atlantic Ocean, using data from 3-Jul-2024, which was used to train the model.

As expected, VIIRS drops to near zero values when away from coastlines. Most of the SWOT data also drops to near-zero values but does show spikes of high CC in some areas where VIIRS does not have it.

4.4.2 Demonstration of Retrieval Algorithm

To evaluate the performance of the retrieval algorithm outside of the training period, it is evaluated on independent data. Specifically, the model is applied to Amazon River data acquired on days excluded from training, nearby open ocean regions where the retrieved signal is expected to remain low, and the Congo River mouth, which represents an independent river plume environment anticipated to exhibit a similar dependence between chlorophyll concentration and MSS anomaly as observed for the Amazon.

4.4.2.1 Amazon River Test Cases

Fig. 4.22 below is a comparison of SWOT and VIIRS CC in the testing region on two different (non-training) days.

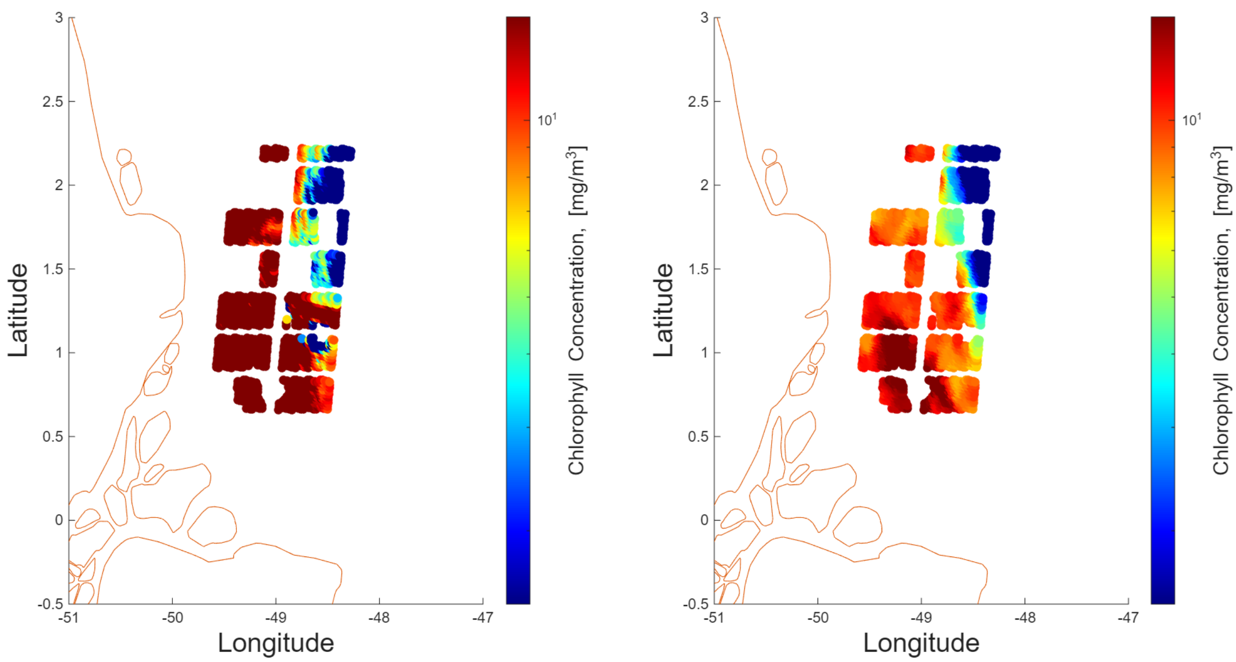

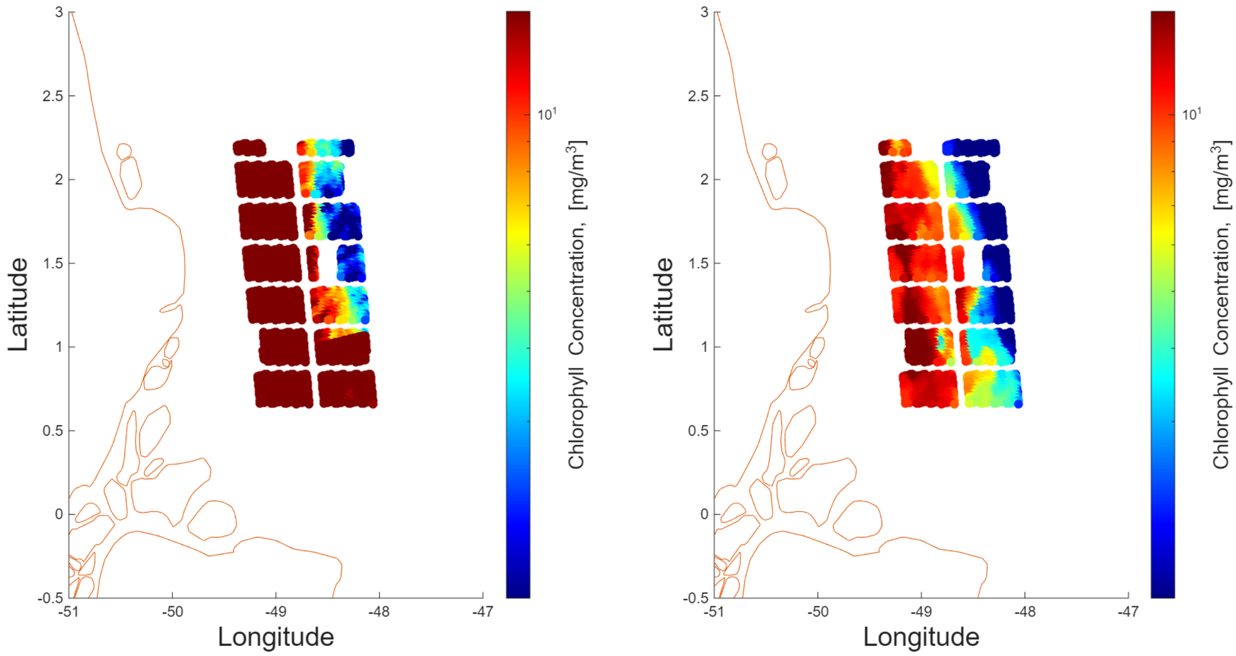

Figure 4.22: Two SWOT (left) and VIIRS (right) overpasses from the Amazon River mouth that were not used for training the model. Data are from 18-Jun-2024 (top) and 15-Oct-2024 (bottom).

Comparing the SWOT and VIIRS results for these two overpasses, there is general qualitative agreement. The boundary where the chlorophyll-a concentration drops off away from the coast generally agree for both overpasses, as does the shift in the boundary between passes. Like the training data set, a density scatter plot is made of the SWOT vs. VIIRS data during the testing data days.

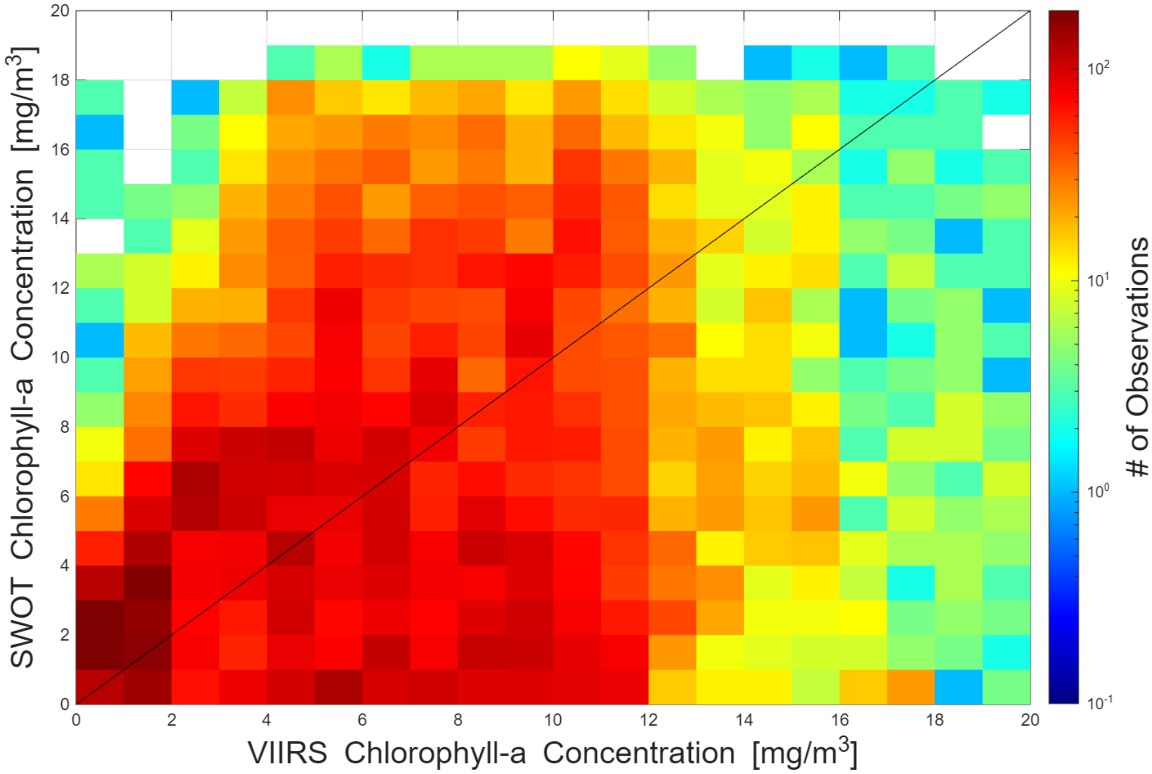

Figure 4.23: Density scatter plot between SWOT and VIIRS for the independent testing data in the Amazon River

Fig. 4.23 shows that while the comparison between SWOT and VIIRS are not perfect, there is some correlation between the two, especially at lower values of chlorophyll.

4.4.2.2 Congo River Test Cases

The SWOT CC retrieval algorithm is also evaluated near the mouth of the Congo River using the algorithm trained by Amazon River data, to assess its robustness. An example of the daily gap-filled NOAA VIIRS product near the Congo River mouth is shown in Fig. 4.24.

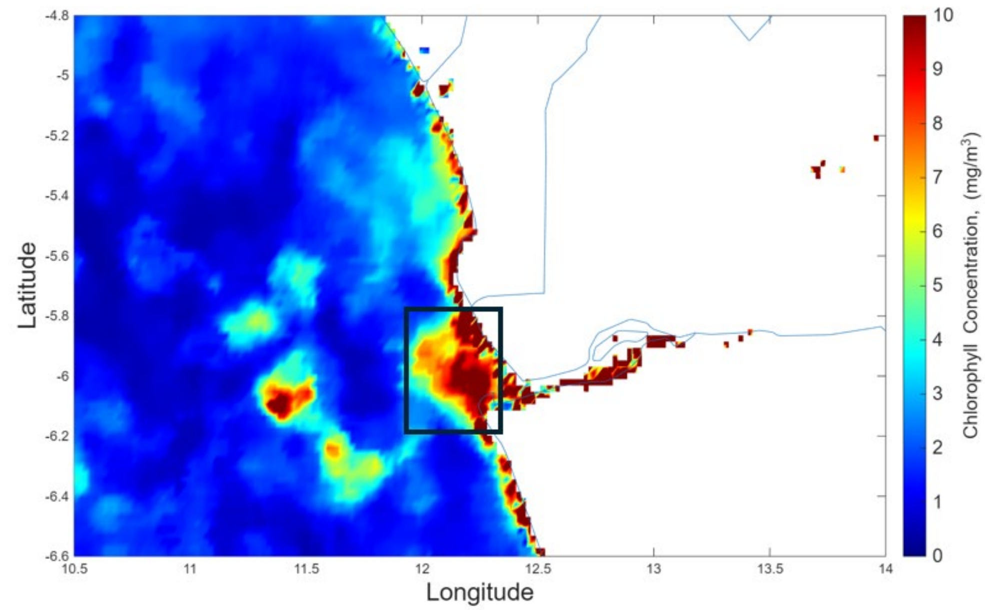

Figure 4.24: Density scatter plot between SWOT and VIIRS for the independent testing data in the Amazon River

Fig. 4.24 has chlorophyll-a concentration around the mouth of the river on 3-January-2024, with a clear algal bloom plume present near lat=6.1˚ S, lon=12.4˚ E. To obtain an accurate estimate of the plumes, a region of coastline near the mouth of the river [5.1˚-6.2˚ S, 12˚-12.4˚ E] is used as the testing zone. This region encompasses a stretch of coastline that includes both the river mouth and the adjacent outflow area. Like the Amazon River test case, the SWOT product and the VIIRS product can be compared. Fig. 4.25 is a side-by-side comparison of SWOT chlorophyll vs. VIIRS chlorophyll.

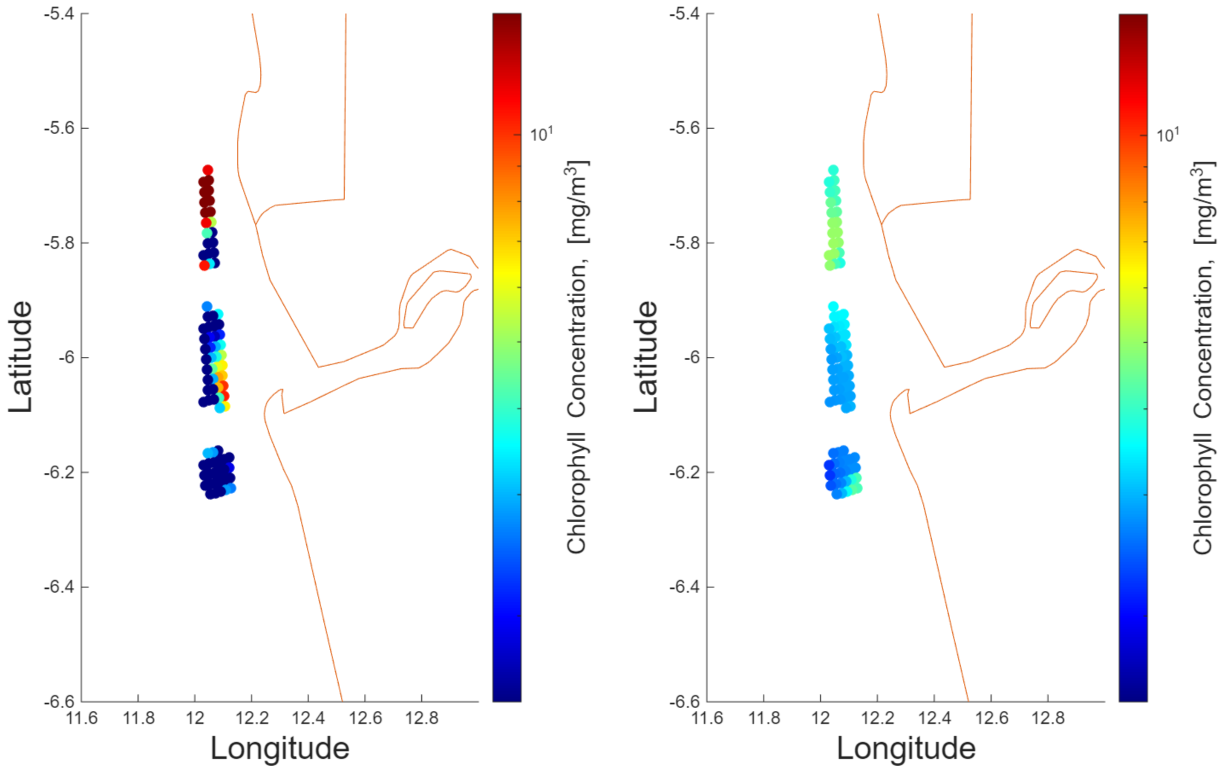
-5.4
-5.6
-5.8
-6
-6.2
-6.4
-6.6
Latitude
11.6
11.8
12
12.2
12.4
12.6
12.8
Longitude
10^1
Chlorophyll Concentration, [mg/m^3]
-5.4
-5.6
-5.8
-6
-6.2
-6.4
-6.6
Latitude
11.6
11.8
12
12.2
12.4
12.6
12.8
Longitude
10^1
Chlorophyll Concentration, [mg/m^3]

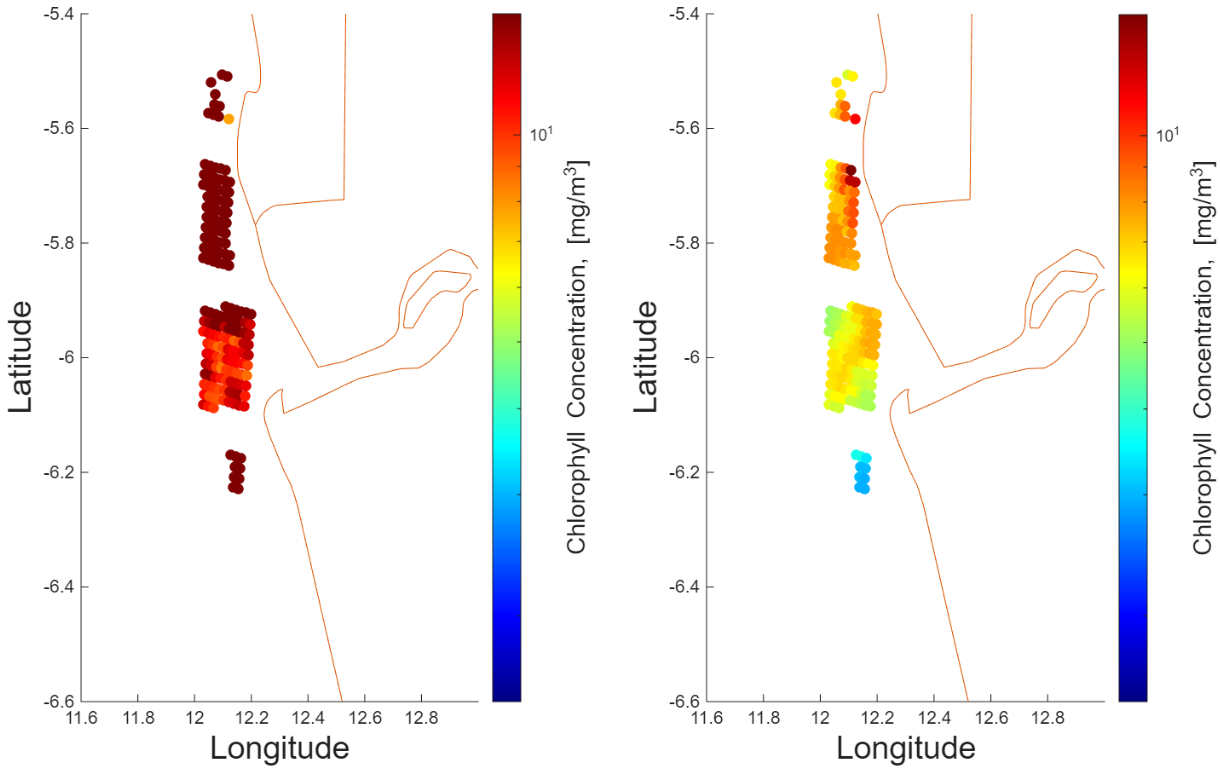

Figure 4.25: SWOT (left) and VIIRS (right) chlorophyll-a data from 21-Jul-2024 (top) and 24-May-2024 (bottom).

In both cases, the SWOT chlorophyll-a product seems to overestimate chlorophyll-a concentration near the Congo River mouth. Fig. 4.26 looks at all the data from the Congo River, in a similar fashion to Fig. 4.20 and Fig. 4.23.

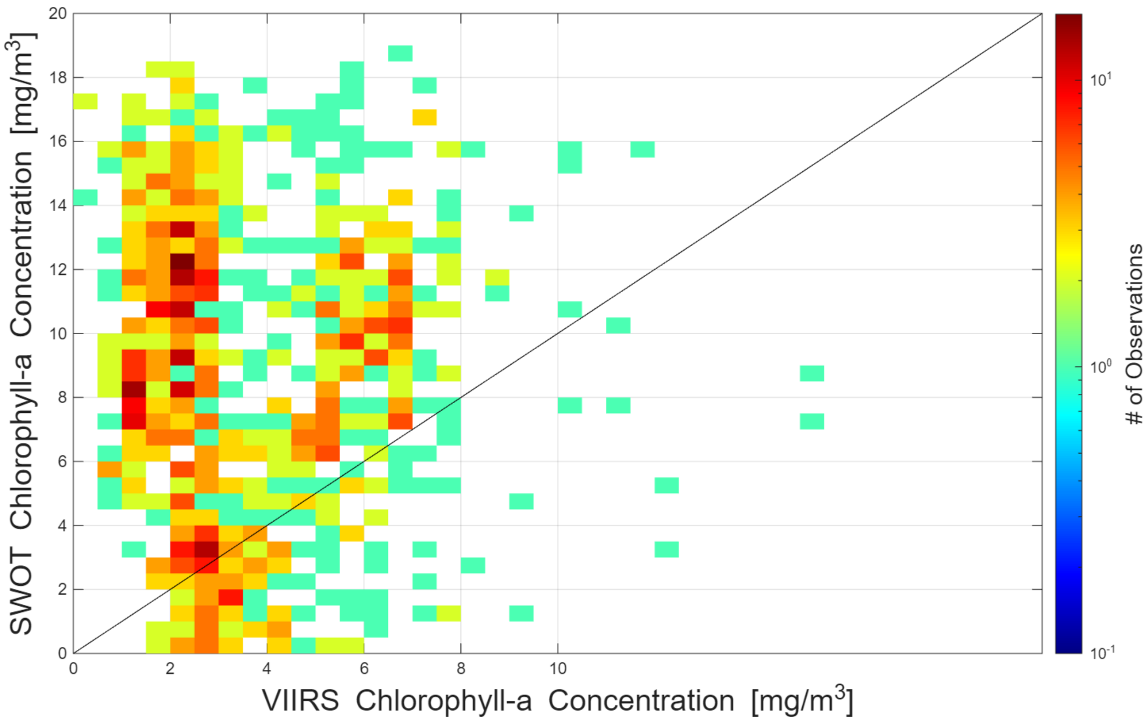

Figure 4.26: Density scatter plot of VIIRS and SWOT chlorophyll-a concentration in the Congo River during 2024.

SWOT systematically overestimates chlorophyll-a concentration in the Congo River. The Congo River on average has a much larger negative MSS Anomaly than the Amazon, due to other contaminants that are discharged from the Congo River [27]. These other contaminants may also be causing MSS Anomalies, which would impact the SWOT radar measurements. The presence of other roughness suppressing contaminants in the Congo River is likely causing false alarms in the SWOT CC algorithm.

4.4.3 Gap-filling of SWOT vs. VIIRS

The SWOT Algal Bloom Product is trained on a model that uses gap-filled chlorophyll-a data to help train this model. The gap-filled data methodology involves merging different products into 1 product. For the VIIRS product used to train the SWOT algal bloom model, it is a combination of data from the VIIRS instrument located on the Suomi National Polar-orbiting Partnership (SNPP) satellite, VIIRS on the NOAA-20 satellite and the Ocean and Land Color

Instrument (OLCI) on Sentinel-3A [28]. OLCI has a similar design to VIIRS, except it has a finer resolution and one less spectral band (21 vs. 22). Because of OLCI's band choices, it performs better closer to the coastlines. Once these three are merged, there is calibration done to ensure OLCI and VIIRS data are gridded to the same resolution. Blank pixels are then filled in using Data Interpolating Empirical Orthogonal Functions (DINEOF). DINEOF is an iterative statistical technique, which initializes missing data with the mean value, and then uses spatial and temporal patterns to reconstruct missing values based on spatiotemporal coherence [29].

On its own, however, the daily non gap-filled VIIRS product loses a lot of information from cloud cover. To show some of the coverage potential of SWOT, Fig. 4.27 is a day where the SWOT data is present, and the daily coverage of VIIRS is obscured.

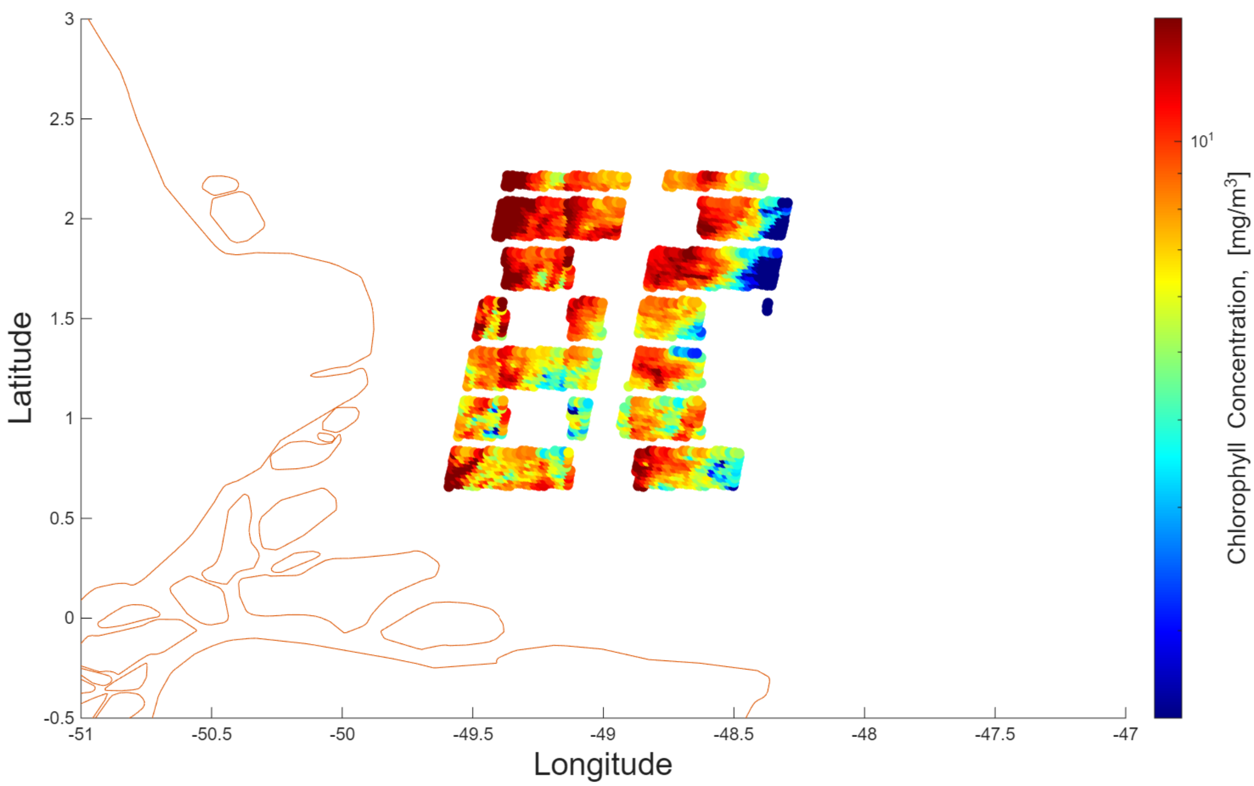

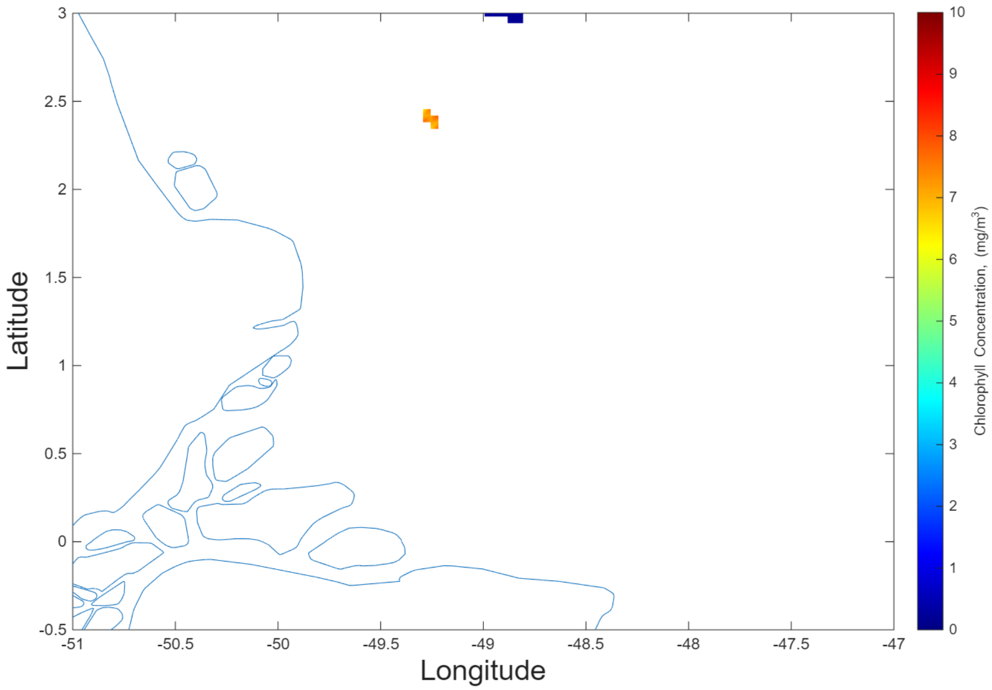

Figure 4.27: (top) SWOT chlorophyll-a data from 21-Oct-2024. Some gaps are present due to rain and σ_0 issues, but the coverage is largely gap-free. (bottom) VIIRS chlorophyll-a data from 21-Oct-2024. Cloud cover and other issues have resulted in almost all the data being flagged and removed.

This demonstrates that using an imager which is insensitive to cloud cover can help mitigate some of the issues visible wavelength imagers have in cloudy areas.

4.4.4 SWOT L3 Product Example

In addition to assessing individual SWOT overpasses, we also consider a larger scale gridded (i.e. Level 3) SWOT chlorophyll-a product. Although full spatial coverage is not achievable from SWOT at daily timescales, generating a gridded composite remains informative for visualizing spatial structure and providing a summary product. Accordingly, we consider a product aggregated across all available passes in a month, acknowledging that sampling gaps and temporal aliasing can occur. An example of such a L3 gridded SWOT chlorophyll-a product is shown in Fig. 4.28.

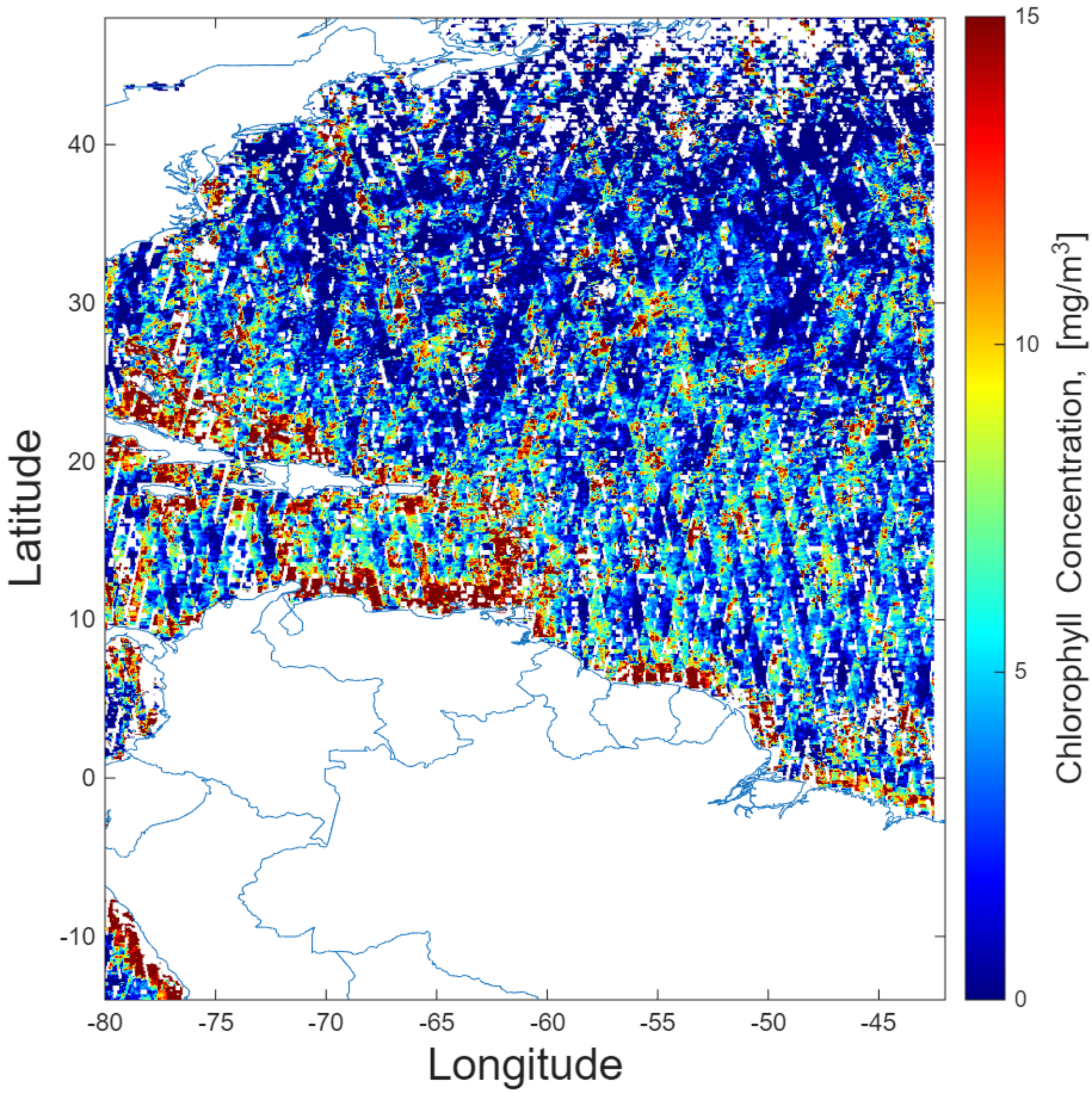

Figure 4.28: An example of a SWOT L3 Gridded Product, using data from all of January 2024.

As seen in Fig. 4.28, coastal areas tend to be areas of high chlorophyll-a, while the open ocean has some areas of high chlorophyll, but mostly medium to low chlorophyll. Looking at the Eastern Seaboard of the United States, an interesting observation is where the areas of high chlorophyll are located. The two areas of high chlorophyll along the coast are at the mouth of the

Chesapeake Bay, an area known for algal blooms [30] and the area near Cape Cod, which is around where the Gulf Stream takes water from the Eastern Seaboard into the Atlantic Ocean. This means that litter from downstream may have been caught by SWOT in this region, coming from both the Gulf Stream, and from nearby Boston and the Charles River.

4.5 Conclusions

A measure of ocean roughness (MSS) was derived from SWOT radar scattering cross section data. Deviations of the MSS from its usual value at a given wind speed (referred to as the MSS Anomaly) are derived from the SWOT data combined with ancillary ERA5 estimates of wind speed. MSS Anomaly is a measure of the suppression of wind-driven ocean surface roughening. It is attributed to the presence of marine litter on the surface. We consider algae as an example of marine litter, as detected by the VIIRS imager, and show that MSS Anomaly can be used to construct an algal bloom detection and tracking product. The product is developed empirically from matchups between SWOT-derived MSS Anomaly and VIIRS-derived chlorophyll-a concentration (CC) across the outflow region of the Amazon River into the Atlantic Ocean. SWOT and VIIRS images of CC are found to generally agree in the Amazon outflow region. The product is then applied to another location, the Congo River outflow, to evaluate the robustness of the empirical relationship between MSS Anomaly and CC. While relative trends in the two CC products agree near the Congo, there is a clear high bias in the SWOT version which is believed to be caused by the presence of other (non-algae) forms of marine litter in the region.

4.6 Discussion

The SWOT-based algal bloom product captures general features of the algal bloom distribution as shown by hyperspectral imagers. The spatial resolution of SWOT also enables a clearer depiction of coastal dynamics that are often smoothed out in coarser satellite products. This improves the ability to resolve finer scale structure in the algal bloom distribution.

However, the SWOT retrieval is fundamentally sensitive to roughness suppression rather than algal biomass directly. As a result, the algorithm flags any process that dampens short (gravity-capillary) wave surface roughness, producing false positives when interpreted as blooms. Common non-algal bloom drivers of roughness suppression include surfactant compounds unrelated to phytoplankton (natural or anthropogenic), oil or ship discharges and rain-induced damping. Some of the above results show regions of strong suppression and high retrieved concentration which do not co-locate with elevated VIIRS chlorophyll (or other ocean-color indicators), suggesting that some of the signal likely reflects these other suppression mechanisms. This is particularly evident near the Congo River.

An interesting next step for this project would be the development of a more comprehensive model for roughness suppression in which the algal product represents one component. As mentioned before, CYGNSS has an MLP that operates using the same algorithm development, and theoretically any satellite that takes measurements of σ_0 could also measure marine litter in this manner too. Therefore, creating a composite product using the strengths of the different sensors and satellite systems would be beneficial.

4.7 References for Chapter 4

1. Application of Novel Nanomaterials for Chemo- and Biosensing of Algal Toxins in Shellfish and Water. in *Novel Nanomaterials for Biomedical, Environmental and Energy Applications* 353–414 (Elsevier, 2019). doi:10.1016/B978-0-12-814497-8.00012-6.
2. Hudnell, H. K. The state of U.S. freshwater harmful algal blooms assessments, policy and legislation. *Toxicon* **55**, 1024–1034 (2010).
3. Lopez, C. B. Scientific assessment of freshwater harmful algal blooms. (2008).
4. Misiou, O. & Koutsoumanis, K. Climate change and its implications for food safety and spoilage. *Trends in Food Science & Technology* **126**, 142–152 (2022).
5. O'Reilly, J. E. & Werdell, P. J. Chlorophyll algorithms for ocean color sensors - OC4, OC5 & OC6. *Remote Sensing of Environment* **229**, 32–47 (2019).
6. Wang, M., Liu, X., Jiang, L. & Son, S. The VIIRS Ocean Color Product Algorithm Theoretical Basis Document Version 1.0. (2017).
7. Ruf, C. S. *et al.* New Ocean Winds Satellite Mission to Probe Hurricanes and Tropical Convection. *Bulletin of the American Meteorological Society* **97**, 385–395 (2016).
8. Hersbach, H. Sea Surface Roughness and Drag Coefficient as Functions of Neutral Wind Speed. *Journal of Physical Oceanography* **41**, 247–251 (2011).

9. Ulaby, F. T. and Long, D. G, “Radar Scattering” in *Microwave Radar and Radiometric Remote Sensing,* 1st ed. Ann Arbor, MI, U.S.A: UofM Press, 2014, ch. 5, sec. 5, pp. 170
10. Zavorotny, V. & Voronovich, A. Scattering of GPS signals from the ocean with wind remote sensing applications. IEEE Transactions on Geoscience and Remote Sensing 38 (2), 951–964. (2000).
11. Ruf, C.S. *et al.* “Level 2 Wind Speed Retrieval Algorithm” in *CYGNSS Handbook,* 2nd ed. Ann Arbor, MI, U.S.A: UofM Press, 2022, ch. 7 sec. 4, pp. 89
12. Evans, M. C. & Ruf, C. S. Toward the Detection and Imaging of Ocean Microplastics With a Spaceborne Radar. *IEEE Transactions on Geoscience and Remote Sensing* **60**, 1–9 (2022).
13. Evans, M. C, Ruf, C. S. & Sundaram, G. B. CYGNSS Microplastic Product Version 3.2 Algorithm Theoretical Basis Document, (2024)
14. Ruf, C. *et al.* In-Orbit Performance of the Constellation of CYGNSS Hurricane Satellites. *Bulletin of the American Meteorological Society* **100**, 2009–2023 (2019).
15. Sun, Y., Bakker, T., Ruf, C. & Pan, Y. Effects of microplastics and surfactants on surface roughness of water waves. *Sci Rep* **13**, 1978 (2023).
16. Surface Water Ocean Topography (SWOT). 2025. SWOT Level 2 KaRIn Low Rate Sea Surface Height Data Product, Version D. Ver. D. PO.DAAC, CA, USA. Dataset accessed [2026-01-14] at https://doi.org/10.5067/SWOT-SSH-D
17. Biancamaria, S., Lettenmaier, D. & Pavelsky, T. The SWOT Mission and Its Capabilities for Land Hydrology. *Surveys in Geophysics* **37**, (2016).
18. H. Hersbach et al., “ERA5 hourly data on single levels from 1940 to present,” Copernicus Climate Change Service (C3S) Climate Data Store (CDS), 2023. [Online] Available: doi:10.24381/cds.adbb2d47. Accessed: Dec. 3, 2025.
19. Ruf, C.S. *et al.* “Level 2 Mean Square Slope Retrieval” in *CYGNSS Handbook,* 2nd ed. Ann Arbor, MI, U.S.A: UofM Press, 2022, ch. 6 sec. 3, pp. 71-72
20. Li, Y. Oil spill detection based on GNSS-R. in *Oil Spill Detection, Identification, and Tracing* 145–159 (Elsevier, 2024). doi:10.1016/B978-0-443-13778-5.00011-4.
21. Liebe, H. J., Hufford, G. A. & Manabe, T. A model for the complex permittivity of water at frequencies below 1 THz. *Int J Infrared Milli Waves* **12**, 659–675 (1991).
22. Hersbach, H. *et al.* The ERA5 global reanalysis. *Quarterly Journal of the Royal Meteorological Society* **146**, 1999–2049 (2020).
23. Meissner, T. *et al*. Remote Sensing Systems SMAP Ocean Surface Salinities, Level 3 Running 8-day, Version 6.0 validated release. Remote Sensing Systems, Santa Rosa, CA, USA. Available online at www.remss.com/missions/smap, doi: 10.5067/SMP60-3SPCS (2024)
24. Tseng, Z.-E. *et al.* Distribution of Plastics of Various Sizes and Densities in the Global Ocean From a 3D Eulerian Model. *Journal of Geophysical Research: Oceans* **130**, e2025JC023272 (2025).
25. Liu, X. & Wang, M. Filling the Gaps of Missing Data in the Merged VIIRS SNPP/NOAA-20 Ocean Color Product Using the DINEOF Method. *Remote Sensing* **11**, (2019).
26. Sundaram, G.B & Ruf, C. S. (2025), Quantifying the Effects of Algal Blooms on Ocean Surface Roughness via a Wave tank experiment and Hyperspectral Imager Data, Abstract EP21B-0500 presented at 2025 AGU Fall Meeting, New Orleans, LA, 15-19 Dec. (2025)
27. Worden, S. *et al.* Congo Basin Carbon Cycle Responses to Global Change. *Glob Chang Biol* **32**, e70688 (2026).
28. NOAA NESDIS Ocean Color Science Team, NOAA CoastWatch, National Center for Environmental Information (NCEI), “Chlorophyll (Gap-filled DINEOF), NOAA S-NPP NOAA-20 VIIRS and Copernicus S-3A OLCI, Science Quality, Global 2km, 2018-recent, Daily” last updated on 01-19-2026T03:05:48,

https://coastwatch.noaa.gov/erddap/files/noaacwNPPN20S3ASCIDINEOF2kmDaily/, Accessed 01-19-2026

29. Beckers, J. M. & Rixen, M. EOF Calculations and Data Filling from Incomplete Oceanographic Datasets. *Journal of Atmospheric and Oceanic Technology* **20**, 1839–1856 (2003).
30. Rattner, B. A. *et al.* Review of harmful algal bloom effects on birds with implications for avian wildlife in the Chesapeake Bay region. *Harmful Algae* **120**, 102319 (2022).

Chapter 5 Conclusions and Future Work

5.1 Brief Review

The original motivation for this dissertation is to identify non-microplastic contributors to microwave remote sensing observations and to begin disentangling their contributions, with the goal of improving anomaly-based detections. This dissertation advances that goal by characterizing residual biases due to geophysical parameters (air-sea temperature difference and precipitation rate), demonstrating how microwave instruments can image algal blooms, and giving a first look at how to detect and track algal blooms using a high-resolution imager. Below is a summary of the results and products from this work along with potential next steps.

5.2 Summary of Contributions

5.2.1 Residual Bias Correction for ASTD and PR in C-band scatterometers and the ERA5 reanalysis winds

Chapter 2 provides a characterization of some of the residual biases in the ASCAT and ERA5 wind speed products. These small persistent biases can substantially affect derived Earth-system quantities, such as latent heat flux, with aggregate impacts on the order of terawatts when integrated over large areas. This contribution is also noteworthy because it identifies underlying causes of these errors. Anomalous Air-Sea Temperature Difference (ASTD) conditions alter the relationship between wind speed and ocean roughness. Most ASTD conditions over the ocean are slightly unstable, but specific pockets, generally where large ocean currents occur, change the stability conditions to either very unstable or neutrally stable conditions.

Precipitation related effects are well known in C-band scatterometry. However, residual errors remain, including cases where ring-wave development alters surface scattering.

These findings help explain features observed in the MSS Anomaly, especially in the cold tongue region of the Pacific ITCZ off the coast of South America.

5.2.1.1 Future Work for Chapter 2

Both ASCAT and ERA5 exhibit residual sensitivities to atmospheric stability and precipitation rate.

The buoy-based corrections applied to ERA5 were global, but buoy coverage is geographically limited, with many buoys near the coast. The ASCAT data also aligned very well with buoy data, even in areas of high bias like the Pacific ITCZ, which implies that in some of the high bias regions, the underlying bias issues may be due to ERA5, rather than ASCAT.

It would be interesting to localize where ERA5 needed to be adjusted for buoys, as in the paper a first-order global correction is given. Localizing the correction may improve anomaly interpretations in high-bias regions. One way to localize the correction for buoys is to only adjust for areas that have sufficient buoy data, inputting a buoy dependent term to adjust only near areas with ground truth.

Another approach is to use stability-dependent GMFs. Anomalous atmospheric stability conditions can change the overall relationship between roughness and wind speed, meaning that the GMF is fundamentally different for those regions. Chapter 2 shows that there are regions where ASTD is consistently anomalous throughout the year, and in those areas, it may be worth using a different GMF. This consideration applies to any GMF that uses σ_0 as an input parameter.

5.2.2 Demonstration of the ability for algal blooms to be detected by microwave remote sensing instruments

Before this work, it had not been experimentally confirmed that an L-band microwave sensor could detect algal blooms present on the ocean surface, rather than just the surfactants contained inside of the algae. Wavetank experiments were conducted that provide supporting evidence that such detection is feasible.

5.2.2.1 Future Work for Chapter 3 Part 1

Future wavetank experiments could build on these results in several ways. Including wind speeds outside of the CYGNSS range of 5-11 m/s is one way to improve the model's capabilities. Another possibility would be to find different forms of algae that could have a different effect on the water surface, as Nannochloropsis had a thin layer of algae living on its surface. The experimental design could be refined and repeated using multiple trials to improve confidence in the results.

5.2.3 MSS-Wind-Chlorophyll Concentration Model for algal blooms using an L-band microwave remote sensor

The wave tank experiment also motivated the development of a model relating MSS, wind speed, and algae concentration. Using this model, detection and tracking with an L-band sensor were evaluated and shown to be feasible (Chapter 3, 4).

5.2.3.1 Future Work for Chapter 3 Part 2

Using a similar approach to what was done for L-band, adjustments can be made to the development of the MSS process to account for Ka-band or C-band conditions. In particular, the cutoff wavenumber used to restrict the limits on the integral expression for MSS should be adjusted to account for its dependence on different satellite frequencies and measurement geometries.

5.2.4 Coastal MSS Anomaly Measurements

Before utilizing SWOT's Ka-band radar observations in this context, neither ASCAT nor CYGNSS could be used within 0.5 degrees of the coastline due to land surface signal contamination issues. Using SWOT in a manner analogous to traditional microwave approaches enables MSS Anomaly estimates to within 0.05˚ in latitude and longitude near coasts.

5.2.5 A SWOT based Algal Bloom product

Chapter 4 presents an initial demonstration of an algal bloom product using SWOT data. The SWOT algal bloom algorithm has potential for future development and use. This product will likely need to be time-averaged due to SWOT's long revisit time, but the spatial resolution to detect and track algal blooms will be finer than any microwave imager used in the past.

Microwave observations also complement hyperspectral imagers because they can acquire data under cloud cover.

5.2.6 More Future Follow Ons to this Dissertation

5.2.6.1 Adjusting the CYGNSS Microplastic Product for changes in atmospheric stability and other marine litter

The dissertation characterizes two classes of GMF error sources. This characterization can be related to CYGNSS MSS Anomaly and an adjustment could be made to the retrieval algorithm for Marine Litter to account for both the geophysical parameters and for algae. CYGNSS operates at L-band, and prior work suggests rain effects are generally small at L-band, with exceptions such as downdraft related wind variability coincident with rainfall.

5.2.6.2 Combining ASCAT, CYGNSS and SWOT measurements to create one set of MSS Anomaly

Because these approaches share σ_0 as a common observable, there is a possibility to combine the data from CYGNSS, ASCAT and SWOT, each with their own benefits. CYGNSS has high temporal coverage, with an average revisit time of 11 hours, SWOT has the spatial resolution to allow for coastal monitoring, and ASCAT allows for 1 to 3-day revisit time, with polar orbiting coverage. Each of these satellites has strengths that complement the other satellites. Therefore, a global composite product of MSS Anomaly could support more frequent marine litter detection with a wider global coverage and is a promising direction for future work.

Appendices

Appendix A: Using U_{zc}, The Ocean Current Adjusted Winds

Throughout this paper, instead of using the standard ERA5 10-meter winds, a different reference wind is used. This reference wind is the zero-current equivalent wind, denoted U_{zc}. Appendix A is dedicated to explaining why it is used.

The quantities being measured by satellite sensors are related to ocean surface properties that are influenced by the relative motion between the air and the water surface, rather than the motion of air parcels relative to an Earth-fixed coordinate system. However, conventional weather and climate models consider wind to be the air motion in relation to an Earth-fixed coordinate system, rather than a water surface relative coordinate system. Thus, a discrepancy exists between remotely sensed wind products and reanalysis wind products due to the motion of the ocean surface relative to an Earth-fixed coordinate system. The main driver of the ocean surface motion is surface currents.

Ocean currents are the continuous, predictable, and directed movements of seawater. They are driven by wind, water density differences, and gravitational tides [26]. Examples of major ocean currents include the North and South Equatorial Currents, the Gulf Stream, and the Kuroshio Current. The Equatorial Currents are located around the Intertropical Convergence Zone (ITCZ) and are primarily westward moving currents. The Gulf Stream is located at the Western boundary of the North Atlantic Ocean, and Kuroshio is located at the Western boundary of the North Pacific Ocean [27].

To account for these ocean surface currents, a new reference wind speed called the zero current equivalent wind (U_{zc}) is introduced to represent the relative motion between the atmosphere and the ocean surface. This new current-adjusted wind product is intended to assess the validity of satellite wind products more accurately and to identify the root cause of some of their previously reported regional wind retrieval biases.

Generation of a zero current equivalent wind begins with selection of a model-based wind product. The ECMWF Reanalysis v5 (ERA5) Winds [28] denoted as U_{ERA5}, are used. ERA5 data is a blend of past weather data rerun with modern weather prediction models, to help fill in the gaps the weather data missed. It provides a consistent wind speed data product on an hourly basis and a 0.2˚x0.2˚grid.

The ERA5 Winds are adjusted using the Ocean Surface Current Analyses Real-time (OSCAR) Currents, denoted as U_{OSCAR}. OSCAR Currents are released every five days on a 0.33˚x0.33˚ grid [29]. The difference in grid size is because the currents do not typically change on the same spatial and temporal scales as the winds. Because of the difference in spatial gridding, a regridding of one variable to match the other is performed. Once these two variables have been spatially and temporally gridded to match, a simple vector wise subtraction is made, given by

$$U_{zc} = |\boldsymbol{U}_{ERA5} - \boldsymbol{U}_{OSCAR}| \quad (A1)$$

Equation (A1) can be shown in component form to fully display what operations are being performed. For Eqn. 2, U is the zonal component of the data product, and V is the meridional component.

$$U_{zc} = \sqrt{(U_{ERA5} - U_{OSCAR})^2 + (V_{ERA5} - V_{OSCAR})^2} \quad (A2)$$

This vector subtraction leads to winds that are modified by the currents. This new set of modified winds is referred to as U_{zc}.

Appendix B: Fresnel Reflection Coefficients

Creating the Fresnel Reflection Coefficients requires use of equation (4), which means using ERA5 Sea Surface Temperature and SMAP Sea Surface Salinity as inputs into the Double Debye model. However, this has an incredibly computationally expensive runtime, so it was imperative to check how SST and SSS impact the Fresnel Reflection Coefficients. Fig. B.1 is an example of the change in Fresnel Reflection Coefficient over various SSTs, with constant SSS. Curves were plotted for multiple different salinities to check if changing salinity would impact the FR Coefficient.

Appendix Figure B.1: Fresnel Coefficients over SST, showing the SSS family of curves

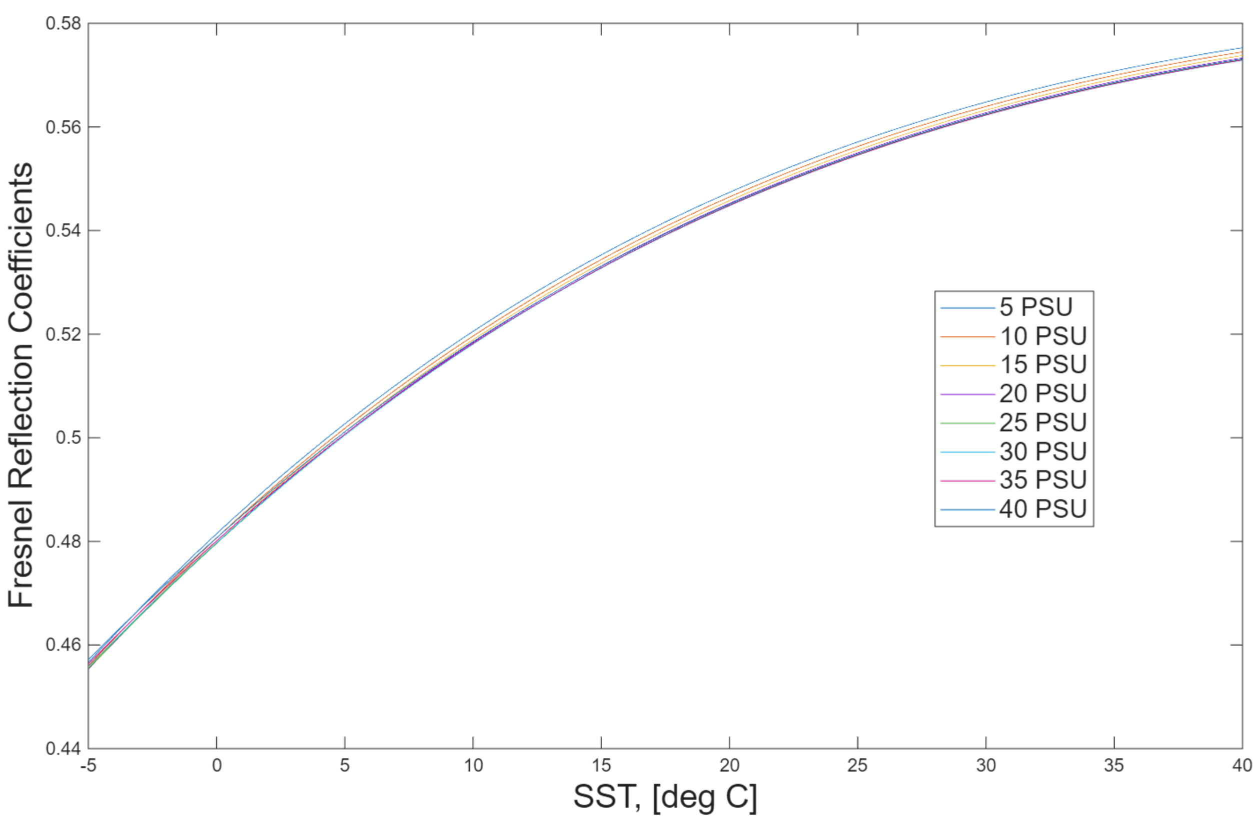

Overall, the change in FR over SST is quite minimal, but the curves start to pull apart from each other as the SST increases. Fig. B.2 is a zoom in on the region with the biggest difference between the curves.

Appendix Figure B.2: Fresnel Coefficients over SST, showing the SSS family of curves

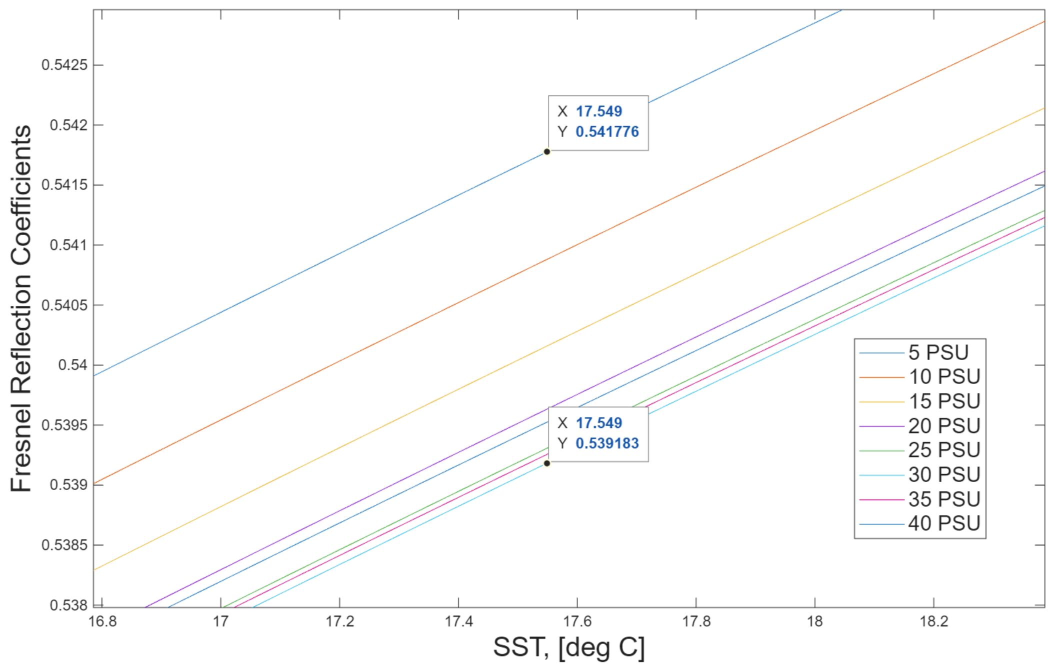

This region has the biggest split between SSS curves, with a max difference between the top curve and bottom curve of 0.0026. Even if there is a split, it may not matter. With this range of FR Coefficients [0.455-0.57], we need to see how much the FR affects MSS, and how much the difference in FR (e.g., 0.539183 to 0.541776) will affect at a given SST will change the MSS. The dynamic range we are currently using for σ_0 is 6-17.5 dB (Ren et al, 2024). Converting into linear units, this means the σ_0 used is between $10^{0.6}$-$10^{1.75}$. Fig. B.3 looks at MSS over the entire FR Coefficient range.

Appendix Figure B.3: MSS over the entire range of Fresnel Coefficients.

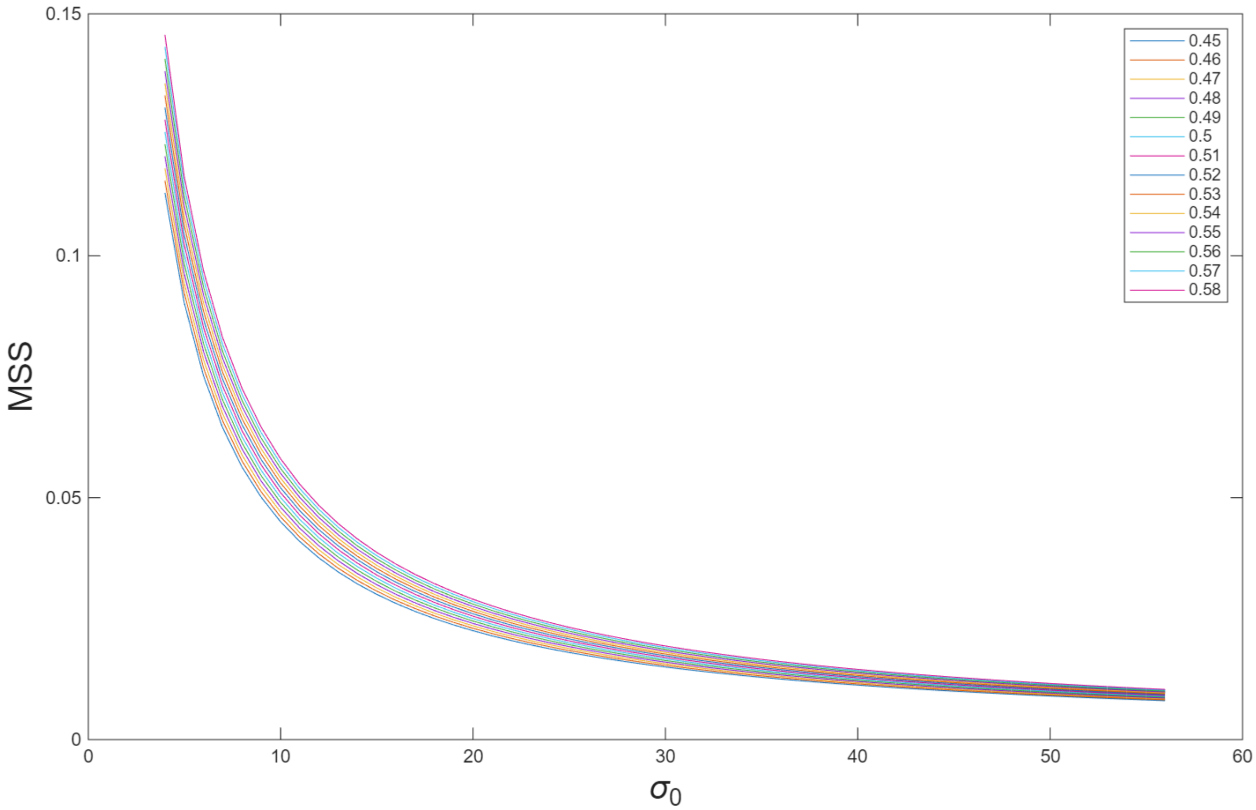

Because of the ~1/x relationship between sigma0 and MSS, this curve carries the shape of 1/x. This means the area where the MSS is most affected by FR is at low sigma0 values.

Taking two curves of FR = 0.539183 and FR = 0.541776, we can compare them and see the MSS difference along the whole curve. The two curves are plotted out in Fig. B.4.

Appendix Figure B.4: MSS over the entire range of Fresnel Coefficients.

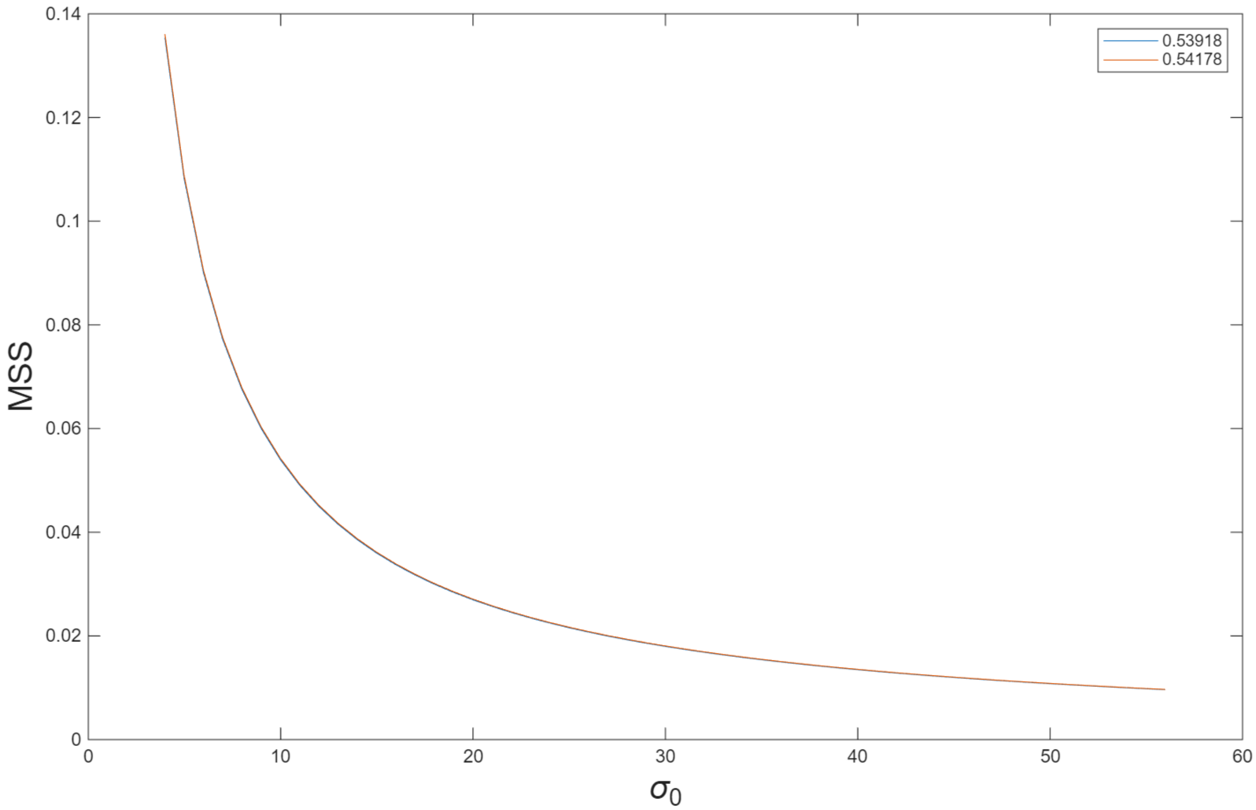

These two curves are incredibly similar. The biggest difference between these curves is $6.51*10^{-4}$, which is negligible. This shows that even the super low SSS does not affect the MSS.

The equation for the Fresnel Reflection Coefficients is

$$R(\epsilon,\theta) = \frac{1}{2}\left[\frac{\epsilon(f,T,S)\cos(\theta) - \sqrt{\epsilon - \sin^2(\theta)}}{\epsilon\cos(\theta) + \sqrt{\epsilon - \sin^2(\theta)}} - \frac{\cos(\theta) - \sqrt{\epsilon - \sin^2(\theta)}}{\cos(\theta) + \sqrt{\epsilon - \sin^2(\theta)}}\right] \qquad (B1)$$

where ε(f,T,S) is the relative dielectric permittivity of seawater, which now can be determined using just frequency and temperature. The other parameter that can affect the FR Coeff is the incidence angle. Incidence angles are varied to see the FR curves over the θ family in a similar manner to SSS.

Varying the incidence angle from 0.8-4 degrees, Fig. B5 has the family of incidence angle curves over SST.

Appendix Figure B.5: (a) FR(θ) across SST. (b) Zoomed in to show difference

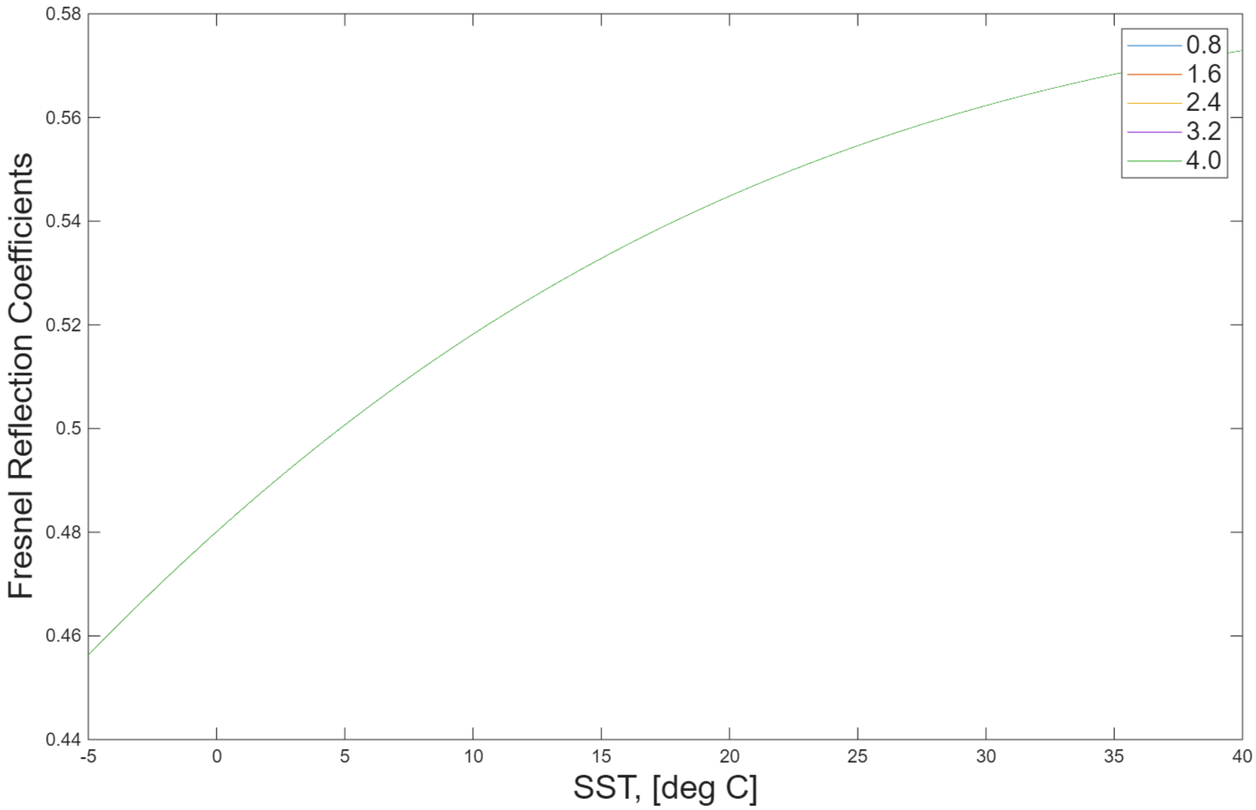

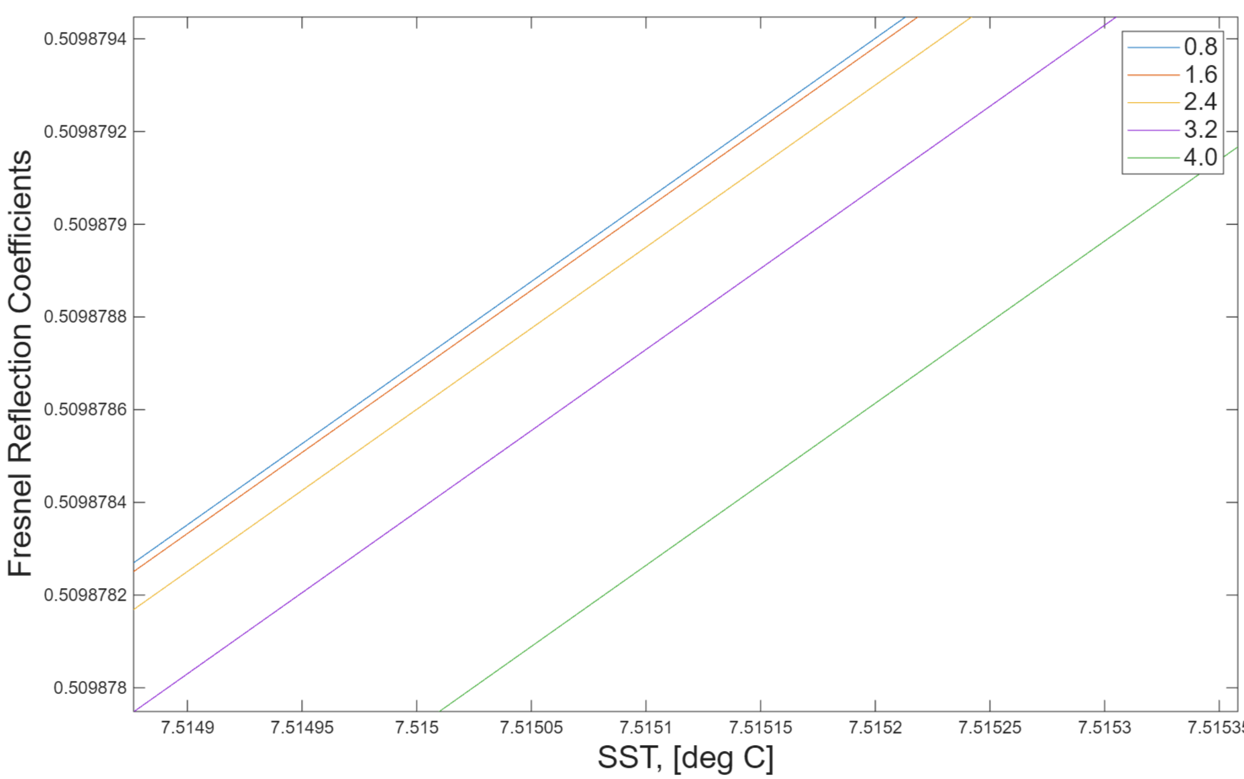

The change in FR for θ is significantly smaller than the one in FR for SSS. Therefore, θ in the FR Coefficient does not seem to matter. The change in MSS is orders of magnitude smaller than the FR change.

This makes Fresnel Reflection Coefficients dependent solely on sea surface temperature. To improve coding runtime and simplify the problem, a look-up table (LUT) is created for as close of a 1 to 1 matchup between FR Coeff and SST as possible.

Bibliography

Adak, S. Time-Dependent Spectral Analysis of Nonstationary Time Series. *Journal of the American Statistical Association*, **93** (444), 1488–1501. (1998).

Advanced Scatterometer (ASCAT) Wind Product User Manual, Version 1.17. Ocean and Sea Ice SAF Project Team, 2021

Amaral-Zettler, L. A., Zettler, E. R. & Mincer, T. J. Ecology of the plastisphere. *Nature Review Microbiology* **18**, 139–151 (2020).

Andreas, E. L. *et al.* Parametrizing turbulent exchange over summer sea ice and the marginal ice zone. *Quarterly Journal of the Royal Meteorological Society* **136**, 927–943 (2010).

Beckers, J. M. & Rixen, M. EOF Calculations and Data Filling from Incomplete Oceanographic Datasets. *Journal of Atmospheric and Oceanic Technology* **20**, 1839–1856 (2003).

Belmonte Rivas, M., and A. Stoffelen, “Characterizing ERA-Interim and ERA5 Surface Wind Biases Using ASCAT,” *Ocean Science*, vol 15, 2019.

Biancamaria, S., Lettenmaier, D. & Pavelsky, T. The SWOT Mission and Its Capabilities for Land Hydrology. *Surveys in Geophysics* **37**, (2016).

Bliven, L. F., et al., “An Analysis of Scatterometer Returns from a Water Surface Agitated by Artificial Rain: Evidence That Ring-Waves Are the Main Feature,” *International Journal of Remote Sensing*, vol 14, 1993.

Campanale, C., Massarelli, C., Savino, I., Locaputo, V. & Uricchio, V. F. A Detailed Review Study on Potential Effects of Microplastics and Additives of Concern on Human Health. *International Journal of Environmental Research and Public Health* **17**, 1212 (2020).

Crout, R., and D. Petraitis, “Physical and Meteorological Data from the Tropical Atmosphere Ocean Array in the Tropical Pacific Ocean,” *NOAA National Centers for Environmental Information Dataset*, 2025.

Delrieu, G., et al., “Quantification of Path-Integrated Attenuation for X- and C-Band Weather Radar Systems Operating in Mediterranean Heavy Rainfall,” *Journal of Applied Meteorology*, vol 39, 2000.

Dohan, K., “Ocean Surface Current Analyses Real-Time Surface Currents—Interim 0.25 Degree,” *PO.DAAC Dataset*, 2022.

Edson, J. B., et al., “On the Exchange of Momentum over the Open Ocean,” *Journal of Physical Oceanography*, 2013.

Elfouhaily, T. A. et al. A unified directional spectrum for long and short wind-driven waves. https://agupubs.onlinelibrary.wiley.com/doi/epdf/10.1029/97JC00467 doi:10.1029/97JC00467.

Evans, M. C, Ruf, C. S. & Sundaram, G. B. CYGNSS Microplastic Product Version 3.2 Algorithm Theoretical Basis Document, (2024).

Evans, M. C. & Ruf, C. S. Toward the Detection and Imaging of Ocean Microplastics With a Spaceborne Radar. *IEEE Transactions on Geoscience and Remote Sensing* **60**, 1–9 (2022).

Fairall, C. W., Bradley, E. F., Hare, J. E., Grachev, A. A. & Edson, J. B. Bulk Parameterization of Air–Sea Fluxes: Updates and Verification for the COARE Algorithm. *Journal of Climate* **16**, 571–591 (2003).

Fleagle, R. G., “Note on the Effect of Air-Sea Temperature Difference on Wave Generation,” *Eos, Transactions American Geophysical Union*, vol 37, 1956.

Foltz, G. R., et al., “Vertical Turbulent Cooling of the Mixed Layer in the Atlantic ITCZ and Trade Wind Regions,” *Journal of Geophysical Research: Oceans*, vol 125, 2020.

Foody, R., et al., “Assessing Air–Sea Surface Turbulent Heat Fluxes from Reanalyses Using Concurrent Shipboard Measurements,” *Journal of Atmospheric and Oceanic Technology*, 2024.

Gkioni, M. D. et al. Ultrasound-Assisted Extraction of *Nannochloropsis oculata* with Ethanol and Betaine: 1,2-Propanediol Eutectic Solvent for Antioxidant Pigment-Rich Extracts Retaining Nutritious the Residual Biomass. *Antioxidants* **11**, 1103 (2022).

Grachev, A. A., and C. W. Fairall, “Upward Momentum Transfer in the Marine Boundary Layer,” *Journal of Physical Oceanography*, vol 31, 2001.

Grachev, A. A., et al., “Wind Stress Vector over Ocean Waves,” *Journal of Physical Oceanography*, vol 33, 2003.

Hersbach, H., et al., “An Improved C-Band Scatterometer Ocean Geophysical Model Function: CMOD5,” *Journal of Geophysical Research: Oceans*, vol 112, 2007.

Hersbach, H. et al., “ERA5 hourly data on single levels from 1940 to present,” *Copernicus Climate Change Service Climate Data Store*, 2023. [Online] Available: doi:10.24381/cds.adbb2d47. Accessed: Dec. 3, 2025.

Hersbach, H. Sea Surface Roughness and Drag Coefficient as Functions of Neutral Wind Speed. *Journal of Physical Oceanography* **41**, 247–251 (2011).

Hersbach, H., Stoffelen, A. & de Haan, S. An improved C-band scatterometer ocean geophysical model function: CMOD5. *Journal of Geophysical Research: Oceans* **112**, (2007).

Hudnell, H. K. The state of U.S. freshwater harmful algal blooms assessments, policy and legislation. *Toxicon* **55**, 1024–1034 (2010).

Hughes, S. A. *Physical Models and Laboratory Techniques in Coastal Engineering.* World Scientific Publishing Co Pte Ltd.

Klaes, K. D. The EUMETSAT Polar System. in 192–219 (Elsevier, 2018). doi:10.1016/B978-0-12-409548-9.10318-5.

Kumar, R., et al., "Post-Launch Calibration-Validation and Data Quality Evaluation of SCATSAT-1," *Current Science*, vol 117, 2019.

Laxague, N. J. M. & Zappa, C. J. The Impact of Rain on Ocean Surface Waves and Currents. *Geophysical Research Letters* **47**, e2020GL087287 (2020).

Li, Y., et al., "Research on the Influence of Microplastics on Marine Life," *IOP Conf. Ser.: Earth Environ. Sci.,* vol 631, 2021.

Li, Y. Oil spill detection based on GNSS-R. in *Oil Spill Detection, Identification, and Tracing* 145–159 (Elsevier, 2024). doi:10.1016/B978-0-443-13778-5.00011-4.

Liebe, H. J., Hufford, G. A. & Manabe, T. A model for the complex permittivity of water at frequencies below 1 THz. *Int J Infrared Milli Waves* **12**, 659–675 (1991).

Lim, N. C. Y., et al., "Review of Temperature and Humidity Impacts on RF Signals," *2020 13th International UNIMAS Engineering Conference*, 2020.

Liu, X. & Wang, M. Filling the Gaps of Missing Data in the Merged VIIRS SNPP/NOAA-20 Ocean Color Product Using the DINEOF Method. *Remote Sensing* **11**, (2019).

Liu, Y. & Yan, X.-H. The Wind-Induced Wave Growth Rate and the Spectrum of the Gravity-Capillary Waves. *Journal of Physical Oceanography* **25**, 3196–3218 (1995).

Lopez, C. B. Scientific assessment of freshwater harmful algal blooms. (2008).

Lungu, T., "QuikSCAT Science Data Product User's Manual: Overview and Geophysical Data Products," *Jet Propulsion Laboratory*, JPL D-18053, 2001.

Marsh, R., and E. van Sebille, "Western Boundary Currents and Drifting Organisms," in *Ocean Currents,* 2021.

Meissner, T. et al. Remote Sensing Systems SMAP Ocean Surface Salinities, Level 3 Running 8-day, Version 6.0 validated release. Remote Sensing Systems, Santa Rosa, CA, USA. Available online at www.remss.com/missions/smap, doi:10.5067/SMP60-3SPCS (2024).

Misiou, O. & Koutsoumanis, K. Climate change and its implications for food safety and spoilage. *Trends in Food Science & Technology* **126**, 142–152 (2022).

Moore, R. K., and W. J. Pierson, "Measuring Sea State and Estimating Surface Winds from a Polar Orbiting Satellite," *International Symposium on Electromagnetic Sensing of the Earth from Satellites*, 1965.

Naderi, F. M., et al., "Spaceborne Radar Measurement of Wind Velocity over the Ocean-An Overview of the NSCAT Scatterometer System," *Proc. IEEE*, vol 79, 1991.

NOAA NESDIS Ocean Color Science Team, NOAA CoastWatch, National Center for Environmental Information (NCEI), "Chlorophyll (Gap-filled DINEOF), NOAA S-NPP NOAA-20 VIIRS and Copernicus S-3A OLCI, Science Quality, Global 2km, 2018-recent, Daily," last updated on 01-19-2026T03:05:48, https://coastwatch.noaa.gov/erddap/files/noaacwNPPN20S3ASCIDINEOF2kmDaily/, Accessed 01-19-2026.

Okoro, V., Azimov, U., Munoz, J., Hernandez, H. H. & Phan, A. N. Microalgae cultivation and harvesting: Growth performance and use of flocculants - A review. *Renewable and Sustainable Energy Reviews* 115, 109364 (2019).

O'Reilly, J. E. & Werdell, P. J. Chlorophyll algorithms for ocean color sensors - OC4, OC5 & OC6. *Remote Sensing of Environment* **229**, 32–47 (2019).

Pizzo, N., Deike, L. & Ayet, A. How does the wind generate waves? *Physics Today* **74**, 38–43 (2021).

Rattner, B. A. et al. Review of harmful algal bloom effects on birds with implications for avian wildlife in the Chesapeake Bay region. *Harmful Algae* **120**, 102319 (2022).

Rochman, C. M. et al. Scientific Evidence Supports a Ban on Microbeads. *Environ. Sci. Technol*. **49**, 10759–10761 (2015).

Ruf, C. S. et al. CYGNSS Handbook, 2nd ed., Michigan Publishing Services, Ann Arbor, MI, ISBN 978-1-60785-549-1, https://doi.org/10.3998/mpub.12741920, 227 pp, 2022.

Ruf, C. et al. In-Orbit Performance of the Constellation of CYGNSS Hurricane Satellites. *Bulletin of the American Meteorological Society* **100**, 2009–2023 (2019).

Ruf, C.S. et al. "Level 2 Mean Square Slope Retrieval" in *CYGNSS Handbook*, 2nd ed. Ann Arbor, MI, U.S.A: UofM Press, 2022, ch. 6 sec. 3, pp. 71–72.

Ruf, C.S. et al. “Level 2 Wind Speed Retrieval Algorithm” in *CYGNSS Handbook*, 2nd ed. Ann Arbor, MI, U.S.A: UofM Press, 2022, ch. 7 sec. 4, pp. 89.

Ruf, C. S. et al. New Ocean Winds Satellite Mission to Probe Hurricanes and Tropical Convection. *Bulletin of the American Meteorological Society* **97**, 385–395 (2016).

Schneider, N. & Gerber, M. Correlation between viscosity, temperature and total solid content of algal biomass. *Bioresource Technology* **170**, 293–302 (2014).

Seager, R., and I. R. Simpson, “Western Boundary Currents and Climate Change,” *Journal of Geophysical Research: Oceans*, vol 121, 2016.

Sun, Y., Bakker, T., Ruf, C. & Pan, Y. Effects of microplastics and surfactants on surface roughness of water waves. *Scientific Reports* **13**, 1978 (2023).

Sundaram, G. B. and C. S. Ruf, "A Zero Current Equivalent Wind Correction for Remotely Sensed Winds," *IGARSS 2024 - 2024 IEEE International Geoscience and Remote Sensing Symposium*, Athens, Greece, 2024, pp. 5973-5975, doi: 10.1109/IGARSS53475.2024.10640526

Sundaram, G. B. and C. S. Ruf, "The Detection and Tracking of Ocean Surface Roughness Suppression by Ocean Pollutants Via Surfactants," *IGARSS 2024 - 2024 IEEE International Geoscience and Remote Sensing Symposium*, Athens, Greece, 2024, pp. 6045-6048, doi: 10.1109/IGARSS53475.2024.10642822

Sundaram, G.B & Ruf, C. S. (2025), Quantifying the Effects of Algal Blooms on Ocean Surface Roughness via a Wave tank experiment and Hyperspectral Imager Data, Abstract EP21B-0500 presented at 2025 AGU Fall Meeting, New Orleans, LA, 15-19 Dec. (2025).

Sundaram, G. B. & Ruf, C. S. Identifying and Correcting for Residual Biases in the ASCAT and ERA5 Wind Speed Products. *IEEE Journal of Selected Topics in Applied Earth Observations and Remote Sensing* **19**, 1438–1451 (2026).

Sundaram, G. B. et al., Characterizing the Effects of Algal Blooms on Ocean Surface Roughness via a Wavetank Experiment and Spaceborne Radar Demonstration (*Nature: Scientific Reports, in review, 2026*).

Sundaram, G. B. & Ruf, C. S., Monitoring Coastal Ocean Pollutant Dynamics with NASA SWOT Remote Sensing Observations (*Remote Sensing, in review, 2026*).

Surface Water Ocean Topography (SWOT). 2025. SWOT Level 2 KaRIn Low Rate Sea Surface Height Data Product, Version D. Ver. D. PO.DAAC, CA, USA. Dataset accessed [2026-01-14] at https://doi.org/10.5067/SWOT-SSH-D.

Tseng, Z.-E. et al. Distribution of Plastics of Various Sizes and Densities in the Global Ocean From a 3D Eulerian Model. *Journal of Geophysical Research: Oceans* **130**, e2025JC023272 (2025).

Ulaby, F. T., and D. G. Long, "Radar Remote Sensing of the Ocean," in *Microwave Radar and Radiometric Remote Sensing*, 1st ed., 2014.

Ulaby, F. T. and Long, D. G, "Radar Scattering" in *Microwave Radar and Radiometric Remote Sensing*, 1st ed. Ann Arbor, MI, U.S.A: UofM Press, 2014, ch. 5, sec. 5, pp. 170.

Wang, M., Liu, X., Jiang, L. & Son, S. The VIIRS Ocean Color Product Algorithm Theoretical Basis Document Version 1.0. (2017).

Wang, T. et al. Improvement of CYGNSS Level 1 Calibration Using Modeling and Measurements of Ocean Surface Mean Square Slope. in *IGARSS 2020 - 2020 IEEE International Geoscience and Remote Sensing Symposium* 5909–5912 (2020). doi:10.1109/IGARSS39084.2020.9323262.

Wentz, F. J., "Measurement of Oceanic Wind Vector Using Satellite Microwave Radiometers," *IEEE Transactions on Geoscience and Remote Sensing*, vol 30, 1992.

Worden, S. et al. Congo Basin Carbon Cycle Responses to Global Change. *Global Change Biology* **32**, e70688 (2026).

Wright, J. W. & Keller, W. C. Doppler Spectra in Microwave Scattering from Wind Waves. *Phys. Fluids* **14**, 466–474 (1971).

Wu, X., Hou, L., Lin, X. & Xie, Z. Application of Novel Nanomaterials for Chemo- and Biosensing of Algal Toxins in Shellfish and Water. in *Novel Nanomaterials for Biomedical, Environmental and Energy Applications* 353–414 (Elsevier, 2019). doi:10.1016/B978-0-12-814497-8.00012-6.

Zavorotny, V. & Voronovich, A. Scattering of GPS signals from the ocean with wind remote sensing applications. *IEEE Transactions on Geoscience and Remote Sensing* **38(2)**, 951–964 (2000).